Coupled fabric deformation and infusion process simulation

A thesis accepted by the Faculty of Aerospace Engineering and Geodesy of the University of Stuttgart in partial fulfilment of the requirements for the degree of Doctor of Engineering Sciences (Dr.-Ing.)

by

Justas Sirtautas

born in Panevėžys

Committee chair:	Priv. Doz. Dr. phil. Anthony Pickett
Committee member:	Prof. Sébastian Comas-Cardona PhD
Committee member:	Prof. Dr.-Ing. Peter Middendorf
Date of defence:	December 18, 2017

Institute of Aircraft Design

University of Stuttgart

2017

Acknowledgements

I thank Dipl.-Ing. Rainer Kehrle, Prof. Dr.-Ing. Klaus Drechsler and Prof. Dr.-Ing. Peter Middendorf for the opportunity to work at the Institute of Aircraft Design (IFB). I thank all my colleges there for unlimited help and support, especially Faserverbund team for unforgettable years together.

Faserverbund team posing casually, December 2014

I thank my supervisor Priv.Doz. Dr.phil. Anthony Pickett for raising the INFUCOMP project financed by European Commission 7th Framework Program, Grant 233926. The project joined efforts of excellent partners on development of infusion simulation technologies for large composite structures. Small part of experience gained is summarised in this thesis under thorough guidance of my supervisor.

For countless discussions and suggestions I thank Dr. Andrew George, whose shoes I have found extremely difficult to fill. I thank Priv.Doz. Dr. Iryna Rybak for the proof-reading, Dr. Anton Tkachuk, Dr. Dmytro Meshcheriakov and Dr. Laurynas Naujokaitis for continuous encouragements and most welcome distractions during the last years. I also thank my family, who was always supportive in all of my aspirations.

Last but not least I thank a girl with a book of Jules Verne in hand.

September 1, 2017 Justas Sirtautas
Panevėžys

Contents

Abstract

The increased interest in high performance composites has led to development of new materials and manufacturing processes and, in turn, an increased demand for simulation tools and modelling techniques. Reliable prediction of manufacturing feasibility and mechanical properties of yet non-existent parts in a virtual environment would save a vast amount of time and resources and contribute to the further widespread use of advanced composite technologies over a greater spectrum of industries supporting everyday life.

In the field of composite preforming increased computing power has reached a level that allows meso-scale (tow) analysis of moderate size (500x500 mm) preforms. Such detailed Finite Element simulation provides certain advantages compared to today's industrial-level macro-scale simulations including increased number of controlled model parameters, new opportunities for simulation of manufacturing processes and greater potential to couple simulation steps in the process chain. In principle, the same physical model (mesh) can be sequentially used for preforming, infusion and mechanical performance simulations all on the same analysis scale.

In this thesis a coupled meso-scale draping and infusion simulation approach of a single layer of biaxial non-crimp fabric with a chain stitch is developed and presented. The approach incorporates mechanical testing and necessary calibrations to characterise fibrous tows and stitch thread, and to represent major fabric deformation modes such as compaction, in-plane shear and bending. Frictional contact between fabric tows and plies is taken into account in the model. Finally, a validation of the constitutive law and modelling methodology is done using a hemisphere draping test, where necessary draping force and resulting shear angle over the circumference are compared with experimental measurements.

Subsequent infusion simulation of the draped hemisphere using measured and estimated permeability parameters has demonstrated feasibility of the coupling the two processes. The need for permeability parameters calibration was observed for certain states of fabric shear deformation. Generally, however, good agreement to the experiments was obtained; additionally, comparison with state-of-the-art macro-scale draping and infusion analysis was made to highlight the advantages and benefits to undertake a meso-scale modelling approach. Some suggestions for meso-model improvement were made, and possibilities for further development of the modelling methodology discussed.

Lastly, simulation of a vacuum assisted resin infusion (VARI) process was undertaken for material permeability characterisation purposes. Analysis included characterisation of preform permeability as function of its compliance. This was necessary because variation of pressure field in time and space during VARI process leads to substantial change of preform thickness and fibre volume

fraction altering the overall flow behaviour. Detailed numerical analysis of through-thickness flow in a preform with distribution media (DM) on top showed that DM permeability has to be defined as orthotropic at the chosen macro-modelling scale. Infusion simulation results from current commercial and an in-house code dedicated to VARI process simulation were compared to experimental observations. Despite many simplifications made, dedicated VARI process simulation tool predictions were observed to provide better estimation compared to a state-of-the-art commercial simulation tool dedicated to RTM infusion.

Deutsche Zusammenfassung

Ein hohes Interesse an den leistungsfähigen Faserverbundwerkstoffen hat eine Entwicklung von enormer Vielfältigkeit an Materialien und Herstellungsprozessen mit einem wachsenden Bedarf an entsprechenden Simulationsmethoden veranlasst. Zuverlässige virtuelle Vorhersagen von Machbarkeit und mechanischen Eigenschaften sparen viel Zeit und Kosten und tragen bei der weiteren Verbreitung von Faserverbundwerkstoffen in alltäglichen Branchen bei.

Heutzutage ist die Rechenleistung ausreichend groß um ein Bauteil (Modell) von 500x500 mm Größe in mesoskopischem Maßstab (Diskretisierung einzelner Faserbündel) zu berechnen. Solche detaillierten Analysen besitzen Vorteile gegenüber makroskopischen Simulationen (Industriestandard), da mehr Modellparameter vorhanden sind und es möglich ist, verschiedene Herstellungsprozesse zu modellieren und diese miteinander zu koppeln. Hierbei kann im Prinzip das gleiche Modell, im gleichen Maßstab in mehreren Simulationsschritten (Drapierung, Infusion und mechanische Berechnung) genutzt werden.

Ein gekoppeltes mesoskopisches Modell für Drapierung und Infusion für biaxiale Kohlenstofffasergelege mit kettförmigem Naht wurde in dieser Dissertation entwickelt. Die Methode beinhaltet eine Materialkennwertermittlung von Faserbündel und Naht zur Charakterisierung der wichtigsten Deformationsformen, nämlich Kompaktierung, Scherung und Biegung. Zusätzlich wurde auch die Reibung zwischen Faserbündeln und Einzellagen berücksichtigt. Eine Modellvalidierung wurde im Experiment durch den Vergleich des Scherwinkels, sowie der Drapierkraft anhand der Drapierung einer Hemisphäre erzielt.

Die anschließende Infusionssimulation der Hemisphäre zur Kopplung der beiden Prozesse wurde demonstriert und die Vorteile und Möglichkeiten aufgezeigt. Permeabilitätskennwerte wurden in Versuchen ermittelt, eine zusätzliche Kalibrierung für bestimmte Deformierungszustände der Modelle war notwendig. Generell wurde eine gute Übereinstimmung mit den experimentellen Versuchen erreicht. Ein Vergleich mit der makroskopischen Simulation zeigte die Vorteile der mesoskopischen Modellierung. Einige Verbesserungsvorschläge für mesoskopische Modelle und Möglichkeiten der Weiterentwicklung der Modelle wurden vorgeschlagen.

Abschließend wurde eine Vakuum Assisted Resin Infusion (VARI) Simulation durchgeführt um die Textilpermeabilität zu charakterisieren. Die Analyse beinhaltete eine geeignete Kompaktierungscharakterisierung der Gelegehalbzeuge beziehungsweise die Bestimmung der Permeabilität abhängig vom Kompaktierungszustand des Textils. Das ist notwendig, weil das auf die Preform wirkende Druckfeld während der VARI Infusion nicht konstant ist. Vielmehr variiert das Druckfeld abhängig von der Fließfrontposition und verursacht wesentliche Änderungen in Dicke und Faservolumengehalt der Gelegehalbzeuge, was auf den gesamt Infusionsprozess eine Auswirkung hat. Detaillierte numerische Analyse von Infiltrationen in die Preformdickenrichtung mit eine Lage

Fließhilfe auf der Oberseite der Preform haben gezeigt, dass die Permeabilität der verwendeten Fließhilfen in dem betrachteten Mesoanalysemaßstab als orthotrop definiert werden muss. Die Simulationsergebnisse wurden mit einer kommerzielle Software und einem dedizierten VARI in-house Programm erzielt, und anschließend mit Versuchsergebnissen verglichen. Trotz vieler Vereinfachungen des dedizierten VARI Programms konnten bessere Ergebnisse im Vergleich mit der kommerziellen Software erzielt werden.

Nomenclature

Acronyms

BC – Boundary Condition
CAPRI – Controlled Atmospheric Pressure Resin Infusion
CFD – Computational Fluid Dynamics
CV – Control Volume
CPU – Central Processing Unit
CRTM – Compression Resin Transfer Moulding
DIC – Digital Image Correlation
DM – Distribution medium
DOF – Degree of Freedom
FE – Finite Element
FEM – Finite Element Method
HP-CRTM – High Pressure Compression Resin Transfer Moulding
HP-IRTM – High Pressure Injection Resin Transfer Moulding
I/CM – Injection/Compression Moulding
LRI – Liquid Resin Infusion
MRI – Magnetic Resonance Imaging
NCF – Non-Crimp Fabric
RIFT – Resin Infusion under Flexible Tooling
RTM – Resin Transfer Moulding
RVE – Representative Volume Element
SCRIMP – Seemann Composite Resin Infusion Moulding Process
UC – Unit Cell
UD – Uni-Directional
VAP – Vacuum Assisted Process
VARI – Vacuum Assisted Resin Infusion
VARTM – Vacuum Assisted Resin Transfer Moulding
VI – Vacuum Infusion

Variables

A – Cross section area, m^2

A_e – Empirical coefficient, m^2

A_s – Spring constant, Pa

b – Width, m

C – Pressure decay coefficient, -

C_c – Linear dashpot characteristic, Pa

C_1 – Fibre arrangement coefficient, -

c_1 – Unsheared fabric constant, m^2

c_2 – Unsheared fabric constant, m^2

Ca^* – Modified capillary number, m

D – Relaxation index, -

d – Equivalent racetrack channel width, m

D_f – Fibre diameter, m

d_{PF} – Picture frame displacement, m

E – Stiffness modulus, Pa

E_c – Slope of compression stress-strain curve, Pa

F – Force, N

F' – Force offset value, N

F_{ele} – Element force, N

F_f – Form factor, -

F_N – Normal force, N

$F_{normalised}$ – Normalised force, N

F_s – Shear force, N

g – Gravitational acceleration, m/s^2

G_b – Bending stiffness modulus, N/m^2

H – Height, m

h – Thickness, m

h_i – Thickness of the *i*-th layer, m

I – Moment of inertia, m^4

K – Permeability, m^2

k_e – Empirical constant, -

k – Carman-Kozeny coefficient, m^2

K_{gap} – Gap permeability, m^2

K_{Li} – Permeability of *i*-th layer, m^2

$\mathbf{K}_{tow}$ – Tow permeability tensor, m^2

K_{xx} – Permeability in x-axis direction, m^2

K_{yy} – Permeability in y-axis direction, m^2

K_{zz} – Permeability in z-axis direction, m^2

K_{xx_fabric} – Fabric permeability, m^2

K_{xx_tow} – Tow permeability, m^2

$K_{\perp}$ – Permeability in perpendicular direction, m^2

k_0 – Shape factor, -

L – Flow front position, m

l – Straight line length, m

l_b – Bending length, m

L_b – Overhang length, m

l_e – Real flow length, m

L_{fabric} – Fabric specimen effective side length, m

L_{frame} – Picture frame side length, m

L_s – Specimen length, m

L_0 – Initial length of the diagonal, m

l_2 – Weft yarn spacing, m

aL – Displacement, mm

al_{ele} – Element elongation, mm

m – Mass, kg

m_s – Stiffening coefficient, -

m_e – Empirical coefficient, -

n – Material parameter, -

n_{ele} – Number of elements, -

N_{stitch} – Number of stitch rows, -

P – Pressure, Pa

P_0 – Initially applied pressure, Pa

Q – Flow rate, m^3/s

q – Distributed load, N/m

q_{crit} – Critical damping coefficient, -

R – Flow front radius, m

r_f – Fibre radius, m

R_0 – Inlet pipe radius, m

S_0 – Specific surface, -

T – Period, s

t_2 – Weft yarn width, m

t – Time, s

v – Velocity, m/s

V_f – Fibre volume fraction, -

V_{f_fabric} – Fabric fibre volume fraction, -

V_{f_gap} – Gap volume fraction, -

V_{f_max} – Maximal fibre volume fraction, -

V_{f_tow} – Tow volume fraction, -

$V_{f\theta}$ – Fibre volume fraction at shear angle θ, -

V_{f0} – Initial fibre volume fraction, -

W – Width of the specimen, m

Greek symbols

$\sim$ – Permeabilities ratio in undeformed state, -

$\bar{\sim}$ – Permeabilities ratio in deformed state, -

γ – Shear angle, deg

γ_{max} – Maximal shear angle, deg

γ_{st} – Surface tension, Pa

δ – Displacement, m

Φ – Transverse flow factor, -

θ – Fibre angle, deg

θ_i – Ply angle of the i-th layer, deg

θ_{lock} – Locking angle, deg

θ_{ply} – Ply angle, deg

θ_{PF} – Picture frame angle, deg

© – Softening coefficient, -

α_f – Friction coefficient, -

$\alpha_{f\_average}$ – Average friction coefficient, -

« – Viscosity, Pa·s

° – Density, kg/m^3

$\pm_{fibre}$ – Normal fibre stress, Pa

² – Shear stress, Pa

S – Aerial density, kg/m^2

¤ – Porosity, -

µ – Angular frequency, s^{-1}

1 Introduction

“Anything one man can imagine, other men can make real”.

Jules Verne

Generations inspired by Jules Verne have made marvellous things possible. Rapid industrial advancement, however, has come at a heavy price. Depleted resources, environmental pollution and climate change will, inevitably, negatively affect the future of humanity on Earth. “Green” technologies are a necessity that must be developed and implemented as soon as possible. Replacing fossil fuel technologies with completely carbon dioxide neutral propulsion concepts will be of greatest priority, and challenges are hardly to be underestimated.

The ever growing transportation market is responsible for over 14% of human created greenhouse emissions worldwide in 2014 [1] with about 20% in the EU [2] to date. A crucial step in reducing this amount will be development of new materials and design concepts that allow weight reduction and increase the overall efficiency when paired with new propulsion systems. Having in mind the rate of road and air transportation market growth worldwide, ground-braking innovations will have to be made to achieve a positive effect.

In order to cope with these challenges lightweight structures will be essential, and carbon fibre reinforced plastics are a popular choice for high-tech applications providing higher stiffness/strength to weight ratio compared to conventional steels and aluminium alloys. Technological processes involving reinforcing textiles are relatively new (since ca.1950) and have evolved constantly. Pre-preg (pre-impregnated) autoclave manufacturing represents the high-end (and most expensive) technology for load bearing parts, using which manufacture of full airliner section have been possible in recent years. However, with the spread of composites technologies over a wider spectrum of industries, an optimal balance between performance, quality and cost must be achieved for effective industrialisation.

Alternative composite technologies will be necessary to replace costly pre-preg methods. For example, one promising concept is the use of dry preforms (e.g. woven or stitched multi-directional fabrics) that can be shaped into complex forms and then impregnated using LRI (Liquid Resin Infusion) processes. Technologies such as Tailored Fibre Placement [3], or braiding [4], can potentially provide a ready to infuse part, distinguishing itself by optimised design and nearly net shape manufacture. However, in order to cope with the increasing complexity of these materials and

their applications it will be essential to develop numerical methods so that optimal manufacturing processes can be created and the final part performance optimised.

In recent years growing computational power has made composite material modelling at an ever finer scales possible, as illustrated in Figure 1.1. Kinematic mapping and macro-scale approaches for draping simulations at research level are now slowly being replaced by meso-scale models, which makes coupling between several manufacturing steps feasible and potentially more accurate ([5], [6]). Furthermore, these techniques open new possibilities such as fabric structure optimisation at an early material design stage [7].

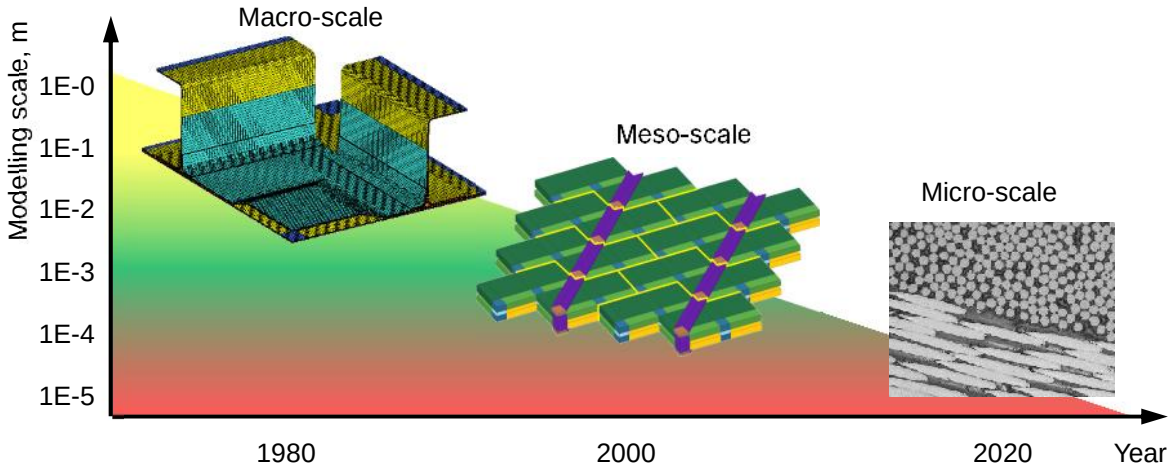

Figure 1.1 Composite materials modelling scales

A large variety of textile reinforcement types is available, which makes any experimental design approach a daunting undertaking. Prediction of whether certain geometries can be draped using certain type of fabrics and, subsequently, properly infiltrated is a challenging task, either experimentally or virtually. A thorough understanding of draping and infusion processes is important because they have a direct impact on final part mechanical performance.

One aspect of research in this thesis concentrates on coupling between forming and infusion processes for a biaxial non-crimp fabric at the meso-scale. A finite element model is proposed that is capable to represent major fabric deformation mechanisms such as compaction, shear and bending including inter-tow friction phenomena. This is done by combining two existing material constitutive laws to represent lengthwise stiff but transversely compliant fibre tows. The fabric model is constructed from 3-D linear solid finite elements representing tows and bar finite elements representing stitches; these two constituents are connected by a tied elements with appropriate constraints. Mechanical tests were performed on fabric specimens to obtain input data for calibration of the fabric drape model.

Subsequent infusion analysis requires that both tow and gap domains are properly represented. Gaps between the tows are ‘filled’ with ‘null’ solid elements, which have no influence on draping

behaviour, and are used only to accommodate flow during an infusion simulation. As will be shown stitches influence resin flow behaviour considerably, thus dedicated solid elements are used to create a stitch flow domain with appropriate constraints to retain stitch geometry during the draping process simulation.

A hemisphere draping and infusion simulations were performed at the macro- and meso-scales to demonstrate advantages and limitations of the two modelling techniques, and validate the new meso-scale approach. Conventional macro-scale simulation, despite being CPU efficient, cannot account for flow in stitch domain and properly predict flow propagation in the chosen type of biaxial non-crimp fabric. Meso-scale analysis, on the other hand, showed the potential to correctly represent an infiltration process for the chosen fabric. Permeability characterisation of tow, gap and stitch domains, though, still needs to be improved as many calibration parameters were found necessary for realistic results with the current model.

A small demonstrator part study of VARI (Vacuum Assisted Resin Infusion) process in 2D at macro-scale is presented to highlight the need for dedicated simulation tools which are able to couple permeability and preform compliance during the infusion process. Such simulation requires material permeability data as a function of fibre volume fraction (or compaction pressure), which must be obtained experimentally or numerically. In this instance, experimental measurements of fabric permeability at fixed fibre volume fractions, compaction tests and preform thickness change measurements during VARI process were combined with numerical analysis to properly characterise fabric compliance and permeability.

The topics mentioned above are covered in 9 chapters of this thesis, which have a general structure as follows:

1. Introduction;
2. Literature review (fabric mechanical properties determination tests and corresponding modelling strategies, permeability tests methodology and infusion simulation);
3. Permeability measurements for selected fabrics and other media used in this thesis;
4. Fabric characterisation tests and coupled macro-scale drape-infusion simulation;
5. Coupled meso-scale drape-infusion simulation;
6. LRI process simulation at macro-scale (VARI process simulation at 2D);
7. Discussion;
8. Conclusions;
9. Future work.

2 Literature review

A review of major deformation mechanisms in a preform and the main moulding technologies are presented in this chapter. Also, macro- and meso-scale modelling approaches for fibrous reinforcement, permeability measurement strategies and infiltration process simulation are reviewed.

2.1 Preform mechanical behaviour and modelling

Combinations of various fabric types and manufacturing methods has led to a large number of possible arrangements and configurations of technical textiles, which can be selectively exploited in many distinct applications. Major textile preform types derived from various 2D and 3D manufacturing techniques are listed in Figure 2.1.

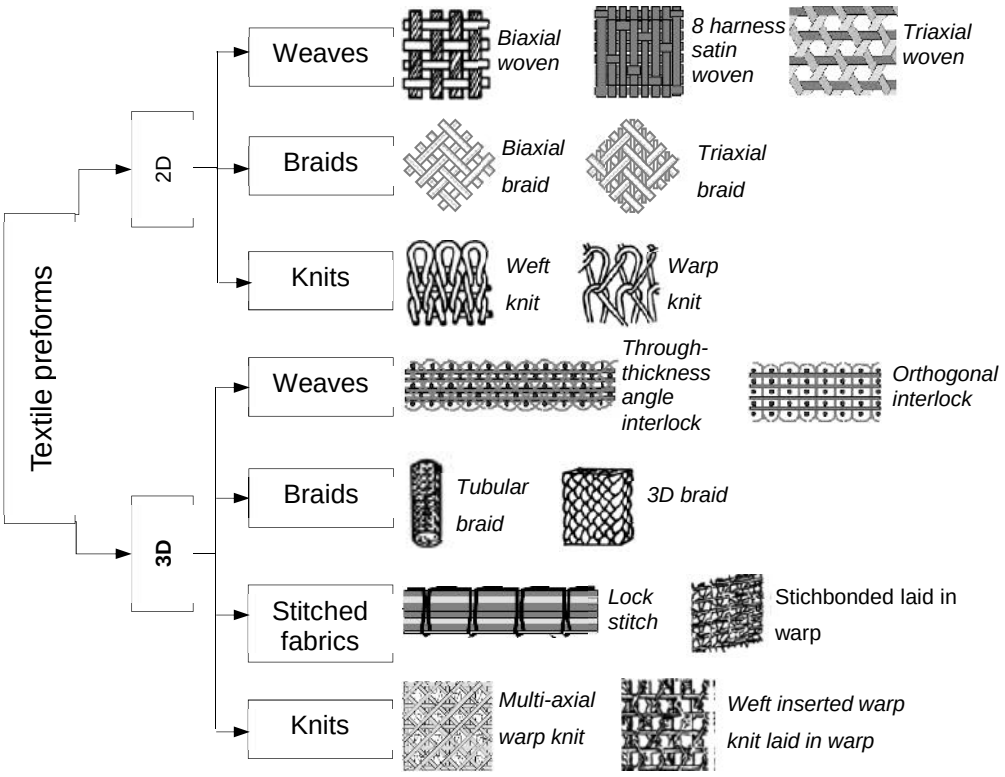

Figure 2.1 Classification of textile preforms [8]

Considering the family of 2D woven fabrics, plane weave is the most conformable for draping applications, followed by 5 harness satin weave, twill and tight weave fabrics as stated in [9]. Knitted fabrics have superior deformation properties compared to other textiles allowing up to 60% local strain at considerably smaller forming energy (up to 25 times) compared to woven textiles [10],

furthermore, wrinkling can be easily avoided using knits. For certain applications these processing qualities may be advantageous despite their lower in-plane mechanical properties for the final part.

Stitched NCF preforms are superior to UD (unidirectional) pre-pregs due to potentially shorter layup time [11]. Also, their low crimp can provide superior in-plane properties compared to woven fabrics and may be used in a design that targets fibre alignment [12]. Non-crimp fabrics with complex architecture (e.g. stitched biaxial NCF) are often chosen for advanced structural applications. Stitching may be used to connect layers of fabric, join multi-material components or exploited as localised reinforcement [13]. Forming of such preforms leads to complex 'structural' deformation behaviour and requires sophisticated numerical simulation methods if a forming simulation is to be undertaken.

The major deformation mechanisms of a fabric have been stated as [14]:

- intra-ply shear and tow sliding (Figure 2.2a, b),
- transverse compaction (Figure 2.2c),
- in-plane tensile behaviour mostly attributed to uncrimping (straightening) of the tows for woven fabrics or extension of the stitches for stitched NCF (Figure 2.2d),
- out-of-plane bending (Figure 2.2e).

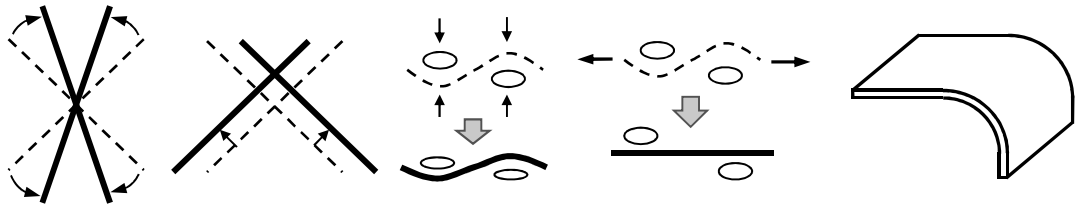

Figure 2.2 Preform deformation mechanisms (macro-scale)

All the deformation modes listed above can be approximated by a macro-scale numerical model, typically realised using shell finite elements. Further refined meso-scale models have the potential to handle deformations at the tow level and can include the following phenomena ([14], [15]):

- tow tension (Figure 2.3a),
- tow shear (Figure 2.3b),
- tow lateral compaction (Figure 2.3c),
- tow bending/straightening (Figure 2.3d),
- tow buckling (Figure 2.3e),
- tow torsion (Figure 2.3f),
- inter-tow sliding, (Figure 2.3g)
- stitch deformation (Figure 2.3h).

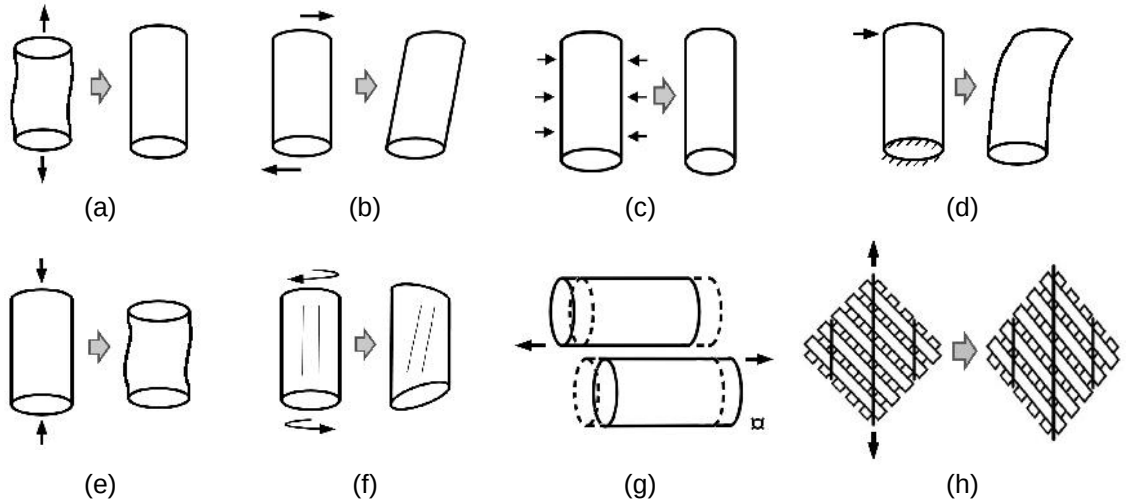

Figure 2.3 Tow deformation mechanisms (meso-scale)

During manual or automated handling (cutting, stacking, forming-draping etc.) preforms are subjected to deformations that have a direct impact on subsequent manufacturing steps and final part properties (e.g. stiffness, damage tolerance, fatigue life) ([16], [17], [18]). Challenges to characterise preforms mechanical properties and build constitutive numerical models arise due to the complexity of a textile architecture, its high compliance, non-elastic and history dependent deformations, high scatter of test results and multiple possible deformation modes [19]. An overview of the main deformation mechanisms, tests to quantify these and numerical analysis methods at the macro- and meso-scales are discussed below.

2.1.1 Compaction behaviour

Textile preform compaction is an important property that relates fibre volume fraction to transverse load and has a direct impact on permeability properties of the preform and mechanical properties of the final composite [20]. Depending on fabric type compaction may be accommodated to varying degrees by the following deformation mechanisms ([21], [22]):

- yarn cross section deformation,
- yarn bending deformation,
- nesting.

Yarn cross section deformation and bending are important factors in compaction of woven textiles, whereas yarn flattening has little impact on non-woven fabrics [21]. Also, yarns under tension exhibit stiffer compaction response ([7], [23]). Thus compaction may depend not only on the fabric itself, but also on moulding process conditions such as in-plane deformation state, saturation state or compression rate [24]. Viscoelastic character of the compaction behaviour of textiles leads to stress

relaxation, load rate dependency and hysteresis phenomena which are schematically illustrated in Figure 2.4.

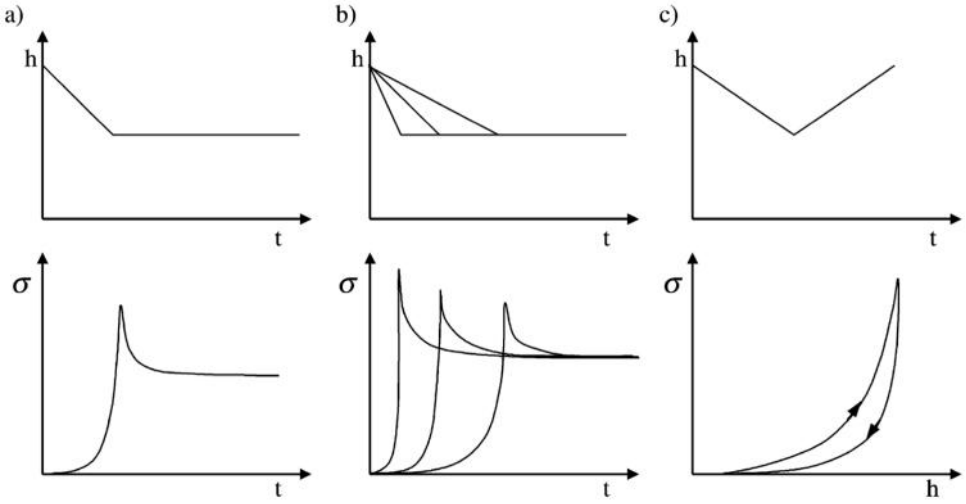

Figure 2.4 Typical fabric viscoelastic behaviour [25] (thickness versus time and stress versus time/thickness diagrams): a) stress relaxation, b) load rate sensitivity and c) hysteresis

A preform response to successive compaction-relaxation cycles is important in vacuum infusion processes since the fabric is compacted under vacuum, unloaded upon injection and reloaded during bleeding and consolidation [14]. Several compaction/relaxation cycles, therefore, may take place before infusion which leads to an increase of fibre volume fraction [26]. Consequently, several compaction-relaxation stages include [27]:

- dry compaction (pre-filling stage),
- wet unloading (filling stage),
- wet re-compaction (bleeding stage).

A typical thickness versus pressure curve for woven and unidirectional knitted fabrics is depicted in Figure 2.5a. The three distinct regions, which are common to many other types of textile reinforcements, are the following [20]:

- a linear region (I) at the beginning of compaction due to fibre slippage and rearrangement, also due to yarn bending in the case of woven fabrics,
- a non-linear region (II) due to reduction of pore space and compaction of tows,
- a linear region (III) at the end of compaction; stiffness of the preform depends on fibre material stiffness as volume of pores does not reduce any further.

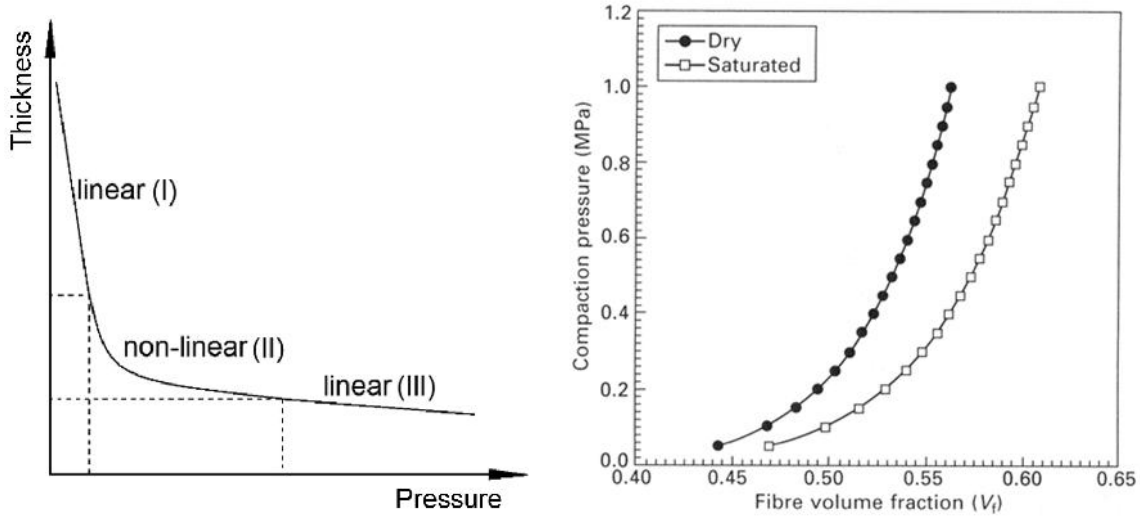

(a) (b)

Figure 2.5 Fabric compaction behaviour: a) typical fabric thickness versus pressure curve (adapted from [28]) and b) effect of saturation [14]

Compaction behaviour of a preform may be influenced by many factors. For example, compaction curve (fibre volume fraction V_f versus pressure P) of saturated specimen is generally shifted to the higher fibre volume fraction range due to fibre lubrication as shown in Figure 2.5b ([14], [24], [29], [30], [31], [32], [33]). This effect was also observed in VARI tests undertaken in this thesis (section 3.2.2), where preform thickness reduction in the saturated zone just after the flow front was identified; similar observations have also been reported by [34], [35] and [36].

Compaction and expansion behaviour of dry fibrous reinforcement is different due to plastic strain present at a coupon level ([24], [29], [32]). Saturated compaction and saturated relaxation behaviour is also not identical as shown in Figure 2.6. Furthermore, a fabrics response to compaction load may depend on loading rate (viscoelastic effects) and loading history ([27], [37])

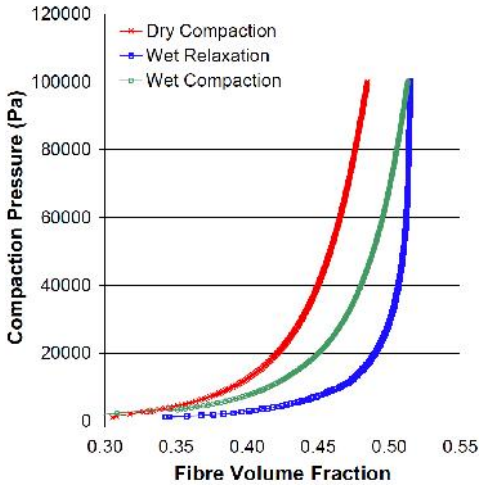

Figure 2.6 Compaction properties of isotropic glass fibre mat [37]

In [27], [38] and [39] it was suggested that fabric compaction measurements relevant to the vacuum infusion process should be obtained by saturating the preform between loading and unloading stages of the test. A considerable variation of preform thickness change scenarios were observed in [39] for various compaction pressure levels which were kept constant during the test in range of 80 kPa to 2 kPa (Figure 2.7). In the test case using 80 kPa compaction pressure, preform thickness decreased (Figure 2.7a), whereas at lower compaction pressure thickness increase was observed (Figure 2.7b, c, d, e and f). A test setup and procedure were presented and implemented in [39] where various glass fabric and flow medium preforms were investigated in detail.

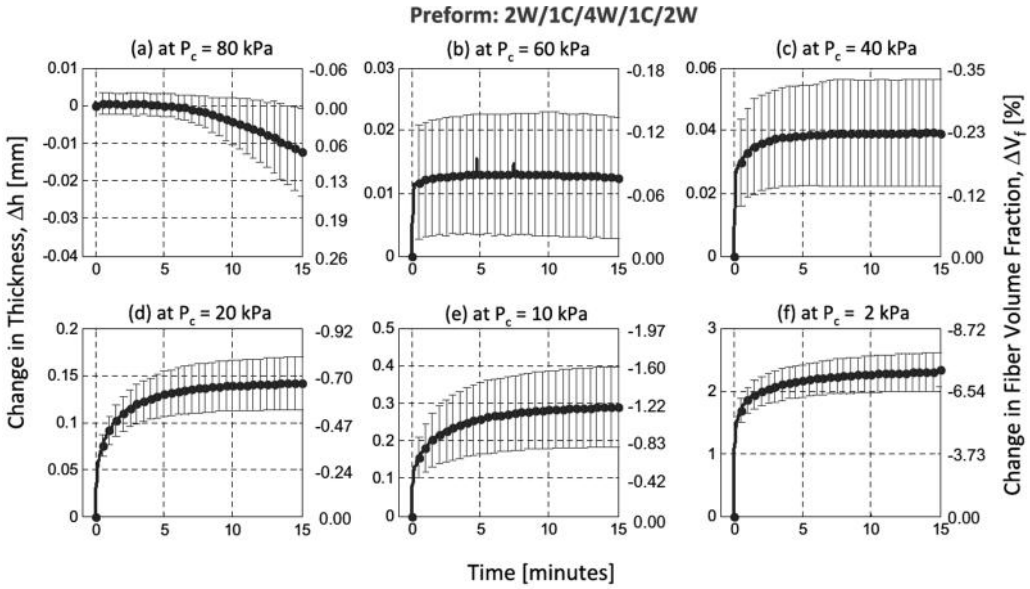

Figure 2.7 Fibre relaxation during compaction characterisation tests at different compaction pressures (80…2kPa) for woven fabric (W) and core (C) preform [39]

Compaction behaviour qualitatively depends on preform thickness, with higher number of layers leading to more pressure relaxation at constant thickness. The pressure decay, defined as the ratio of the pressure observed after 5 minutes and the maximum applied pressure, is typically reduced by up to 10% [14]. In thick preforms consolidation is greater near the plates than in the centre of the preform [24]. However, some studies have shown an opposite trend for dry fabrics and attributed this to higher friction between the fabric layers than between the fabric and steel plates [40]. Investigations of multi-layered preforms in [41] have shown that each layer experiences a different compaction state depending on its boundary conditions: in-plane shifting of layers can lead to both stiffer and softer response of inner layers compared to the outer layers as illustrated in Figure 2.8.

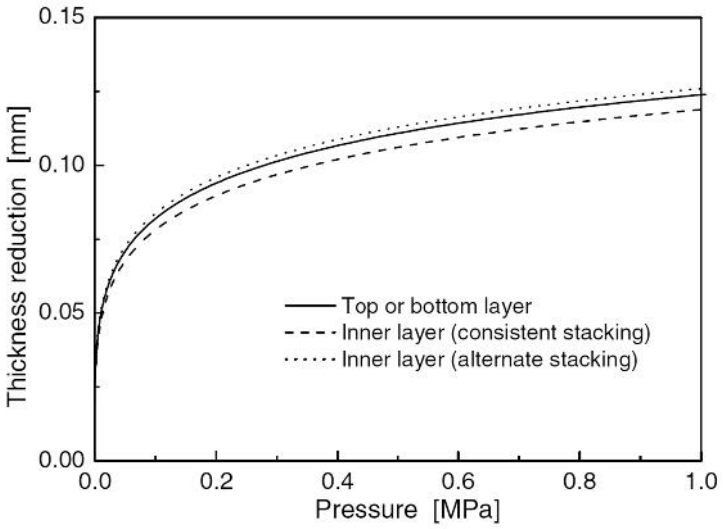

Figure 2.8 Thickness reduction versus compaction pressure for woven carbon fabric [41]

With increasing number of plies and layers, the fibre volume fraction will increase due to greater nesting effect [30] reaching a steady state by 10 layers ([21], [41]). If a stack is made of several layers with adjacent plies having the same orientation (e.g. 0/90 and 90/0), the thickness is reduced by 3-5% [36]. However, experimental work in [42] and [33] resulted in an opposite trend for biaxial non-crimp glass fabric suggesting the importance of layup order and quality on the overall preform compaction behaviour.

Repeatedly performed compaction increases the fibre volume fraction by rearranging fibres and eliminating pores. The thickness equilibrates after about 10 cycles for a plain weave fabric as reported in [30]. Spring-back effect is less pronounced after such repeated compaction and is especially effective for a saturated preform [43].

In-plane shear deformation of the NCF type textiles results in less pronounced nesting effect as tightness of the fabric increases [44]. An opposite trend is observed for woven or twill weave fabrics where increase of shear angle leads to elevated surface roughness and a more pronounced nesting effect [19]. Nesting of stitched NCF also depends on the stitch type; for example, a chain stitch typically allows nesting, whereas a tricot stitch creates gaps between the layers [44].

Overall preform compaction behaviour during a resin infusion process under flexible cover depends on local resin pressure and reinforcement through-thickness stress, both of which change in time and space and depend, also, on fabric loading-unloading history. Thus material, preform and process properties must be taken into account for an accurate compaction representation in infusion simulation and should include the following effects ([42], [45]):

- non-linear elastic behaviour,
- viscoelasticity,
- cyclic effects,
- hysteresis between loading and unloading,

- compaction pressure level and rate,
- permanent deformation,
- saturation effects,
- number of layers.

Modelling of textile reinforcements compaction that allow incorporation of the above listed phenomena are reviewed below.

Compaction modelling

A compaction model should be able to uniquely describe fibre volume fraction as a function of thickness, compression load (history), compaction pressure, or other process parameters. Numerical methods to describe compaction behaviour have been classified in [46] as:

- force approaches,
- energy approaches,
- FE modelling approaches.

A simple relationship that relates fibre volume fraction to fabric aerial weight and thickness is [47]:

$$V_f = \frac{s}{\rho \cdot h}, \tag{2.1}$$

where V_f – fibre volume fraction,

s – fabric aerial density, kg/m^2,

ρ – fabric density, kg/m^3,

h – fabric thickness, m.

In RTM (Resin Transfer Moulding) process no fabric unloading is possible so compaction and stress relaxation are described by a single (or piecewise) non-linear elastic material model [48]. An empirical power law can be used to relate fibre volume fraction V_f with compaction pressure P ([27], [37], [49]):

$$V_f = V_{f0} P^{m_s}, \tag{2.2}$$

where V_{f0} – initial fibre volume fraction,

m_s – stiffening coefficient (m_s <1).

The compaction behaviour of a single fibre bundle was investigated in [50], where it was noted that applied pressure may not uniquely describe fibre volume fraction in a bundle due to its deformation and rearrangement of filaments. However, the bundle tends towards an equilibrium state, which can be used as a functional relationship between applied load and transverse deformation. The introduction of time dependent current/initial pressures ratio and additional coefficients can be used to characterise preform relaxation behaviour using the following equation ([42], [49]):

$$\frac{P}{P_0} = 1 - C \cdot t^{(1/D)}, \tag{2.3}$$

where P_0 – initially applied pressure, Pa,

C – pressure decay after 1 s,

t – time, s,

D – relaxation index.

A model with several empirical parameters was used in [34] to relate fabric stress (compaction pressure) and fibre volume fraction:

$$\pm_{zz}(V_f) = k_e E\left(V_f^{m_e} - (V_{f0} + ©)^{m_e}\right), \tag{2.4}$$

where E – fibre stiffness, Pa,

k_e, m_e – empirical constants obtained from tests,

© – softening coefficient (equal to 0 for dry fabric, greater than 0 for wetted fabric).

The above equation, however, cannot differentiate between loading and unloading of the wetted preform [27].

Another representation of stress $\pm_{zz}$ inside a compressed preform can be obtained using a mixed elastic law that combines a selection of elastic models (saturated or dry, static or dynamic) and is also based on experimental data. Fabric stress can then be expressed by a polynomial function, which can be modified to account for, e.g. relaxation behaviour, by introducing time dependent parameters [51]:

$$\pm_{zz}(V_f) = aV_f^4 + bV_f^3 + cV_f^2 + dV_f + e. \tag{2.5}$$

Compaction stress can also be composed of two functions depending on loading velocity and fibre volume fraction as [51]:

$$\pm_{zz}(v, V_f) = f_\alpha(v) \cdot f_\beta(V_f) \tag{2.6}$$

where $f_\alpha(v)$ – function of velocity,

$f_\beta(V_f)$ – function of fibre volume fraction.

Functions $f_\alpha(v)$ and $f_\beta(V_f)$ are obtained experimentally at some reference or typical values of loading velocity and fibre volume fraction.

In [19] an energy balance approach (including bending potential energy and yarn compaction energy) and experimental characterisation of a single yarn was used to predict 2x2 twill weave fabric thickness evolution at high compression loads. Fabric draping and lateral interaction (overlap) of yarns were found to be the most important factors defining fabric thickness change; yarn bending rigidity, if ignored, can lead to 10-20% error in estimating thickness.

In this work a FE modelling approach from [52] with non-linear material law (section 2.5) is exploited to represent tow compaction behaviour in a meso-scale fabric model (section 5.1.2).

2.1.2 Shear behaviour

Trellis shear deformation is the primary deformation mechanism in draping of textiles over doubly curved shapes [14]. In practical applications it may cause changes to part thickness, induce wrinkling and lead to problems in rigid mould processes such as RTM [19]. A simple counter-measure such as cutting the fabric decreases mechanical performance of the part, is labour intensive and thus not appropriate for high volume production [53] or manufacture of structural parts. Generally, shear stiffness of a fabric increases with shear angle [54].

It is important to know the maximum shear angle ¥$_{max}$, or its counterpart a so-called locking angle ¯$_{lock}$=90–¥$_{max}$, at which wrinkles appear and which is often a limiting criterion for technical draping applications. For woven textiles locking angle can be estimated analytically as a function of warp and weft yarns width and their spacing as illustrated in Figure 2.9. The locking angle is then calculated using the equation [10]:

$$\bar{}_{lock} = \arcsin\left(\frac{t_2}{t_2 + l_2}\right), \tag{2.7}$$

where ¯$_{lock}$ – locking angle, °,

t_2 – weft yarn width, m,

l_2 – weft yarn spacing, m.

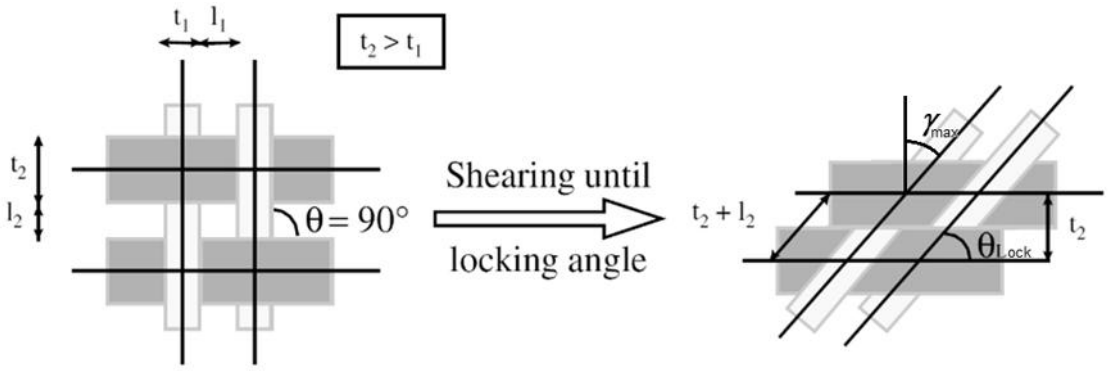

Figure 2.9 Illustration of woven fabric shear until locking angle [10]

Shear deformation beyond the locking angle cause reduction of tow width and increase of its thickness. Generally, the smaller the tow width (for a certain spacing), the smaller is the locking angle. Similarly, larger spacing also leads to smaller locking angle [53]. In practice, however, a combination of compression, compaction and friction forces may cause fabric wrinkling before or after the theoretically estimated locking angle [55].

Wrinkling may also appear under zero shear conditions. Tows of a woven fabric may buckle under a tow-lengthwise compression forces indicating the importance of tow bending stiffness [56]. In-plane tension, from application of blank holder forces to restrain the fabric, may considerably increase the range of drapeability of a fabric and help to avoid wrinkles as was demonstrated in [57]. For example, an increase in holding force leads to higher fibre tension and reduction of in-plane buckling during the hemisphere forming test [58].

Depending on the reinforcement type different shearing deformation mechanisms can take place. For woven fabrics no sliding of undulating tows is usually possible and shear deformation is facilitated only by rotation of the weft and warp tows relative to each other [59]. Plies of multiaxial NCF's are usually held together by a stitch (e.g. chain or tricot) which facilitates the handling of the preform, but imposes additional stiffness that modifies shear behaviour (non-symmetric shear) [60]. It also causes local deviation in fibre directions, variation of fibre volume fraction and formation of voids [61]. Possible inter-ply slip distance may vary depending on the type and density of stitching. Relative inter-tow sliding of up to 14 mm was reported for weft-warp tows stitched with tricot stitch in [60]. The ability of plies to slide relative to each other reduces wrinkling compared to woven or pre-preg fabrics at corresponding shear angles [59].

A 'tow pull-out test' was used in [62] to characterise tow-stitch interaction. The test was performed for a set of tows from both plies of the biaxial NFC with tricot stitch. Poor repeatability of the results was observed indicating a wide variation in force needed to cause relative stitch-tow movement. A conventional test to obtain shear stiffness is torsion loading of a cylindrical specimen [63]. This is, however, not possible for a flexible textiles. Consequently several alternative tests have been developed to characterise fabric shear behaviour [64]:

- simple shear test (Figure 2.10a),
- bias extension test (Figure 2.10b),
- picture frame test (Figure 2.10c).

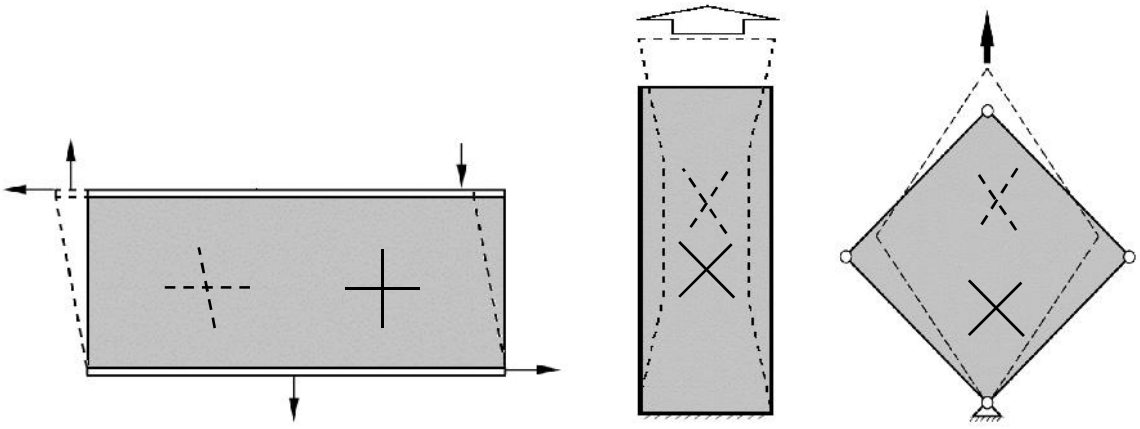

Figure 2.10 Fabric shear characterisation: a) simple shear, b) bias extension and c) picture frame tests

2.1.2.1 Simple shear test

The simple shear test, schematically shown in Figure 2.11, is exploited in the Kawabata testing system for textiles in the clothing industry [65]. This test is simple, but exhibits some major drawbacks. At the very beginning of the test the upright tows of the fabric tend to buckle under compressive load. This needs to be counteracted by applying a tensile force, the amount of which influences the test result by inflicting a complicated stress field to the specimen [64]. The specimen is thus not subjected to uniform shear, which in this case varies from zero at the corners to a maximum at the centre [17].

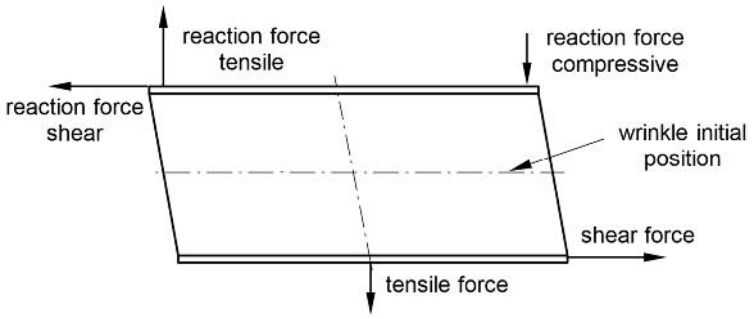

Figure 2.11 Forces acting in simple shear test [64]

The Kawabata test is discussed in [63] where a methodology to properly evaluate test data is proposed. Based on an analytical solution it was shown that actual fabric shear stiffness lies about 25…30% above the measured value. Tensile forces only account for a small part (2%) of the discrepancy; the main deficiency is non-uniform shear strain and stress fields over the specimen due

to boundary conditions. A maximal rotation angle for the test is about 8° resulting in about 5° of shear angle, which is not sufficient to test most technical fabrics. Thus the Kawabata setup is only appropriate where small strain deformation is of interest [7].

2.1.2.2 Bias extension test

The bias extension test involves clamping a rectangular piece of fabric with tows oriented at ± 45° to the direction of applied tensile force [14]. The specimen has uniform shear only in central area (labelled ‘A’ in Figure 2.12). Shear angle in area ‘B’ is smaller than in area ‘A’ and area ‘C’ does not undergo any deformation due to clamping, although a reduction of zone ‘C’ for woven fabric at high shear states was reported in [66] based on full field strain measurements technique. Consequently, all measurements for extension ratio, thickness and shear angle have to be made in zone ‘A’. Specimen length to width ratio (H/W) should be greater than 2 so that a region of pure shear exists ([54], [64], [67], [68]).

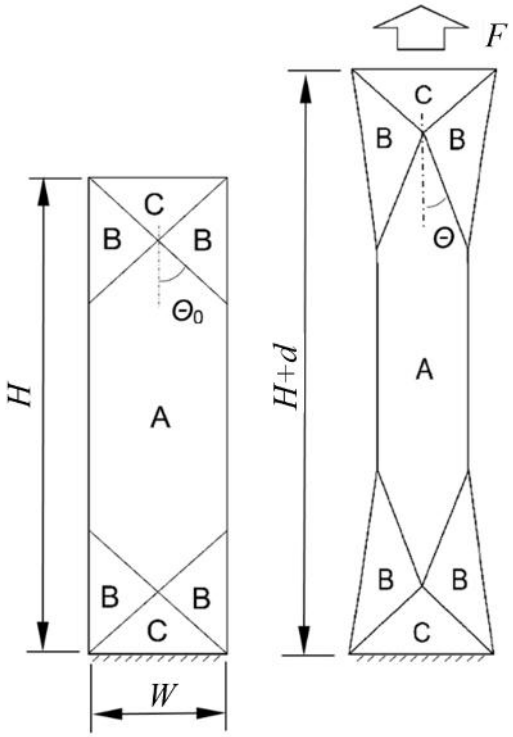

Figure 2.12 Scheme of fabric deformation during bias extension test

In the bias extension test intra-ply slip of two types is possible, namely, crossover (Figure 2.13) and inter-tow slip (Figure 2.14) [54]. The higher the aspect ratio the more slippage is expected to occur [64]. Typically, slippage takes place under the influence of lateral bending at boundaries of the different deformation zones as was demonstrated using a slightly painted specimen in [69]. Yarn slippage is most pronounced at large deformations as it is a lower energy deformation mode than shear deformation ([54], [69]).

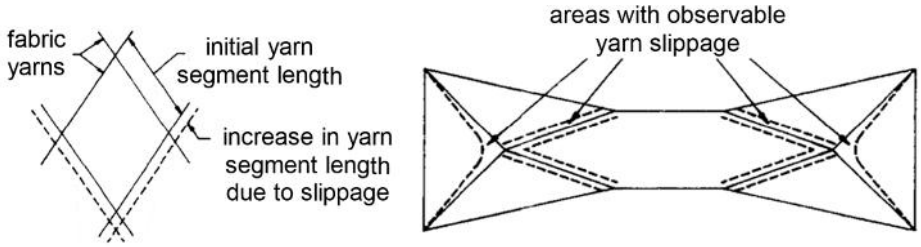

Figure 2.13 Cross-over yarn slip and locations for its occurrence in a specimen [64]

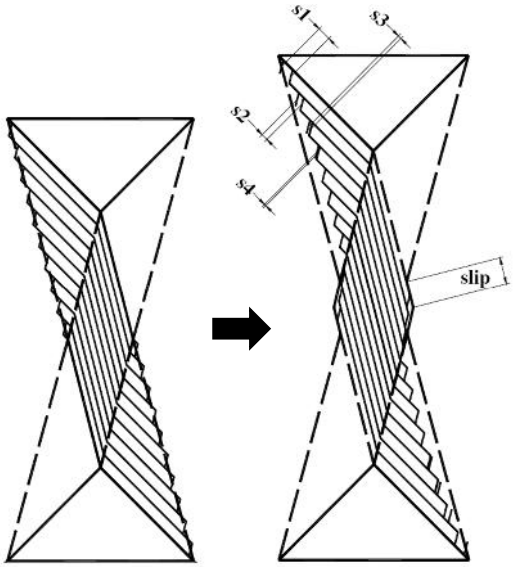

Figure 2.14 Inter-tow slip in bias extension test [54]

It was shown in [66] and [70] that slippage effect can be reduced if specimen width is wider than the grips as shown in Figure 2.15. In this case the pure shear zone ‘A’ is not trimmed and resembles a picture frame specimen geometry. Tow slippage is then postponed to a later stage of deformation at about 50° shear for a woven fabric.

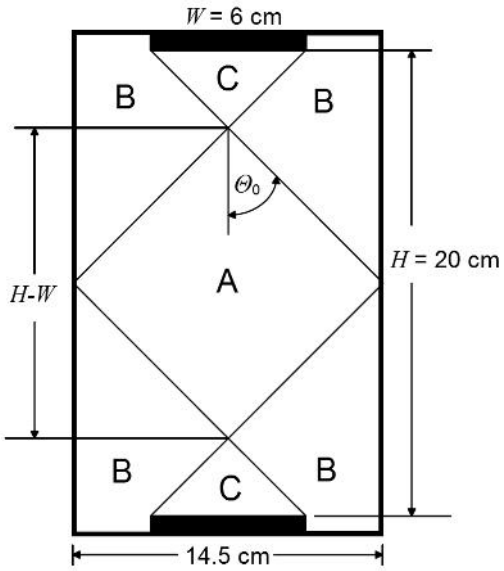

Figure 2.15 Wider bias extension shear specimen with shear zones indicated (adapted from [66])

Shear angle ¥ can be calculated from the fibre angle ¯ by using the following analytical equations [67]:

$$¥ = 90° - 2¯ = 90 - 2\arccos\left(\frac{L_0 + d}{\sqrt{2}L_0}\right), \tag{2.8}$$

where $L_0 = H - W$, (2.9)

$$\cos¯ = \frac{H + d - W}{2(H - W)\cos¯_0} = \cos¯_0 + \frac{d}{2(H - W)\cos¯_0}. \tag{2.10}$$

These equations are derived under the following assumptions [67]:

- shear angle is uniform in each zone (‘A’, ‘B’ and ‘C’) of the specimen,
- shear angle in zone ‘A’ is twice as large as in zone ‘B’,
- zone ‘C’ remains undeformed,
- initially the specimen has a perfectly orthogonal configuration (± 45°).

These assumptions are reasonably valid for a plain weave fabric, whereas for a non-crimp stitched material the discrepancy between theoretical and measured values increases with increasing shear angle. This happens due to additional deformation mechanisms such as inter-tow sliding and stitch-tow interaction [62]. Loading rate does not affect the measured tensile force [67]; however, it is relevant for pre-pregs as viscous resistance is introduced by the presence of matrix [70].

Normalisation of bias extension test results with respect to axial force or specimen size has to be done to compare different test methods as discussed in [54]. Normalised shear force per unit length is obtained iteratively as a function of shear angle [67]:

$$F_s(¥) = \frac{1}{(2H - 3W)\cos¥}\left(\left(\frac{H}{W} - 1\right) \cdot F \cdot \left(\cos\frac{¥}{2} - \sin\frac{¥}{2}\right) - W \cdot F_s\left(\frac{¥}{2}\right)\cos\frac{¥}{2}\right). \tag{2.11}$$

Comparison of normalised bias extension test results may highlight substantial contribution of alternative deformation mode (slip). 5-harnes satin weave pre-preg shear test results from [54] are shown in Figure 2.16a, where force from bias extension tests increases without further increase of shear angle suggesting the specimen is deforming in a different mode than shear. If, alternatively, force is plotted against normalised displacement (Figure 2.16b), all the deformation mechanisms in the bias extension test are taken into account.

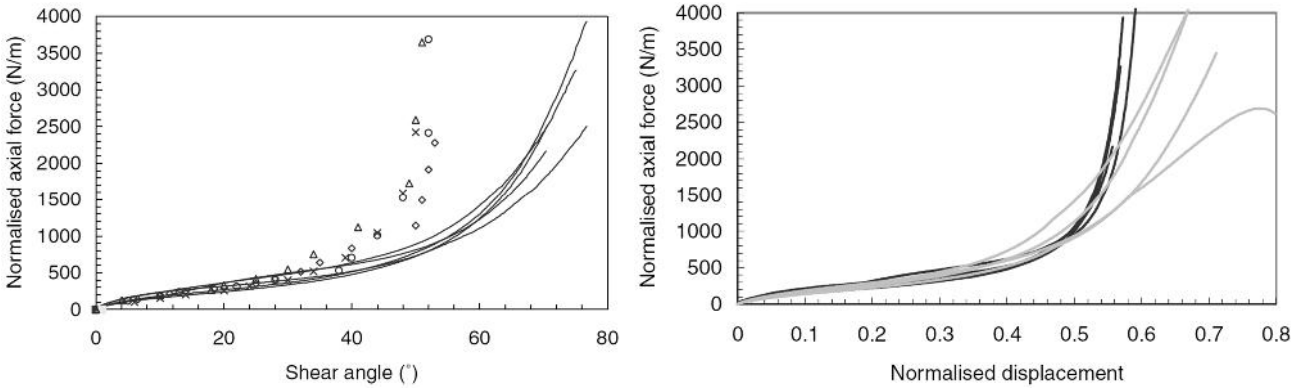

(a) (b)

Figure 2.16 Bias extension (symbols, grey lines) and picture frame (black lines) tests [54]: a) normalised axial force versus shear angle and b) normalised axial force versus normalised displacement

Shear angle measured by optical methods shows up to 5° difference compared to analytical estimation in a range up to 30-40° as shown in Figure 2.17. This discrepancy increases further at higher shear angles, thus an optical measurement system has to be used [68]. Reduced accuracy of analytical shear angle prediction for a plain weave fabric above 30° shear angle was reported in benchmarking work [67].

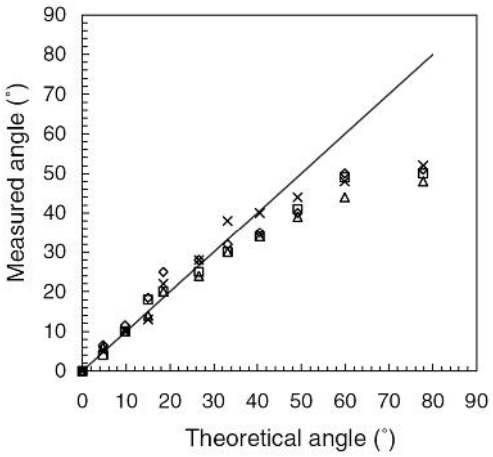

Figure 2.17 Theoretical (line) versus measured (symbols) shear angle in a bias extension test for 5-harness satin weave fabric [54]

Some additional effects are specific to stitched NCF in the bias-extension test. Chain stitches resists tow movements and, if loaded in tension, undergo straightening, stretching and interaction with tows. If a specimen is loaded in a direction perpendicular to the stitches, yarns rotates freely as smaller friction force acts between these [68]. Extracting mechanical properties for the stitch is difficult since the coupon has a non-uniform internal load distribution [14].

In [12] tests on stitched NCF were presented. As expected, stitches loaded in tension contributed to an increase of shear stiffness. Shear modulus information is a common input parameter in numerical simulation codes, thus a methodology was proposed to extract shear modulus from shear stress

versus shear angle data. The method was based on assumption that power created by tensile force is dissipated in the sheared areas of the specimen. Shear modulus was obtained as a derivative of a regressive equation quantifying shear stress (normalised shear force divided by fabric thickness) versus shear strain relationship.

2.1.2.3 Picture frame test

In contrast to the bias-extension test, the picture frame test deforms a fabric uniformly in shear as shown in Figure 2.18. Nevertheless, this test often results in poor repeatability. Misalignment of fibres in the frame, specimen preparation and fibre pretension are the most common sources of errors ([15], [71]). Fibre misalignment of 0.5° already has a significant effect on the measured shear stiffness [72].

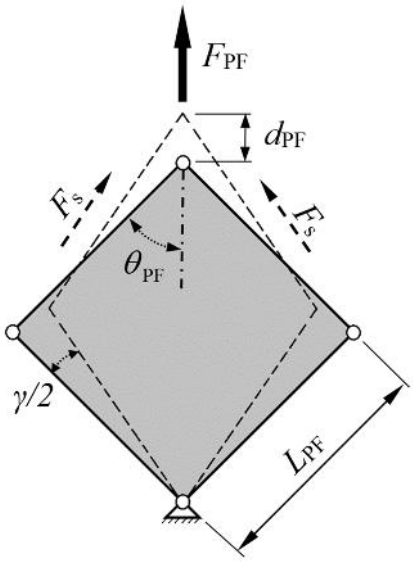

Figure 2.18 Picture frame shear test parameters (adapted from [73])

It is possible to calculate fabric shear angle from frame angle, but the actual shear angle of the fabric may differ, especially at higher shear angles [67]. Shear angles difference of up to ±2° when calculated from the frame displacements and obtained using optical measurement tools have been reported in [74]. However, averaged values of the shear angles obtained using optical measurements are comparable with analytical estimations from a frame angle [67], thus simplicity of the former shear angle evaluation method is often preferred.

Fabric shear angle ¥ defined by frame angle $\bar{}_{PF}$ is expressed by:

$$¥ = \frac{®}{2} - 2\bar{}_{PF} . \tag{2.12}$$

Shear angle defined by cross head displacement d_{PF} is:

$$¥ = \frac{®}{2} - 2\cos^{-1}\left[\frac{1}{\sqrt{2}} + \frac{d_{\mathrm{PF}}}{2L_{\mathrm{PF}}}\right], \tag{2.13}$$

where L_{PF} – picture frame side length, m.

Shear force F_{s} acting on a specimen is calculated from resistance force acting on a picture frame clamps [67]:

$$F_{\mathrm{s}} = \frac{F_{\mathrm{PF}} - F'}{2\cos\overline{}_{\mathrm{PF}}}, \tag{2.14}$$

where F_{PF}– axial force measured on picture frame, N,

F' – offset value due to inertia, friction in bearings and weight of the frame, N.

Shear stress in fabric specimen is obtained under a constant volume assumption (thickness increases proportionally to reduction of specimen area):

$$² = \frac{F_{\mathrm{s}}}{L_{\mathrm{PF}} \cdot h}, \tag{2.15}$$

where h – fabric thickness, m.

The constant volume assumption, however, may be neglected depending on the reinforcement type. For dry fabrics constant thickness assumption is valid ([17], [75]). This was also justified in [55] where efficiency of energy consumption for determination of initial wrinkling for woven glass fabric was used. It was observed that the more compaction the fabric undergoes (inter-yarn gap reduction and closure, yarn compaction), the higher is its shear stiffness increase rate. Thus the extent of thickness change depends on the textile architecture; a sparsely spaced adjacent weft and warp tows in a plain weave fabric may not come into contact until very high shear angles are reached, and fabric thickness remains constant up to that point. Another ‘constant thickness’ argument is that fabric thickness stays within the bounds of measurement accuracy before wrinkling occurs anyway. Constant volume assumption is thus truly justified only for pre-pregs [75].

Equations (2.14) and (2.15) should only be used to compare tests executed under the same loading rate [55]. In [17] it was reported, however, that the effect of shear rate on measured stiffness for woven and satin fabrics remains within experimental error range and no consistent trends could be observed. A discussion on pre-preg rate dependent shear deformation behaviour can be found in [76].

In order to compare shear stiffness data obtained using different picture frames or specimen sizes (Figure 2.19a), results need to be normalised. Normalised shear force according to energy method [77] is calculated using expression:

$$F_{\text{normalised}} = F_{\text{s}} \cdot \frac{L_{\text{PF}}}{L_{\text{fabric}}^2}, \tag{2.16}$$

where L_{fabric} – side length of the fabric sheared area, m.

Note that for the case that a fabric specimen occupies the whole frame area ($L_{\text{fabric}} = L_{\text{PF}}$), the equation simplifies to

$$F_{\text{normalised}} = \frac{F_{\text{s}}}{L_{\text{fabric}}}. \tag{2.17}$$

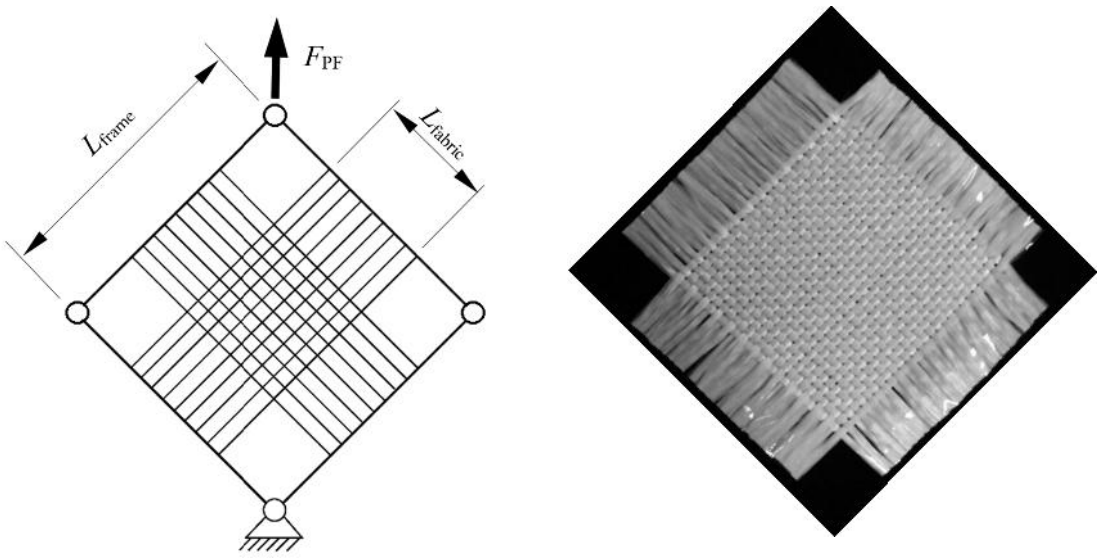

(a) (b)

Figure 2.19 Picture frame test: a) schematic view of setup with corner cut-outs (adapted from [77]) and b) specimen with yarns removed from the arms [67]

The motivation to normalise picture frame test results with respect to specimen side length rather than its area [78] was presented in [54]. Also, when dealing with different shear stiffness measurement methods (picture frame, bias extension), it is recommended to compare normalised axial force acting on the specimen rather than shear force, since bias extension test does not exert pure shear deformation on the specimen and tow slippage may be present. It has been found in [55] that normalised picture frame test results of small and larger specimens are nearly identical before wrinkling appears, as shown in Figure 2.20.

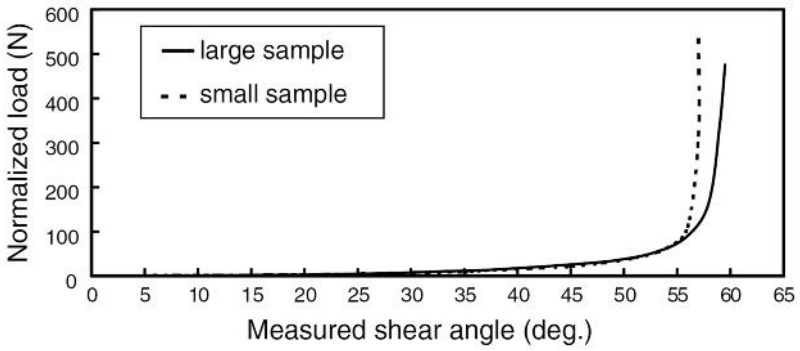

Figure 2.20 Normalised picture frame test results for woven glass fabric [55]

Picture frame specimens should be prepared in such a way that shear occurs only in the central area of the specimen and not in the arms where a sets of longitudinal yarns should be removed to reduce their contribution to force measurements ([67], [68]), as illustrated in Figure 2.19b. Modification of the picture frame specimen can help to reduce influence of the fibre misalignment on the measurements; a specimen clamped only near the corners of the frame (Figure 2.21b) was used in [79] reporting better reproducibility of the results.

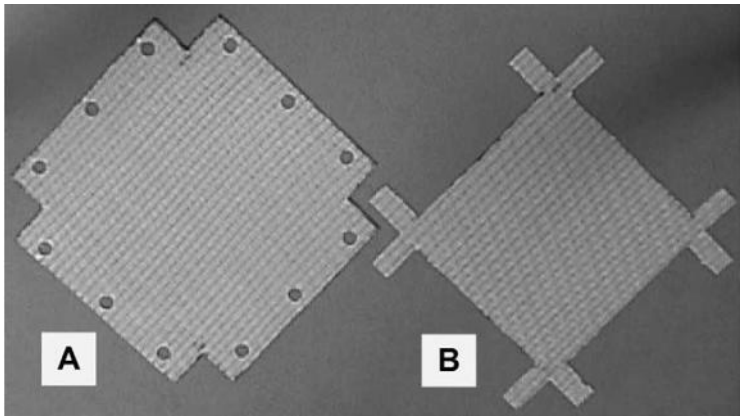

Figure 2.21 Picture frame specimens [79]: a) standard and b) modified

Misalignment of fibres is a major source of test data scatter leading to overestimation of shear stiffness [72]. Shear stiffness of a 2x2 twill weave fabric was experimentally measured in [72] with deliberate 1° to 5° fibre misalignment angles. Combined with tensile test data and corresponding bias extension test data (with the same shear area as in a picture frame test), a methodology was proposed to calculate a statistical effective misalignment angle. Statistical evaluation was necessary as tensile forces and fibre misalignment are not uniformly distributed over the specimen. A macro-scale simulation approach with included representative fibre misalignment data yielded good agreement to tests as shown in Figure 2.22.

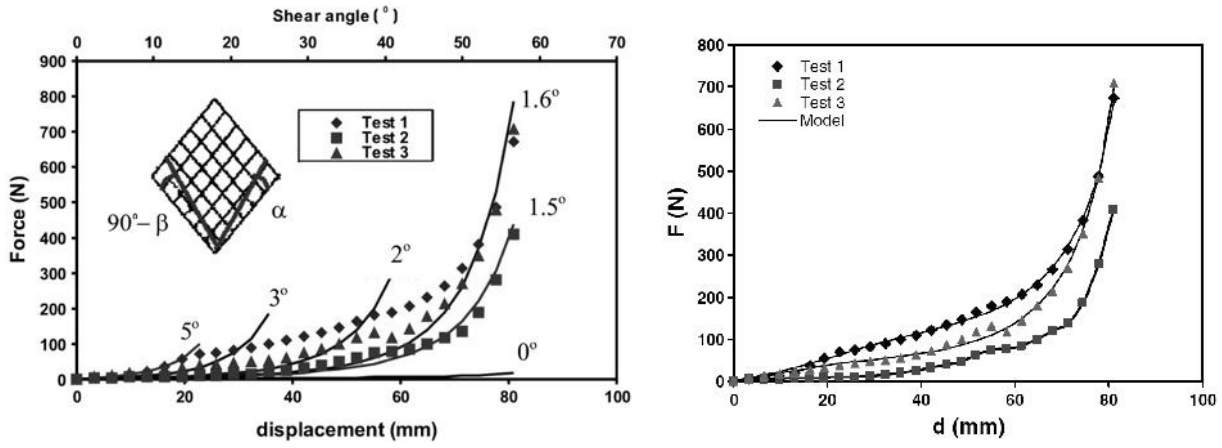

(a) (b)

Figure 2.22 Picture frame test and simulation results (2x2 twill weave) [72]: a) uniform fibre misalignment angle and b) effective fibre misalignment angle

As mentioned earlier, some reinforcing textiles (e.g. biaxial NFC with chain stitch) exhibit unsymmetrical shear behaviour due to the stitching. A typical shear force versus shear angle curves for stitched NCF obtained using a picture frame test are shown in Figure 2.23.

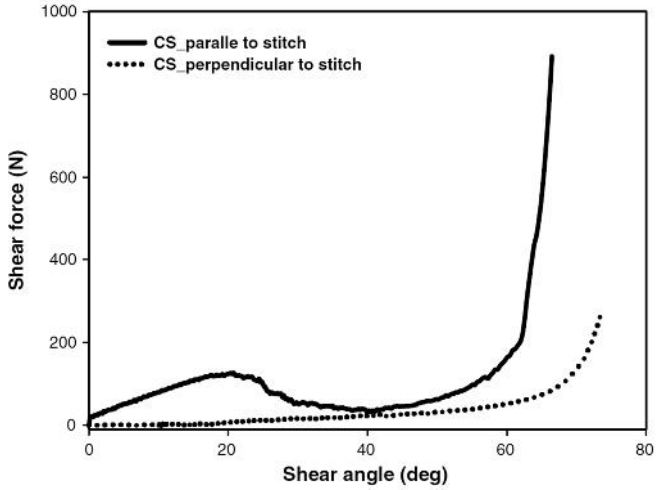

Figure 2.23 Typical picture frame test curves for stitched NCF [58]

Stitches increase shear resistance of the NCF up to a certain shear angle. Beyond that angle thread tension loosens and its contribution to shear resistance reduces [58]. Several researchers have reported very pronounced change of shear properties during cyclic loading ([15], [68]). Preconditioning of the specimens is often used to improve repeatability of picture frame test results [67] as a mean to reduce spurious tension [80]. However, while such practice may be applicable to woven type reinforcements, it is questionable in the case of stitched fabrics since preconditioning leads to partial destruction of fabric-stitch integrity. Inherent sources of errors and data scatter in a picture frame test arise from the following factors [74]:

- pretension of fabric and variation of pretension over the specimen;

- in-plane bending of tows near the grips (Figure 2.24); this suggests the need of free rotating boundary conditions at the ends of individual bundles [17];
- friction in the bearings of the frame (also dependent on fabric pretension).

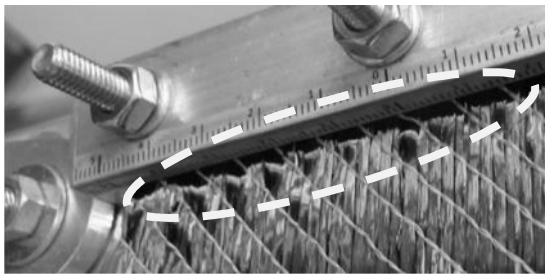

Figure 2.24 Bending of the tows near the fixed edge of the picture frame

A parametric study in [15] addressed shear stiffness of glass woven fabrics as a function of the yarn roving properties (linear density, tightness, pretension). A detailed analysis showed the profound influence that pretension can have on picture frame shear test results. Due to the tensile strain in the yarns the shear force increases as friction between perpendicular yarn systems increases. The formation of wrinkles is also greatly influenced by reduction of yarns width [55].

In [78] it was suggested that intra-yarn shear may substantially contribute to shear behaviour of the fabric, especially if high transverse (compression) force is applied. An in-depth analysis of the picture frame test and boundary conditions was made in [7]. A meso-scale plain woven fabric model was used to investigate the influence of different boundary conditions at a unit cell (UC) level. Some interesting observations were found: 1) at high shear angle yarn lateral compaction is the main energy dissipation source, whereas 2) shear within the yarn (inter filament sliding) is a significant contributor to deformation resistance for low shear angle (Figure 2.25) contradicting the findings in [81], where shear of tows was stated as negligible. Thus a detailed meso-scale FE simulation model should incorporate intra-yarn shear behaviour and appropriate boundary conditions.

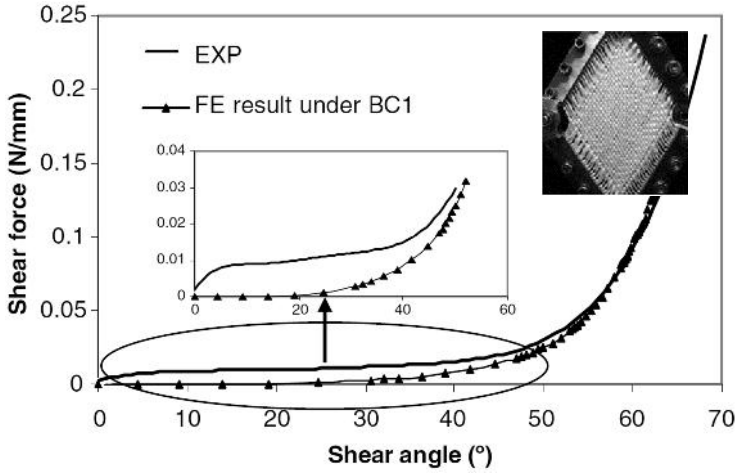

Figure 2.25 Picture frame simulation and test data comparison [7]

2.1.2.4 Which fabric shear test to use?

The major difference between the bias extension and picture frame tests lies in the fabric deformation mechanisms. In a bias extension test intra-ply slip is possible, in addition to shear, and tows are under a tensile stress field, whereas a picture frame test imposes a state of pure shear over the whole specimen area except the edges near the frame [54].

Fabric shear modulus obtained from these two tests differ, with the picture frame test giving a higher shear modulus than bias extension test [82]. Possible reasons for this may be spurious tension of the fibres, fibres misalignment and coupling between pretension and shear in picture frame test. Consequently, the use of picture frame data in a simulation may lead to underestimation of shear angles. Figure 2.26 shows a comparison between the experimentally measured and simulated shear angles for a double dome specimen using bias extension and picture frame test data from [82].

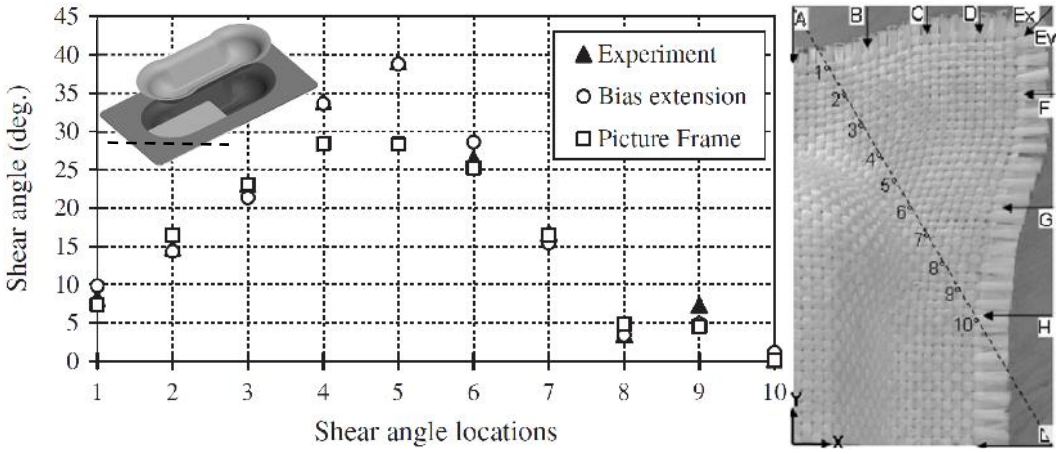

Figure 2.26 Fabric shear angles and a view of the double dome specimen [82]

A bias extension test exerts looser constraints on a specimen compared to severe boundary conditions of a picture frame which leads to lower measured shear stiffness. It is suggested that the true shear stiffness of the fabrics lies between these two extremes [54]. However, benchmarking efforts for woven fabric shear characterisation and comparison between the bias extension and picture frame tests presented in [67] has shown that properly normalised shear stiffness results from the two tests are close to each other.

There is no general agreement which test is the best. Advantages and disadvantages of each test are listed below. Advantages of bias extension test [54]:

+ good repeatability of results,
+ less sensitive to boundary conditions,
+ less sensitive to fibre misalignment than a picture frame test [70],
+ in the case of testing at elevated temperatures clamping has less influence on temperature field in the area of interest in the specimen.

Disadvantages of bias extension test [54]:

- inhomogeneous deformation field over the specimen requiring special analysis of results,
- pure shear deformation mode is mixed with intra-ply slip,
- shear angle should to be measured by optical tools (especially for higher shear angles).

Advantages of picture frame test:

+ homogeneous shear angle field over the specimen,
+ cyclic deformation testing is possible.

Disadvantages of picture frame test:

- poor repeatability of the results due to sensitivity of boundary conditions (e.g. in-plane bending of yarns at the edges for most frame designs),
- possible fibre misalignment leading to overestimation of shear stiffness.

2.1.3 Bending and friction behaviour

Dry textile reinforcements have very low out-of-plane bending rigidity which often leads to it being neglected [23], or a 'knock down' factor being used (~0.001) in FE analysis to diminish its effect compared to in-plane stiffness [83]. However, bending properties play an important role in formation of wrinkles ([57], [71]) and therefore have to be included for accurate draping simulation. Bending rigidity depends mainly on geometry, mechanical properties and contact between the yarns [71]. It is greatly influenced by the tow filaments, their arrangement in a fabric, stitches, possible use of binder [84] and the fabric deformation state, e.g. degree of shear [7].

In [46] bending of textiles was quantified using the Kawabata Evaluation System [65], which is a standard in the clothing industry. Alternatively, a simple cantilever beam bending test according to ASTM 1388 standard (Figure 2.27) can be used ([5], [57], [85]). Depending on the reinforcement type, several tests with different fabric orientations may be needed for a proper characterisation.

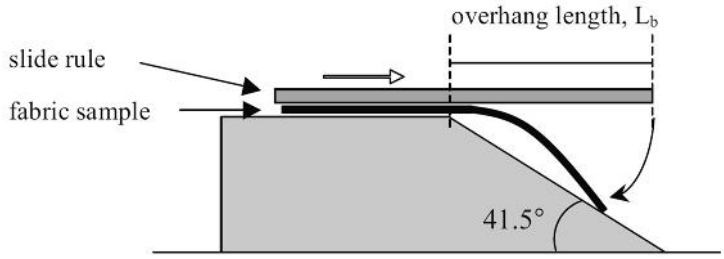

Figure 2.27 Fabric flexural rigidity test setup according to ASTM 1388 [5]

According to ASTM 1388 bending stiffness is characterised using the following equation [86]:

$$G_b = s \cdot l_b^3, \tag{2.18}$$

where l_b – bending length, m,

with $l_b = \frac{L_b}{2}$, (2.19)

where L_b – overhang length, m.

Comparison of different fabric bending behaviour can be made using expression (2.18), but it provides only subjective estimate. Numerical models require different quantification based on physical and geometrical properties of the fabric. A FE approach is presented in section 4.1.3 for bending behaviour characterisation of biaxial NCF.

Friction mechanisms in draping processes also play an important role. These include friction between the fibre filaments and tows in fabric deformation behaviour, as shown in Figure 2.28 for relative movements of contacting tows in a biaxial fabric. Fabric-to-tooling friction is important for accurate prediction of force needed to drive a forming process [87]. Blank holder force generates friction that strongly influences the quality of the draping operation by expanding the range of possible shear strain before wrinkles can occur [16].

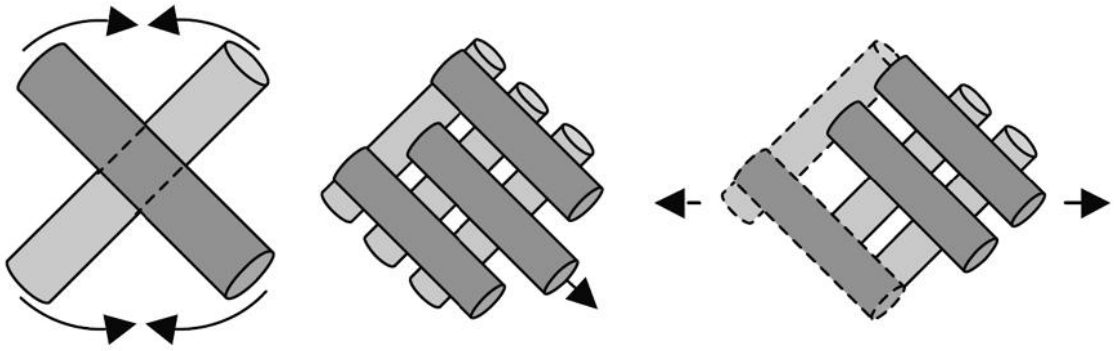

(a) (b) (c)

Figure 2.28 Examples of friction between the tows of biaxial fabric [5]: a) inter-tow shear, b) inter-tow sliding and d) cross-over point sliding

Experimental measurements of fabric-to-fabric friction have been undertaken by numerous researchers, for example [5], [88], [89] and [90]. A schematic view of a simple fabric-to-tool friction test setup is given in Figure 2.29, where friction coefficient is calculated according to Coulomb's law of friction:

$$\mu_f = \frac{F_{fr}}{F_N}, \tag{2.20}$$

where F_{fr} – pulling force (friction force), N,

F_N – normal force (= $m \cdot g$), N.

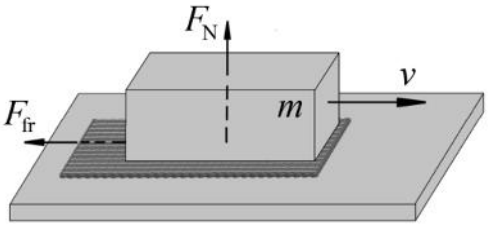

Figure 2.29 Illustration of a typical fabric-to-tool friction test setup

In some fabric forming problems a variable friction coefficient must be used in the numerical model. In [91] thermostamping of a commingled glass-polypropylene plain weave fabric was investigated where a friction model for fabric-to-tool interface was developed. It was shown that friction coefficient mostly depends on punch velocity, tool temperature and normal force, whereas fibre orientation, bending properties and initial fabric temperature were found to have minor effect. Consequently, a friction model may have to be based on numerous process parameters.

2.1.4 Fabric forming simulation

Numerical modelling may be especially useful for prototyping fabric architecture and predicting material behaviour in the initial design state ([23], [92]). Forming simulation of quasi isotropic random fibre mats can be done in an analogous manner to elasto-plastic sheet metal forming [93]. Drape of directional reinforcements for small deformations can be effectively modelled using sets of explicitly solvable equations and pin-joined fabric model assumption [93]. Such kinematic mapping methods are also known as geometric mapping and fishnet algorithms.

Finite element fabric forming simulation is represented by a set of equations describing mechanics of the process (equilibrium), a constitutive material model and boundary/loading conditions [16]. The solution of this equations system is done numerically, e.g. using explicit finite element solvers [23], which are advantageous for complex models compared to earlier implicit methods [71]. Kinematic mapping, macro- and meso-scale finite element modelling approaches are reviewed below. Micro-scale simulations that attempt to model a fabric at the fibre scale will not be addressed in this thesis, interested reader is referred to [94], [95] and references therein.

2.1.4.1 Kinematic mapping

In-plane shear is the main deformation mechanism of a fabric, therefore early numerical models such as kinematic mapping [96] addressed only this type of deformation. Kinematic mapping does not take into account material properties ([14], [16]) or process parameters [82], thus only locking angle

information is used to define fabric processing limits. The main assumptions of kinematic mapping are as follows ([60], [64], [96], [97]):

- fibres are inextensible,
- warp-weft intersection points are fixed (no tow slip),
- rotations at intersection points are free (no shear locking),
- surface curvature is much larger than length of the cell side (lines are straight between the crossover points),
- fabric is in perfect contact with the surface.

Limitations of kinematic mapping were discussed in [53], [83] and [98]. The approach is only suitable for axisymmetric shapes with forming initialisation at a single point and carefully chosen generator paths for initialisation and propagation of fabric drape. Kinematic mapping is approximate, but it does provide useful information in an early design stage. Practical tips for a draping operator were derived from 'fishnet' simulation in [99] where fundamental assumptions for drapeability of a generic part and a forming strategy was determined based on curvature information of weft and warp tows (e.g. local manipulation on concave surface to avoid bridging versus global manipulation on convex surface).

In [53] a combined kinematic mapping and a mechanistic approach was used to investigate shear behaviour of satin and plain weave glass fabrics. A pin-joint model was enriched with inter-tow friction, tow width and spacing information, enabling parametric studies on how these parameters influence locking angle. It was observed that wider tow, smaller spacing and higher inter-tow friction lead to earlier onset of shear locking and wrinkling.

A modified kinematic mapping approach exploiting minimisation of fabric shear energy was proposed in [98]. Shear energy data could be obtained from mechanical test (e.g. picture frame) or numerical model. An iterative scheme was then used to calculate lowest fabric energy needed for each draping simulation step. Fabrics exhibiting symmetric (e.g. plain woven) and non-symmetric (e.g. stitched NCF) shear were investigated numerically, showing that the proposed model was capable to yield reasonable shear angle distribution results for both fabric types and thus account for non-symmetric shear behaviour as illustrated in Figure 2.30. Friction between the fabric yarns and their compaction behaviour was inherently taken into account by specifying material compliance, however, ply-to-ply or fabric-to-tool friction could not be represented.

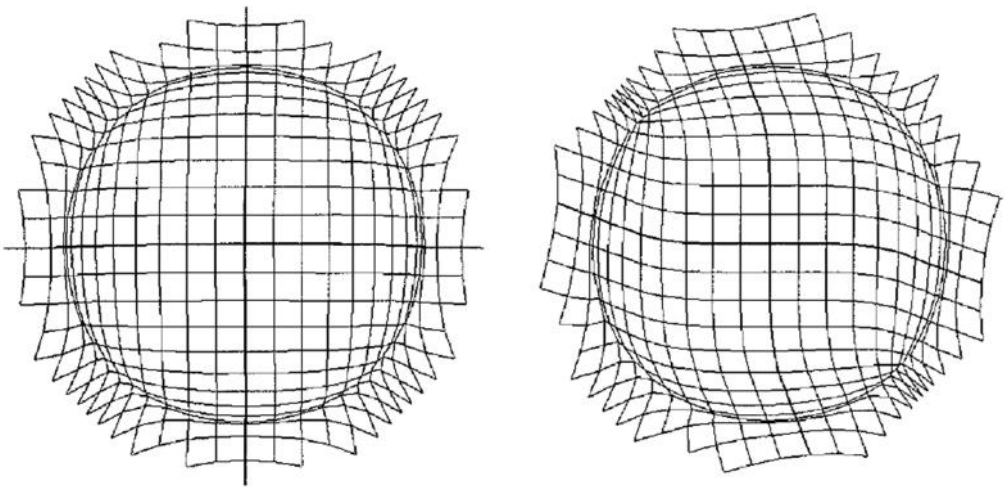

(a) (b)

Figure 2.30 Results of iterative modified kinematic mapping drape simulation over the hemisphere [98]: a) satin weave and b) ±45° pillar warp knit NCF

Another kinematic mapping type approach with the ability to account for material stiffness properties and, potentially, rate effects was proposed in [100]. A unit cell model was constructed using 3D truss elements pin joined to a rectangular shape as shown in Figure 2.31a. A diagonal bar was calibrated to represent shear behaviour during deformation to a rhomboidal shape.

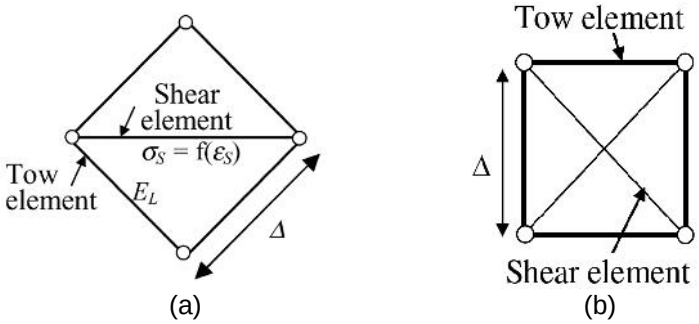

(a) (b)

Figure 2.31 Woven fabric UC truss models: a) with one diagonal element [100] and b) with two diagonal elements [56]

A slightly modified model of [100] was presented in [56] with the aim to provide a quick and efficient optimisation tool for draping applications. An additional truss element on the diagonal was added and wrinkling was identified by truss elements that are loaded in compression (Figure 2.31b). A non-linear rate dependent material model was implemented for draping of woven pre-preg fabric and friction effect was treated using an ideal-plastic pseudo truss element connecting fabric and blankholders nodes. Good comparison to a hemisphere draping test was obtained.

Further details on kinematic mapping methods can be found in [18], [101] and references therein.

2.1.4.2 Macro-scale FE modelling

Macro-scale FE modelling approaches treat fabric as a continuous medium and employ either membrane or shell finite elements. In contrast to the kinematic mapping method, wrinkling is identified by occurrence of in-plane compressive forces, rather than exceeding of specified locking angle [98]. Material properties such as tensile and shear moduli, interface friction and process parameters such as forming speed and boundary conditions can be included in a FE draping simulation [102].

In general a major difficulty in constitutive modelling of fabric is a correct treatment of large strains and deformations. Note that due to large deformations updating the orthotropic material law with respect to rotation of tow directions is important [97]. If material law is not updated, fictitious tensile stresses are introduced and the fabric specimen is elongated as illustrated in Figure 2.32. Better prediction of shear angle and shear stresses compared to a non-updated material model or kinematic mapping approach can then be obtained.

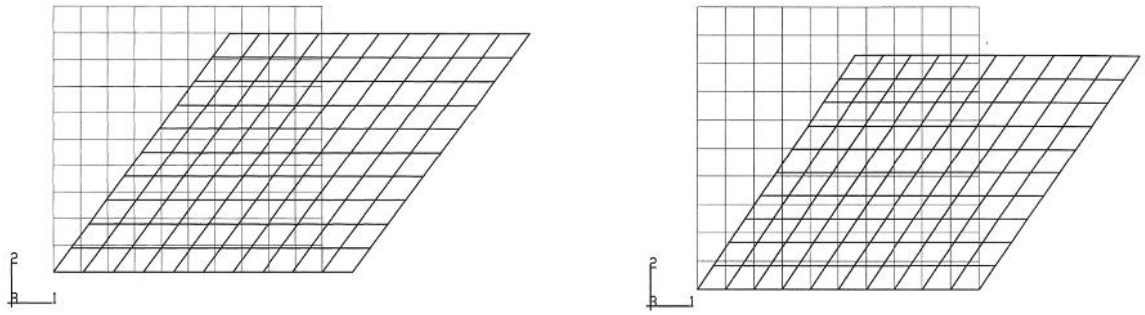

(a) (b)

Figure 2.32 Shear simulation model [97] with a) non-updated and b) updated material model

Truss finite elements can be exploited to simulate inextensibility of the tows, whereas shells or membrane elements can be used to account for inter-tow friction, tow jamming and fibre sliding effects ([18], [69]). Such a model is depicted in Figure 2.33, which if properly calibrated can represent tri-linear character of the fabric normal stress-strain relationship.

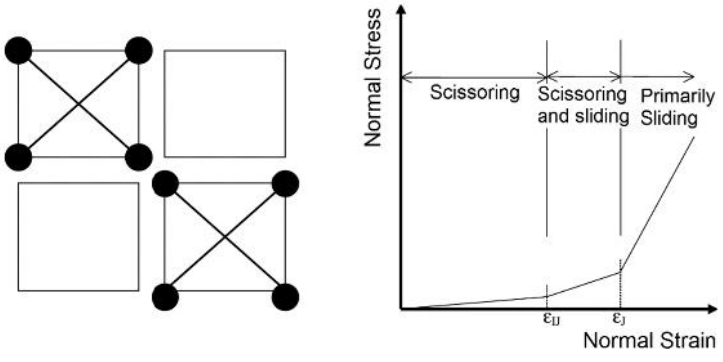

(a) (b)

Figure 2.33 A shell-truss FE model for plain weave fabric [69]: a) a unit cell and b) tri-linear normal stress-strain relationship curve

A non-orthogonal FE model is necessary to represent non-symmetric shear behaviour. In [75] a constitutive equation consisting of two parts was considered which took into account stiff response of the fibre tows in tension and shear stiffness of the fabric. Shell and membrane FE elements were tried in the simulations, with the latter proving to be about three times less CPU expensive, but lacking the ability to account for through-thickness stress field and out-of-plane bending, which is important in order to characterise the formation of wrinkles. The model could represent non-symmetric shear of E-glass ±45 tricot warp knitted fabric as shown in Figure 2.34.

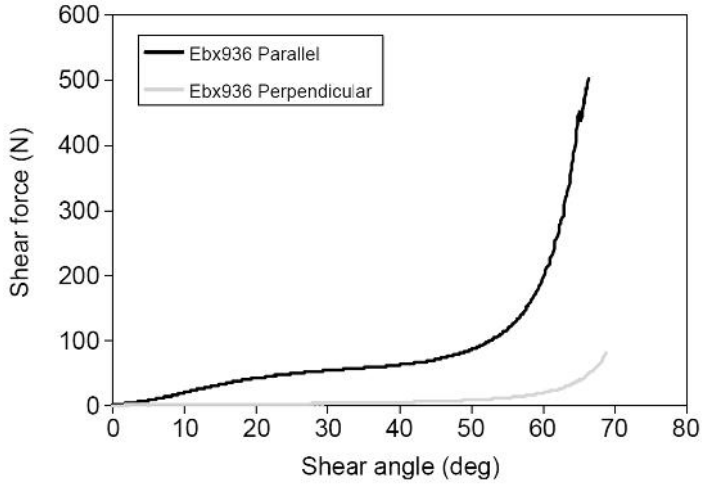

Figure 2.34 Shear angle versus shear force curves for E-glass ±45 tricot warp knitted fabric exhibiting non-symmetrical shear behaviour [75]

A similar approach was presented in [16] where woven fabric was modelled using a three node membrane elements with arbitrary warp and weft tow directions relative to the element edges (Figure 2.35). Only tensile and shear properties were taken into account, neglecting bending behaviour and axial strain coupling between perpendicular yarn systems. Implementation of the model using shell elements in [57] has, however, demonstrated the importance of bending stiffness to properly model wrinkles formation.

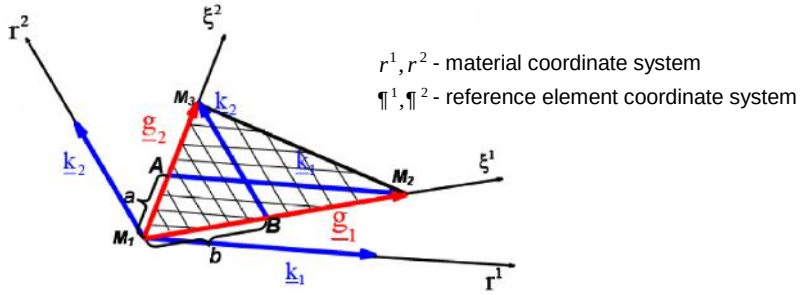

Figure 2.35 Three node finite element for textiles modelling [16]

Analogous work on non-orthogonal modelling was presented in [87] and clearly showed the superiority of the model compared to an orthogonal approach. Also, a parametric study on friction

showed its importance to accurately model blank holder forces for correct shear angle distribution over a draped hemisphere and predict the force exerted on the punch.

Draping process of stitched woven fabric was modelled in [13] using the truss-shell model [69] discussed earlier, which was adapted by adding beam cable elements to represent stitches. Different patterns of stitches and their influence on fabric drape behaviour were investigated. Stitch elements stiffness, breaking strength, slack and initial tension properties were obtained from tests and are schematically illustrated in Figure 2.36.

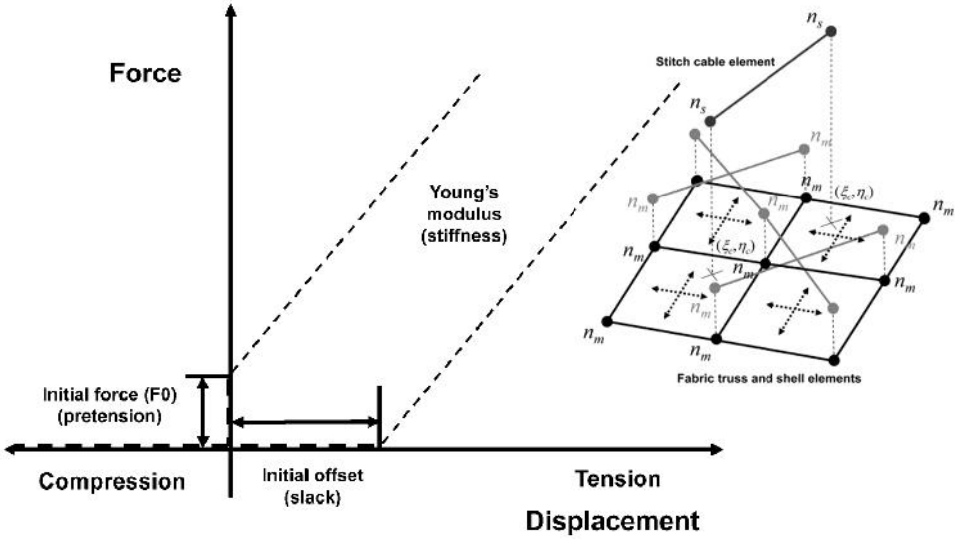

Figure 2.36 Beam element cable material model parameters for stitch [13]

Macro-scale analysis using continuum FE models has limitations if excessively large strains are involved [16]. Common usage of empirical, semi empirical coefficients or inverse methods makes it difficult to extend the models to other types of textiles [7]. Meso-scale FE modelling can overcome some of these limitations and is discussed below.

2.1.4.3 Meso-scale FE modelling

In [103] an overview of modelling strategies ranging from macro- to micro-scale was presented with special emphasis on general meso-scale modelling approaches. [103] gave a road map illustrating the main steps needed for detailed characterisation and analysis of material behaviour (including damage, failure, permeability etc.) together with an extensive list of cited publications that demonstrate the strong interest and potential of meso-level modelling for fabric forming simulation.

A meso-scale model incorporates fabric distinct geometrical features at the tow level where yarn cross section shape and relative frictional movement between the yarns and layers can be represented. In [104] deformation behaviour of dry woven fabrics was considered for investigation of a unit cell with different geometrical parameters as illustrated in Figure 2.37. Tow geometrical non-

linearity due to waviness, friction between the warp and weft yarns, yarn compaction behaviour and its dependency on tensile load were taken into account. Compressive stiffness of the yarn was assumed to be very low and fabric shear stiffness was neglected with no translational slip of warp and weft yarns. A parametric study yielded some insight into formability of the fabric as a function of undulation, weave type and material properties.

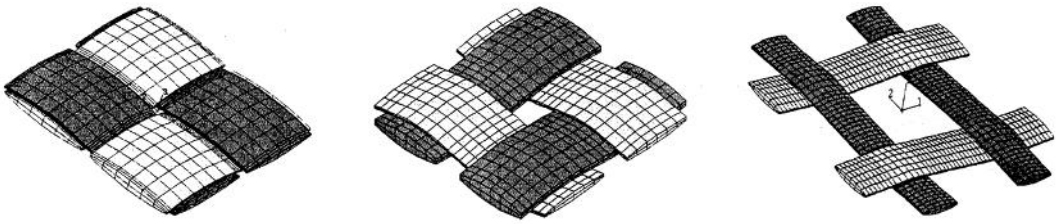

Figure 2.37 Plane weave FE models with different distances between the yarns [104]

An in depth study of tensile behaviour of 2x2 satin woven fabric was presented in [23]. The initial FE model geometry was built based on micrographs. Yarns contact with friction was implemented, yarn transverse stiffness modulus, which is dependent on yarns axial load, was obtained using inverse method. Final validation was done against a hemisphere draping test.

A similar approach was exploited in [92] there the influence of the chosen unit cell boundaries for material calibration was investigated with Figure 2.38a and Figure 2.38b showing two possible UC models for the same plain weave woven fabric. Kinematic BCs can only be applied on material boundary making the model in Figure 2.38b more attractive. Usage of the model depicted in Figure 2.38a requires more sophisticated BC treatment allowing a contact description at the edges of the unit cell that depends on contact information at the UC centre. Thus the choice of representative unit cell should be made carefully when modelling textiles with a complex architecture.

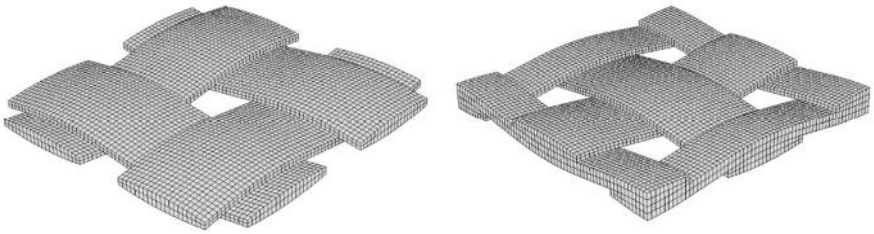

(a) (b)

Figure 2.38 Two types of UC for woven fabric [92]

Work in [85] demonstrated the importance of accurate yarn anisotropy and cross section geometry modelling; also, appropriate contact description was found necessary to model normal force distribution between the tows. Friction was modelled by defining large axial stiffness of gap elements (normal force transfer) with tuned tangential stiffness to approximate friction.

In [81] woven fabric FE simulation results were compared to biaxial tension and picture frame tests illustrating the importance of tow uncrimping modelling. A biaxial tension test with a set of yarns

(warp or weft) not loaded in tension leads to a characteristic non-linear behaviour of the load-strain curves due to straightening of the tows. Unit cell analysis yielded the necessity of accurate yarns cross section change description.

In [7] a plain woven glass fabric UC model was build using TexGen [105] software where yarns were defined by their centrelines and cross section geometries. An orthotropic constitutive model with some empirical parameters for transverse compaction and in-plane shear of tows was implemented. A sensitivity analysis of fabric shear stiffness to yarn fibre volume fraction and yarn in-plane shear stiffness illustrated the necessity to accurately model tow behaviour as considerable variations within realistic parameter boundaries were observed (Figure 2.39).

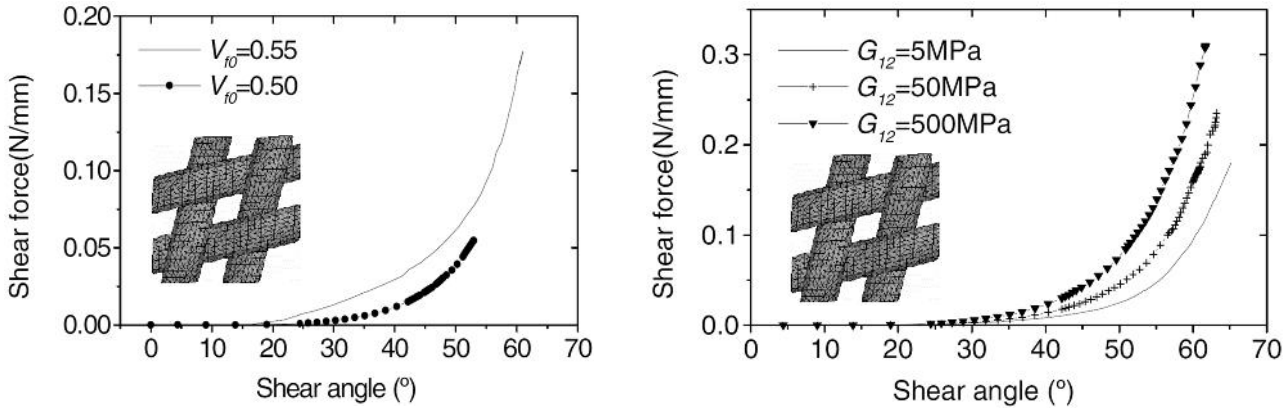

Figure 2.39 Woven glass fabric UC shear simulation results [7]: effects of a) tow fibre volume fraction and b) tow in-plane shear stiffness on shear force

In [62] a coupled draping and structural (failure) meso-scale simulation of biaxial fabric with a tricot stitch was presented. The FE draping model was able to represent a large set of deformation mechanisms, including:

- tow compaction,
- in-plane shear,
- inter-tow friction,
- cross-over point sliding,
- stitch deformation,
- frictional stitch sliding,
- stitch-fibre interaction.

Yarns were modelled using an orthotropic bi-phase material model consisting of ‘fibre’ and ‘matrix’ constituents; stitch-fibre sliding was modelled using additional stitch-to-tow connection elements. Material numerical parameters were obtained from tests with some additional calibration. Validation of the draping model was made using a hemisphere draping simulation, which yielded better correlation with experimental measurements than a macro-scale simulation [5]. A similar fabric modelling approach is also used in this thesis (chapter 5).

In [106] the whole data acquisition and data exchange process was presented and discussed in detail with the aim to obtain a general modelling strategy to build versatile meso-scale fabric models suitable for analysis of permeability, damage, failure, etc. Common meshing problems were discussed and solutions to avoid usual difficulties such as inter-tow penetrations and UC representation were discussed. It was proposed to create a virtual material database (e.g. permeability as function of fibre volume fraction and shear) which would be a great advantage over extensive testing.

Meso-scale analyses could be especially valuable to develop new manufacturing techniques by combining several technologies. For example [107] investigated experimentally the influence of local stitch patterns on the hemisphere draping of a twill weave fabric. Numerous tests were needed to identify general trends of fabric deformation and select the most promising stitching patterns. Numerical meso-scale simulation would greatly improve the development efficiency of such novel manufacturing schemes allowing optimisation of both process and material parameters.

Once a dry preform has obtained its shape during the draping process it needs to be impregnated with liquid resin and cured for a structural component. In the next section a short overview of LRI (Liquid Resin Infusion) technologies, permeability determination methods and infusion simulation approaches is given.

2.2 Liquid resin infusion technologies

LRI technologies for composites manufacturing can usually be subdivided into two distinct types; namely, Resin Transfer Moulding (RTM) and Resin Infusion (RI). The main difference between these two are the boundary conditions exerted by the tooling on the preform and the manner resin can be forced to enter the preform. In the former case two matched rigid moulds are used with pressure injection (Figure 2.40a), whereas in the latter case a one-sided form is used with a flexible cover on top and vacuum infusion (Figure 2.40b). Many variations of these two processes exist, some of these are listed in Table 2.1.

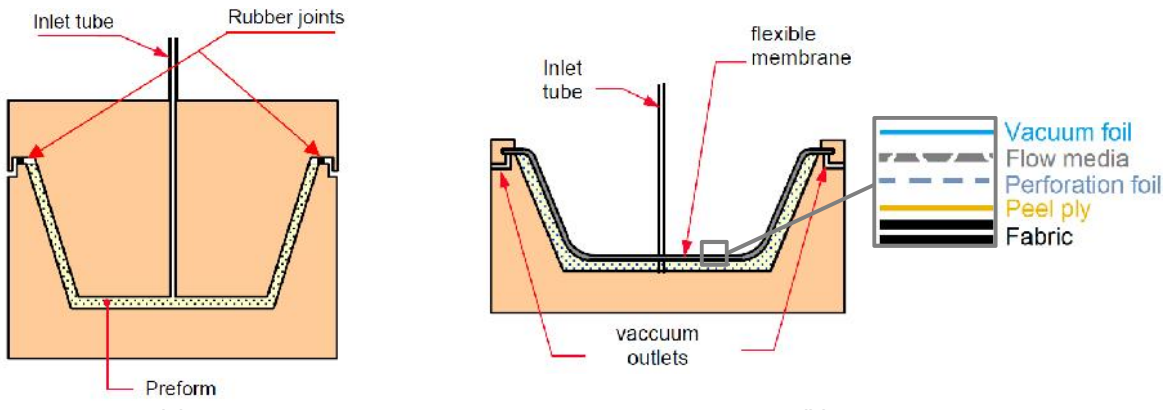

Figure 2.40 LRI technologies: a) Resin Transfer Moulding and b) Resin Infusion [108]

LRI (Liquid Resin Infusion) Processes	
RTM (Resin Transfer Moulding)	**RI (Resin Infusion)**
CRTM (Compression Resin Transfer Moulding)	**CAPRI** (Controlled Atmospheric Pressure Resin Infusion, Boeing patent)
HP-CRTM (High Pressure Compression Resin Transfer Moulding)	**RIFT** (Resin Infusion under Flexible Tooling)
HP-IRTM (High Pressure Injection Resin Transfer Moulding)	**RTM Light**
I/CM (Injection/Compression Moulding)	**SCRIMP** (Seemann Composite Resin Infusion Moulding Process)
SRIM (Structural Reactive Injection Moulding)	**VAP** (Vacuum Assisted Process, EADS patent)
VARTM (Vacuum Assisted Resin Transfer Moulding)	**VARI** (Vacuum Assisted Resin Infusion)
…	…

Table 2.1 Overview of Liquid Resin Infusion technologies

Either RTM or RI techniques may be preferred depending on the design constrains. A two-sided RTM tool makes it possible to obtain high quality parts with high V_f ratio and good upper and lower surface finish. Resin can be injected using either flow rate or pressure control, with flow being driven by up to 20 atm pressure gradient [109]. The RTM process is thus advantageous for net-shape production and short cycle times [110]. Due to high tooling costs it is usually used for small to medium sized parts where a relatively high manufacturing rate is needed (typical cycle time is ~3…50 min [111]). For shorter cycle time HP-IRTM (High Pressure Injection Resin Transfer Moulding) and HP-CRTM (High Pressure Compression Resin Transfer Moulding) processes may be considered, offering ~75…140 atm injection pressure and cycle time below 6 minutes with fast curing resin systems [109].

RI technology generally results in one smooth surface (inserts can be used locally to enhance the second surface properties). As the tooling is simpler (only a male or female form is needed) considerably larger parts may be produced at acceptable cost. Typical examples of RI application at a large scale are manufacture of yacht hulls [112] and wind turbine blades [113]. Since only vacuum pressure is available to drive the flow, possible resin flow rates are limited. Applied pressure gradient is the most important factor, though influence of gravity (for parts with large vertical dimensions) and capillary effects may also have a significant effect. A typical cycle time for a RI is ~5…180 min [111].

2.3 Permeability tests methodologies and material characterisation

Permeability testing of fabrics is a challenging task considering the amount of tests needed to achieve certain confidence, number of materials available and all relevant configurations of their use including stacking sequence, compaction, etc. The majority of permeability measurements in the

literature are obtained from 3 to 5 tests, whereas 95% confidence may only be achieved by doing at least 20 tests of a single configuration [114].

In [115] a promising numerical lattice Boltzmann method was proposed based on microscopic models and mesoscopic kinetic equations with fluid 'particles' interacting on a lattice. A detailed textile input model can represent compaction, shear deformation and nesting effects accurately (e.g. WiseTex pre-processor [61]). However, while providing a good agreement to theoretical permeability data, the lattice Boltzmann method was found to be extremely CPU expensive.

Due to complexity of the fabric architecture (e.g. variation of gap and tow cross section area and shape [116]) permeability measurements generally show considerable scatter. However, the test methodology itself is important in order to achieve consistent measurement results as was observed in recent benchmarking efforts [117]. In [118], [119] and [120] the use of a high precision anisotropic reference specimen produced using stereo lithography was suggested. Such an approach excludes measurements variability due to fabric irregularities and serves to compare and improve different permeability measurement setups and methodologies. Meanwhile, however, each laboratory continues to perform permeability measurements based on its own 'best practice' and there are no standardised test procedures to date.

An overview of permeability measurement techniques (experimental and numerical) is given in the following sections.

2.3.1 Experimental permeability measurement approaches

Permeability of a porous medium describes its resistance to flow of fluid (or gas) through it. The clothing industry has its own permeability measurement standards, but they cannot be adopted directly to technical textiles. A permeability benchmark exercise took place [117] showing a considerable scatter of measured permeabilities (by up to 90%) and high variation of ratio of principal permeabilities (by a factor of up to 2). Implementation of recommendations on testing methodologies have led to a reduction of test measurements scatter to 20 % [121].

All permeability test methods can be grouped by a) flow geometry (linear or radial), b) injection BC (constant pressure or constant flow rate) and c) saturation state of the specimen (saturated or unsaturated) [117]. Linear flow permeability tests are usually performed on a rectangular specimens cut in two principal permeability directions. If principal directions are not known, three tests are needed in 0°, 45° and 90° directions relative to a reference direction of the fabric (e.g. warp or weft for a woven fabric). Edges of the specimens must be carefully sealed to avoid the occurrence of racetracking. An even flow front across the cross section is expected; from information of flow front position versus time it is possible to estimate the in-plane permeability of the material using the following equation [122]:

$$K = \left(\frac{L^2}{t}\right)\frac{¤«}{2\Delta P}, \tag{2.21}$$

where L – flow front position at time t, m,

¤ – porosity,

« – fluid viscosity, Pa·s,

ΔP – difference between inlet and outlet pressure, Pa.

The above equation can be used for unsaturated specimen test with constant inlet pressure. In the case of a saturated specimen test resin flow rate and pressure gradient are monitored. The permeability (in-plane or through-thickness) is then estimated using the following equation [117]:

$$K = \frac{Q«L_s}{A\Delta P} \tag{2.22}$$

where Q – fluid flow rate, m^3/s,

L_s – specimen length, m,

A – specimens cross section area, m^2.

Linear flow infusion tests often suffer from race tracking along the specimen edges. Radial flow experiments eliminates this problem as inlet is positioned in the middle of the specimen and test data is acquired as the flow front moves to the edge of the specimen [123]. A hole through the preform has to be cut to accommodate a pure in-plane flow. If the medium tested is isotropic and inlet pressure is constant, the permeability may be estimated using the following equation [117]:

$$K = \frac{¤«R_0^2}{4\Delta P t}\left(\left(\frac{R}{R_0}\right)^2\left(2\ln\left(\frac{R}{R_0}\right)-1\right)+1\right), \tag{2.23}$$

where R – flow front position (radius) at time t, m,

R_0 – inlet pipe radius, m.

In the case of constant flow rate permeability is estimated using the following equation [117]:

$$K = \frac{Q«}{2®h\Delta P}\ln\left(\frac{R}{R_0}\right), \tag{2.24}$$

where h – cavity height, m.

If the fabric is anisotropic, permeabilities can be calculated from the equivalent isotropic permeability by measuring the axes of flow front ellipse [124]. Although equations (2.23) and (2.24) includes the inlet hole diameter, inlet size variation may inconsistently influence measured permeability [125]. This is attributed to different fabric architectures and local arrangement of fibre tows under the inlet. Common sources of errors in permeability measurement tests includes the following factors ([114], [117], [126]):

- material heterogeneity due to manufacturing (e.g. different nesting is possible at identical fibre volume fraction),
- random experimental errors,
- human factors (e.g. specimen preparation),
- variation in temperature field (e.g. difference between fluid and tool temperatures),
- local changes in fibre orientation, superficial fabric density and nesting effects,
- sample deformation (e.g. shear, compaction),
- micro-flow within the tows.

Due to fabric variability permeability is a statistically distributed parameter even for a single V_{f} value [127]. Experimental work in [128], showed that fibre volume fraction and thus (saturated) permeability varies with injection pressure in through-thickness permeability tests, especially for lower V_{f} values. Saturated and unsaturated permeabilities may be different and depend on the reinforcement type, size of the saturation zone and the ratio between capillary pressure and inlet pressure [117]; $K_{\mathrm{sat}} / K_{\mathrm{unsat}}$ ratio may vary from 0.4 to 1 ([129], [130]). The main reasons for these variations suggested in [130] are:

- flow through the gaps,
- capillarity effects,
- air entrapment,
- fibre surface roughness,
- wetting of tows.

For unsaturated permeability testing of dual scale reinforcements (e.g. fabrics with clear tow-gap structure), care must be taken to account for the capillary flow [121]. In [123] a specific non-crimp fabric was investigated and saturated and transient (unsaturated) through-thickness permeabilities were measured yielding a difference between the two of up to 10 times ($K_{\mathrm{transient}} \approx 10 \cdot K_{\mathrm{saturated}}$). It was also noted that the structure of one fabric side (which is often different due to stitching) has an impact on the transient permeability measured. A short overview of various permeability measurement tests can be found in [131].

Permeability test setups

A set of material and test parameters such as resin flow length, temperature, pressure, preform thickness, etc. needs to be measured or monitored depending on the type of permeability test. A list of various monitoring techniques and their applicability is given in Table 2.2.

Monitoring technology	Process parameter			
	Flow front	Temperature	Pressure	Cure
Visual	+	-	-	-
Pressure sensors	+	-	+	-
Optical fibres	+	+	+	+
DC Resistivity	+	-	-	+
AC Resistivity	+	-	-	+
Ultrasound	+	-	-	+
Piezo sensor	+	-	+	-
IR sensor	+	+	-	+
X-Ray radioscopy	+	-	-	-
MRI (Magnetic Resonance Imaging)	+	-	-	-

Table 2.2. Infusion process parameters and monitoring technologies ([132], [133], [134])

MRI is the most advanced (and expensive) tool which allows tracking of fluid flow on very distinct scales (m to µm) and to visualize the transition zone between saturated and unsaturated preform areas [134].

A 2D in-plane unsaturated permeability test setup using electrical sensors in a non-transparent mould was proposed in [135] and further developed in [127]. In Figure 2.41 a view of the test plate is given with the injection gate, vent and sensor positions indicated. Electrical sensors were employed, which required electrically conductive fluid to be used, whereas the material tested had to be non-conductive. A diluted corn syrup was used as a test fluid, its exact viscosity for every test was measured using a viscosimeter.

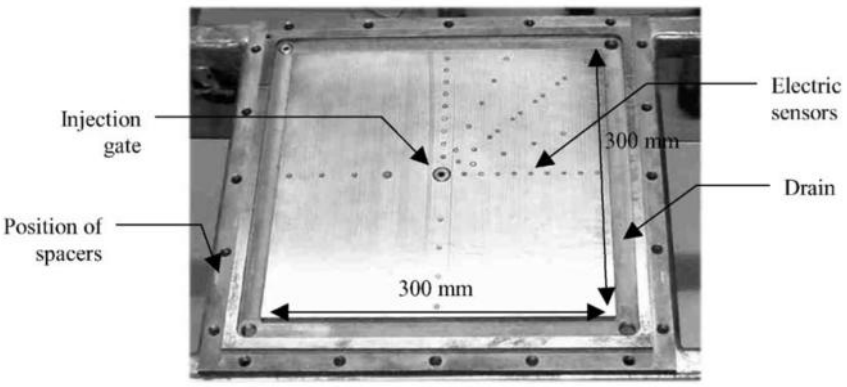

Figure 2.41 Radial flow permeability measurement setup plate with sensors [135]

A test setup, which enabled saturated in-plane permeability measurements with respect to compaction pressure (i.e. varying V_f) was proposed in [136]. The test rig was incorporated into an Instron testing machine. It was noted that depending on fabric architecture and compaction pressure resin channels may have a smaller or larger impact on flow propagation at the interfaces, and that it is important to include this kind of effect in the simulations.

In [137] a transverse permeability (saturated flow test) during continuous compression loading was measured for different types of reinforcements (flax mats, flax NCF, carbon plain weave and glass satin weave). This type of test method is especially relevant to RFI (Resin Film Infusion) composites manufacturing due to variable compaction pressure. It is also advantageous as the time needed to perform experiments at different V_f ratios is reduced.

A radial infusion experimental setup with electronic sensors was used in [138]. An optimisation algorithm was applied to solve the inverse problem and obtain all 3 principal permeability values. Through-thickness permeability was measured more precisely than in Advani's method [124], since more points were available for fitting; on the other hand it was noted in [124] that the presence of sensors often leads to racetracking and flow disturbances.

An inverse numerical approach employing V_f optical measurement (light transmission) and a level set method was proposed in [139] to calculate in-plane permeability accounting for porosity variability in the specimen. This method avoids sensor-induced disturbances, but is only suitable for transparent preforms such as glass fabric.

In [140] a mould design which enables unsaturated and subsequent saturated in-plane permeability measurements on the same specimen with different fibre volume fractions and boundary conditions (constant inlet pressure or constant flow rate) was presented. Rigid mould design, careful sealing of the specimen edges and visual flow front propagation monitoring helped to reduce the appearance of many problems such as mould deflections and racetracking. Unsaturated and saturated permeabilities of various fabrics were measured demonstrating a general trend that the former is higher due to capillary effects. However, an exception was observed for $(0/90)_8$ specimens of biaxial stitched glass fabrics under very low compaction pressure conditions. Also, constant flow rate experiments resulted in higher permeability compared to constant inlet pressure tests, with the exception of the above mentioned fabric at a low fibre volume fraction.

An in-plane permeability measurement methodology based on flow front angle measurement in 1D type test was proposed in [141]. Rectangular specimens were cut at 45° with respect to principal permeability direction in order to obtain flow front formation at an angle to the flow direction. In general, such an approach can reduce the necessary permeability tests to two. It was stated that the methodology could be further adapted for saturated permeability and sheared fabric permeability measurement.

Fluids used in permeability tests

A fluid for permeability testing must satisfy certain requirements in order to apply Darcy's law. It must be Newtonian (with a linear relationship between shear stress and shear strain rate) and the flow itself should be laminar in the range of low Reynolds number between 0 and 10, but not too low as capillary pressure effect would become dominant ([135], [142]). Care should be taken to measure and maintain constant temperature of the test fluid and test equipment to limit possible viscosity variations. A variety of fluids are used for the permeability measurement, some of these are:

- corn syrup ([43], [47], [110], [114], [127], [135], [138], [140], [143], [144], [145], [146], [147], [148], [149], [150], [151], [152]);
- DOP oil (Diphenyl-octyl-phthalate) [153];
- gas ([154], [155], [156], [157]);
- glycerine [158];
- hydraulic oil [159];
- motor oil ([35], [37], [48], [119], [120], [145], [160], [161], [162], [163], [164], [165]);
- neutral oil (ISO 150) [123];
- paraffin oil [166];
- PEG (polyethylene glycol) [167];
- reactive resins ([33], [150], [151], [168], [169], [167], [170], [171]);
- reactive resins without hardener ([35], [172], [167]);
- silicon oil ([11], [121], [137], [141], [154], [173], [174], [175], [172], [176], [177], [178])
- thermoset resins [38];
- vegetable oil ([33], [36], [139], [179], [180], [181]);
- water ([150], [177]).

Corn syrup is the most 'popular' test fluid as it has advantages of being Newtonian, nontoxic and easy to handle. Its viscosity can be adjusted by diluting with water and visibility enhanced with various dyes. However, tests with corn syrup result in lower permeability values compared to e.g. motor oil due to different surface wetting properties as the corn syrup needs external pressure to wet the fabric [142]. Lower surface tension leads to a smaller contact angle and contributes to a better fabric wet out and less pore formation during infusion ([150], [182], [183]). Furthermore, one should be aware that a viscosity change (5% in 2 hours) can occur due to sedimentation of the corn syrup [140].

The difference in measured permeability due to use of different fluids (water, corn oil and epoxy resin) was investigated in [150]. Viscosity variation had little impact on permeability results for both steady state (saturated) and transient (unsaturated) flow experiments. It was stated that various fluid-fibre combinations result in different contact angles and wettability of the preform, thus the use of the same resin system for testing and manufacturing was recommended.

The capillary effects observed using different test fluids may result in different measured permeability values [184]. Unsaturated permeability dependence on surface tension of the resin is mentioned in [183]. Some reports (e.g. [172]), however, stated that no substantial difference in measured permeability occurred when using fluids with different properties if normalised to viscosity; for example, silicon oil ($\mu = 0.12$ Pa·s, $\gamma_{st} = 23 \cdot 10^{-3}$ N/m, $\theta_w = 21°$) and epoxy resin ($\mu = 1.7$ Pa·s, $\gamma_{st} = 44 \cdot 10^{-3}$ N/m, $\theta_w = 57°$) were compared in [172] showing negligible difference in measured permeability values.

Capillary pressure may be small compared to total flow driving pressure, but it may have a significant impact on void formation, especially for dual scale fabrics [167]. In [167] a non-wetting behaviour of an epoxy resin injected under constant pressure was reported. However, constant flow rate experiments yielded velocity dependence of the dynamic wetting angle. Thus the same fluid may behave as wetting, or non-wetting, depending on process parameters.

There exist a correlation between permeabilities measured using fluid and gas ([154], [157]) thus it is possible to use air for permeability measurement and then calculate corresponding fluid permeability. If Reynolds number is lower than 0.1, compressibility and inertial effects of gas flow can be neglected [154]. In [142] permeability measured using gas was found to be higher than that obtained using a fluid.

2.3.2 Numerical permeability estimation approaches

A purely numerical approach to calculate in-plane permeability of woven fabric was presented [185]. That work used a geometrical model of a unit cell with Stokes flow law for the free flow domain and Darcy's law for impregnation of the tows.

In [171] resin flow through single and multilayer preforms of unidirectional fibres with a clear tow structure was investigated both experimentally and numerically. Darcy's law was used to model impregnation of both fibre bundles and voids in-between. Effective orthotropic gap permeability was estimated from laminar flow equations, transverse tow permeability was back-calculated from the experiments. Issues regarding incompatible interfaces between the two regions were recognised; nevertheless, useful simulation results were obtained. An important aspect of the work was recognition of the three dimensional nature of flow in a multi-layered preform, especially in a stitched one as stitches significantly influence flow behaviour.

A universal hierarchical upscaling approach (fibre → yarn → textile → preform → composite) for modelling of textile reinforcements and predicting their permeability properties was presented in [186]. At each scale a minimum of necessary tests were performed and data transferred to the next higher scale analysis. A lattice-Boltzmann approach [187] provided a solution for micro-scale fluid

flow in complicated fabric architectures for undeformed and deformed states. This method solves fluid flow problem within a unit cell and uses a velocity field to predict the total flow under a prescribed pressure. Flow simulation was tackled using Brinkman's (flow inside the yarn) and Stokes (flow between the yarns) equations, with fluid velocity and its gradient matched at the interfaces.

A homogenisation scheme for multi-layered preforms taking into account coupling of in-plane and through-thickness flows was developed in [188]. A tortuosity factor and overlapping degree were used as preform geometry parameters, together with defined interface layers to calculate effective permeability of the layup. Good agreement with the experimental permeability data was achieved, demonstrating the ability to account for different layup configurations.

The influence of relative ply orientations on through-thickness permeability of the preform was investigated in [149]. It was observed that an averaging schemes may introduce large errors when estimating through-thickness permeability of the laminate, if relative ply angle changes considerably (more than 30°). A UD fabric with a clear tow structure exhibiting pronounced resin pathways formation was considered in the simulations; different type of fabric, however, could show a different trend and should be investigated separately. It was suggested that an accurate model for through-thickness permeability should account for both the number and relative angle of UD layers.

In [189] the influence of nesting on out-of-plane permeability was investigated numerically and experimentally using a unit cell simulation and exploiting an analogy between fluid flow and electrical resistance. A difference of two orders of magnitude in permeability was observed for minimum and maximum nesting cases, thus explaining the substantial scatter of measured permeability values, since nesting is hardly controllable in practical preform layup processes.

A universal saturated permeability calculation method, based only on reinforcement geometry was proposed in [190]. A 3D image of the specimen was acquired by X-ray computer tomography from which a pore network model was created where each pore is characterised by its geometry and connectivity to the other pores (an assumption of impenetrable tows was made). Local conductivity was then computed using Poiseuille law. Exploiting an analogy to the electrical circuits, Kirchhoff resistance law was applied to calculate flow flux through the specimen with an applied pressure gradient. With fluid flux at hand hydraulic conductivity was obtained and, consequently, the permeability determined in a chosen direction. To define all three principal permeability values, three simulations in corresponding directions have to be made. The method was claimed to yield good results and to be considerably faster than Computation Fluid Dynamics (CFD) approaches.

Recently CFD methods have been exploited for various LRI process simulations [191] and for calculation of permeability values ([165], [192]). Viability of the approach was demonstrated in [193] and [194]. Voxel (equal volume elements) based methods have been applied using a finite difference Stokes solver in FlowTex [193] to give efficient numerical estimation of permeability yielding results of similar accuracy to the general purpose CFD solvers. With integration of automated X-ray tomography image analysis for fabric geometry creation ([195], [196], [197]) the approach has

shown a potential to provide a reliable tool for numerical permeability estimation. Furthermore, CFD infusion simulations are currently making their way into industrial applications; for example a OpenFOAM CFD code has been applied to simulate infusion of a braided fabric RVE (Representative Volume Element) in [198] with resulting simulation time of 1 hour for 50x50x50 mm part on a 3 GHz machine.

2.4 Fluid flow in textile reinforcements and preforms

Resin infiltration of a preform is influenced by many technological parameters and material properties such as pressure gradient, temperature field, layup and orientation, fibre surface, resin properties, etc. [199]. Incompressible fluid flow in an open region (e.g. volume between the tows) is described by the Navier-Stokes equation [200]:

$$\rho\left(\frac{\partial \mathbf{v}}{\partial t} + \mathbf{v}\cdot\nabla\mathbf{v}\right) + \nabla P = \rho\mathbf{g} + \mu\nabla^2\mathbf{v}\,, \tag{2.25}$$

where $\mathbf{v}$ – flow velocity, m/s,

P – pressure, Pa,

$\mathbf{g}$ – body force, m/s^2,

μ – dynamic viscosity, Pa·s.

The Navier-Stokes equation for steady-state, laminar fluid flow with no body forces reduces to the Stokes equation [187]:

$$\mu\nabla^2\mathbf{v} = \nabla P\,. \tag{2.26}$$

For the case of fluid flow through a porous medium (e.g. fibrous tows) an additional ‘resistance’ term appears on the left hand side of the above relationship, and the Brinkman equation is obtained [187]:

$$\mu_e\nabla^2\langle\mathbf{v}\rangle - \frac{\mu\cdot\langle\mathbf{v}\rangle}{\mathbf{K}_{\text{tow}}} = \nabla\langle P\rangle\,, \tag{2.27}$$

where μ_e – effective viscosity, Pa·s,

$\langle\mathbf{v}\rangle$ – average velocity, m/s,

$\mathbf{K}_{\text{tow}}$ – tow permeability tensor, m^2,

$\langle P\rangle$ – average pressure, Pa.

The Stokes equation describes fluid flow in open regions; the Brinkman equation can be applied to model flow in both open and porous regions. In the latter case viscous term with the effective viscosity μ_e and permeability are used to switch between the porous and free flow regions with or without transition zone [201]. If medium permeability is higher than 10^{-3} m^2, Brinkman equation should be used to model fluid flow in porous media [202]. The Brinkman equation (2.27), reduces to Darcy's law [203] for low velocity gradient zones (far from the open regions):

$$\langle \mathbf{v} \rangle = -\frac{\mathbf{K}_{tow}}{\phi\mu} \nabla \langle P \rangle . \tag{2.28}$$

where ϕ – porosity.

For one dimensional saturated flow of a viscous liquid through a porous medium Darcy's law is expressed as follows:

$$v_{xx} = -\frac{K_{xx}}{\phi\mu} \frac{\partial P}{\partial x}, \tag{2.29}$$

where v_{xx} – flow velocity in x-axis direction, m/s,

K_{xx} – principal permeability in x-axis direction, m^2,

$\frac{\partial P}{\partial x}$ – pressure gradient in x-axis direction, Pa/m.

Darcy's law was developed for saturated flow (water through soil). For unsaturated flow an additional term for capillary pressure needs to be included as follows [47]:

$$v_{xx} = -\frac{K_{xx}}{\phi\mu} \frac{\partial \left(P + P_{cap}\right)}{\partial x}, \tag{2.30}$$

where P_{cap} – capillary pressure, Pa,

Studies have reported both pronounced and negligible influence of capillary pressure effect in permeability tests. Generally, capillary pressure at the fluid flow front is small compared to applied pressure [150]. It was stated in [172] that measured permeability remains constant if P_{cap} is taken into account and the error of neglecting it decreases with increasing flow driving pressure. In [47] capillary pressure values ranged from 3 to 5 kPa accounting for 3 to 5 % of the total resin flow driving pressure if maximum vacuum pressure is used. At low flow rates, however, the interaction between external driving force and wetting force becomes significant [204] and capillary effects have to be taken into account.

Capillary pressure depends on fibre and fluid properties. For UD composites it can be calculated using the equation [183]:

$$P_{\text{cap}} = \frac{F_{\text{f}}}{D_{\text{f}}} \frac{1-¤}{¤} ¥_{\text{st}} \cos ¯_{\text{w}}, \tag{2.31}$$

where F_{f} – form factor, m,

D_{f} – fibre diameter, m,

$¥_{\text{st}}$ – surface tension, Pa,

$¯_{\text{w}}$ – contact angle.

Form factor F_{f} takes into account fabric architecture. For transverse flow in UD reinforcements F_{f} ranges from 1 to 2 m, for longitudinal flow it is about 4 m [47]. In the case of a complex fibre arrangement (e.g. woven fabric) the form factor needs to be evaluated experimentally ([172], [183]).

Decreasing porosity leads to an increase of the surface area to volume ratio and thus an increase of capillary pressure, but at the same time it reduces permeability of the tow [182]. Capillary pressure is generally lower for random mats compared to directional textiles due to larger fractional pore volume in the tows of the latter ([172], [182]).

Contact angle depends on fibre material and not on fabric architecture. Smaller wetting angle leads to an increase of capillary pressure and better wettability of the fibres ([26], [150]). However, capillary pressure is directly proportional to surface tension which, in turn, can vary significantly more than contact angle [26]. A lower value of surface tension helps to prevent void formation [150].

Void formation can be quantified using capillary number, which depends on reinforcement scale properties and defines the balance between viscous and capillary (surface tension) forces ([150], [184]). Void formation mechanisms, their mobility and modelling approaches were discussed in detail in [182] and [205]. Optimal impregnation speed can be obtained using the following equation [133]:

$$v = \frac{Ca^{*} ¥_{\text{st}} \cos ¯_{\text{w}}}{«}, \tag{2.32}$$

where Ca^{*} – modified capillary number that depends on the wetting angle, m.

Optimisation of the flow front propagation velocity may be used to hinder formation of voids ([133], [205], [206]). In purely UD preforms void formation may be almost completely avoided. In the case of more complex fabric structure, e.g. biaxial NCF, it is not possible to create an optimal in-plane flow in all plies which leads to higher void content [207].

2.4.1 Permeability

Permeability is a tensorial quantity that relates local velocity vector of fluid flow with associated pressure gradient [208]. Permeability of an orthotropic medium in the principal permeability frame is described by a 3D tensor with principal permeability values on the diagonal:

$$K = \begin{bmatrix} K_{xx}(V_f) & 0 & 0 \\ 0 & K_{yy}(V_f) & 0 \\ 0 & 0 & K_{zz}(V_f) \end{bmatrix}, \tag{2.33}$$

where $K_{xx}(V_f)$, $K_{yy}(V_f)$, $K_{zz}(V_f)$ – principal permeability values as functions of fibre volume fraction, m^2.

Permeability of a textile material is highly dependent on fibre volume fraction. A simple empirical relationship with experimentally obtained constants a, b and c may be used to quantify this relationship for fibre volume fractions ranging from 0.1 to 0.35 [130]:

$$K = a + b\exp(c(1 - V_f)) \tag{2.34}$$

Another simple law to quantify $K(V_f)$ is the Carman-Kozeny relationship, which was derived for granular beds of ellipsoidal particles [209] and is used to relate permeability, fibre volume fraction and fibre diameter. For fluid flow along the fibres this relationship has the following form ([210], [211], [212]):

$$K = \frac{r_f^2(1 - V_f)^3}{4kV_f^2}, \tag{2.35}$$

where r_f – fibre radius, m,

k – Kozeny constant.

The Kozeny constant k accounts for the tortuosity and non-uniformity of the pores, thus it is different for longitudinal and transverse flows in the same reinforcement; also, it may vary with fibre volume fraction depending on reinforcement [210]. The Kozeny constant k can be obtained analytically for flow through e.g. triangular or square arrangement of cylinders. However, in real composites the fibre arrangement is non-uniform, resulting in underestimation of k values compared to experimental measurements [211]. For fluid flow perpendicular to fibres the Carman-Kozeny equation is expressed using equation [210]:

$$K_{\perp} = C_1 \left(\sqrt{\frac{V_{f\_max}}{V_f}} - 1 \right)^{5/2} r_f^2 , \tag{2.36}$$

where C_1 – coefficient dependent on fibre arrangement (e.g. quadratic or hexagonal),

$K_{\perp}$ – permeability in perpendicular to fibres direction, m^2,

V_{f_max} – maximal fibre volume fraction.

Numerous publications have stated the limited accuracy of the equations (2.35) and (2.36) over a wide range of fibre volume fraction values, especially at lower V_f, which typically varies from 0.3 to 0.6 ([49], [153], [183], [212], [213], [214]). Numerical analysis in [215] showed variability of the Carman-Kozeny constant over a wide range of fibre volume fractions for various reinforcements as illustrated in Figure 2.42.

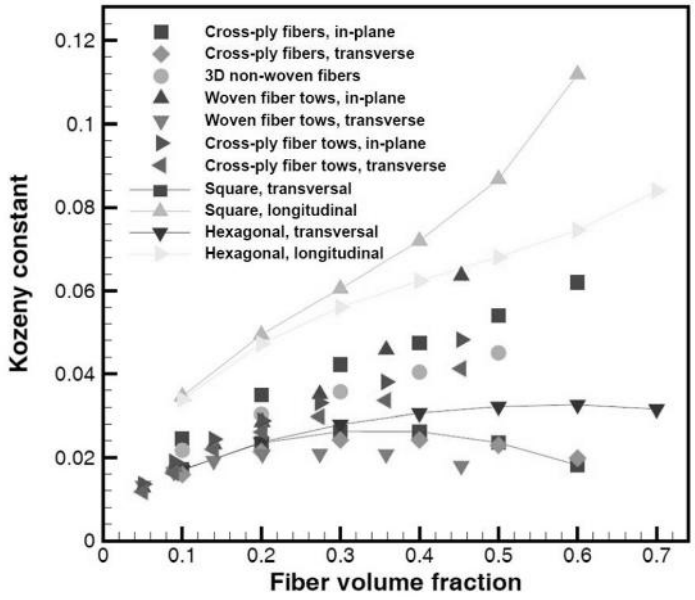

Figure 2.42 Variation of Carman-Kozeny constant with fibre volume fraction for various textile reinforcements [215]

A so-called modified Carman-Kozeny model provides a better fit over wider V_f ratios ([37], [130], [143], [153], [214]) and includes additional empirical parameters:

$$K = \frac{1}{C} \frac{\left(1 - V_f\right)^{n+1}}{V_f^{\,n}} , \tag{2.37}$$

where n – material parameter,

$$C = k_0 \left(\frac{l_e}{l} \right)^2 S_0^2 , \tag{2.38}$$

with k_0 – shape factor,

$\frac{l_e}{l}$ – tortuosity (l_e – real flow length between two points, l – straight line length connecting these two points),

S_0 – specific surface (interfacial area / volume),

Despite limited accuracy, simple estimation of $K(V_f)$ using equations (2.35), (2.36) or (2.37) is widely preferred ([27], [32], [35], [37], [52], [130], [177], [163], [214], [216]). However, if a fabric exhibits very strong dual scale flow effect, the Carman-Kozeny equation is only suitable to characterise permeability of the tows [121].

2.4.2 Dual scale flow effect

Many technical textiles have a very clear tow structure with gaps between the tows. In such case a dual scale flow effects is observed during infusion as faster resin flow in void volumes (gaps) and slower flow into the fibrous tows. The characteristic resin flow pattern in dual scale fabric can be visualised using a two-colour experiment ([153], [217]) where a green-coloured resin is injected into the stitched glass fibre preform first followed by a blue-coloured resin [217]. It could be clearly identified that green resin sinks into the tows and remains there. The later injected blue resin travels only through the gaps between the tows as shown in Figure 2.43. The importance to account for such an effect in the case of non-isothermal reactive resin infusion can be illustrated by the temperature difference in tow (old resin) and gap regions (fresh resin) where differences as high as 15°C may be observed [218]. This leads to considerable heat fluxes and local changes in resin viscosity and cure kinetics.

Figure 2.43 Two-colour experiment [217]: specimen and micrograph of the cross section

There have been a number of studies dealing with dual stale effect representation by numerical models. For example in [204] it was observed that impregnation of tows slows down axial fluid flow in the gaps. A parameter accounting for change of axial velocity component was suggested to model interaction between the two scales of unidirectional woven fabric.

Two permeabilities to describe resin flow in dual scale fibrous medium were suggested in [219] with one permeability value for saturated fluid flow inside the tows and another for partially saturated intra-tow flow (gap spaces between the tows). Fluid flow in the saturated region was modelled using Darcy's law, whereas permeability of partially saturated region was set dependent on a dimensionless parameter that varies with saturation and determines an effective permeability value for the flow front region. A schematic model of the approach is depicted in Figure 2.44; it was postulated that resistance of flow through medium with impermeable tows (regions 1-2) is always higher than flow through medium with permeable tows. The proposed methodology [219] was capable to replicate typical non-linear inlet pressure development observed in unsaturated flow experiments on dual scale fabrics as illustrated in Figure 2.45.

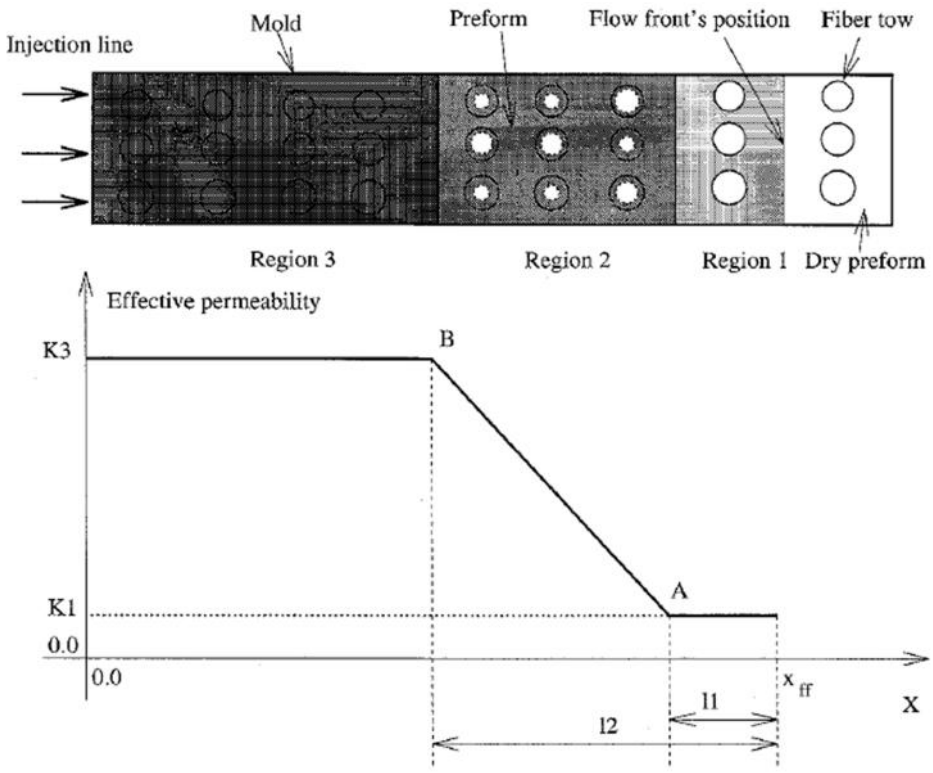

Figure 2.44 Permeability versus position in flow domain [219]

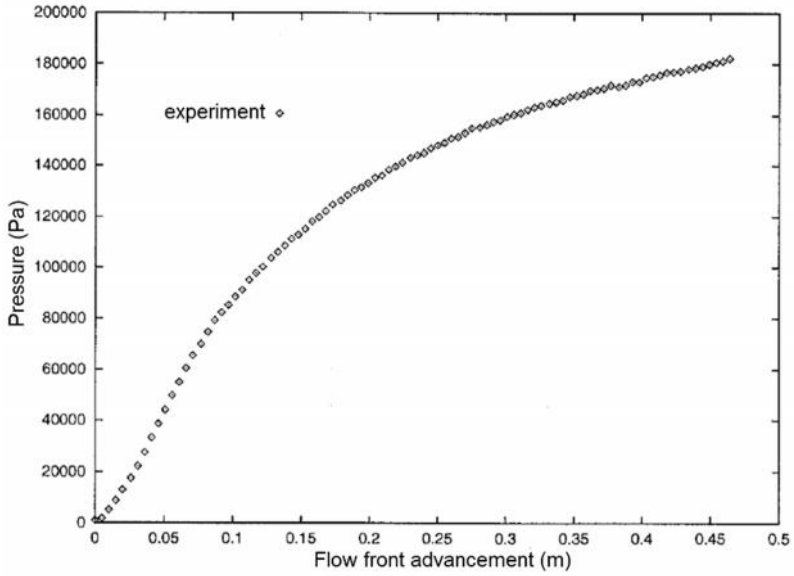

Figure 2.45 Inlet pressure versus flow front advancement (fibre-mat made of fibre tows) [219]

It was noted in [184] that unless flow velocity is very low and capillary pressure is dominant, unsaturated permeability is lower than saturated permeability (with corresponding ratio of 0.4 for UD reinforcements and 0.8 for fibre mats [129]). The linear pressure distribution between inlet and flow front, assumed by Darcy's law, is then invalid due to partial saturation zone shown in Figure 2.46. A so-called degree of saturation was suggested in [129] to account for this effect in the numerical model and to define a saturation dependent permeability. However, for some natural fibres that exhibit fluid absorption and swelling, unsaturated permeability is reported to be higher than saturated permeability [214].

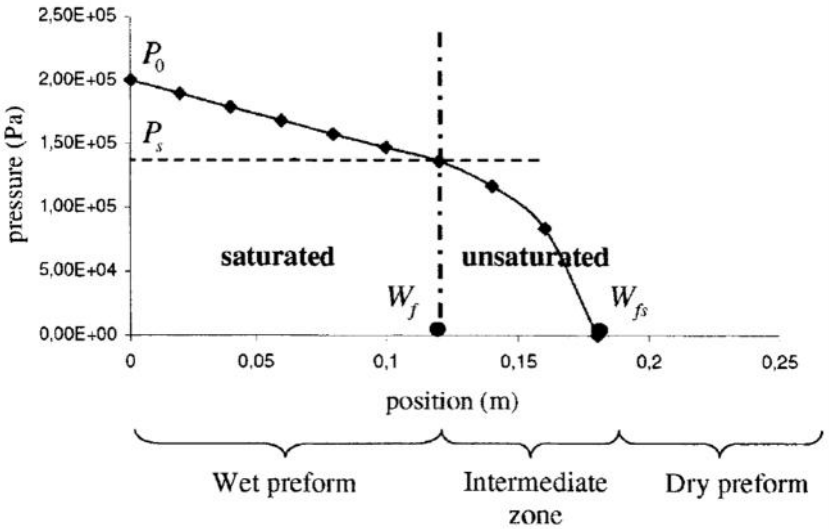

Figure 2.46 Pressure distribution over the preform during unsaturated constant inlet flow rate experiment [129]

Due to dual scale effects the resin flow in woven or stitched fabrics is very different from the flow in random fibre mats ([161], [220], [221]). Tow impregnation is governed by surface tension and

capillary pressure of the fluid [205], besides, tow permeability is much lower than fabric permeability ([222], [223]), and thus impregnation speeds are also very different. Macro-pore flow velocity can drop by up to 60% due to fluid absorption in tows [204]. In [162] it was concluded, that continuous uninterrupted macro-channels along the flow direction are necessary to observe a pronounced unsaturated dual scale flow behaviour.

In [145] to model the flow in dual scale medium the sink term in the continuity equation was related to the capillary number; if the capillary number (which depends on fibre and fluid properties) is sufficiently low, sink influence (intra-tow suction) can be neglected, whereas higher capillary number lead to a logarithmic increase of the sink term and pronounced non-linear inlet pressure profile development.

In [161] unsaturated dual scale infiltration was modelled using a two scale volume averaging method. Global (gap) and local (tow) flows were coupled through the sink term describing the absorption of the fluid by tows. Longitudinal and transverse tow permeabilities were estimated using the Carman-Kozeny relationship with micro-flow modelled by the Navier-Stokes equation. A CV/FE (Control Volume/Finite Element) solution algorithm implemented in the PORE-FLOW© [224] code was used for these simulations and provided a good agreement with experimental data for 1D flow.

Two permeability values to characterise dual scale fibrous reinforcement (biaxial woven carbon and glass fabric, biaxial stitched glass fabric) was used in [180]; namely, a bulk permeability of a fabric and a tow permeability. The former was obtained experimentally and the latter calculated using numerical analysis in LIMS [225]. ‘Duality’ of the reinforcement was taken into account using 1D elements to model sink effects; experimental inlet pressure profiles were used for calibration of tow permeability.

At lower driving pressure, capillary pressure becomes increasingly important as resin flow in micro-pores is driven by it ([183], [199]). Thus saturated and unsaturated permeabilities of the stitched fabrics may vary by a factor of 6 to 10 [202]. Accurate dual-scale flow modelling in [135] included capillary pressure only in equations describing the micro-flow (inside the tow). However, as pressure gradient increases, capillary effect at the wetting front becomes negligible [160], nevertheless care must be taken regarding the final quality of the part due to possible void formation.

In [52] it was noted that dual scale effect may considerably reduce the quality of the final part because air bubbles may become trapped in tows (micro-pores), or in the volumes between the tows (macro-pores) as illustrated in Figure 2.47. Void entrapment depends on fibrous bed, fluid properties and flow speed. If viscous forces are smaller than capillary forces macro-pores are likely to form (Figure 2.47a), conversely if capillary forces are dominant micro-pores may form (Figure 2.47b).

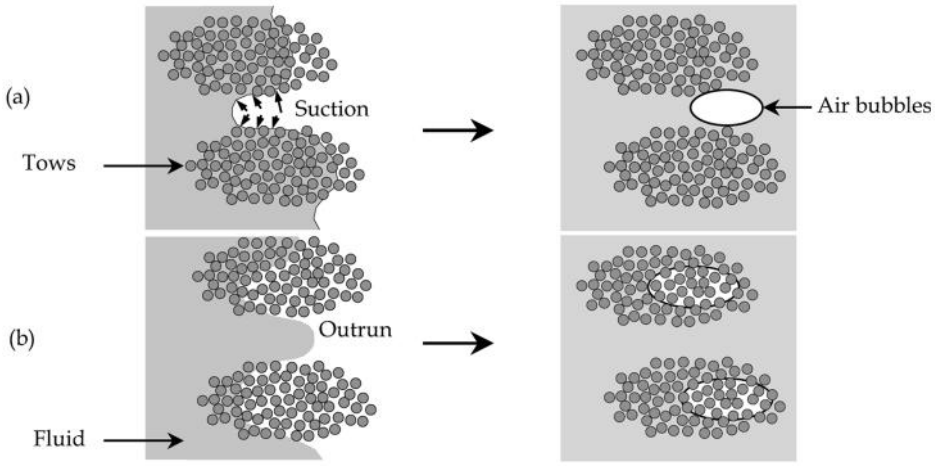

Figure 2.47 Air bubble formation in unsaturated regime: a) macro-pore formation and b) micro-pore formation [123]

Final void content depends on initial air content in the resin, void formation during impregnation and void growth or shrinkage during cure [199]. Under constant inlet pressure conditions the fluid flow speed is initially very high at the inlet region leading to dominant inter-tow flow and formation of micro-pores inside the tows. As flow front progresses bulk flow speed reduces and capillary pressure leads to premature impregnation of tows and macro-void formation ([150], [170], [184], [205], [207]).

The existence of a partially saturated zone at the flow front is the reason bleeding is applied as a mean to improve part quality. Air bubbles trapped inside the tow stay stationary if bubble pressure is smaller than the sum of outside and capillary pressures ([205], [207]). Bubble movement speed depends on difference of surface tension forces between front and rear bubble boundaries [221]. Bleeding with some flow resistance at the vent reduces void content since more time is available to saturate tows; also, less resin is wasted [170]. It was suggested in [220] that an adjustable flow rate, i.e. flow front propagation velocity regulation, may be used to optimise the flow and reduce formation of voids [172].

A concise yet detailed overview of the methods devoted to dual scale flow modelling, formation and movement of voids may be found in [221] and references therein.

2.4.3 Flow in stitched fabrics

The significance of the stitch type on fluid flow through a preform was investigated in [151]. Stitches block resin flow in the channel between tows and change the permeability in that direction. In [226] a simulation model quantifying this blockage of channels and a permeability model was proposed. Sensitivity of through-thickness permeability of stitched fabric was experimentally investigated in [227] and a conclusion made that the area of voids formed by the adjacent stiches has a greater impact on permeability than the density of the stitches.

A detailed numerical study on influence of stitches on permeability of inter-bundle channel was undertaken in [228]. It included investigation of stitch radius, position, inclination, array and distribution density influence on the permeability of the channel. It was showed that all these parameters have a pronounced influence on the fluid flow and should not be ignored.

The influence of stitch (or thread) on the permeability of the fabric was also acknowledged and investigated in [229]. Several UC configurations of biaxial NCF with chain thread were investigated (Figure 2.48).

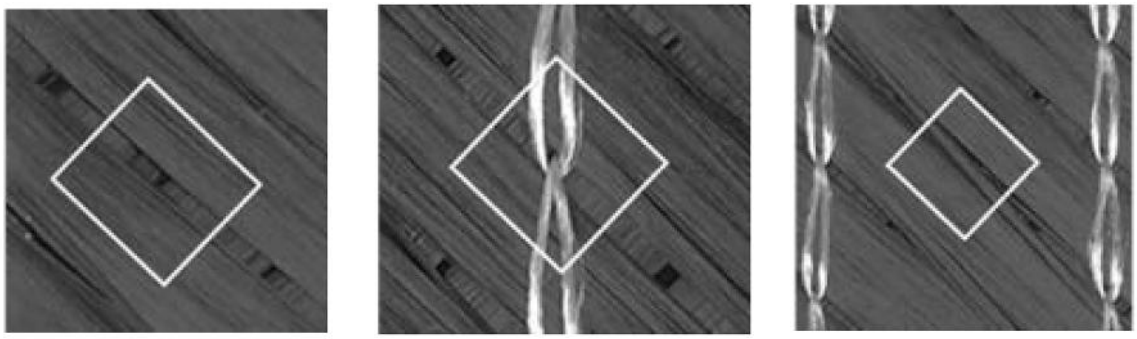

(a) (b) (c)

Figure 2.48 Different unit cells identified on a biaxial NCF [229]: a) plain UC, b) thread UC and c) crossing UC

Permeability values obtained from Darcy's law and flow rate analysis using CFD simulations showed that stitches can reduce local permeability of a unit cell by 5.5-28% [229]. The fibres inter-tow crossing can lower permeability even by 75-90% compared to plain UC with varying channel width. Another important observation was made regarding gap size and found that gap width variation has much greater impact on permeability in the parallel direction compared to the perpendicular direction. Necessity to include statistical variability of the UC geometrical features for accurate prediction was stated.

Similar conclusions regarding the sensitivity of permeability to the meso-channel width were made in [11]. The stitched glass NCF permeability was predicted by modelling the fluid flow in channels and tows using Stokes and Darcy's flow models respectively; injection and capillary pressures were taken into account. It was concluded that a detailed microstructural analysis is necessary for accurate flow simulation.

2.4.4 Flow in distribution medium and racetracks

Foils such as distribution medium (DM), perforated ply and peel ply used in VARI type infusions need to be characterised in detail for accurate infusion analysis [230]. Distribution medium is used to enhance resin distribution over the part. Perforated foils help to distribute resin evenly over a large area of the preform before it impregnates in the thickness direction. Peel ply is needed to remove

distribution medium and perforated foil after part has cured. All these plies contribute to a complex 3D flow formation ([26], [231]) and this process cannot be ignored or simplified using boundary conditions such as defining a filled distribution medium volume at the start of the simulation. Consequently, flow in these media needs to be modelled accurately and will be addressed in section 6.3.2.

Distribution medium permeability is generally considered to be isotropic ([168], [232], [233], [234], [235]). Several experimental arrangements were considered in [232] to test DM permeability for which a high porosity (0.85-0.88) knitted fabric was taken. Tests were performed on a stand-alone specimen on a glass surface and in actual SCRIMP (Seemann Composite Resin Infusion Moulding Process) configuration. A considerable influence of nesting and thus reduction of effective DM porosity was observed. The distribution medium was considered to be isotropic thus only in-plane permeability was measured. In order to obtain only in-plane fluid flow in SCRIMP configuration, a thin impermeable Mylar film was placed between the peel ply and the distribution medium ensuring there was no through-thickness flow into the preform, while still accounting for the fabric nesting effects. A so-called ‘leakage flow model’ was proposed to numerically investigate the infiltration process using a CV/FE approach assuming no in-plane flow into the preform and peel ply, that is, the fabric was saturated only by transverse flow of the fluid from the distribution medium as shown in Figure 2.49.

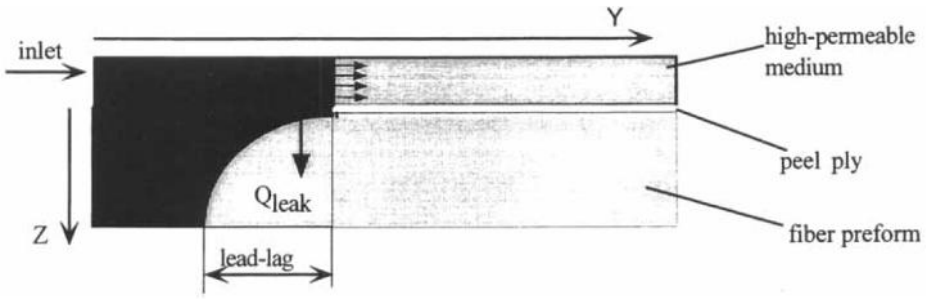

Figure 2.49 ‘Leakage flow model’ for SCRIMP [232]

The presence of a peel ply increases flow resistance in the through-thickness direction and reduces effects of fabric nesting [232]. In-plane permeability of the peel ply was assumed to be equal to the preform permeability and peel ply through-thickness permeability was fitted numerically in [232]. The study also reported a linear trend of the square of flow length versus time in SCRIMP configuration justifying application of Darcy’s law to describe the flow process.

In [233] it was stated that distribution medium and preform thickness ratio has an impact on the filling process. DM, however, was characterised with in-plane permeability only. In [168] permeability of distribution medium was also considered to be isotropic and was characterised using 1D flow experiments on a ‘stand-alone’ DM specimen. Variations in DM permeability measured in different test arrangements was noted in [234] where a difference of 45% was reported for distribution medium

tested in isolation and in a VARTM type test setup. Conventional layers such as perforated and peel plies were, however, not included in these tests.

A single test to obtain fabric in-plane and through-thickness permeabilities and distribution medium in-plane permeability was proposed in [236] where an effective (combined) permeability of both distribution medium and fabric was estimated for flow simulation in a VARI process. Thickness variation due to pressure field change was not considered.

Figure 2.50 illustrates an intuitive approach used in [170] to include distribution medium in a 2D numerical simulation using 1D elements with assigned high permeability values and cross section corresponding to the distribution medium properties. The main focus of research in [170] was to investigate void formation in dual scale fabric flow under different bleeding conditions where it was noted that flexible distribution medium acts as a resin source after the inlet gate is closed. Consequently, flow sources were added to the distribution medium in order to simulate the bleeding process.

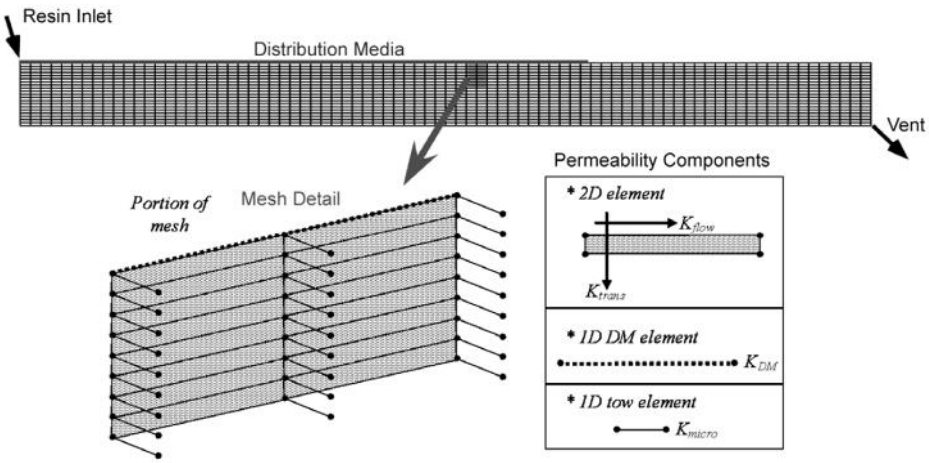

Figure 2.50 FE mesh for investigation of voids formation in VARI process [170]

Resin flow in high porosity regions at part edges and corner radii (i.e. racetracking), can significantly change the flow front pattern [110]. If racetracks are intentional, they are called runners and may be used deliberately for fast resin distribution over the preform [181]. On the other hand, in practice, it may be impossible to avoid racetracks forming around the edges of a part or at corner radii. Due to the impact racetracks have on overall filling process it is necessary to include these high permeable zones in the simulation, for example as 1D elements ([237], [238]).

Geometrical parameters for racetracks were investigated experimentally and numerically in [152] where the Navier-Stokes (open channel flow) and the Poiseuille law (flow in a tube) equations were used to describe flow at the preform edges. Comparison with experiments yielded applicability limitations of each model. It was noted that existence of transverse flow, which depends on permeability of the reinforcement, strongly influences flow in the channel as illustrated in Figure 2.51.

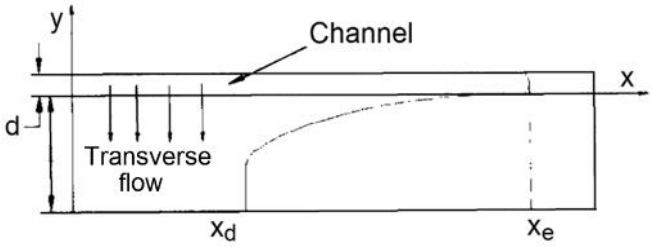

Figure 2.51 In-plane transverse flow from the channel [152]

A transverse flow factor was introduced, which depends on the reinforcement permeability anisotropy ratio [152]:

$$\dagger = \frac{12 \cdot K_{yy}}{d^2} \cdot \sqrt{\frac{K_{yy}}{K_{xx}}}, \tag{2.39}$$

where d – equivalent racetrack channel width, m.

From equation (2.39) it is clear that the same channel size with a different reinforcement permeability will lead to different transverse flow factor values. A simple method based on equivalent permeability of edge elements was proposed to account for racetrack effects [152].

A methodology based on FE simulation and the Carman-Kozeny equation was proposed in [216] to identify and compensate for racetracking effect in a 1D flow permeability test. From one ‘proper’ (no racetrack) test result it was possible to estimate permeability of the ‘racetracked’ specimen and thus not reject the test.

2.5 VARI process simulation

In the VARI process the flexible bagging membrane does not restrain preform expansion when the resin enters the mould. Consequently, pressure borne by the fabric reduces and preform expansion occurs in the thickness direction (Figure 2.52b). Unlike modelling RTM filling (Figure 2.52a), which uses a rigid control volume and can justifiably assume constant porous material properties, equations for VARI modelling must be derived using a non-rigid control volume and compaction dependent material properties [52].

‘Effective’ permeability (also termed ‘flexible’ permeability [176], or ‘equivalent’ permeability [239]) has been used by some researchers (e.g. [236], [240], [241]) to distinguish permeability measured in VARI type test conditions, neglecting preform thickness changes. A ‘representative thickness’ assumption may be justified if, for example, only a qualitative flow front progression is of interest for optimisation of inlet and outlet locations [240], or thickness change is small [239], or an error in estimated permeability is acceptable to describe VARI process through a RTM type simulation. A

dedicated study in [242] showed that the 'effective' permeability assumption can be reasonably acceptable, and that advanced (more CPU expensive) simulations accounting for preform compliance could be used only to cross-check the results.

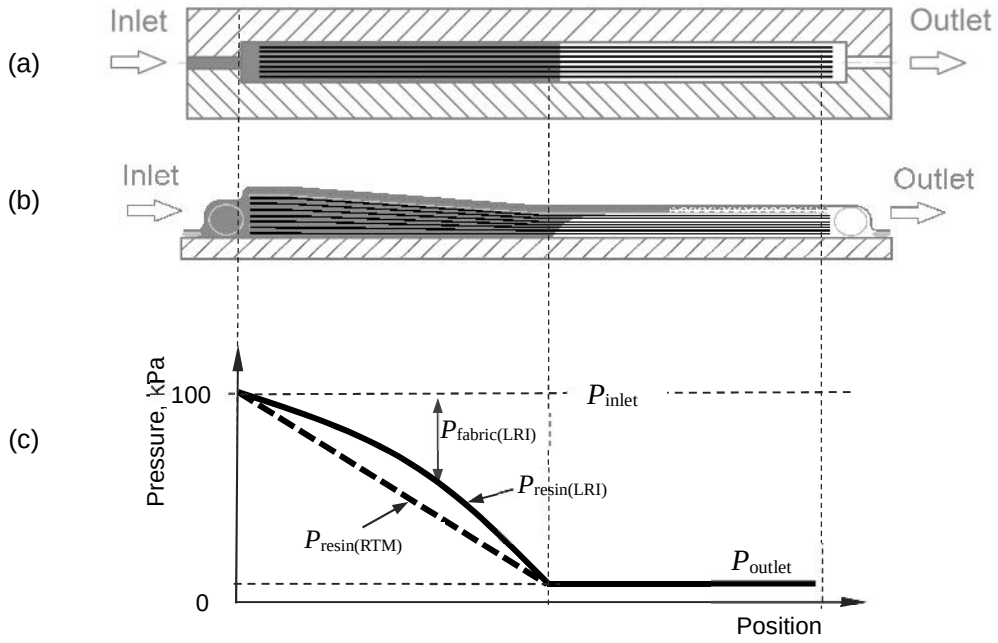

Figure 2.52 Schematic comparison of flow and pressure distribution in RTM and LRI

Actual resin pressure in VARI process varies non-linearly between the inlet, which is usually at atmospheric pressure (~100 kPa), and the flow front, which is usually close to vacuum (~ 0 kPa), as depicted in Figure 2.52c. For pressure equilibrium external atmospheric pressure must balance the internal fabric and resin pressure (equation (2.40)) and, depending on resin pressure, the fabric will have a different state of compaction, or fibre volume fraction, related to resin pressure [52]:

$$P_{atm} = \pm_{zz} + P_{resin}. \tag{2.40}$$

The effect of gravity may need to be included in the right hand side of equation (2.40) for accurate simulation of parts with large height variations [176]:

$$\Delta P_g = \circ_{resin} g \Delta z. \tag{2.41}$$

The filling process and a moving flow front is shown schematically in Figure 2.53, where h_0 is the initial fabric thickness under vacuum pressure and h is the modified thickness. The flow front moves with velocity v between two states at time I and II.

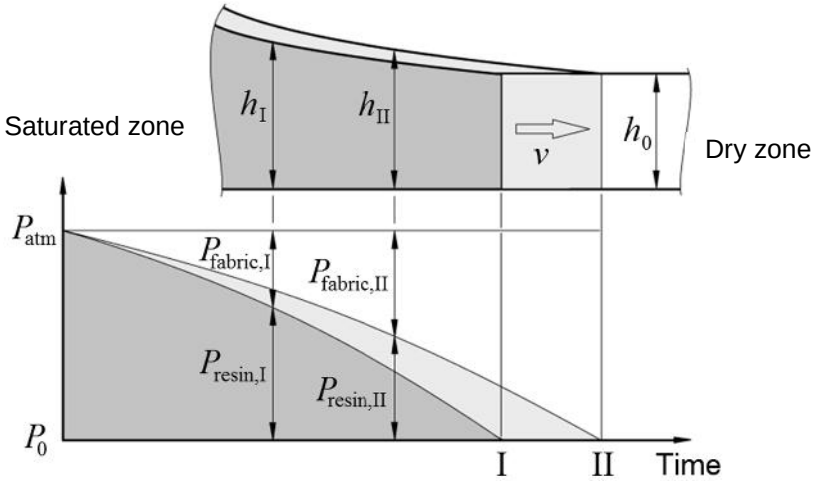

Figure 2.53 Pressure (P) and fabric thickness evolution (h) during flow advance in LRI under flexible cover

Numerical solution for flow advancement must ensure mass conservation. Figure 2.54 shows 1D flow over a volume element; the preform expansion rate is dh/dt, inflow and outflow velocities are given by $v(x)$ and $v(x+dx)$ respectively. The mass conservation for an incompressible fluid is given in [29] as:

$$\frac{\partial(vh)}{\partial x} = -\frac{\partial h}{\partial t}, \tag{2.42}$$

where h – height of the preform, m,

v – volume averaged velocity, m/s.

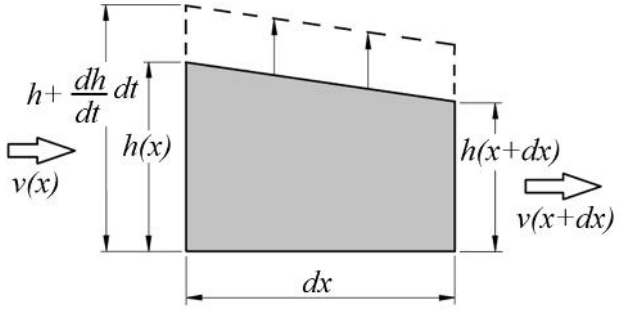

Figure 2.54 Flow through a volume element with preform expansion rate dh/dt [29]

By combining Darcy's law (2.29) and the mass conservation equation (2.42) the following governing equation is obtained (assuming small thickness gradient):

$$\frac{\partial}{\partial x}\left(-\frac{\text{©}}{\text{¶«}}\frac{\partial P}{\partial x}\right)h = -\frac{dh}{dt}. \tag{2.43}$$

With $\frac{dh}{dt} = \dot{h}$ the mass conservation equation (2.42) takes the following form [243]:

$$\nabla v = \frac{\dot{h}}{h}. \tag{2.44}$$

In RTM type processes rate of thickness change $\dot{h}$ is equal to zero, thus mass is conserved a priori. However, if the thickness of the part is changing, which is the case for VARI, an additional variable h needs to be taken into account.

In [52] a fully coupled infusion process simulation approach was presented where preform compaction was modelled using a method proposed in [244] which imitates a non-linear spring behaviour that equilibrates pressure between the resin and preform as illustrated in Figure 2.55 (a similar approach is used in this thesis in section 6.3). Compaction pressure versus fibre volume fraction can be obtained from fabric compaction testing or, as in [52], the following empirical relation can be applied:

$$\pm_{zz} = A_s \frac{\left(\sqrt{\frac{V_f}{V_{f0}}} - 1\right)}{\left(\sqrt{\frac{V_{f\_max}}{V_f}} - 1\right)^4} \tag{2.45}$$

where A_s – empirical spring constant, Pa,

V_{f_max} – maximal possible fibre volume fraction.

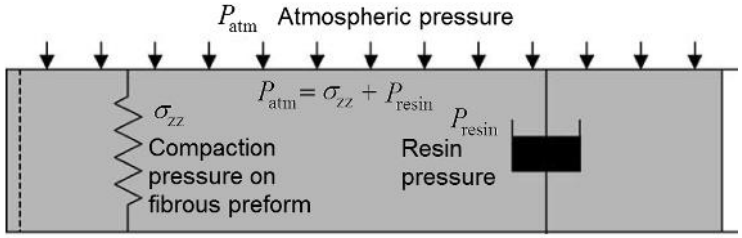

Figure 2.55 Sum of pressures acting on a preform during VARI process [52]

Governing equation (2.43) is solved using a finite element scheme where continuous pressure distribution is interpolated from shape functions and nodal pressures. The Galerkin method yields the following system of equations:

$$[K]\{P\} = \{b\} + \{s\}, \tag{2.46}$$

where $[K]$– global conductivity (permeability) matrix,

$\{P\}$– nodal pressure,

$\{b\}$ – internal nodal flow vector (equal to zero except at prescribed injection nodes or the flow front),

$\{s\}$– set of nodal flows due to change in volume of the preform (sink terms).

This thesis (section 6.3) exploits an approach presented in [245], where pressure dependent parameters such as permeability, fibre volume fraction and preform thickness are taken into account using an equivalent porosity definition. This numerical procedure allowed variable preform compliance modelling using a stationary mesh by treating porosity as an internal variable as illustrated in Figure 2.56.

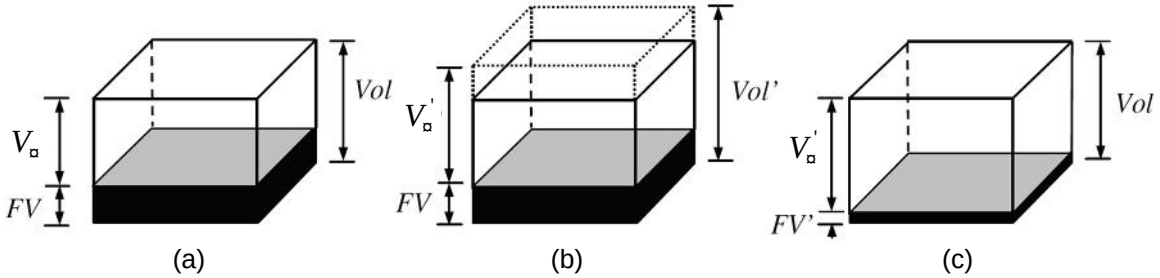

Figure 2.56 Illustration of a) initial element volume and fibre volume, b) updated element volume and fibre volume and c) original element volume with updated fibre volume resulting in equivalent fibre volume fraction [245]

The major steps of the exploited CV/FE approach to solve equation (2.46) system of equations are as follows [246]:

1) determination of pressure distribution,

2) calculation of resin flow rates,

3) determination of a new resin flow front from the velocity vector.

In the CV/FE approach each node has an associated control volume as illustrated in Figure 2.57. Each control volume is assigned a fill factor ranging from 0 for empty volumes to 1 for filled volumes. Pressure is calculated for nodes with filled control volumes from prescribed pressure at the inlet and applied vacuum pressure at nodes with empty volumes. At each time step only one CV is filled to ensure mass conservation.

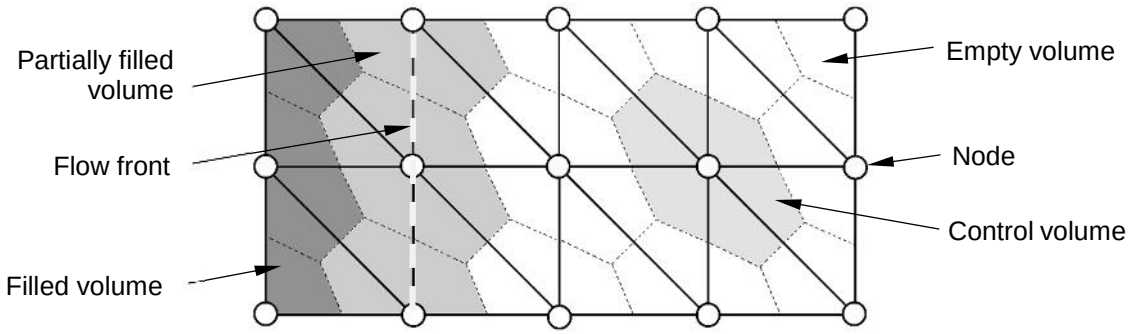

Figure 2.57 FE mesh division into control volumes and numerical flow front

Material parameters will vary in time and space depending on fabric compaction, thus fibre volume fraction, permeability and porosity are updated during each time step. The iterative pressure calculation algorithm is shown in Figure 2.58 ([29], [245]). Convergence at each time step is reached once the nodal flows becomes sufficiently small due to fabric expansion, or the change in nodal pressures is sufficiently small.

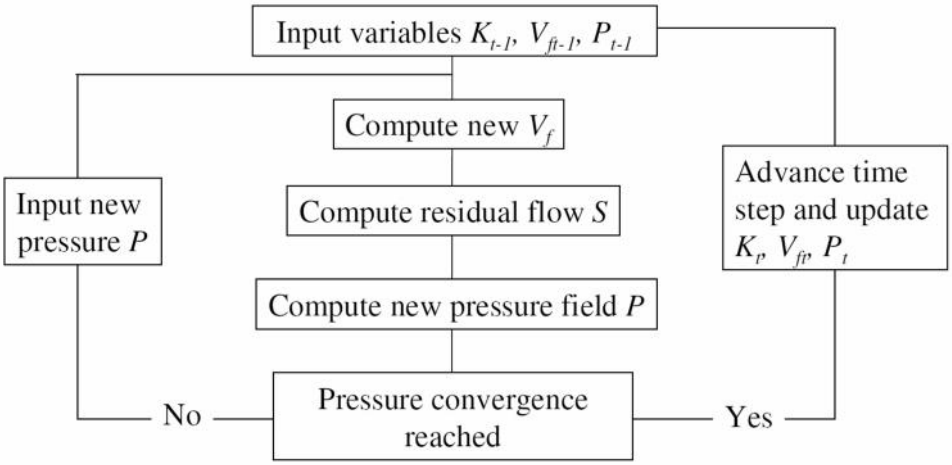

Figure 2.58 Pressure calculation algorithm [245]

There are a number of commercial and research codes available for infusion process simulation. Some of these are listed below:

- PAM-RTM© [247],
- LIMS [225],
- RTM-WORX (Polyworx package) [248],
- FlowTex (WiseTex package) [61],
- myRTM [249],
- PORE-FLOW© [224],
- SimLCM [143],
- CFD codes (e.g. CFX-4 [34]).

Some of the codes (e.g. PAM-RTM, LIMS) have options for simulating VARI type infusion process accounting for non-linearly variable pressure field in 2D; fully coupled 3D flow simulation, however, remains a challenging task and a topic of numerous studies.

2.6 Fabric in-plane forming and permeability

Various deformation mechanisms may occur during fabric forming. Among these are in-plane shear, inter-fibre and inter-layer slipping, in- and out-of-plane bending, tow buckling, stretching torsion and compression [173]. All these deformation modes can substantially change permeability and flow behaviour during infusion process. Furthermore, handling history can substantially change fabric

meso-scale geometry and permeability [165]. Possible tow and gap width changes under cyclic shear load is illustrated in Figure 2.59.

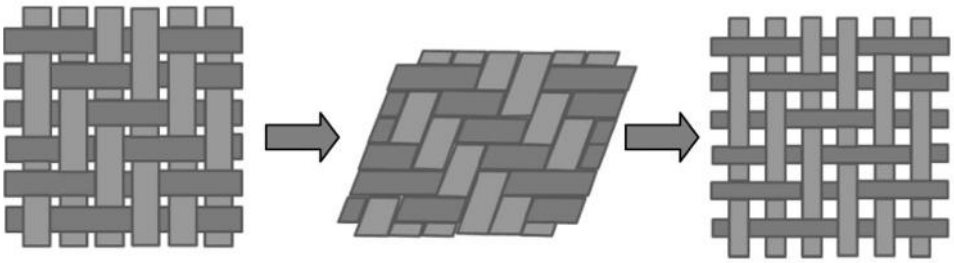

Figure 2.59 Residual effect of cyclic in-plane shear on fabric geometry [165]

In-plane shear and compaction are the most important deformation modes and will be addressed here in relation to permeability. Three parameters fully characterise anisotropic in-plane permeability of a sheared fibrous preform, namely principal permeabilities K_1, K_2 and their orientation. These can be obtained using three 1D tests performed at different directions (e.g. 0°, 45°, 90°) or using a radial infusion test with iterative ellipse method as described in [174]. A trend of initially increasing principal permeability K_1 with increasing shear angle is observed for bi-directional fabrics (increase of the ratio K_1/K_2). Also, principal permeability directions rotate typically more than the shear angle ([144], [250]) as shown in Figure 2.60. After a certain shear angle K_1 starts to reduce as porosity is lowered due to inter-tow gap closure. The second in-plane permeability K_2 gets steadily lower as the shear angle increases [173].

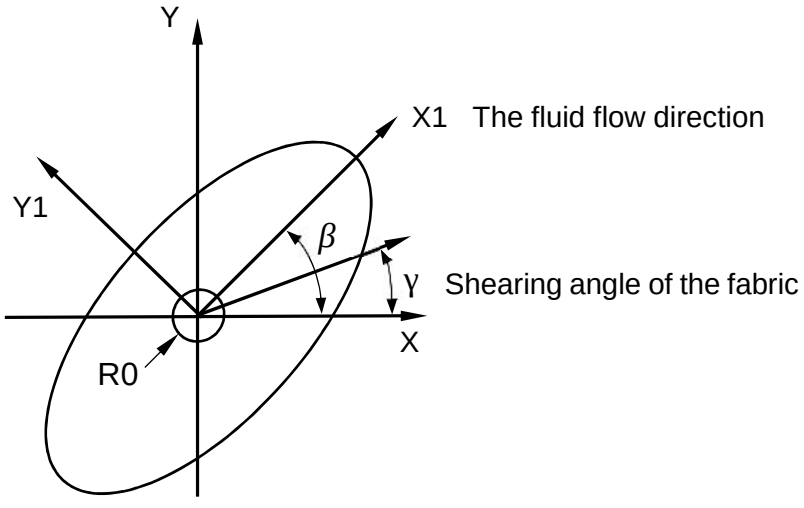

Figure 2.60 Fluid flow direction change with shear angle (adapted from [144])

In [159] investigation of changes in woven fabric principal permeabilities due to shear deformation exploiting a radial infusion test was done. It was observed that inter-tow gap width change influenced the flow speed and shape of the flow front considerably. Under the assumption that principal

permeability directions stay aligned with their respective fibre tows (weft and warp) experimentally obtained flow front ellipses were fitted using analytical equations and a correction factor to account for discrepancies. Permeabilities were expressed by empirical equations:

$$K_x = \sqrt{\frac{\sim}{=}}\, c_1 e^{c_2(1-V_{f^-})} \tag{2.47}$$

$$K_y = \sqrt{\sim =}\, c_1 e^{c_2(1-V_{f^-})} \tag{2.48}$$

where c_1, c_2 – constants obtained from a test on unsheared fabric, m^2,

V_{f^-} – fibre volume fraction at shear angle $^-$,

$\sim = \frac{K_2}{K_1}$ – permeabilities ratio in undeformed state,

$= = \frac{K_y}{K_x}$ – permeabilities ratio in deformed state.

Increase of fabric shear angle leads to change of permeability by changing the fibre volume fraction [159]. Under the assumption of no tow slippage, no fabric wrinkling, constant thickness and pure rotation at cross over points a simple analytical equation for estimation of fibre volume fraction change with the shear angle can be obtained ([9], [151], [251]):

$$V_f = \frac{V_{f0}}{\cos ¥}, \tag{2.49}$$

where V_{f0} – initial (unsheared) fabric volume fraction,

¥ – shear angle.

The above equation has been found to underpredict fibre volume fraction by 10-20% due to tow slippage [151]. Another simple relation for a sheared stack of two UD non-crimp fabric layers exploits empirical coefficients to calculate permeability as ([164], [251]):

$$K_{xx'} = K_1 \cos^{2^-}{}_{ply}, \tag{2.50}$$

with $$K_1 = A_e (1-V_f)^{m_e}, \tag{2.51}$$

where A_e, m_e – empirical coefficients (obtained from tests or numerical fitting),

$K_{xx'}$ – permeability along the major axis of layers assembly, m^2,

θ_{ply} – ply angle.

Estimation of in-plane effective permeability of a laminate containing multiple plies with different fibre orientations may be done using the following equation [251]:

$$K_{\text{eff}} = \frac{1}{h}\sum_{i=1}^{n}\left(K_1 \cos^2\theta_i + K_2 \sin^2\theta_i - \frac{(K_2 - K_1)^2 \cos^2\theta_i \sin^2\theta_i}{K_2 \cos^2\theta_i + K_2 \sin^2\theta_i} \right) \cdot h_i , \tag{2.52}$$

where K_1, K_2 – major and minor permeabilities of a i-th ply, m^2,

θ_i – ply angle of the i-th layer,

h_i – thickness of i-th layer, m,

h – total thickness of the preform, m.

In [208] fluid flow within gap and tow domains of a plain woven fabric was modelled taking into account nesting and compaction deformation of the preform. Fibre volume fraction of the unsheared fabric was estimated by the Carman-Kozeny relationship. Fibre volume fraction of sheared tow was estimated using equation (2.49). The permeability values of the sheared preform were then obtained by multiplying permeabilities of unsheared fabric with a correction factor calculated using the following equation [208]:

$$K_{\text{corr}} = \frac{V_{\text{f0}}^2\left(1 - V_{\text{f}\theta}\right)^3}{V_{\text{f}\theta}^2\left(1 - V_{\text{f0}}\right)^3} . \tag{2.53}$$

In [151] the influence of a draping process on the fluid propagation pattern through biaxial stitched fabric was investigated. Draping simulation was accomplished using a kinematic mapping approach (DRAPE in house code) and ignoring ‘locking angle’ obtained experimentally to avoid wrinkles in the numerical model. Fibre volume fraction was estimated using equation (2.49), which was also compared to experimental measurements from ‘burn-off’ tests. Permeability tensor components were obtained assuming flow in the channels to be governed by the Stokes equation and fluid flow in tows by Darcy’s law. 2D filling simulations were accomplished using LIMS software [225] under both constant pressure and constant flow rate boundary conditions. Results indicated that shear angle was overpredicted (no inter yarn slip) and the need for a more comprehensive analysis was noted.

A unit cell model was used in [250] to investigate the influence of deformation on permeability of woven and biaxial stitched fabrics. Fluid flow in the channels was described by the Stokes equation, with flow in tows by Darcy’s law. Flow was assumed to be fully saturated, nesting and gap width variation within UC were not accounted for and average values were used. It was pointed out that variation of tow permeability causes only minor changes in the overall preform permeability.

A technique for full characterisation of permeability tensor as a function of the fibre angle, with only principal permeabilities of undeformed fabric known, was presented in [173]. Only scissor and slide deformation mechanisms of a bi-directional fabric unit cell were considered. The ratio of principal permeability values K_1/K_2 of sheared fabric was calculated based on invariance of injected fluid volume, coordinates transformation and addition of vectors of fluid flow along the fibre directions in a layered structure. The change in porosity with increasing shear angle was taken into account, since it changes the absolute values of both K_1 and K_2. The influence of the stitch on the permeability of the fabric was not considered.

A plain weave fabric was modelled in [80] at the meso-scale, allowing representation of complex mechanical behaviour of the yarns, including contacts and boundary conditions. A hypoelastic material law with transverse isotropy was used for tow modelling. Deformed numerical model RVE of the fabric was used to build another model of the fluid domain for saturated flow simulation.

A 2D modelling approach to calculate permeability of triaxially braided preforms was proposed in [163]. Presented UC model with a weighted averaging scheme to different local configuration of constituents (e.g. zones of yarn overlap) proved to be CPU efficient and provided good quantitative and qualitative assessment of preform permeability. Complex architecture of the preform and nesting effects could be taken into account. It was also noted that gaps between the tows, as expected, have significant impact on permeability.

The same trend that the gaps having major role in flow behaviour was also observed in [194], where permeability of plain weave and 2x2 twill weave fabrics, in unsheared and sheared states including nesting of multiple layers, were calculated using CFD. Meso-scale geometry of the fabrics was obtained from CT and flat scans taking into account a statistical gap width distribution. Models were sheared by kinematic rules allowing yarns to rotate and change cross section shape to maintain a given fibre volume fraction. Considering that no calibration was involved, the simulations yielded good permeability predictions within 10-20% of the experimental results.

2.7 Summary of literature review

Technical textiles forming is relevant to many advanced engineering applications and has been a topic of considerable research over the last decades. With continuously increasing computational power one can clearly observe a refinement of length scales used for numerical simulation of fibrous preforms. Kinematic mapping and mixed mechanistic modelling approaches are now being replaced by macro-scale finite elements simulations with some recent research starting to look at the meso-scale modelling approaches. Major fabric deformation mechanisms, such as shear, compaction and bending are dependent on geometrical, mechanical and process parameters. A high number of

possible combinations makes exploitation of numerical modelling strategies very attractive compared to experimental material testing.

Permeability characterisation of textile materials is another challenging task being undertaken in both research and industry. A recent worldwide permeability benchmark exercise ([117], [121]) reflects the high level of interest to improve tests methodology, accuracy, efficiency and reduce cost. Automated analysis tools and increasing computational power makes detailed numerical simulation approaches for permeability estimation feasible. Also, infusion simulation tools which are capable to account for a specific infusion process related phenomena, such as 3D flow and preform compliance in VARI, need to be further developed and implemented on an industrial level.

Coupling between the forming and infusion processes is another milestone towards a reliable virtual design chain. Today the ‘standard’ industrial scale for draping and infusion simulations is the macro-scale, in the future it can be expected the finer meso-scale analysis will eventually make its way into industry by providing an acceptable trade-off between accuracy and CPU efficiency. One of the main parts of this work presented in chapter 5 is devoted to the development of a general textile modelling strategy for coupled fabric deformation and infusion simulation at the meso-scale allowing practical analysis of relatively large components.

3 Permeability measurements

As discussed previously in section 2.3, no standard procedures yet exist for permeability testing of technical textiles. In this thesis several strategies were examined to measure permeability of three types of fabrics used for structural applications in the aerospace industry. The same fabrics were then used for further research applications. Testing difficulties encountered are discussed and alterations to test methods are presented.

Materials tested include the following carbon fibre fabrics and distribution medium:

- bindered biaxial NCF with chain stitch (Saertex), 548 g/m^2 (biaxial NCF) [252],
- bindered UD NCF (Saertex), 278 g/m^2 (UD NCF) [252],
- bindered quasi-UD NCF G1157 D1300 (Hexcel), 290 g/m^2 (quasi-UD NCF) [253],
- distribution medium XS6262-003 ”X60“X650FT (Flugzeug Union Süd) [254].

Table 3.1 summarises the type of permeability tests used for each fabric and lists where the data obtained is exploited in this thesis.

<table>
<tr><th>Test type</th><th>Material</th><th>Permeability measured</th><th>Exploited as</th></tr>
<tr><td rowspan="7">Constrained cavity height</td><td>Biaxial NCF</td><td>K_{xx}, K_{yy} (section 3.1.1)</td><td>Fabric permeability in macro-scale hemisphere infusion simulation (section 4.3)</td></tr>
<tr><td rowspan="2">UD NCF</td><td>K_{xx}, K_{yy} (section 3.1.2)</td><td rowspan="2">Tow permeability in meso-scale hemisphere infusion simulation (section 5.3)</td></tr>
<tr><td>K_{zz} (section 3.2.1)</td></tr>
<tr><td rowspan="2">Quasi-UD NCF</td><td>K_{xx}, K_{yy} (section 3.1.3.2)</td><td rowspan="5">Material permeabilities for demonstrator part VARI infusion simulation (section 6.3)</td></tr>
<tr><td>K_{zz} (section 3.2.2)</td></tr>
<tr><td rowspan="2">Distribution medium</td><td>K_{xx}, K_{yy} (section 3.1.4)</td></tr>
<tr><td>K_{zz} (section 3.2.3)</td></tr>
<tr><td>Unconstrained cavity height</td><td>Quasi-UD NCF</td><td>K_{xx} (section 3.1.3.1)</td></tr>
</table>

Table 3.1 Materials permeability tests

A simple 1D infusion test setup was developed to measure fabric orthotropic permeability in different configurations, that is, with either constrained or unconstrained cavity height. The same setup in different arrangements was used for both in-plane and through-thickness permeability measurements.

The fluid used for all permeability tests was epoxy resin RIMR 235 with RIMH 237 or RIMR 238 hardener [255]. Viscosity information was available from the manufacturer datasheets and is included in Appendix I. For test evaluations viscosity data was interpolated according to resin temperature which was measured before the beginning of each test and assumed to be constant throughout the test, so viscosity is assumed to depend only on time. The use of a reactive resin has drawbacks, including limited time for the test and temperature sensitive viscosity in the case of an exothermic reaction. However, advantages of using the actual resin system are realistic wetting and capillary related effects that match conditions in real part infusion as discussed in section 2.3.1. Also, fibre volume fraction can be measured according to standard DIN29971 [256] after the specimen is cured.

Visual flow front monitoring was used in all experiments. A Digital Image Correlation (DIC) ARAMIS system was used to measure the preform thickness change during unconstrained cavity height tests on quasi-UD NCF. This provided some necessary data to relate permeability to fibre volume fraction and compaction pressure presented in section 6.3.

3.1 In-plane permeability tests

The test rig used for permeability measurements is depicted in Figure 3.1. A glass plate and a pair of mirrors allow visual flow monitoring on upper and lower surfaces of the preform. In each run of the test three carefully sealed (‘tacky tape’) specimens (50x200 mm in size) with different fibre orientations or different flow driving pressures could be tested simultaneously. Glass caul plates were used to maintain constant thickness (i.e. constant fibre volume fraction) of the preforms during the test. It should be noted that caul plates were placed on top of the specimens only after these had been compacted by a chosen level of vacuum pressure (typically 1 atm).

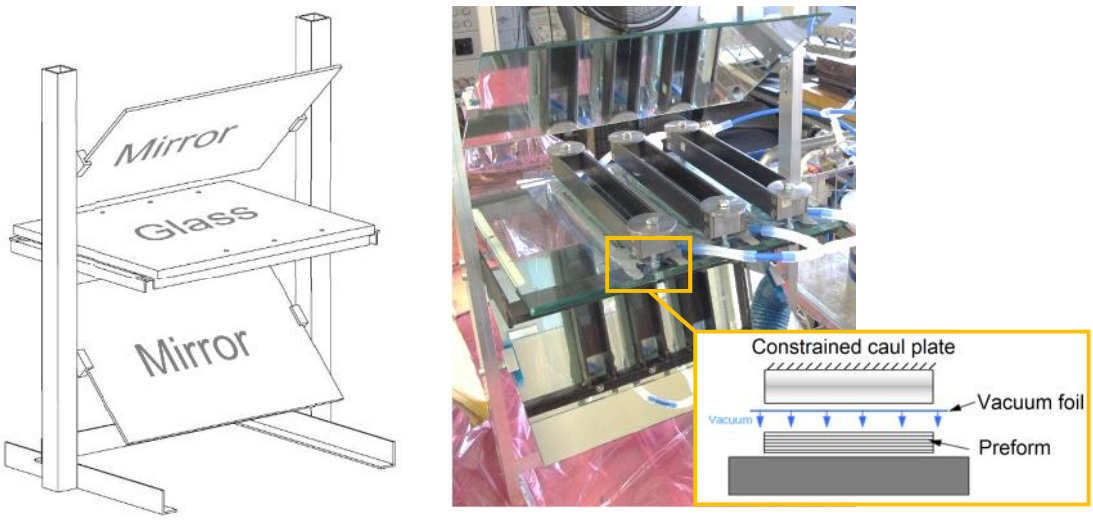

(a) (b)

Figure 3.1 Permeability test setup: a) schematic illustration and b) setup view

3.1.1 Biaxial non-crimp fabric

Permeability of biaxial NCF from Saertex was measured and is used in a macro-scale infusion simulation of a draped hemisphere to be presented in section 4.3. Figure 3.2 shows upper and lower surfaces of the bindered biaxial NCF (548 g/m^2) [252] with indicated principal permeability directions. This fabric was tested with a constrained cavity height configuration.

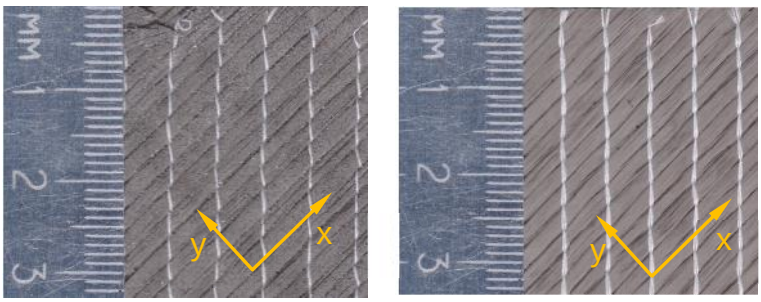

(a) (b)

Figure 3.2 Biaxial NCF views with principal permeability directions marked: a) upper and b) lower surfaces

Strips were cut, laid up in $(0/90)_8$ stacks and infused. Resin flow length development is shown in Figure 3.3. The caul plates maintained a constant specimen height during infusion giving a final fibre volume fraction of 60.57 % which was measured according to DIN29971 standard [256] after specimens were cured. The flow front length versus time diagrams are given in Figure 3.4a and the plot of square of flow length versus time is shown in Figure 3.4b. This latter representation is conveniently used to estimate permeability since ratio L^2/t is present in equation (2.21).

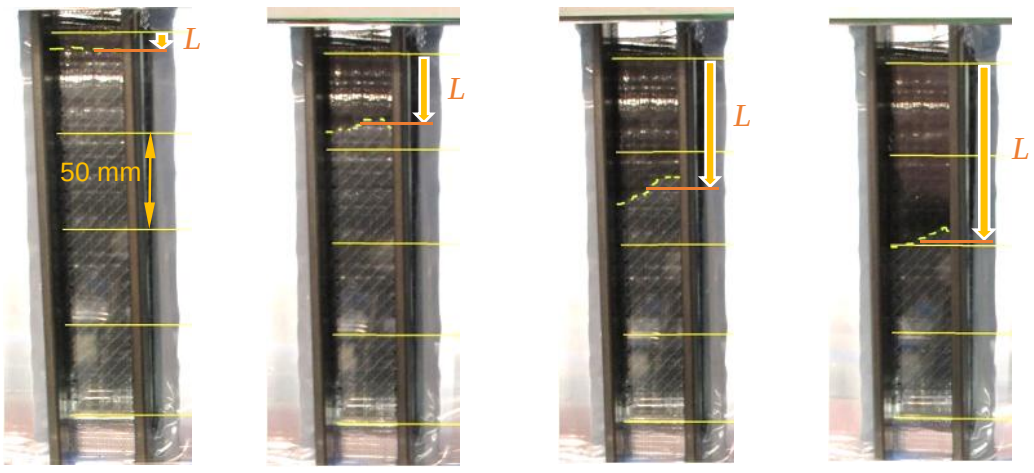

10 s 58 s 196 s 372 s

Figure 3.3 Biaxial NCF permeability test views (K_{xx})

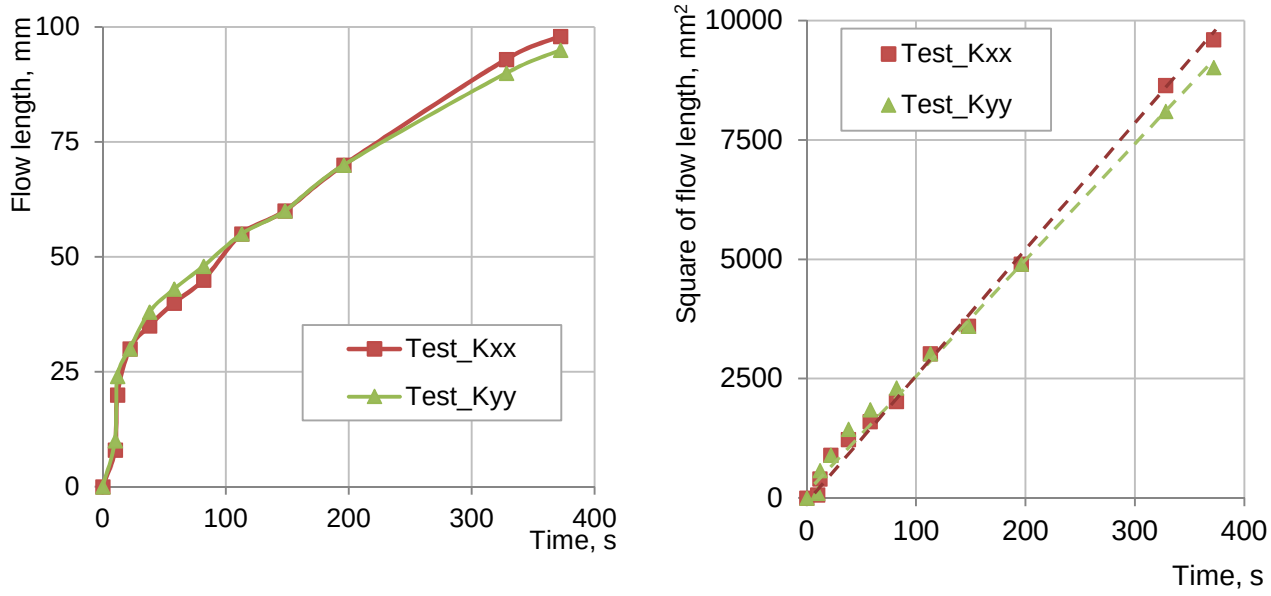

(a) (b)

Figure 3.4 Biaxial NCF permeability estimation test: a) resin flow length and b) square of flow length versus time diagrams

Principal permeabilities are calculated using equation (2.21) as:

$$K_{xx} = \left(\frac{L_{xx}^2}{t}\right)\frac{¤«}{2\Delta P} = \left(\frac{9604}{372}\right)\frac{0.39\cdot 0.30}{2\cdot 100000}\cdot 10^{-06} = 1.51\cdot 10^{-11}(\mathrm{m}^2), \tag{3.1}$$

$$K_{yy} = \left(\frac{L_{yy}^2}{t}\right)\frac{¤«}{2\Delta P} = \left(\frac{9025}{372}\right)\frac{0.39\cdot 0.30}{2\cdot 100000}\cdot 10^{-06} = 1.42\cdot 10^{-11}(\mathrm{m}^2), \tag{3.2}$$

where « ≈ 0.30 Pa·s,

$\Delta P \approx 100\,000$ Pa,

$¤ = 1 - V_f \approx 0.39$.

The porosity value was obtained as $1-V_f$, where V_f is the measured fibre volume fraction.

It should be noted that biaxial NCF is a typical 'dual-scale flow' material, where resin propagation speed differs in the gaps and tows of the fabric. Due to delayed tow impregnation ('sink') the square of the flow length versus time diagram is expected to be non-linear [223]. However, the experimental data presented shows a nearly linear character of L^2/t and thus justifies use of Darcy's law to predict flow propagation.

3.1.2 Unidirectional non-crimp fabric

Permeability measurement of unidirectional NCF with areal weight of 274 g/m^2 from Saertex [252] is used as an estimate for tow permeability in a meso-scale coupled drape-infusion simulation of a

hemisphere presented in section 5.2. Figure 3.5 shows both surfaces of the fabric, which was tested with a constrained cavity height.

Two layup configurations of $(0)_{20}$ and $(90)_{20}$ were infused to determine principal permeabilities K_{xx} and K_{yy} respectively. Views of the K_{xx} permeability test are shown in Figure 3.6.

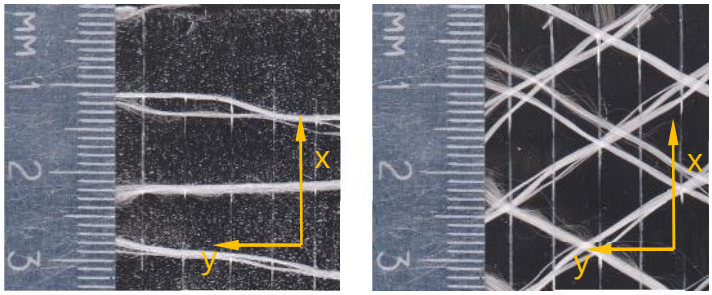

(a) (b)

Figure 3.5 UD NCF fabric views with principal permeability directions marked: a) upper and b) lower surfaces

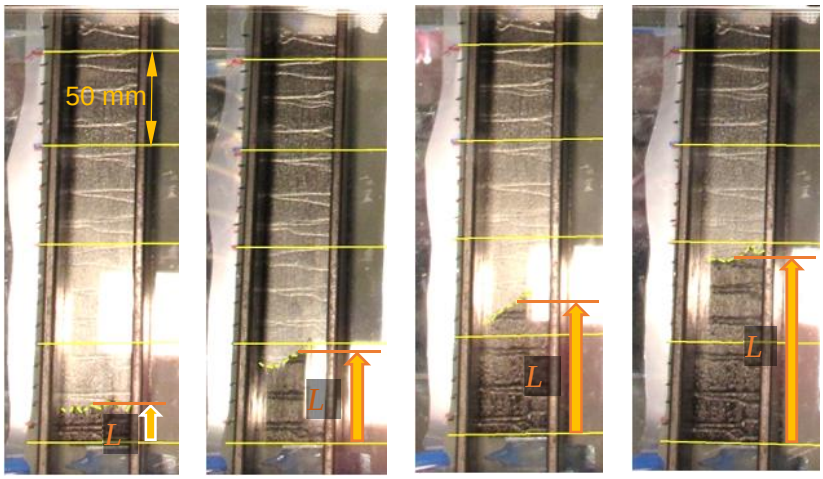

21 s 185 s 641 s 2114 s

Figure 3.6 UD NCF permeability test views (K_{xx})

Resin flow length versus time diagrams are given in Figure 3.7a. This fabric has a dense structure with V_f=61.5 % (measured according to DIN29971 standard [256]) and no pronounced inter-tow gaps, thus resin propagation was found to be much slower than the other tested fabrics.

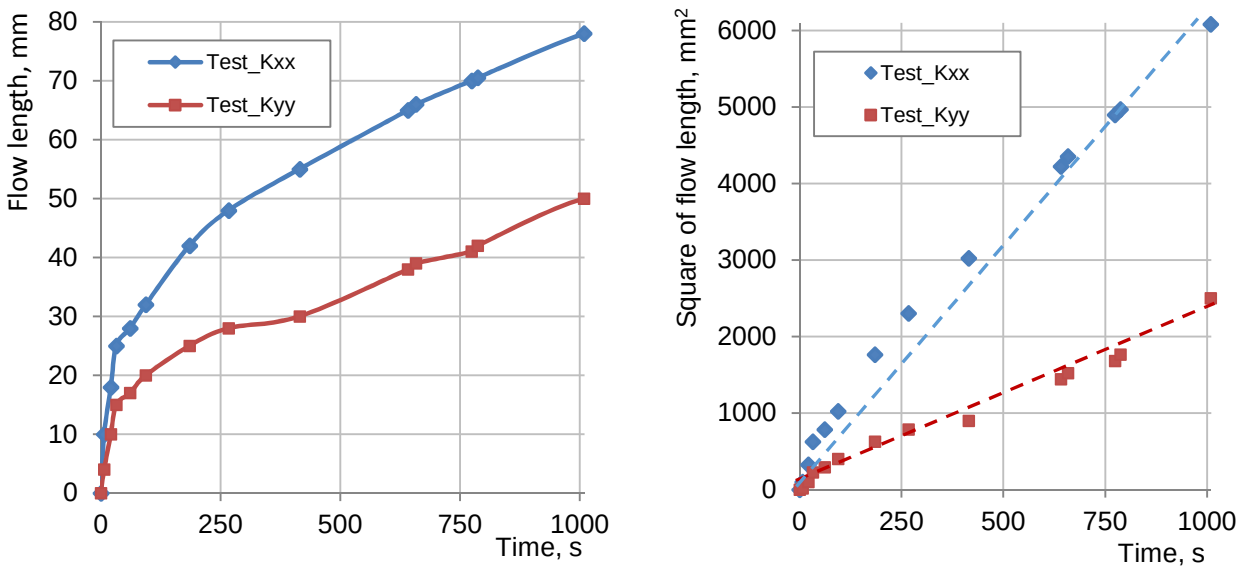

(a) (b)

Figure 3.7 UD NCF permeability tests: a) flow length and b) square of flow length versus time diagrams

From Figure 3.7b principal in-plane permeabilities K_{xx} and K_{yy} were estimated as:

$$K_{xx} = \left(\frac{L_{xx}^2}{t}\right)\frac{¤«}{2\Delta P} = \left(\frac{6084}{1009}\right)\frac{0.39\cdot 0.31}{2\cdot 100000}\cdot 10^{-06} = 3.60\cdot 10^{-12}(\mathrm{m}^2), \tag{3.3}$$

$$K_{yy} = \left(\frac{L_{yy}^2}{t}\right)\frac{¤«}{2\Delta P} = \left(\frac{2500}{1009}\right)\frac{0.39\cdot 0.31}{2\cdot 100000}\cdot 10^{-06} = 1.48\cdot 10^{-12}(\mathrm{m}^2), \tag{3.4}$$

where « ≈ 0.31 Pa·s,

$\Delta P \approx 100\,000$ Pa,

$¤ = 1 - V_f \approx 0.39$.

3.1.3 Quasi-unidirectional fabric

Figure 3.8 shows quasi-unidirectional fabric G1157 D1300 with areal weight of 290 g/m^2 from Hexcel [253], which was tested in both unconstrained and constrained cavity height configurations with different compaction pressures. In the first case it was necessary to measure thickness variation of the preform resulting from preform relaxation. In the second case it was necessary to obtain permeability data corresponding to different fibre volume fractions. These results are used in VARI type infusion process simulation of the demonstrator part presented in section 6.3.3.

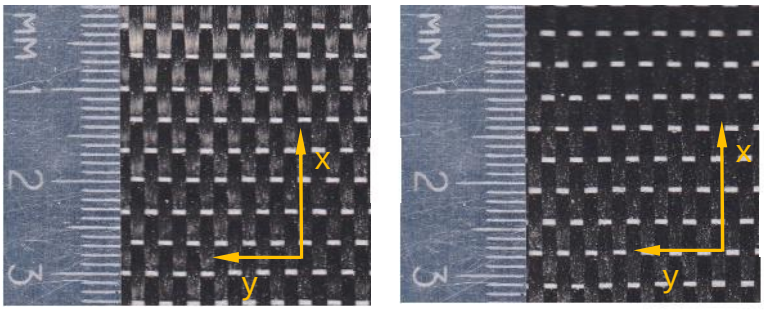

(a) (b)

Figure 3.8 Quasi-UD NCF views with principal permeability directions marked: a) upper and b) lower surfaces

3.1.3.1 Quasi-unidirectional fabric in unconstrained cavity height configuration

Preform thickness varies during VARI infusion if the cavity height is not constrained. GOM Aramis optical measurement system [257] was used to continuously monitor thickness change of a $(0)_8$ quasi-UD NCF preform. A view of the test setup is given in Figure 3.9a together with example results of thickness variation during infusion in Figure 3.9b.

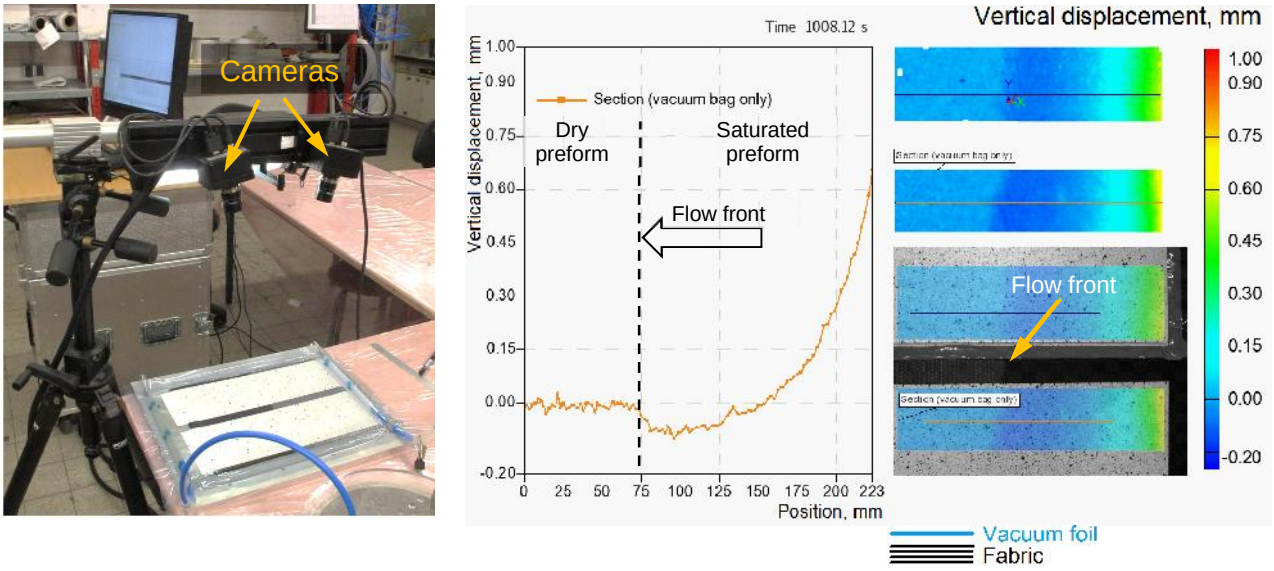

(a) (b)

Figure 3.9 Preform thickness measurement: a) optical system and b) quasi-UD NCF preform thickness diagram

From Figure 3.9b several characteristic phenomena of VARI type infusion stand out. There is a decrease of preform thickness right behind the flow front followed by thickness increase. This thickness decrease is explained by reduced inter-fibre friction (also reported in [32], [35], [38]). Subsequent thickness increase is a result of reduced difference between resin and atmospheric pressure that effectively compacts the preform. Exploitation of thickness measurement data to obtain permeability as a function of compaction pressure will be discussed and applied in section 6.3.1.

3.1.3.2 *Quasi-unidirectional fabric in constrained cavity height configuration*

A test configuration similar to the previously described tests was used for permeability measurements, except that different values of vacuum pressure were applied to obtain different compaction and, consequently, different fibre volume fraction (note – the thickness is constrained using caul plates). $(0)_8$ and $(90)_8$ stacks were prepared for estimation of principal permeabilities of K_{xx} and K_{yy} under maximal vacuum pressure. Test views of resin front propagation for the K_{xx} specimen are given in Figure 3.10. Resin flow length and its square versus time diagrams are shown in Figure 3.11a and Figure 3.11b respectively.

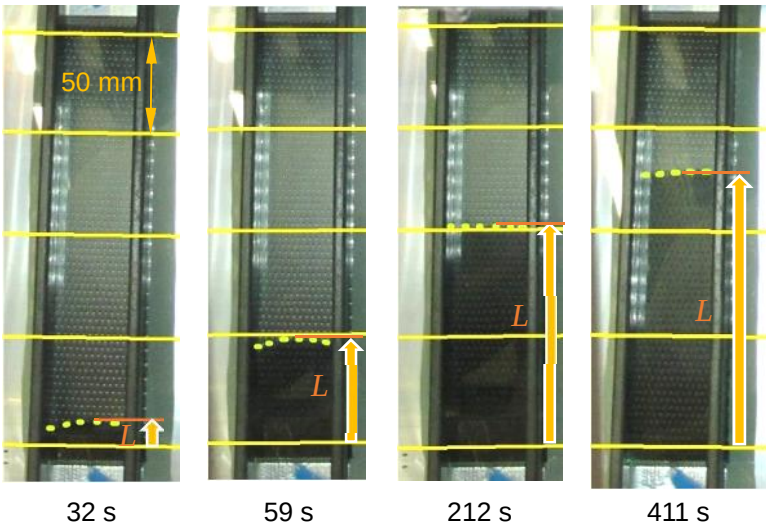

Figure 3.10 Quasi-UD NCF permeability test views (K_{xx})

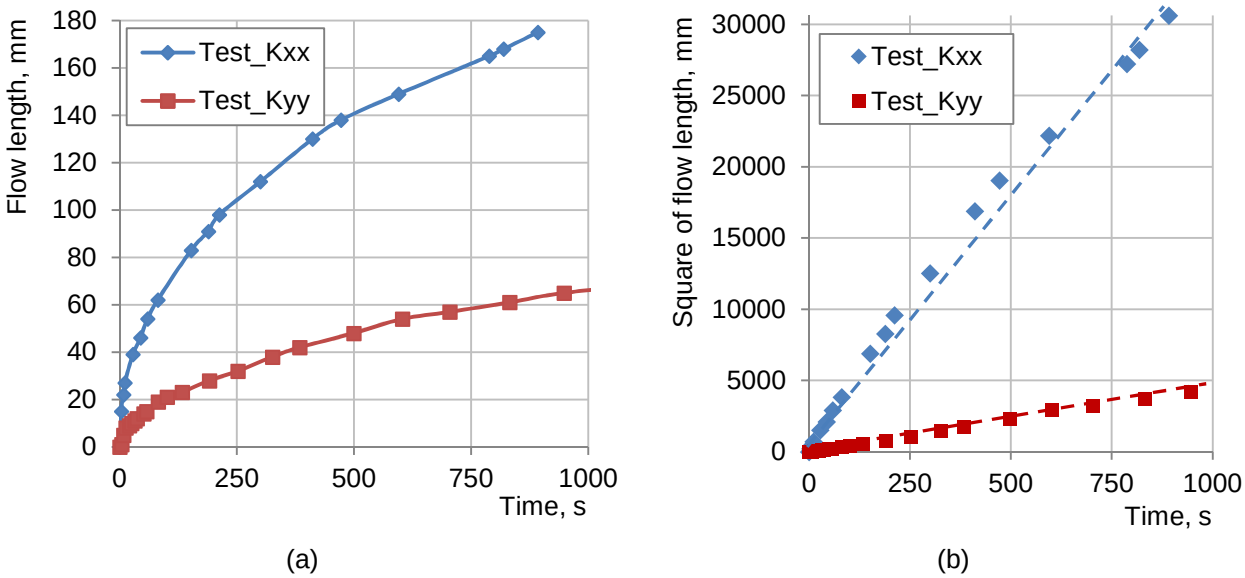

(a) (b)

Figure 3.11 Quasi-UD NCF permeability test: a) flow length and b) square of flow length versus time diagrams

Principal in-plane permeabilities were estimated as:

$$K_{xx} = \left(\frac{L_{xx}^2}{t}\right)\frac{¤«}{2\Delta P} = \left(\frac{30625}{892}\right)\frac{0.41\cdot 0.30}{2\cdot 100000}\cdot 10^{-06} = 2.11\cdot 10^{-11}(\mathrm{m}^2), \quad (3.5)$$

$$K_{yy} = \left(\frac{L_{yy}^2}{t}\right)\frac{¤«}{2\Delta P} = \left(\frac{5000}{1000}\right)\frac{0.41\cdot 0.30}{2\cdot 100000}\cdot 10^{-06} = 3.08\cdot 10^{-12}(\mathrm{m}^2). \quad (3.6)$$

where « ≈ 0.30 Pa·s,

ΔP ≈ 100 000 Pa,

$¤ = 1 - V_f \approx 0.41$.

Permeability tests under lower vacuum pressure (40 and 60 kPa) were made only in one principal direction (K_{xx_40} and K_{xx_60}), since only this data was required for the 2D infusion simulations to be presented in section 6.3. Resin flow length and its square versus time diagrams are depicted in Figure 3.12.

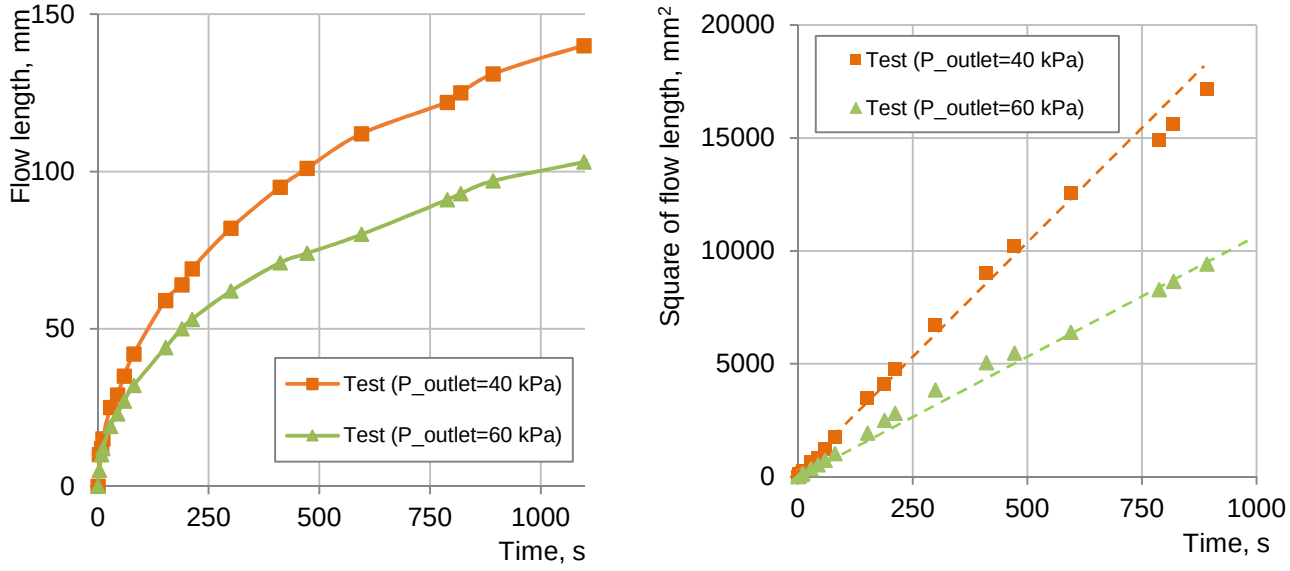

(a) (b)

Figure 3.12 Quasi-UD NCF permeability tests (K_{xx}) under different outlet pressure: a) flow length and b) square of flow length versus time diagrams

Permeabilities for reduced outlet pressures resulting in fibre volume fractions V_{f_40}= 0.5522 and V_{f_60}= 0.5419 respectively were calculated as:

$$K_{xx\_40} = \left(\frac{L_{xx\_40}^2}{t}\right)\frac{¤«}{2\Delta P} = \left(\frac{12544}{595}\right)\frac{0.45\cdot 0.30}{2\cdot 60000}\cdot 10^{-06} = 2.37\cdot 10^{-11}(\mathrm{m}^2), \quad (3.7)$$

where « ≈ 0.30 Pa·s,

ΔP ≈ 60 000 Pa,

$¤ = 1 - V_f \approx 0.45.$

$$K_{xx\_60} = \left(\frac{L_{xx\_60}^2}{t} \right) \frac{¤ «}{2\Delta P} = \left(\frac{6400}{595} \right) \frac{0.46 \cdot 0.30}{2 \cdot 40000} \cdot 10^{-06} = 1.86 \cdot 10^{-11} (\mathrm{m}^2), \quad (3.8)$$

where $«$ ≈ 0.30 Pa·s,

ΔP ≈ 40 000 Pa,

$¤ = 1 - V_f \approx 0.46.$

A summary of permeability values obtained from the constrained cavity height tests is given in Table 3.2.

Absolut outlet pressure, kPa	K_{xx}, m²	K_{yy}, m²	Fibre volume fraction, %
0	2.11E-11	3.08E-12	59.03
40	2.37E-11	-	55.22
60	1.86E-11	-	54.19

Table 3.2 Estimated permeabilities of G1157 D1300 quasi-UD NCF

3.1.4 Distribution medium

Two test configurations to measure permeability of distribution medium XS6262-003 ”X60“X650FT from Flugzeug Union Süd [254] have been applied and compared. In the first configuration a DM specimen was placed between a glass plate and vacuum foil (constrained by a glass plate on top) and tested in isolation as shown in Figure 3.13a. Distribution medium permeability measured in this case, however, is likely to be different from that in a real LRI process where DM interacts with separation foils and the deformable fabric. Consequently, separation ply T0098 from Wela Handelsgesellschaft [258] and perforated sheet ET Foil HN400-0025-1550 from Novoflow [259], which are used in VARI infusions presented in this thesis, were included in the second test configuration as shown in Figure 3.13b.

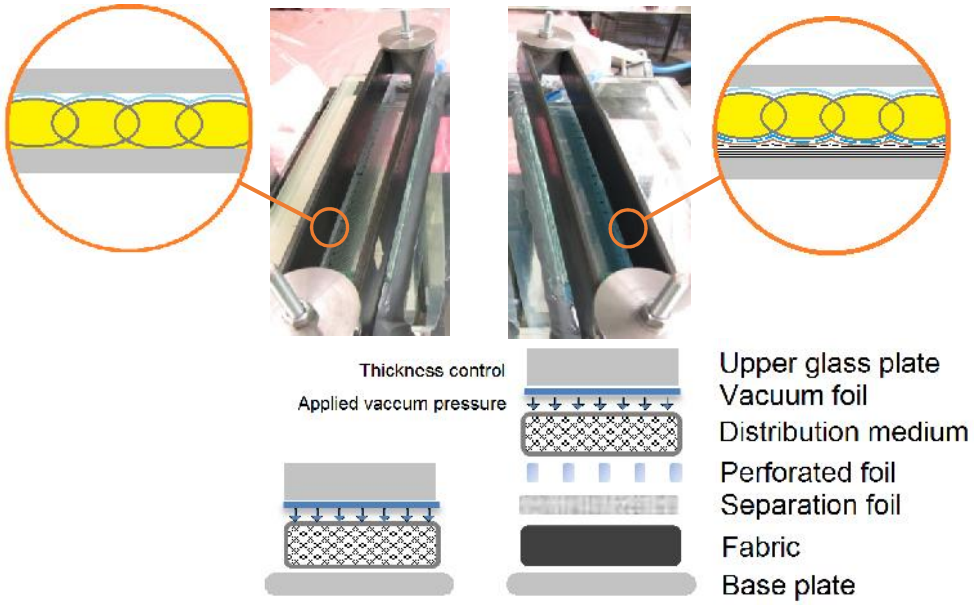

(a) (b)

Figure 3.13 Distribution medium permeability test setup and schematic layup configurations: a) DM on glass and b) DM in VARI layup

Infusion test results for the two test arrangements are shown in Figure 3.14a. As can be seen in Figure 3.14b the slope L^2/t is nearly constant implying that Darcy's law is valid for both configurations for this highly permeable material.

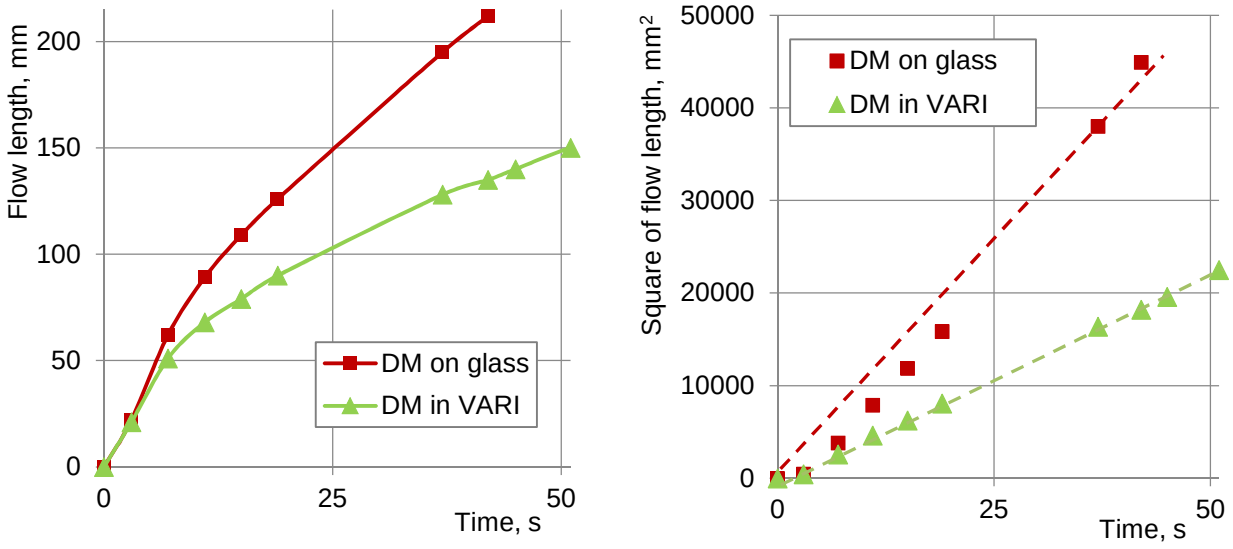

(a) (b)

Figure 3.14 Distribution medium permeability test results: a) flow length and b) square of flow length versus time diagrams

An estimate of DM permeabilities for the two configurations is as follows:

$$K_{\mathrm{FM\_glass}}=\left(\frac{L^2_{\mathrm{FM\_glass}}}{t}\right)\frac{¤«}{2\Delta P}=\left(\frac{50000}{50}\right)\frac{0.5\cdot 0.3}{2\cdot 77000}\cdot 10^{-06}=9.7\cdot 10^{-10}(\mathrm{m}^2), \tag{3.9}$$

$$K_{\mathrm{FM\_VARI}}=\left(\frac{L^2_{\mathrm{FM\_VARI}}}{t}\right)\frac{¤«}{2\Delta P}=\left(\frac{22500}{51}\right)\frac{0.5\cdot 0.3}{2\cdot 77000}\cdot 10^{-06}=4.3\cdot 10^{-10}(\mathrm{m}^2), \tag{3.10}$$

where « ≈ 0.30 Pa·s,

ΔP ≈ 77 000 Pa,

¤ ≈ 0.5.

These results show that resin flow velocity for the ‘DM on glass’ test is much faster (circa 50%) than the ‘DM in VARI’ test, as can be seen in Figure 3.14a. Furthermore, DM permeability information from VARI test still cannot be obtained directly from Figure 3.14b since there is an interaction of resin flow in the distribution medium and fabric due to through-thickness flow, similar to interaction of a racetrack and adjacent fabric observed in [152]. An ‘inverse’ finite element analysis will be used to estimate orthotropic permeability governing flow in the distribution medium in section 6.3.2.

3.2 Through-thickness permeability tests

Radial infusion test

Through-thickness permeability tests were made following the approach proposed in [124], where all three principal permeability values were measured in a single radial infusion test. However, after numerous tests were performed on different types of fabrics a large scatter of results was observed (also noted in [122]). Thus, some modifications to the test arrangement was made to enhance flow initiation and significantly reduce scatter of through-thickness permeability measurements.

Effectiveness of the inlet (tube of 6 mm inner diameter) is highly sensitive to the local fabric features (tows, gaps) directly under the tube when it is placed on a preform. Figure 3.15a shows a cured inlet standing directly on a tow of the UD NCF. Due to such placement, resin flow is partially obstructed leading to substantially lower permeability measurements. A simple counter-measure to enhance flow initiation is to use an inlet pipe of larger diameter, or to place a patch of distribution medium under the inlet pipe as shown in Figure 3.15b, to help distribute the resin and eliminate random blockage of the inlet tube giving less scatter of test results.

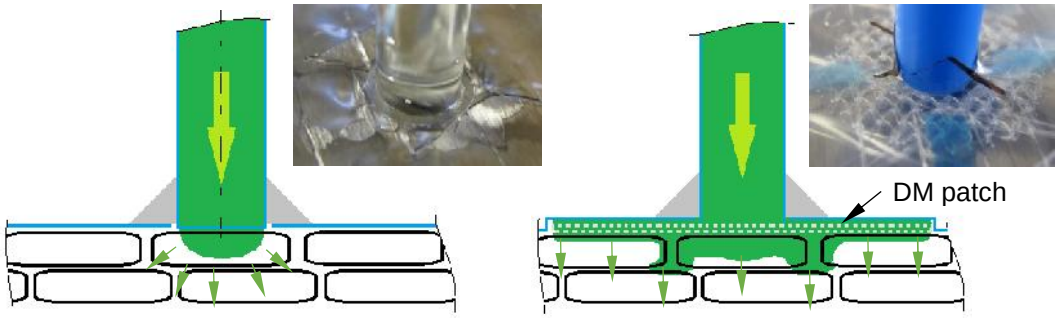

Figure 3.15 Resin inlets views and schematic cross sections: a) cured 6 mm inlet and b) inlet with a 24 mm DM patch

A set of tests were performed to investigate the influence of distribution medium patch size on results (resin flow bottom hit time). The fabric used for these trial tests was Saertex UD NCF (278 g/m^2, bindered) [252] and the resin was RIMR235/RIMH238 [255]. A view of the test setup is depicted in Figure 3.16, where three specimens with 12 mm, 24 mm and 48 mm diameter DM patches are shown. The results of these tests are summarised in Table 3.3 and Figure 3.17.

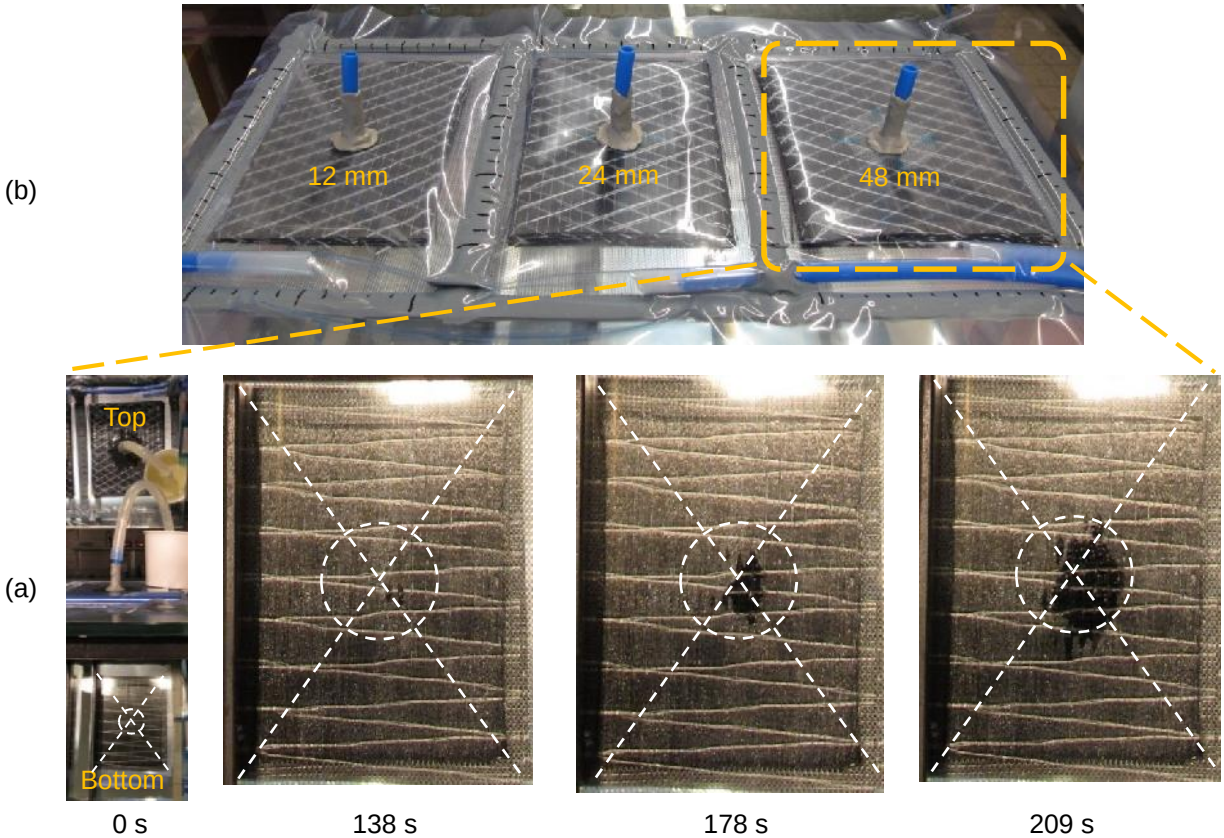

Figure 3.16 Through-thickness permeability tests: a) fabric specimens with different DM patch size (12 mm, 24 mm and 48 mm), b) test views for 48 mm patch specimen (bottom view of the stack)

	UD NCF (278g/m^2) layup				
	$(0)_{10}$, binder side down			$(0)_{14}$, binder side down	
Patch diameter, mm	6 (tube only)	12 (I)	12 (II)	24	48
'Bottom hit' time, s	447	26	69	177	138

Table 3.3 Radial infusion test results with different distribution medium patch sizes

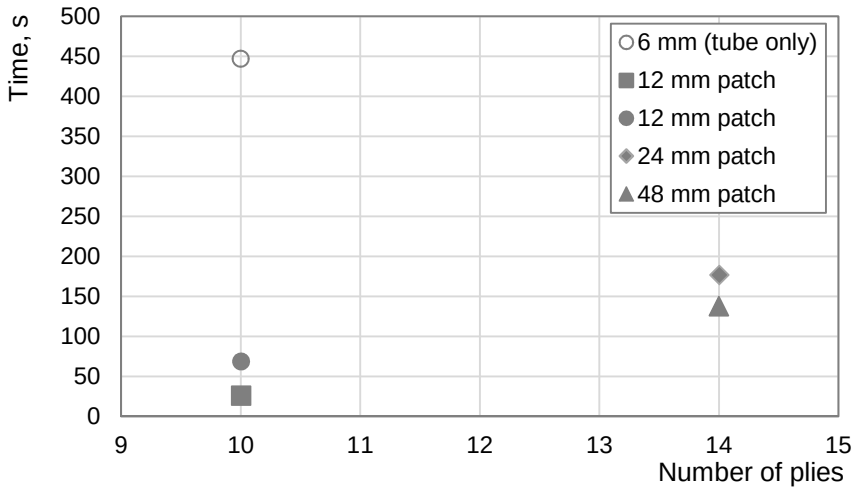

Figure 3.17 UD NCF (278 g/m^2) through-thickness radial infusion test results

These limited test results indicate a significant time reduction (circa -66%) and smaller scatter of data when using a DM patch under the inlet tube. It is suggested that a 24 mm diameter patch is sufficient to properly initiate flow and avoid local blockage effects. The use of at least 25 mm inlet diameter to obtain repeatable measurements was also suggested in [178]. However, despite this improvement a limitation of this test is that V_f ratio varies throughout the infused region making it impossible to assign a permeability value to a definite fibre volume ratio. Thus an alternative method for through-thickness permeability measurement was considered and is presented below.

Enforced 3D flow test

The test procedure used previously for in-plane fabric permeability tests was modified to measure through-thickness permeability by changing the inlet on one of the specimens as shown in Figure 3.18b. The idea is to exploit the difference between the flow fronts on the upper and lower surfaces, since it depends on the thickness and through-thickness permeability of the preform. With known fabric in-plane permeability (e.g. K_{xx}), a numerical simulation and inverse engineering was used to calibrate through-thickness permeability so that experimental and numerical results for 3D flow agree on both upper and lower surfaces of the preform.

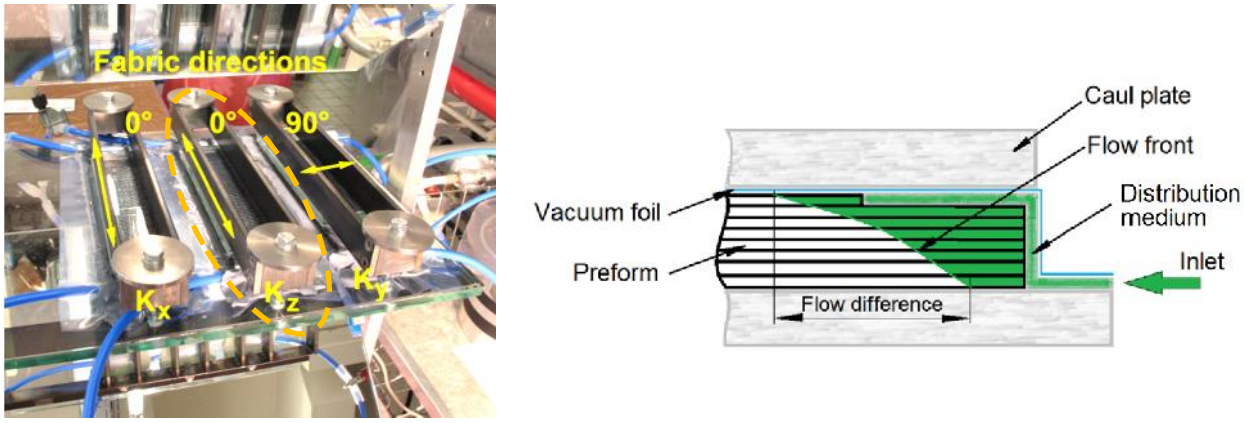

(a) (b)

Figure 3.18 Through-thickness permeability test: a) setup view and b) modified inlet schematic cross section

3.2.1 Unidirectional non-crimp fabric

Through-thickness permeability of unidirectional NCF with areal weight of 274 g/m^2 from Saertex [252] is used as through-thickness tow permeability in meso-scale infusion simulation of a draped hemisphere (section 5.2.1). Two test layups of $(0)_{24}$ (for K_{xx} and K_{zz}) and one layup of $(90)_{24}$ (for K_{yy}) were prepared and infused. A typical test view is depicted in Figure 3.19 with upper and lower flow fronts indicated at 1009 s. Corresponding flow length curves are shown in Figure 3.20.

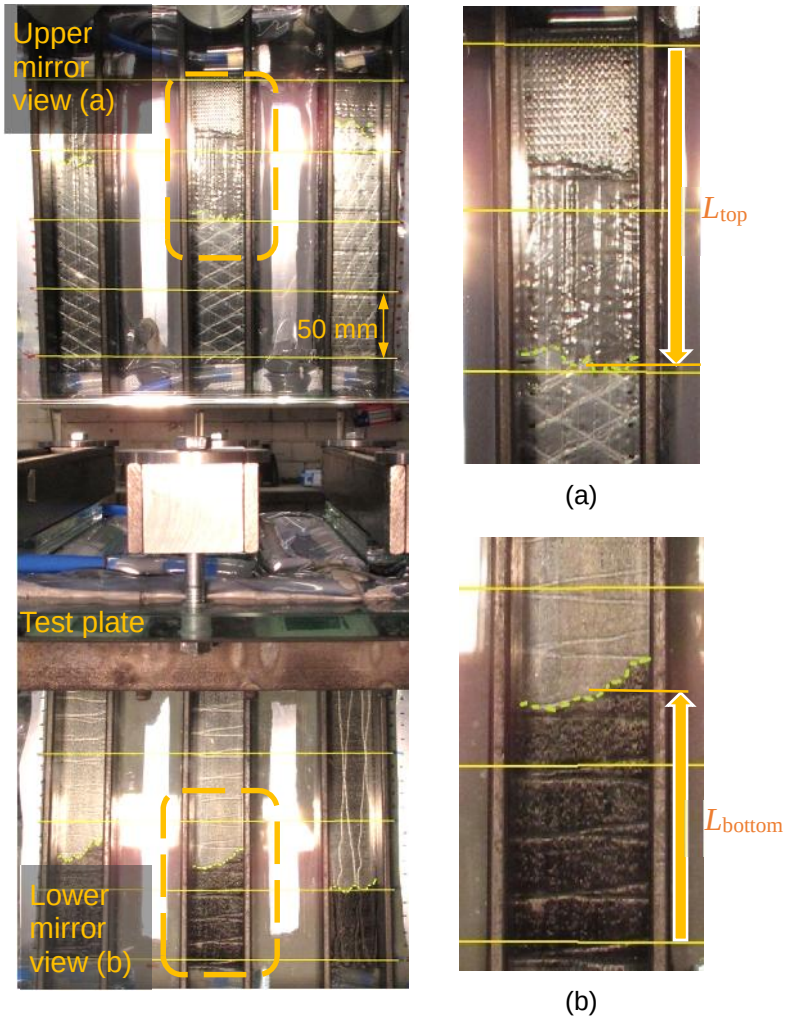

Figure 3.19 UD NCF permeability (K_{zz}) test view at 1009 s: a) upper surface and b) lower surface

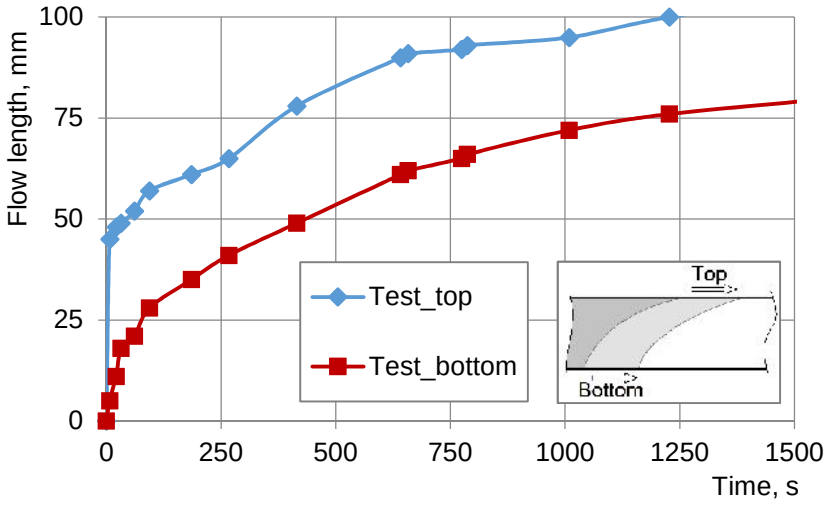

Figure 3.20 UD NCF permeability test (K_{zz}) flow length versus time diagrams (top and bottom surfaces)

As can be seen in Figure 3.20 there is a pronounced difference between the lines indicating the top and bottom flow lengths. The homogeneous (‘gapless’) architecture of this particular UD fabric

resulted in a smooth flow front development. It was observed that fabrics which have a distinct tow and gap structure (e.g. quasi-UD NCF as presented in the next section) do show less pronounced difference between top and bottom flow lengths.

Through-thickness permeability estimation by means of numerical simulation is presented in section 5.2 where analysis yielded a value of K_{zz} = 3.00E-15 m^2.

3.2.2 Quasi-unidirectional fabric

A test procedure analogous to that used in the previous section was repeated for the quasi-UD type Hexcel G1157 D1300 fabric. Results from this test will be used for a macro-scale VARI process simulation of a demonstrator presented in section 6.3.1. Two layups of $(0)_{12}$ (for K_{xx} and K_{zz}) and one layup of $(90)_{12}$ (for K_{yy}) were prepared and tested. Top and bottom views of the test for the K_{zz} specimen are shown in Figure 3.21 and Figure 3.22 respectively.

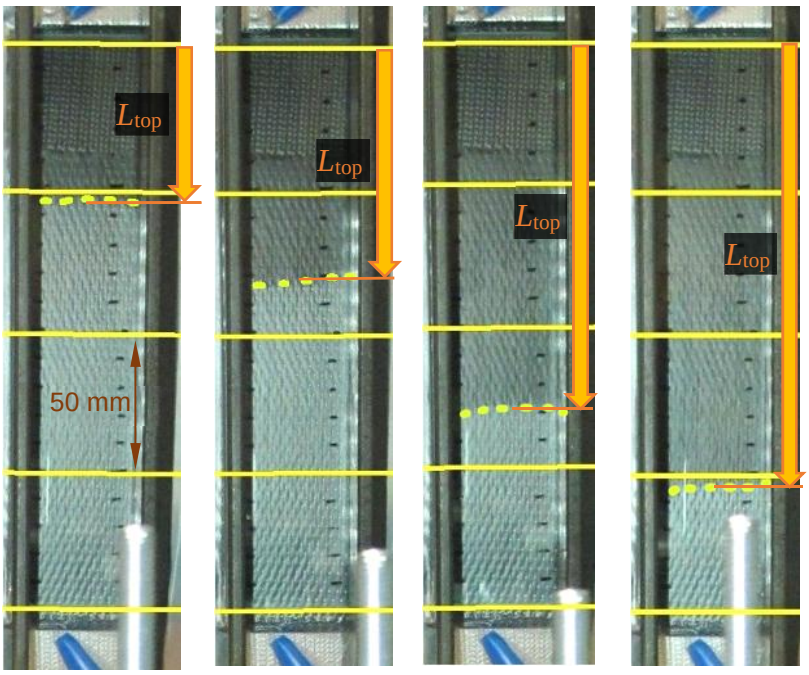

Figure 3.21 Quasi-UD NCF permeability test top views (K_{zz})

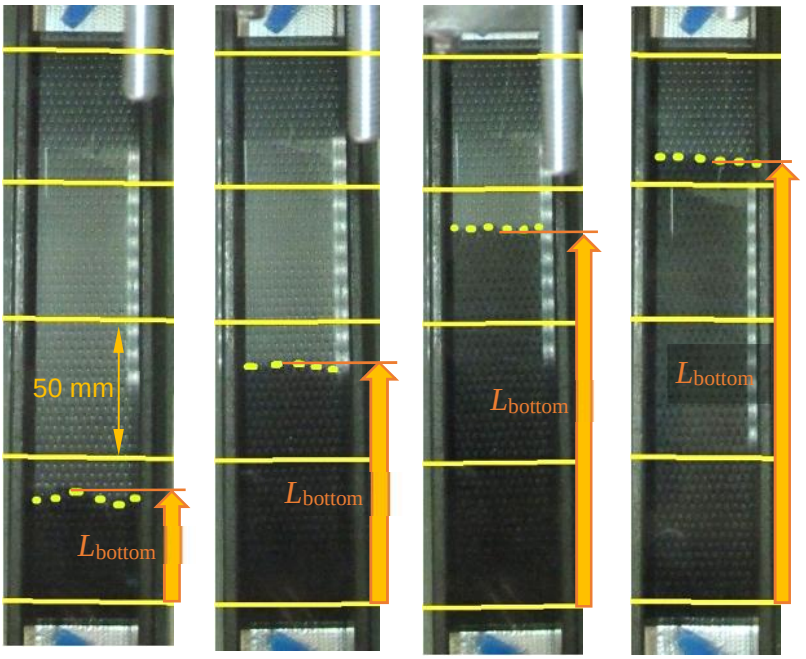

Figure 3.22 Quasi-UD NCF permeability test bottom views (K_{zz})

Flow length versus time diagrams in Figure 3.23 show only a small difference in flow front propagation between the top and bottom surfaces of the preform. This is due to presence of gaps resulting in fast through-thickness flow (quasi-UD fabric has a plain weave architecture, where 4% of tows are in the weft direction). After about 100 s from the start of test the flow front on the bottom of the preform starts to advance slightly faster than on the top of the preform. This may be explained by the presence of gaps at the glass-fabric and fabric-vacuum foil interfaces. These gaps form due to undulation of warp tows between the weft tows. At the fabric-vacuum foil interface the gaps are partially eliminated by deformation of the vacuum foil.

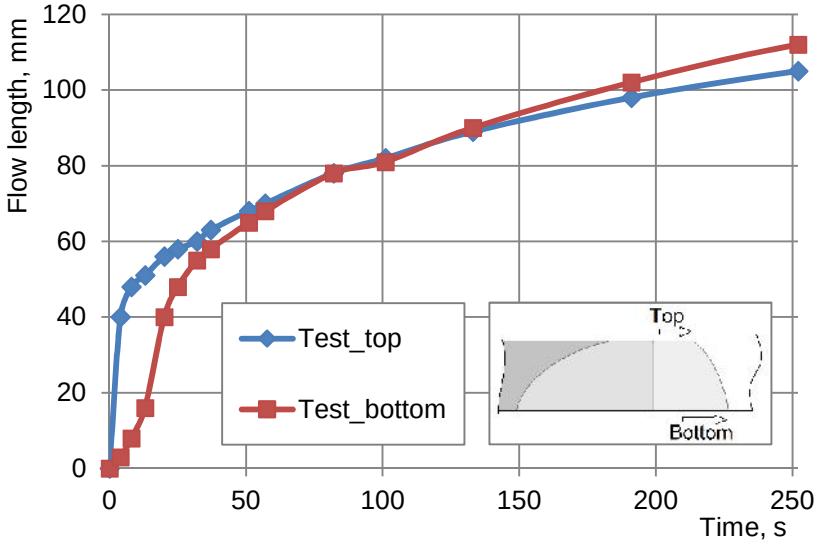

Figure 3.23 Quasi-UD NCF permeability test (K_{zz}) flow length versus time diagrams (top and bottom surfaces)

The numerical simulation model and methods used to estimate through-thickness permeability are the same as those used for the UD fabric presented in section 5.2. The estimated value for the through-thickness permeability is 4.94E-13 m^2.

3.2.3 Distribution medium

Through-thickness permeability estimation of the distribution medium XS6262-003 ”X60“X650FT from Flugzeug Union Süd [254] was performed using perforated and separation foils in a setup similar to actual VARI type infusion. Quasi-UD G1157 D1300 fabric from Hexcel [253] was used to accommodate the nesting effect. Separation and perforated plies were similar to those used for in-plane permeability tests in section 3.1.4. DM through-thickness permeability test results will be used in a demonstrator part VARI infusion simulation in section 6.3.3.

Test views and resulting flow length versus time diagrams are shown in Figure 3.24a and Figure 3.24b respectively. Estimation of DM orthotropic permeability is done using the numerical model presented in section 6.3.2. Obtained in-plane and through-thickness permeability values are 9.5E-10 m^2 and 1.0E-13 m^2 respectively.

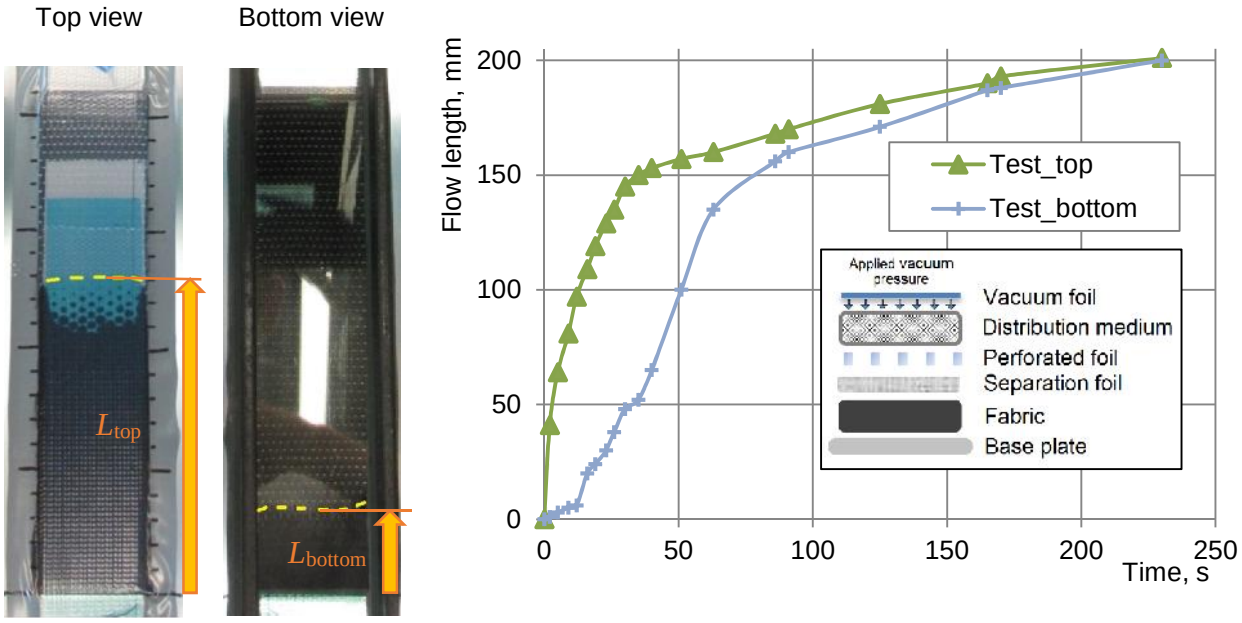

(a) (b)

Figure 3.24 DM permeability test: a) flow front views at 23 s and b) flow length versus time on upper and lower surfaces with schematic layup

3.3 Summary of permeability measurement tests

Several approaches were applied to estimate permeability of the selected fabrics and distribution medium. It was found that radial infusion tests, which were considered for through-thickness permeability measurement, generally resulted in a poor repeatability. Modification of the inlet using patches of distribution medium was successful to reduce data scatter; however, both initial and modified versions of the test suffer from the zone of non-uniform compaction near the inlet area and varying fibre volume fraction during the test. Consequently, an alternative 1D test setup was employed for both in-plane and through-thickness permeability measurement. Through-thickness permeability tests exploited the enforced flow front difference between the top and bottom of the preform. In-plane permeabilities were obtained directly from tests using Darcy's relationship, through-thickness and distribution medium permeabilities were obtained using numerical simulations calibrated to test results which will be presented in sections 5.2 and 6.3.1.

Tested preforms were constrained under caul plates to keep fibre volume fraction constant. This allowed association of permeability with a fixed fibre volume fraction which was measured from a cured specimen according to DIN29971 standard [256]. Varying preform thickness in unconstrained cavity height tests was measured using an optical measurement system. Variation of permeability with fibre volume fraction is then estimated numerically in section 6.3.1.

Tests on distribution medium showed that flow in this highly permeable material can be characterised using Darcy's law. It was also observed that interfaces have significant impact on the flow behaviour; e.g. resin in-plane flow through distribution medium in a VARI configuration is slower compared to flow through an isolated specimen tested on a glass plate. Nesting and through-thickness flow are responsible for this effect. Finally, distribution medium will be characterised by defining an orthotropic permeability in the FE model simulations to be presented in section 6.3.2.

A summary of permeability data for all tested materials is given in Table 3.4.

Material	K_{xx}, m²	K_{yy}, m²	K_{zz}, m²	V_f, %	Remarks
Biaxial NCF (Saertex), 548 g/m²	1.51E-11	1.42E-11	-	61.57	No tests for K_{zz}
UD NCF (Saertex), 274 g/m²	3.60E-12	1.48E-12	3.00E-15	61.50	K_{zz} determined numerically in section 5.2
Quasi-UD NCF G1157 D1300 (Hexcel), 290 g/m²	2.11E-11	3.08E-12	4.93E-13	59.03	$K = f(P)$ determined numerically in section 6.3.1
	2.37E-11	-	-	55.22	
	1.86E-11	-	-	54.19	
Distribution medium XS6262-003 "X60"X650FT	9.7E-10		-	-	Test on a glass plate
	4.3E-10				Test in a VARI type setup
	9.5E-10		1.0E-13	-	Orthotropic permeability determined in section 6.3.2

Table 3.4 Fabrics and distribution medium permeability data

4 Fabric characterisation tests and coupled macro-scale drape-infusion simulation

Finite element draping simulation most often employs a macro-scale modelling approach which can provide an acceptable balance between accuracy and computational cost. Nevertheless, not all deformation phenomena of technical textiles can be represented properly at this scale; also, it is difficult to accurately couple analyses of several manufacturing steps. Certain simplifications acceptable in one process model may not be acceptable in the subsequent process model, or relevant information may not be transferred due to the scale of the model. For example, macro-scale draping analysis of the stitched biaxial NCF may be accomplished without explicitly modelling the stitching, since its mechanical effect can be included in the homogenised material model. However, stitches are important in a subsequent infusion analysis as they influence preferential resin flow directions, and their neglect will lead to inaccurate prediction of flow front propagation.

In order to highlight distinct features of meso-scale modelling and analysis of textiles, which is one of the main objectives of this thesis, some limitations of a macro-scale modelling are presented. This is demonstrated in this chapter via coupled fabric draping and subsequent infusion processes analysis at the macro-scale. Tests that are necessary to characterise fabric constitutive model are listed in the flowchart in Figure 4.1.

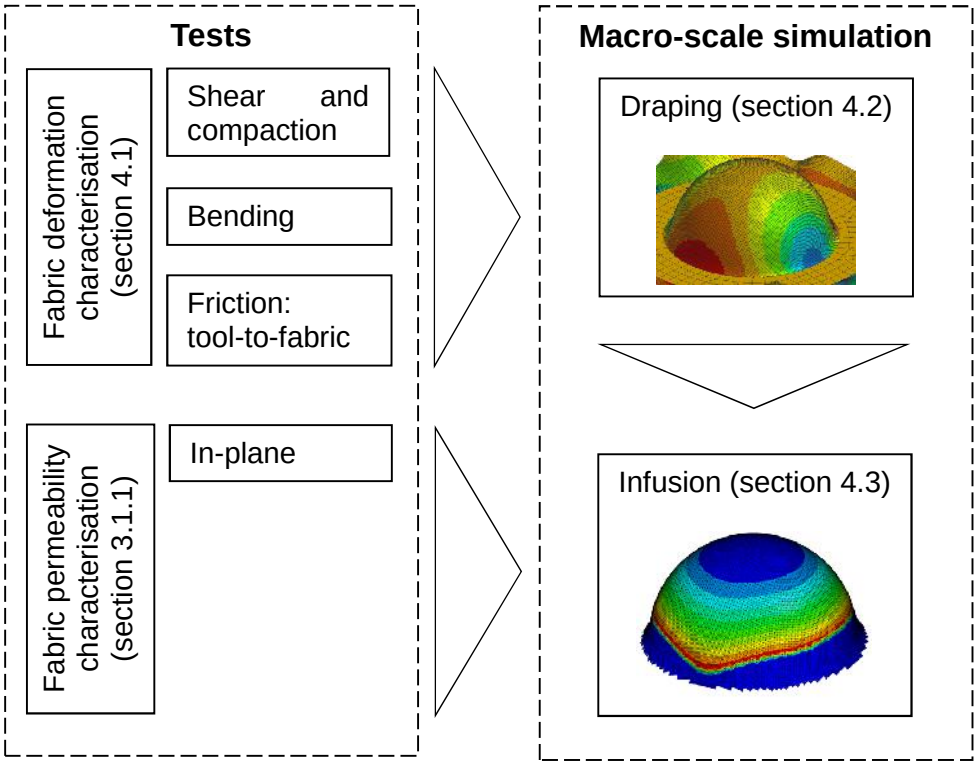

Figure 4.1 Test and simulation flowchart for fabric coupled draping and infusion simulation at the macro-scale

In this chapter biaxial NCF is modelled as a homogeneous material using continuum shell finite elements. Draping model material properties are obtained from shear, bending and fabric-to-tool friction tests. Fabric in-plane permeability was measured previously in section 3.1.1. The macro-scale numerical models are assessed using a hemisphere forming test coupled to subsequent infusion analysis; these are presented in sections 4.2 and 4.3 respectively.

4.1 Fabric deformation characterisation

Bindered biaxial non-crimp fabric tested in section 3.1.1 is considered for this investigation. This fabric consists of two UD plies stitched together with a chain stitch. Fibres in the plies are oriented at ±45° angle with respect to the stitch direction as shown in Figure 4.2.

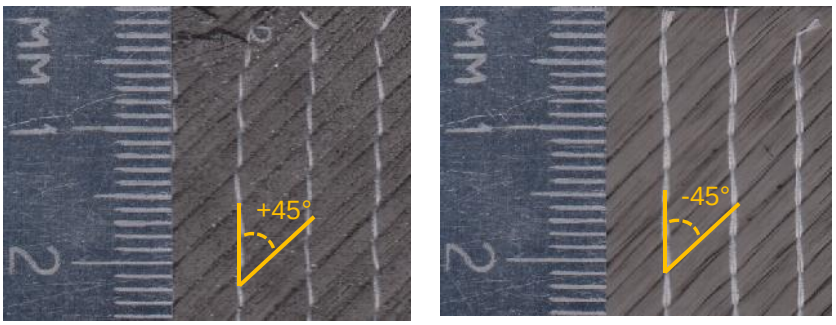

(a) (b)

Figure 4.2 Biaxial chain stitched fabric: a) upper side and b) lower side

Deformation behaviour of this type of fabric is rather complicated due to its architecture. The following characterisation tests were conducted:

- non-symmetric shear characterisation. This fabric exhibits non-symmetric shear behaviour which depends on whether the stitch is loaded in tension or compression;
- bending stiffness. Tests in +45/-45 and 0/90 fabric directions were performed since bending properties depend on tow orientation;
- fabric-to-tool contact friction.

4.1.1 Fabric shear characterisation

Fabric shear behaviour was quantified using the picture frame test. Views of the test setup are given in Figure 4.3 with details of the picture frame geometry presented in Appendix II. A Schenk-Trebel RM 250 testing machine with 500N load cell was used to load the frame at a constant velocity of 10 mm/min. Fabric shear angle was calculated from the frame angle.

For a sheared fabric in which stitches are loaded in tension (Figure 4.3a) stitches are inevitably damaged during the first loading cycle. The contribution of stitches to shear stiffness of the sample during the second load cycle is therefore strongly reduced. This effect is observed in Figure 4.4 where the curve corresponding to ‘stitch in tension’ (ST) load case is much higher in the first cycle compared to the second cycle. However, it cannot be concluded that only damage of stitches contributes to reduction of force since binder breakage also takes place. In addition, some fibre misalignment, which cannot be avoided during preparation and clamping of the specimen, also occurs.

If shearing direction causes stitches to be loaded in compression they are only rearranged and undergo less, or no damage, during the first load cycle. This rearrangement of stitches may partially explain the slightly higher picture frame force during the second load cycle for the specimen with stitch loaded in compression (SC) in Figure 4.4.

Considering these behaviours in the picture frame test it was decided to use the first cycle of shear with stitch in tension (curve labelled ‘Test_ST (1st_cycle)’ in Figure 4.4) and the second cycle of shear with stitch in compression (curve labelled ‘Test_SC (2nd_cycle)’ in Figure 4.4) to represent fabric shear behaviour, since in the first case stitching should be properly represented and in the second case spurious tension due to fibre misalignment is reduced.

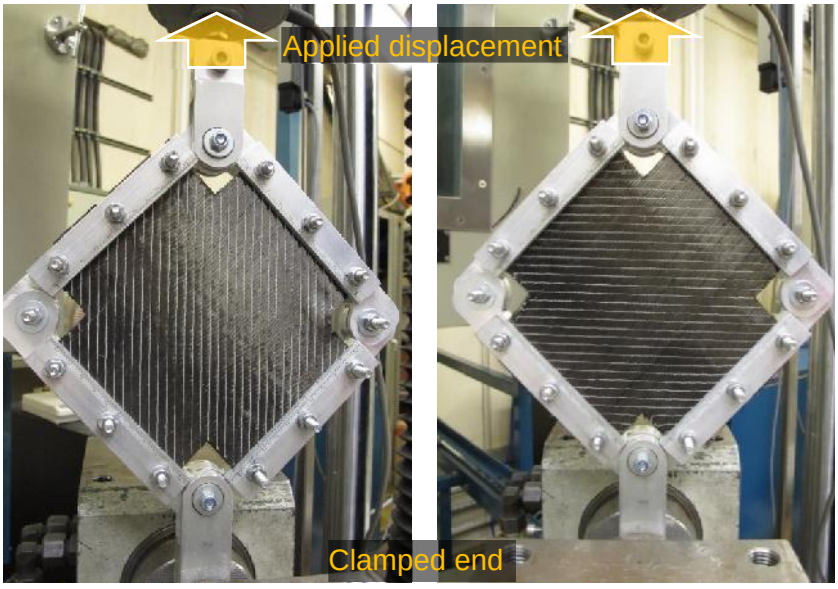

(a) (b)

Figure 4.3 Picture frame test views: a) stitch in tension (ST) and b) stitch in compression (SC) configurations

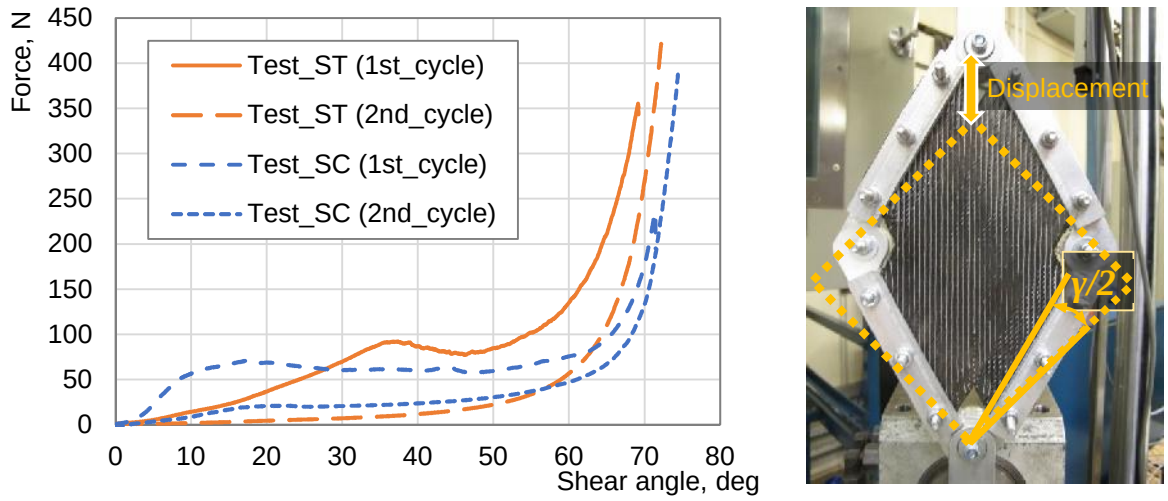

Figure 4.4 Picture frame test results (1st and 2nd load cycles)

A fabric shell element material model with thermo-visco-elastic matrix and elastic fibres (material model No. 140 in PAM-FORM [260]) is used to represent the NCF with unsymmetric shear behaviour. This model is schematically depicted in Figure 4.5. The required input for this model is a shear modulus multiplied by cosine of double frame angle versus cosine of double frame angle (G·cos(2·theta) versus cos(2·theta)) curve which is included in Appendix III. Following the methodology in [260] conversion of applied energy (picture frame force multiplied by displacement) to internal fabric energy (strain energy) is made which assumes that the volume of fabric undergoing shear deformation is constant.

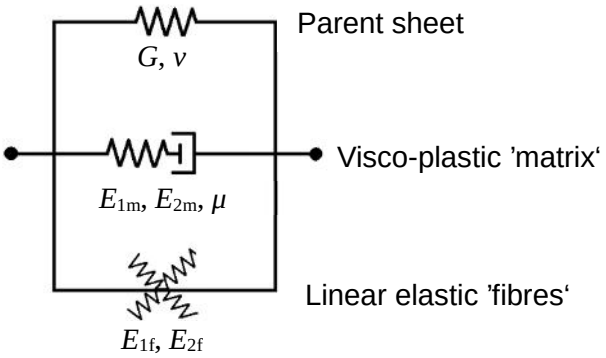

Figure 4.5 PAM-CRASH [260] material model No. 140

Figure 4.6a shows test and simulation results for the considered picture frame load cases. A reasonable agreement up to about 25° of shear angle is obtained, but after this angle results diverge considerably. The numerical model was thus calibrated to provide a better fit over the full range of shear angles as shown in Figure 4.6b. This was done by modifying the G·cos(2·theta) versus cos(2·theta)) curve sections corresponding to higher shear angle range (Appendix III). The need to perform calibration for better fit at a higher shear angle range may indicate some limitations of the analytical model to characterise fabrics shear behaviour.

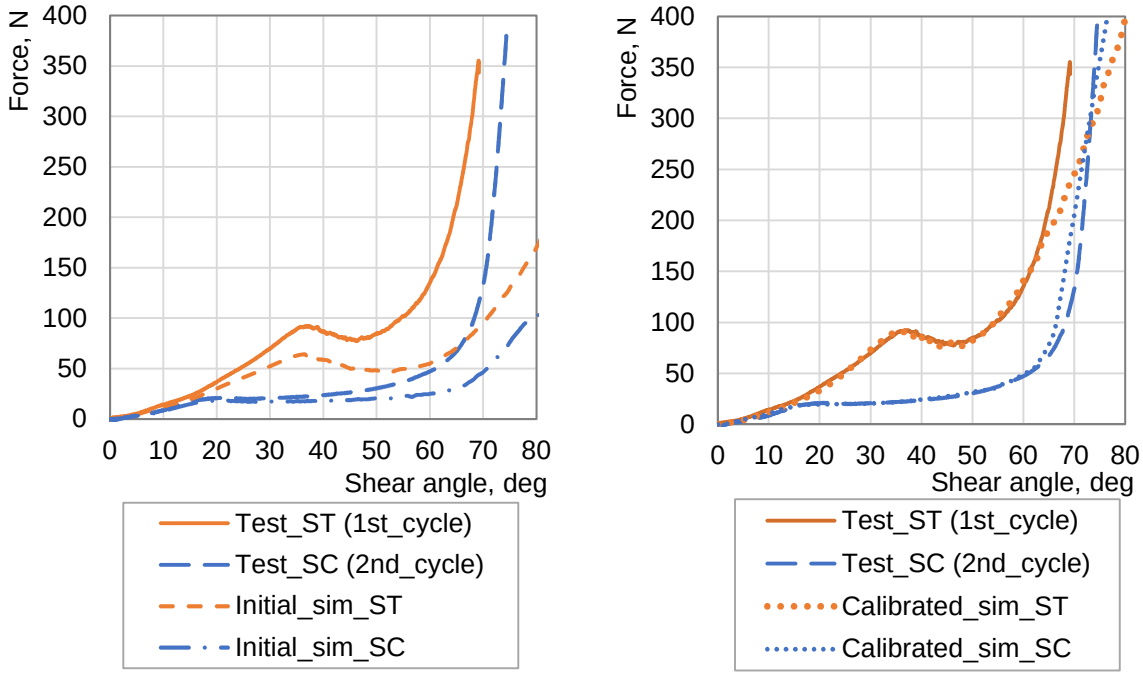

(a) (b)

Figure 4.6 Picture frame resistance force versus fabric shear angle diagrams: a) simulation with initial shear stiffness data and b) simulation with calibrated shear stiffness data

4.1.2 Fabric compaction characterisation

Thickness of the fabric will change during shear deformation. Therefore thickness evolution should be characterised by in-situ measurements during a picture frame test. Such test data for the considered fabric was available from reference [261]. Figure 4.7 reproduces this data in the form of thickness versus cosine of frame angle (angle between fibre directions) which is required input for the simulation model.

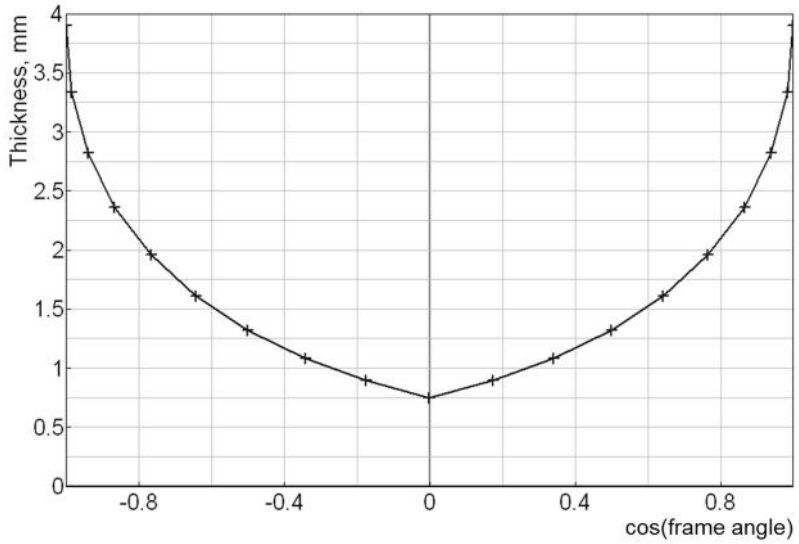

Figure 4.7 Biaxial NCF thickness versus cos(frame angle) diagram [261]

Thickness measurements were available only for specimens sheared in the stitch tension direction. It is reasonably assumed here that thickness change will not depend on shear direction, thus the thickness diagram in Figure 4.7 is assumed to be symmetric with respect to the ordinate axis.

4.1.3 Bending characterisation

Simple bending tests under gravitational load were performed following the procedure in ASTM 1388 [86]. Coupons of 40 mm width were used with one end fixed and the other end free to deflect under self-weight as a cantilever beam. The overhang length and end tip vertical deflection were measured when the specimen tip touches a plane inclined at 41.5° to the horizontal as illustrated in Figure 4.8.

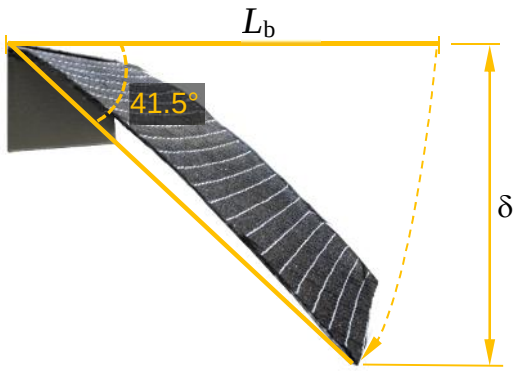

Figure 4.8 Illustration of fabric bending test with +45/-45 fibre direction

Bending deformations create a tension stress state in the fabric upper ply with compression in the lower ply. Therefore, it can be expected that fibre orientations are important so both +45/-45 and 0/90 ply orientations were tested. Tests, however, found there was no significant difference between 0/90 and 90/0 specimens. In-plane shear and bending stiffness are decoupled in PAM-FORM shell fabric model No. 140 therefore no experimental effort was made to characterise bending properties of sheared fabric.

Bending characterisation in ASTM 1388 standard gives a subjective relationship (equation (2.18) in section 2.1.3), which allows comparison of bending properties of different fabrics, but is not an engineering quantity appropriate to quantify bending behaviour for an FE code. Thus the first estimate of fabric bending stiffness was done analytically using the Euler-Bernoulli equation for cantilever beam with uniformly distributed load [73]:

$$G_b = \frac{q \cdot L_b^4}{8 \cdot ¢}, \tag{4.1}$$

with $q = \frac{m \cdot g}{L}$, (4.2)

$$m = \left(L \cdot b \cdot h\right) \cdot \circ \ , \tag{4.3}$$

where q – distributed load, N/m,

L – specimens length, m,

¢– specimens end deflection, m,

m – mass of the specimen, kg,

g – gravitational acceleration (9.81 m/s^2),

b – width of the specimen, m,

h – thickness of the specimen, m,

$\circ$ – density of the specimen, kg/m^3.

Table 4.1 summarises bending stiffness test and calculated results for +45/-45 and 0/90 fibre directions.

Fibre orientation	L_b , m	¢ , m	b , m	h , m	$\circ$, kg/m^3	G_b , kN·mm^2
+45/-45	0.135	0.101	0.040	0.00075	2.2E3	0.27
0/90	0.177	0.131				0.60

Table 4.1 Biaxial NCF bending stiffness for +45/-45 and 0/90 fibre orientation

PAM-FORM model No.140 only allows a single value of bending stiffness so an average value of G_b = 0.43 kN·mm^2 is assumed for the numerical model. A summary of material parameters used for the macro-scale bending simulation material model is given in Table 4.2.

Parameter	**Value**
Shear stiffness	(Appendix III)
Aerial density, kg/mm^2	0.548E-6
Fabric thickness, mm	0.75
Density, kg/mm^3	2.2E-6
Bending stiffness, kN·mm^2	0.43

Table 4.2 Material parameters for macro-scale bending simulation model

4.1.4 Fabric-to-tool friction test

A simple test was performed to estimate dynamic fabric-to-aluminium tool friction which is required for the hemisphere validation study to be presented in section 4.2.2. This test involves pulling the fabric, with an added mass m over the tooling plate surface at a constant velocity v and recording the necessary pulling force F_{fr}. A schematic view of the test setup is given in Figure 2.29. The pulling

force was measured with a PSE-FM200 force measurement device and friction coefficient was calculated according to Coulomb's law as described in section 2.1.3. Experimental data and results for three tests are listed in Table 4.3.

Test No.	m, kg	F_N, N	F_{fr}, N	μ_f	$\mu_{f\_average}$
1	2.99	29.2	6.25	0.213	0.22
2			6.00	0.204	
3			7.20	0.245	

Table 4.3 Friction test results for fabric-to-aluminium tooling

Additional tests were performed by pulling the fabric in different directions with respect to the stitch, but no substantial variation of measured force was observed. It was therefore concluded that fabric-to-tool friction coefficient is independent of velocity direction.

4.2 Fabric draping model validation

A hemisphere draping test is considered here due to its simplicity and ability to shear the fabric up to its limit shear angle with loading the stitch both in tension and in compression. The force needed to form the fabric and resulting shear angles can be accurately measured. It is therefore considered to be a suitable test to validate simulation results.

4.2.1 Hemisphere draping test

A test frame similar to the one described in [5] was developed to hold and drape the fabric. A 400x400 mm piece of fabric was placed between the two rings (blankholders), to which a constant pressure of 3.35 kPa was applied by springs. The frame was then driven over the hemisphere in a Schenk-Trebel RM 250 testing machine at a constant velocity of 10 mm/min. The resulting vertical force necessary to drape the fabric was measured with a 500 N load cell. The test setup is shown in Figure 4.9 with setup dimensions and loading conditions given in Table 4.4. Punch force and punch displacement versus time diagrams, together with selected views of the deformation sequence are provided in Figure 4.10. The displacement versus force diagram and measured fibre rotation angles are used to validate and assess the hemisphere draping simulation results presented in the following section.

Figure 4.9 Hemisphere draping test setup

Parameter	Value
Hemisphere diameter, mm	150
Inner diameter of blankholder, mm	164
Outer diameter of blankholder, mm	244
Blankholders pressure, kPa	3.35
Rate of loading, mm/min	10

Table 4.4 Hemisphere draping test parameters

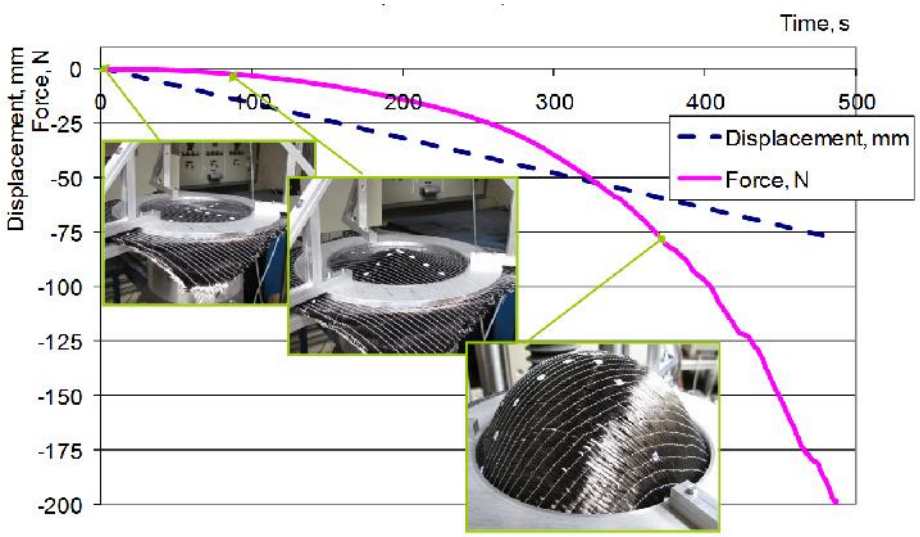

Figure 4.10 Force and displacements versus time diagrams and views of fabric drape sequence

4.2.2 Hemisphere draping simulation

A view of a hemisphere draping FE model is given in the Figure 4.11. This model represents the test setup with fabric, a pair of a blank holders and a hemisphere punch. The fabric was modelled with

4-node shell finite elements using a visco-elastic material model No.140 available in PAM-FORM [260] software package with material parameters from Table 4.2 and Table 4.3.

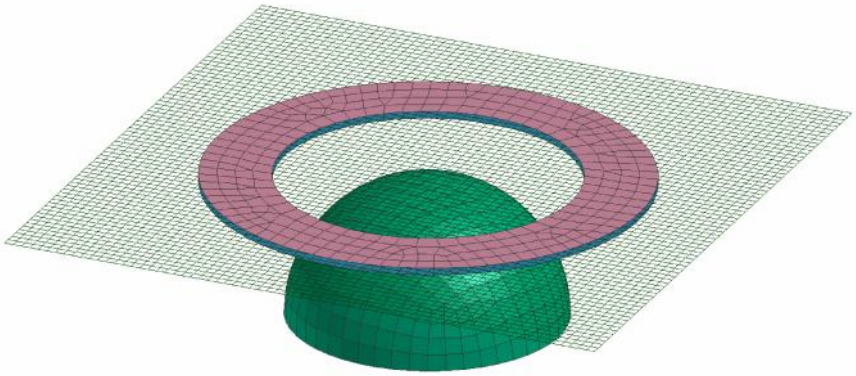

Figure 4.11 FE model for a macro-scale hemisphere draping simulation

A diagram of vertical force exerted on the punch versus its displacement in depicted in Figure 4.12. Explicit solvers uses a very small time step (<0.1μs) due to stability reasons, thus loading velocity has to be increased in the simulations to limit CPU cost. Three simulation curves are plotted for various forming velocities and show a slight influence of loading speed on the results due to dynamic inertia effects with tendency towards a quasi-static test diagram.

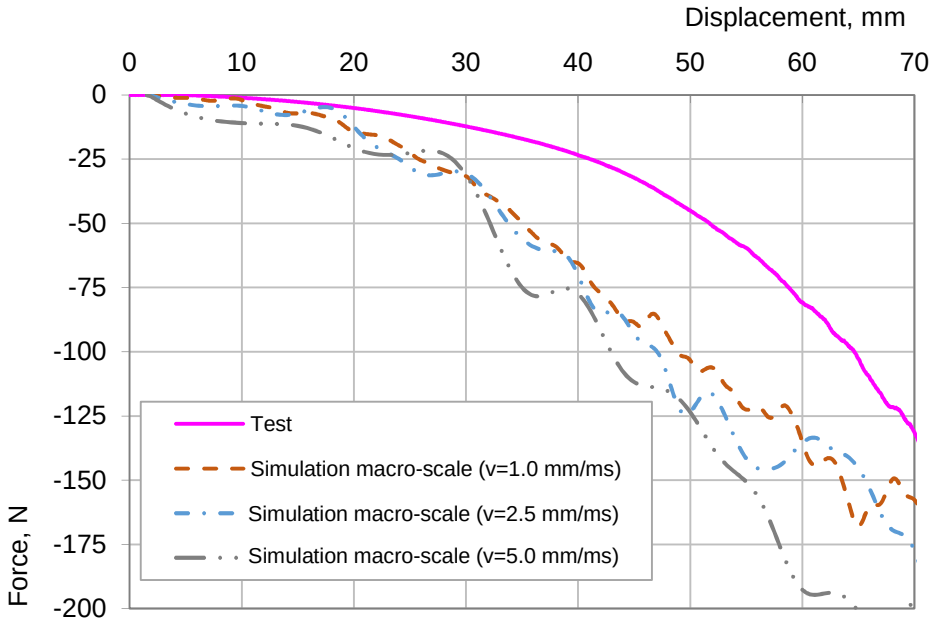

Figure 4.12 Punch force versus displacement diagrams from test and macro-scale FE simulations for various punch velocities

Shear angle results are presented in Figure 4.13. The initial fibre angle (90°) in two opposing quadrants decreases (stitch in tension) and in the other two quadrants it increases (stitch in compression).

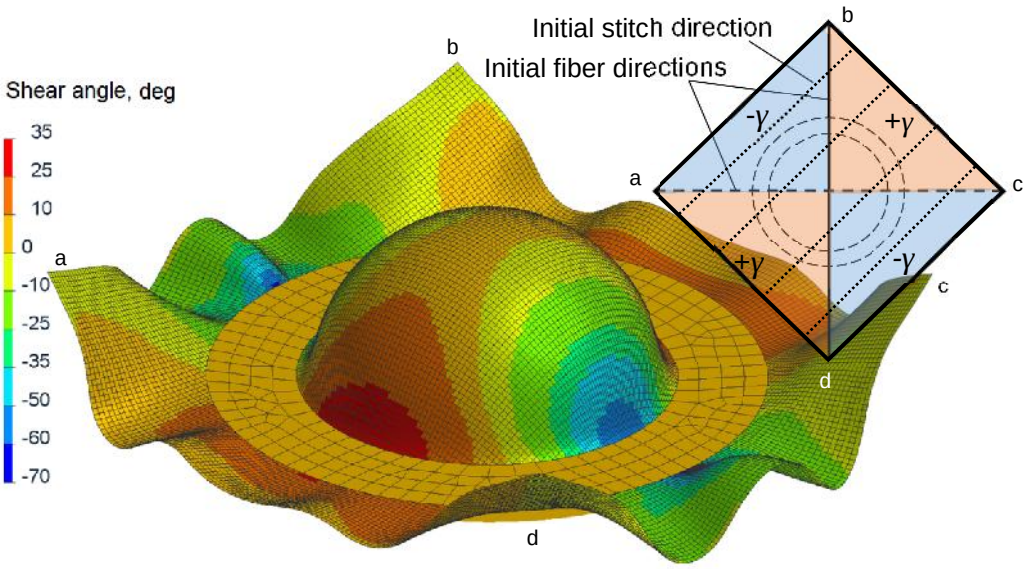

Figure 4.13 Shear angle distribution over the hemisphere from macro-scale draping simulation

A quantitative comparison of shear angle between test and simulation around the circumference of the hemisphere is given in Figure 4.14 where, generally, the simulation show a good agreement to experimentally measured values. These sheared fabric results are used in the following section for infusion simulation where permeability directions and porosity are modified depending on fabric shear.

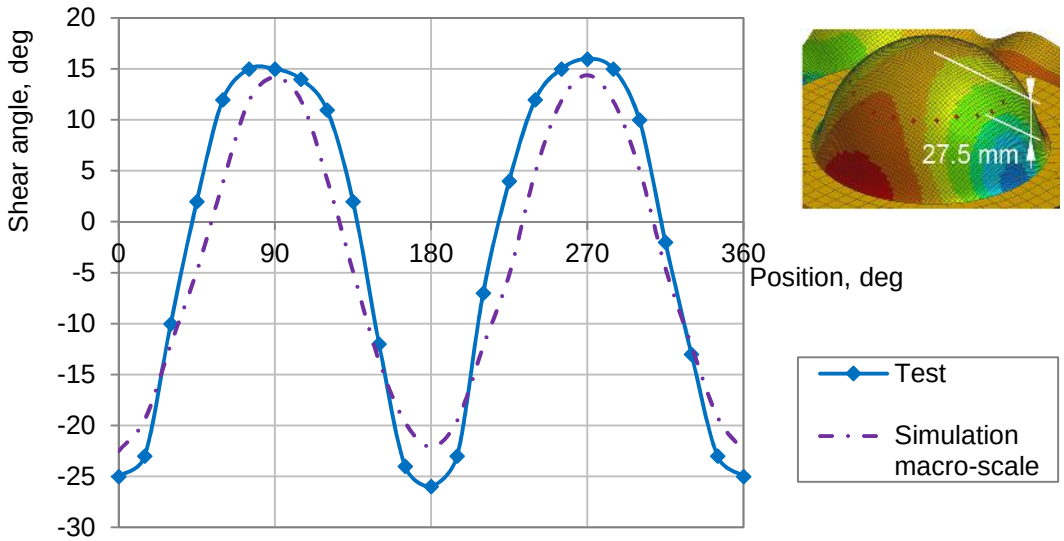

Figure 4.14 Shear angle distribution over the circumference of the hemisphere from test and macro-scale simulation

4.3 Hemisphere infusion test and simulation

A schematic view of the infusion test setup is given in Figure 4.15. An inlet tube with a 15 mm diameter patch of distribution medium was placed on the top of the hemisphere, an outlet was formed

by placing a distribution medium strip around the base of the hemisphere. Vacuum foil was formed over the hemisphere shape pushing it over a preheated aluminium tool to give a sufficiently large wrinkle-free area that matches the sphere geometry.

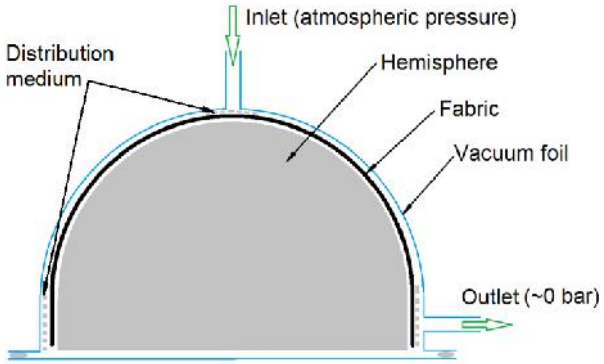

Figure 4.15 Schematic cross section of the hemisphere infusion test

An infusion simulation of the draped hemisphere was performed using the PAM-RTM [247] software. Hemisphere mesh from forming simulation was imported and fibre direction information transferred as depicted in Figure 4.16. Local porosity was calculated using the equation (2.49), which modifies porosity as a cosine function of shear angle. Fabric first local permeability direction is calculated as function of shear angle; second principal permeability direction is set orthogonal to the first as illustrated in Figure 4.17. Fabric permeability data was measured in infusion tests presented in section 3.1.1 and is listed in Table 4.5. A PAM-RTM user can provide permeability as a function of fibre volume fraction, but in this instance such data was not available.

Material	K_{xx}, m²	K_{yy}, m²
Biaxial NCF	1.51E-11	1.42E-11

Table 4.5 Permeability values of biaxial NCF (results from section 3.1.1)

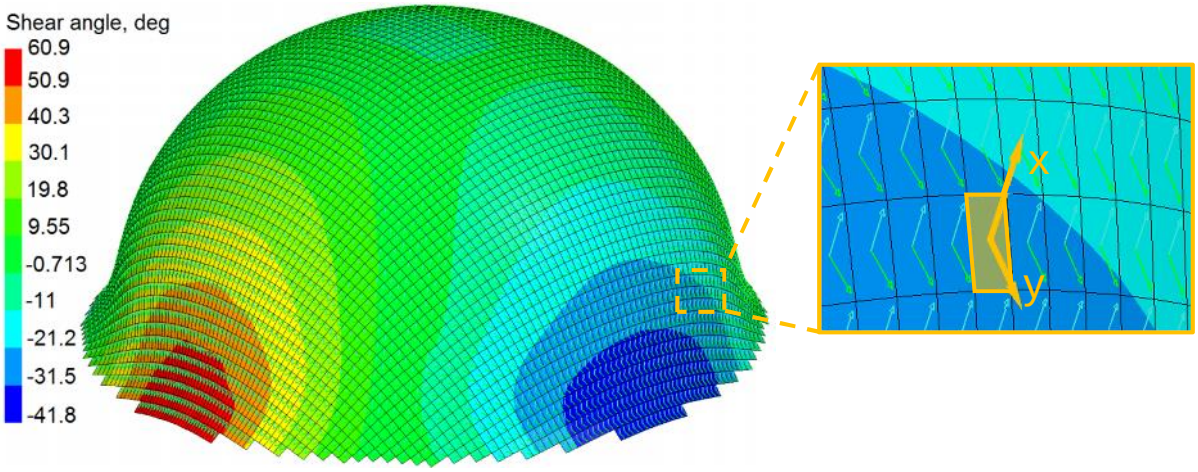

Figure 4.16 Hemisphere infusion simulation model with imported shear angle and local fibre direction data

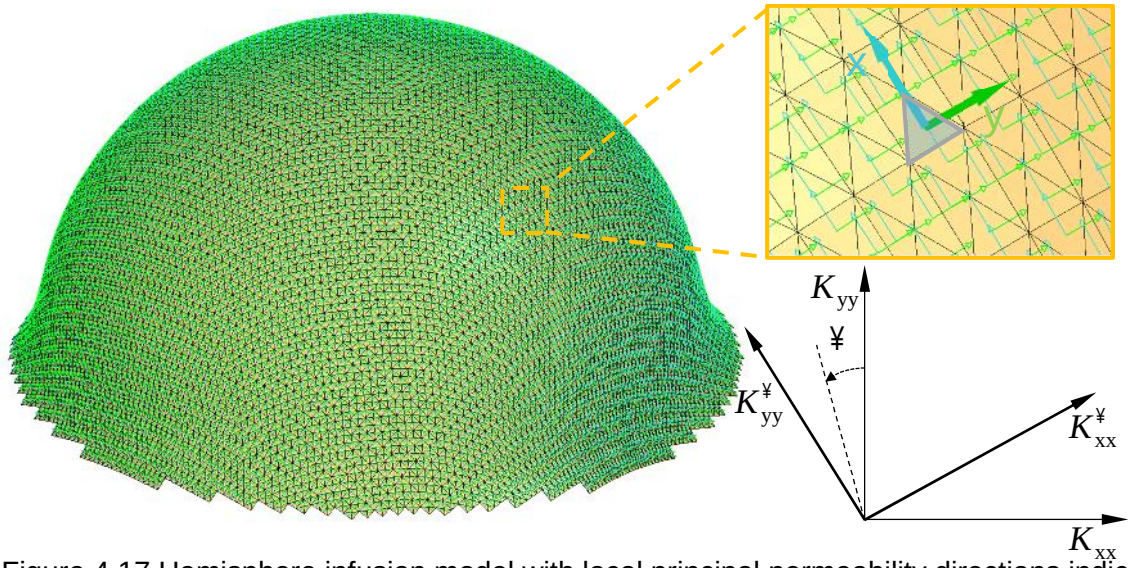

Figure 4.17 Hemisphere infusion model with local principal permeability directions indicated

Qualitative comparison of infusion test and simulation is made in Figure 4.18. It could be observed that an anisotropic flow propagation shape in the simulation is less pronounced than in the test. In the physical hemisphere test anisotropic flow was caused by the presence of stitches along which fluid racetracked; this effect was not possible to capture in the macro-scale finite element model, where anisotropic flow formed only due to local porosity variations. Thus the phenomenological observation of resin flow along the stitches could not be recreated using the considered macro-scale model.

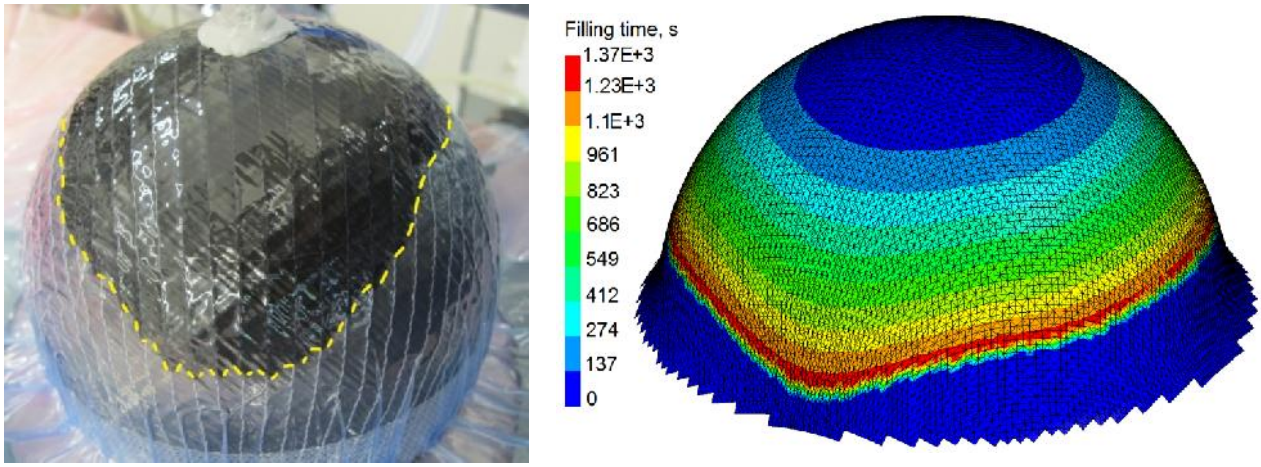

(a) (b)

Figure 4.18 Hemisphere infusion flow front views at 23 min from a) test and b) meso-scale simulation

4.4 Summary of fabric characterisation tests and coupled macro-scale drape-infusion simulation

A state-of-the-art macro-scale FE modelling approach for coupled drape and infusion of biaxial non-crimp fabric has been undertaken. Material mechanical characterisation tests for shear, compaction, bending and friction properties were performed and applied. A hemisphere draping test has been performed and used to validate the deformation behaviour of the FE simulation which showed good agreement for shear angle distribution around the circumference and reasonable results for punch force versus displacement.

Analysis of the draped hemisphere infusion has shown important limitations of the macro-scale infusion modelling for the stitched NCF where only shear angle, porosity and corresponding permeability data is included in the model. Stiches, however, were found to have a profound effect on flow propagation by acting as racetracks that significantly alter flow behaviour. Since stitches cannot be represented in the macro-scale model, correct flow propagation prediction is not possible. These limitations are addressed in the following chapter where coupled drape and infusion simulations are performed using a fabric model developed at the meso-scale.

5 Coupled meso-scale drape-infusion simulation

A meso-scale draping analysis requires fabric architecture modelling and mechanical properties characterisation of its constituents at a tow and stitch scale. In addition to major deformation mechanisms, such as compaction, shear and bias tension behaviour, a meso-scale model has the potential to capture local effects, such as tow buckling, tow separation and inter-ply slip; in addition, tool-to-fabric friction, inter- and intra-ply friction can be represented. Additional material characterisation tests include measurement of stitch tensile properties, inter-ply and intra-ply friction coefficients for draping, and permeability of the tow, gap and stitch domains for infusion simulation.

Figure 5.1 depicts a flowchart of the additional experimental data that is necessary.

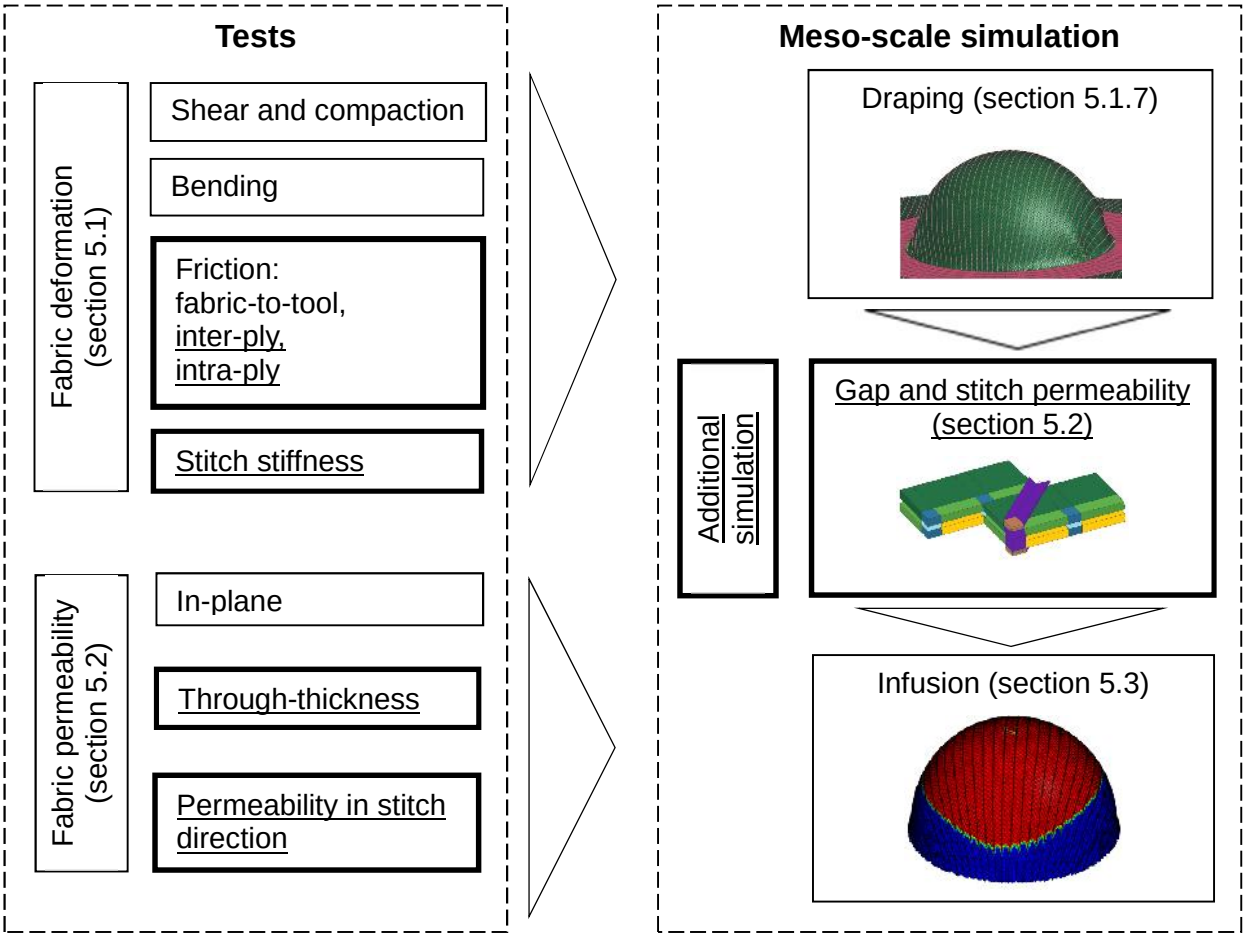

Figure 5.1 Test and simulation flowchart for meso-scale fabric draping and infusion simulation

Characterisation of permeability properties for a meso-scale model is a challenging task as each model's constituent (tow, gap, and stitch) has to be assigned a permeability value that may not be directly measurable. Furthermore, the 3D resin flow through the fabric is strongly coupled in all three directions. Thus the first estimations for permeability properties were based on a rule of mixtures for equivalent permeability (gap-tow flow), followed by numerical 'fine tuning' which was found

necessary due to model simplifications, irregularity of the real fabric architecture and limited available test data. Model validation was undertaken exploiting hemisphere drape and subsequent infusion analysis, similar to the approach followed in the previous chapter.

5.1 Fabric deformation characterisation

A biaxial non-crimp fabric unit cell (UC) model suitable for drape and infusion simulations is proposed in this section, followed by material model implementation and characterisation of mechanical properties. Fabric compaction, bending and shear deformation behaviour are represented by the model, also, inter-ply, intra-ply and fabric-to-tool friction is included. The fabric model is validated by comparing shear angle distribution and punch force versus displacement diagrams from hemisphere draping test and numerical simulation.

5.1.1 Biaxial NCF unit cell and material modelling

A unit cell of the fabric is depicted in Figure 5.2. The cell is constructed from 8-node solid finite elements representing both tow and gap volumes. Intra-ply gap elements are running parallel to the tows in a ply, additional inter-ply gap elements connect upper and lower plies. Gap elements do not contribute to mechanical behaviour of the model and are only used to facilitate resin flow in a subsequent infusion simulation.

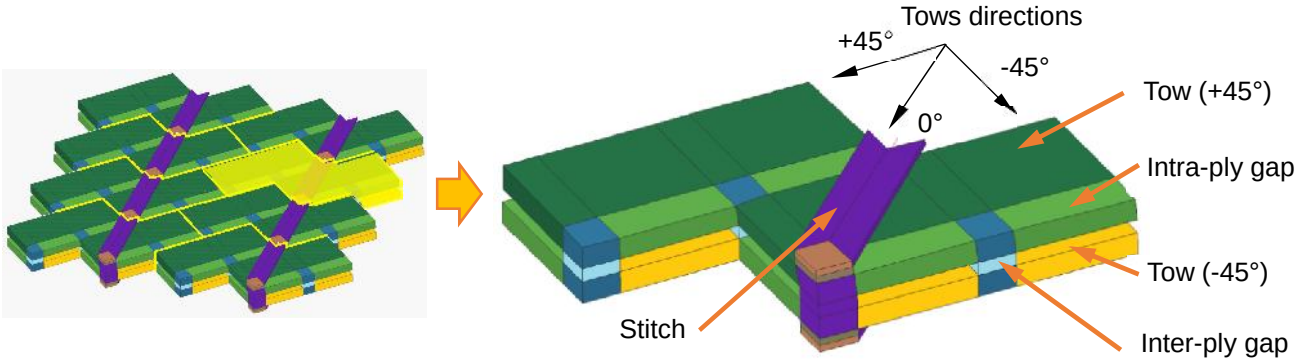

Figure 5.2 Unit cell of biaxial NCF with chain stitch

Plies are held together by stitches, which are modelled using bar finite elements overlaid with 8-node solid finite elements (Figure 5.3c). Bars contributes to fabric stiffness, stitch solid elements, similarly to gap elements, have zero stiffness and are only used for subsequent infusion simulation. Horizontal stitch elements (Figure 5.3c) have non-linear behaviour when loaded in tension, whereas vertical stitch elements acts as soft linear springs that hold plies together. Nodes of bar elements are tied to the appropriate nodes of the tow solid elements. Since bar elements are used, rotational degrees of freedom (DOF) are not constrained at their attachment points.

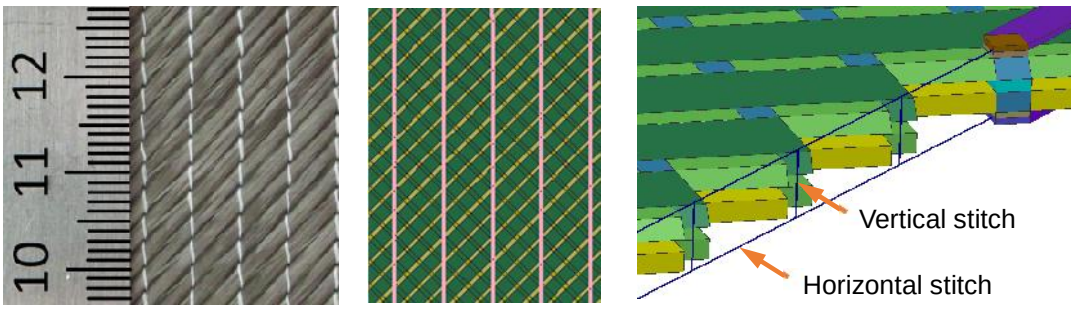

(a) (b) (c)

Figure 5.3 Biaxial NCF: a) fabric view, b) FE model and c) stitch bar FE detail

Physically a tow comprises many thousands of filaments that are very stiff in tension, but are easily rearranged by sliding mechanism under transverse load. In order to model this behaviour two standard material models in PAM-CRASH are used by overlaying two elements each with its own constitutive model. A bi-phase composite model (Figure 5.4), available in PAM-CRASH™ [262], was used for stiff fibre response in tension, while keeping transverse response negligibly low. This is done by choosing appropriate stiffness matrix parameters in equations (5.3) and (5.4).

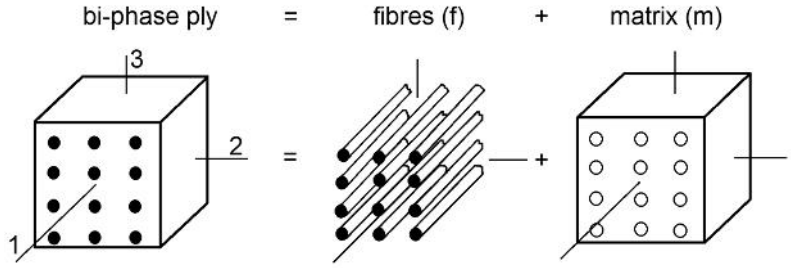

Figure 5.4 Bi-Phase rheological composite model (PAM-CRASH™ material model No. 30) [262]

Orthotropic tow is described by the following constitutive relationship:

$$\boldsymbol{\sigma} = \mathbf{C}\boldsymbol{\varepsilon}\,, \tag{5.1}$$

with stiffness matrix $\mathbf{C}$ combined from stiff fibre and pseudo-matrix contributions:

$$\mathbf{C} = \mathbf{C}^{\mathrm{f}} + \mathbf{C}^{\mathrm{m}}\,. \tag{5.2}$$

The fibre and pseudo-matrix orthotropic matrices are

$$\mathbf{C}^{\mathrm{f}} = \begin{bmatrix} V_{\mathrm{f}} E_{11}^{\mathrm{f}} & 0 & 0 & 0 & 0 & 0 \\ & 0 & 0 & 0 & 0 & 0 \\ & & 0 & 0 & 0 & 0 \\ & & & 0 & 0 & 0 \\ & sym & & & 0 & 0 \\ & & & & & 0 \end{bmatrix}, \tag{5.3}$$

$$\mathbf{C}^{\mathrm{m}} = \begin{bmatrix} (1-V_{\mathrm{f}})E_{11}^{\mathrm{m}} & -\neg_{12}E_{22}^{\mathrm{m}} & -\neg_{13}E_{33}^{\mathrm{m}} & 0 & 0 & 0 \\ & E_{22}^{\mathrm{m}} & -\neg_{23}E_{22}^{\mathrm{m}} & 0 & 0 & 0 \\ & & E_{33}^{\mathrm{m}} & 0 & 0 & 0 \\ & & & G_{12} & 0 & 0 \\ & sym & & & G_{13} & 0 \\ & & & & & G_{23} \end{bmatrix}, \tag{5.4}$$

where V_{f} is the fibre volume ratio. Fibre elastic modulus E_{11}^{f} is much higher compared to matrix modulus E^{m} and ensures inextensibility of the tows. Numerical values used in the simulations are summarised in Table 5.1.

Response to transverse compaction is governed by another material model (No. 45 in PAM-CRASH™ [262]) that allows a highly compressible non-linear behaviour of tows to be represented using an additional set of overlaid elements. Figure 5.5 shows a schematic representation of the superimposed linear elastic (orthotropic) tow and non-linear elastic compaction models. Fabric characterisation tests and modelling are discussed step-by-step in the next sections.

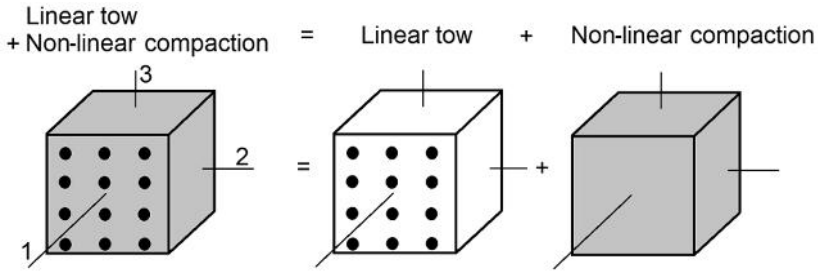

Figure 5.5 Superposition of the linear tow and non-linear elastic compaction models

5.1.2 Fabric compaction characterisation

As mentioned above, fabric compaction behaviour is modelled using material No. 45 in PAM-CRASH [262], which exploits a Kelvin type model with non-linear spring and linear dashpot, as illustrated in Figure 5.6. Only non-linear compaction characterisation is considered there, other model capabilities to represent cyclic loading, dissipative behaviour and strain rate dependency are not exploited.

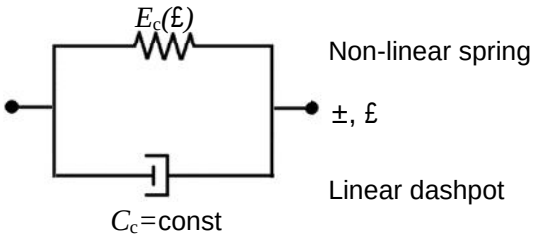

Figure 5.6 Kelvin type material model for fabric compaction modelling [262]

Stress-strain relationship for compaction modelling is as follows [262]:

$$\sigma = E_c(\varepsilon)\varepsilon + C_c\dot{\varepsilon}, \tag{5.5}$$

where $E_c(£)$ – slope of compression stress-strain curve, Pa,

C_c – linear dashpot characteristic, Pa.

Compaction test data for a similar biaxial NCF was available from [261] and is depicted as a solid line in Figure 5.7a. Thickness versus pressure dependency is used as a first estimate of stress versus strain for the non-linear elastic compaction law in the numerical model. Within a few iterative simulations, which were necessary due to interaction of overlaid elements, the final stress-strain dependency, which is an input for the simulation code, was obtained and is depicted in Figure 5.7b. The compaction simulation result using this calibrated data is shown in Figure 5.7a as a dashed line, together with a FE model used for this simulation which represents a 15x15 mm square patch of fabric.

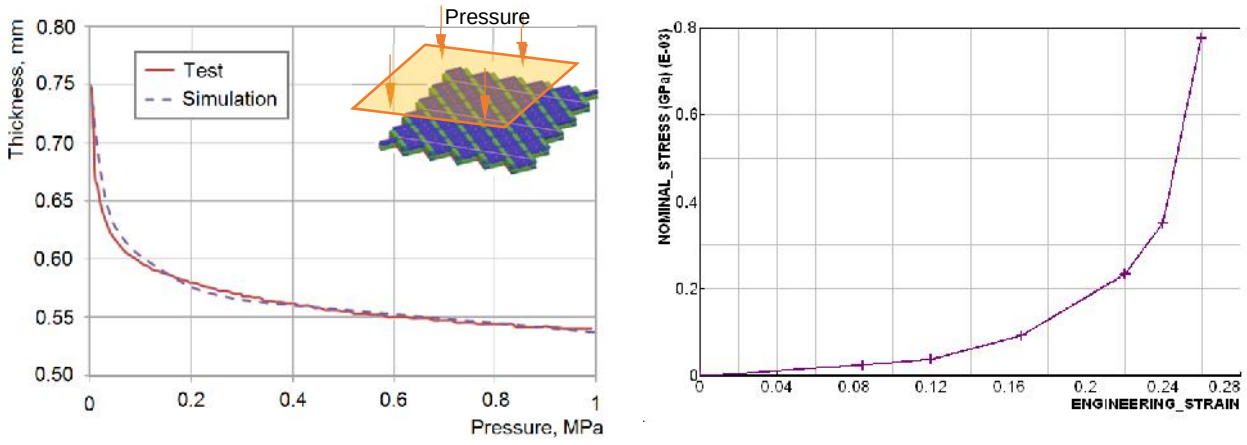

(a) (b)

Figure 5.7 Biaxial NCF (a) thickness versus pressure diagrams and (b) nominal compaction stress versus engineering strain diagram

5.1.3 Fabric inter-ply and intra-ply friction

Fabric-to-tool friction coefficient was estimated in section 4.1.4 yielding $\mu_{average}$=0.22. However, additional friction data is needed to represent inter-ply and intra-ply slip behaviour for the meso-scale drape simulation. Inter-ply friction coefficient quantifies resistance of plies to move relative to each other, whereas intra-ply friction acts between adjacent tows of the same ply. When a fabric undergoes shear deformation and transverse load is applied, as in typical draping, both friction mechanisms are active.

In [89] friction coefficients between the tows lying parallel and transverse to each other were measured yielding values of $\mu_{parallel}$=0.51 and $\mu_{transverse}$=0.19 respectively. A pronounced difference between the two coefficients is due to the nesting of the filaments in the case of adjacent plies with fibres in the same orientation as illustrated in Figure 5.8. In this thesis a value of $\mu_{transverse}$=0.19, is assumed for inter-ply friction coefficient, and does not depend on shear angle. Intra-ply friction between adjacent parallel tows was characterised by the friction coefficient $\mu_{parallel}$=0.51.

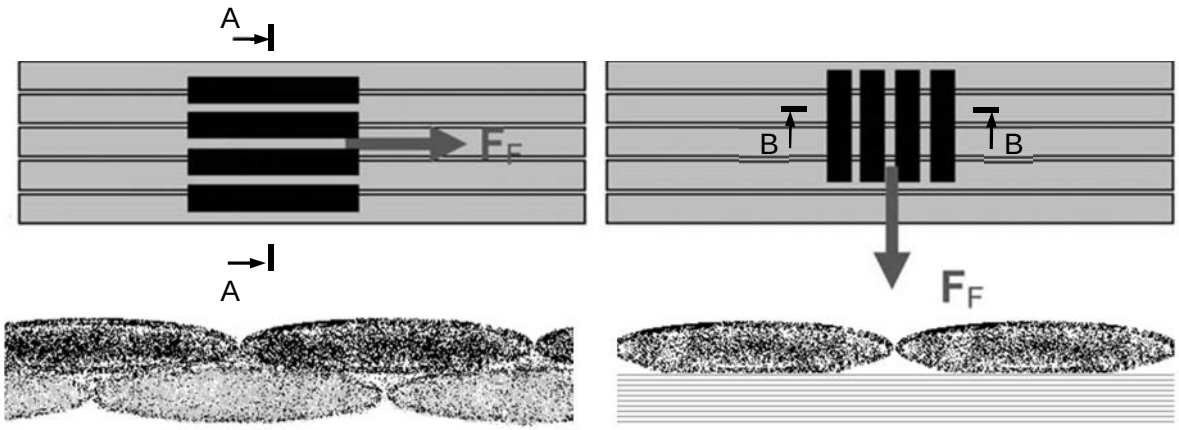

Figure 5.8 Nesting of a) parallel and b) perpendicular fabric plies (adapted from [89])

5.1.4 Stitches characterisation for fabric in-plane stretch behaviour

Stitches effectively hold fabric plies together and play an important role in fabric shear behaviour. To quantify mechanical behaviour of the stitches a simple fabric stretch test was used resembling a bias extension test as illustrated in Figure 5.9. A relatively wide and short coupon (150x200 mm in size with 27 stitch rows) was used since only small amount (~15%) of stretch was of interest and the number of loaded stitch threads had to be maximised. The force needed to deform the specimen was measured using a 500 N load cell in a Schenk-Trebel RM 250 tensile machine at a displacement

rate of 5 mm/min. Force versus nominal strain results for three coupons are given in Figure 5.10a where it is seen that progressive stiffening occurs as relatively loose stitches start to stretch, tighten and interact with the tows. Variations in measured force is attributed to the variations in fabric structure and discrepancies due to misalignment when clamping the specimens.

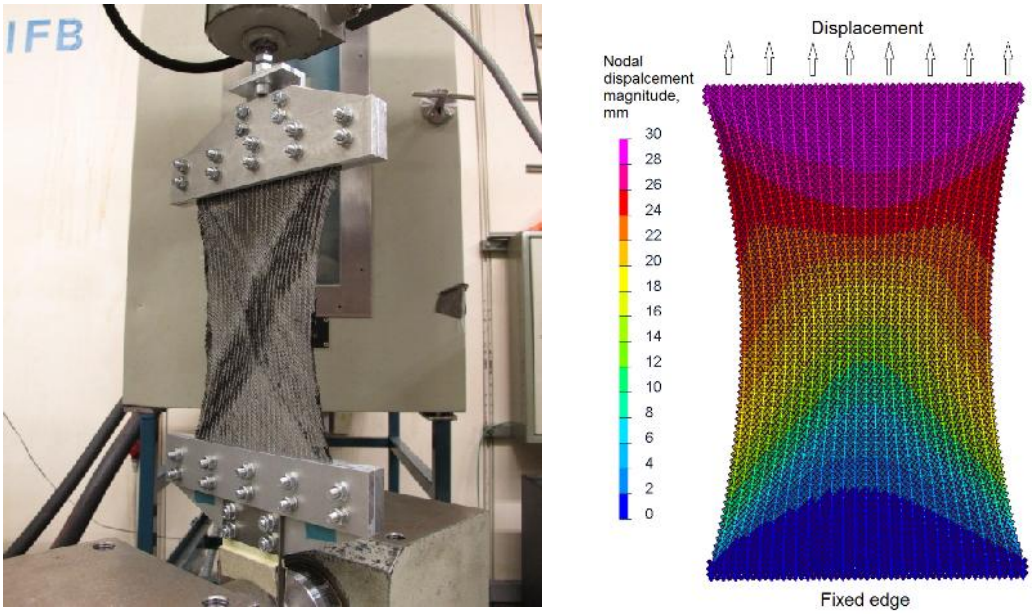

(a) (c)

Figure 5.9 Fabric stretch test: a) test setup and b) FE model with 15% strain

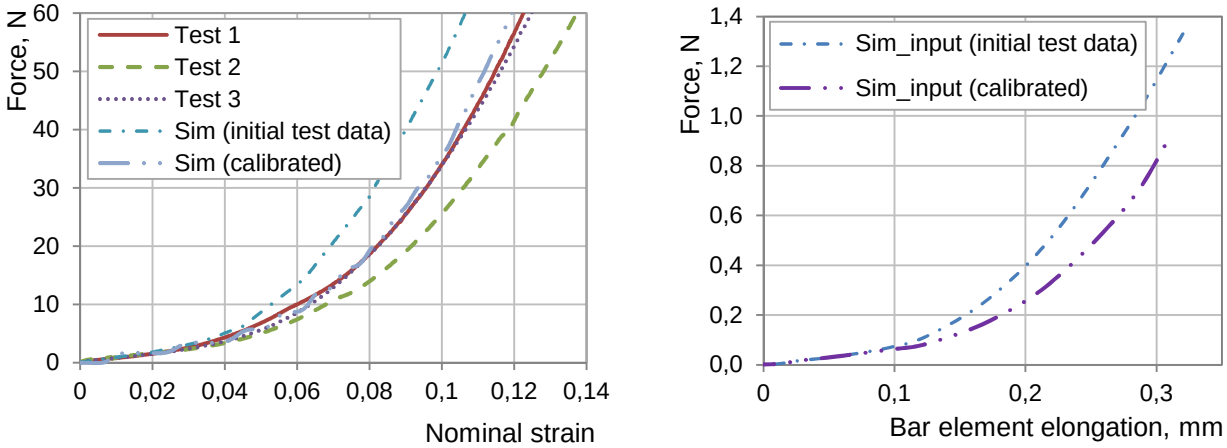

(a) (b)

Figure 5.10 Stitch characterisation: a) force versus elongation of the stitch bar element and b) simulation model input

An initial estimation of force versus elongation for a single bar element was made under the assumption that only stitches take tension load and force is evenly distributed among all stitch elements parallel to the loading direction, as illustrated in Figure 5.11. Single bar element length and cross section area were assumed to be equal to 2.9 mm and 0.2 mm^2 respectively.

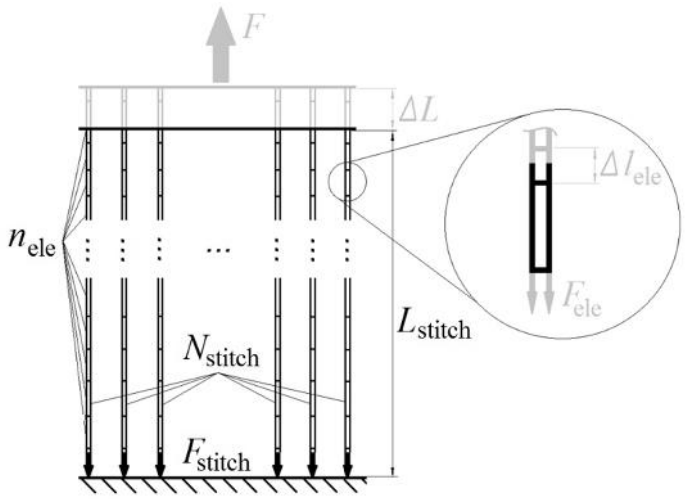

Figure 5.11 Schematic model for stitch bar elements force versus elongation characterisation

Elongation and force of a single bar element were estimated using the simple relations:

$$\Delta l_{\text{ele}} = \frac{\Delta L}{n_{\text{ele}}}, \tag{5.6}$$

$$F_{\text{ele}} = \frac{F}{N_{\text{stitch}} \cdot 2}, \tag{5.7}$$

where Δl_{ele} – bar element elongation, mm,

ΔL – crosshead displacement of the testing machine, mm,

n_{ele} – number of bar element pairs in one stitch row,

F_{ele} – force acting on a single bar element, N,

F – force measured by the testing machine, N,

N_{stitch} – number of stitch rows running in parallel.

Results of support force obtained from the simulation using an initial stitch stiffness estimation was found to be higher than the experimentally measured values given by the curve labelled ‘Sim (initial test data)’ in Figure 5.10a. This is due to neglect interaction of tows and stitches. Thus bar element stiffness had to be calibrated to account for this effect and obtain a better agreement of force versus strain diagram compared to test measurements. Calibrated results are given by the curve labelled ‘Sim (calibrated)’ in Figure 5.10a. Force versus displacement input curves for the simulation model are given in Figure 5.10b.

5.1.5 Fabric bending behaviour

A meso-scale numerical model was calibrated to experimental data from the bending test presented in section 4.1.3. It was found that tow shear stiffness G_{12} most strongly influences bending behaviour of the coupon model, since local FE directions 1 and 2 are respectively parallel to tows and perpendicular to the surface of the fabric, as shown in Figure 5.12. Thus G_{12} was used as the only parameter to calibrate the model for correct bending behaviour.

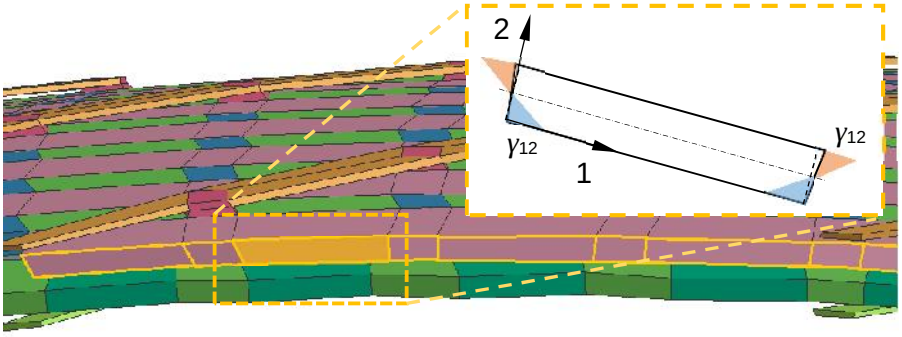

Figure 5.12 Finite element of a bent meso-scale model showing shear deformations

Table 5.1 gives details of the final assumed elastic mechanical properties for the tows. Some values ($E_{11}^{m}, E_{22}^{m}, E_{33}^{m}$) were set very small to minimise their interaction with the transverse non-linear elastic tow compaction model.

E_{11}^{f}, GPa	E_{11}^{m}, GPa	E_{22}^{m}, GPa	E_{33}^{m}, GPa	G_{12}^{m}, GPa	G_{23}^{m}, GPa	G_{13}^{m}, GPa	¬	°, kg/mm³
0.30	1.0E-5	1.0E-5	1.0E-5	0.60	0.0038	0.60	0.09	1.0E-6

Table 5.1 Tow properties for PAM-CRASH™ material model No. 30 (^{m}– matrix, ^{f} – fibre)

5.1.6 Fabric model shear test

Stitches can be characterised using either a fabric stretch test, discussed in section 5.1.4, or a picture frame test. Both approaches have been tried and found to lead to considerably different results. Figure 5.13 illustrates stitch data extracted from the two simulations of the respective tests.

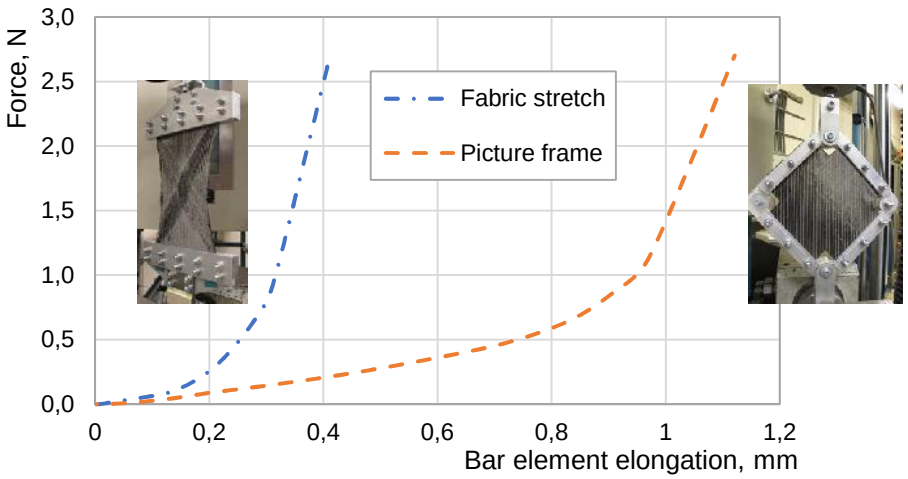

Figure 5.13 Stitch data from fabric stretch test and picture frame test

Data from the two tests were used in a representative 16.5x16.5 mm FE model of the fabric loaded in shear as shown in Figure 5.14. Individual tows were not deformed in shear (rotation DOFs at the frame edges are not constrained), thus the current meso-scale fabric model has a shear angle limit up to which it can reproduce picture frame results accurately. This limit, which depends on the width of the tows and gaps, can be calculated analytically using the equation (2.7). For the assumed tow width of 2 mm and gap width of 0.5 mm the gap is closed at 30° of shear angle. Above this limit adjacent tows come into contact and lateral jamming leads to out-of-plane wrinkling and an increase of shear stiffness due to tow lateral compaction.

Figure 5.14 shows normalised force (equation (2.16) in section 2.1.2.3) versus shear angle results from test and simulations. Simulation curves correspond to models with stitch data calibrated to picture frame test and stitch data estimated from the fabric stretch test.

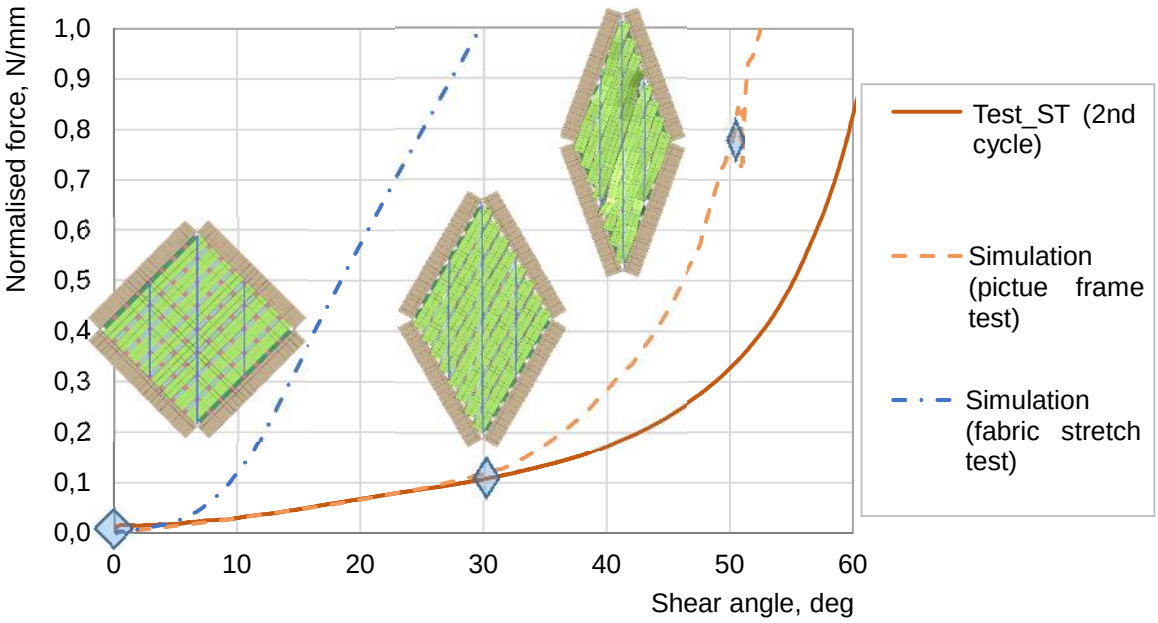

Figure 5.14 Normalised force versus shear angle from picture frame test and meso scale simulation

As can be seen from Figure 5.14 stitch data obtained from a fabric stretch test results in a much stiffer shear response when used to model the picture frame. This difference may be explained by:

- contribution of tow deformations during a stretch test, leading to overestimation of stitch stiffness,
- non-uniformity of the shear deformation field and, consequently, non-uniformity of tension loads exerted on stitches in the stretch test.

In the next section hemisphere draping simulations are presented. The effect of using stitch data obtained from both stretch and picture frame tests will be examined in more detail and compared.

5.1.7 Meso-scale hemisphere draping simulation

A hemisphere draping simulation was performed using 330x330 mm fabric model consisting of 410.000 solid elements and 21.000 stitch bar elements. The hemisphere tool and blank holders were modelled using shell elements and defined as rigid bodies. A blank holder pressure of 3.35 kPa was imposed. The fabric-to-tool, inter-ply and intra-ply friction coefficients were defined using values given in sections 4.1.4 and 5.1.3. A general view of the FE model is shown in Figure 5.15.

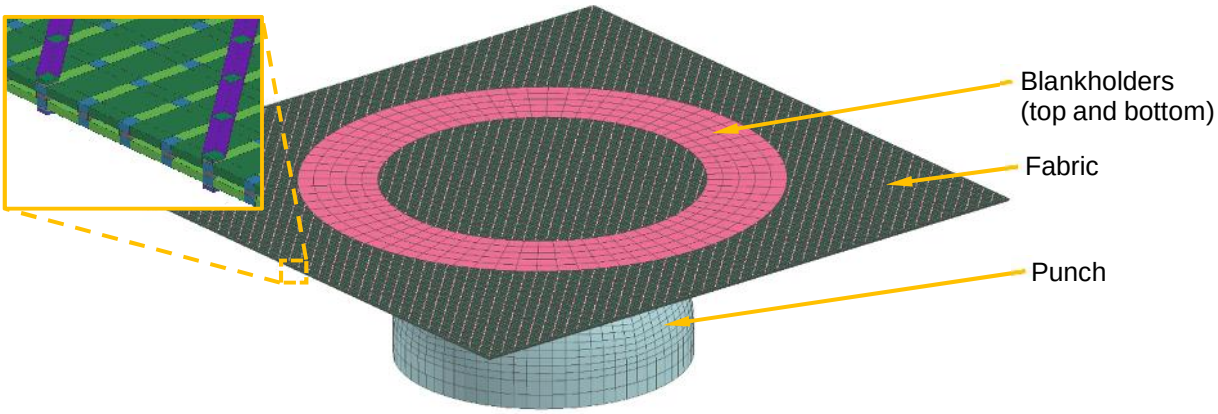

Figure 5.15 Meso-scale FE hemisphere draping simulation model

Due to the very small stable time step size (<0.1μs) of this model in the explicit FE integration method it was necessary to increase the true loading velocity to limit CPU cost. This is a common practice, however, it must be done carefully or results will be significantly influenced by the inertia (mass) effects. Analyses with different loading rates have shown that a punch velocity of 2.5 mm/ms gives only small inertia forces with deformations largely controlled by element internal forces. Results of punch contact force versus punch displacement for punch velocities of 1.0 mm/ms, 2.5 mm/ms and 5.0 mm/ms are shown in Figure 5.16. These simulations required 16, 8 and 4 hours, respectively, on a 16 processor 2.53 GHz machine.

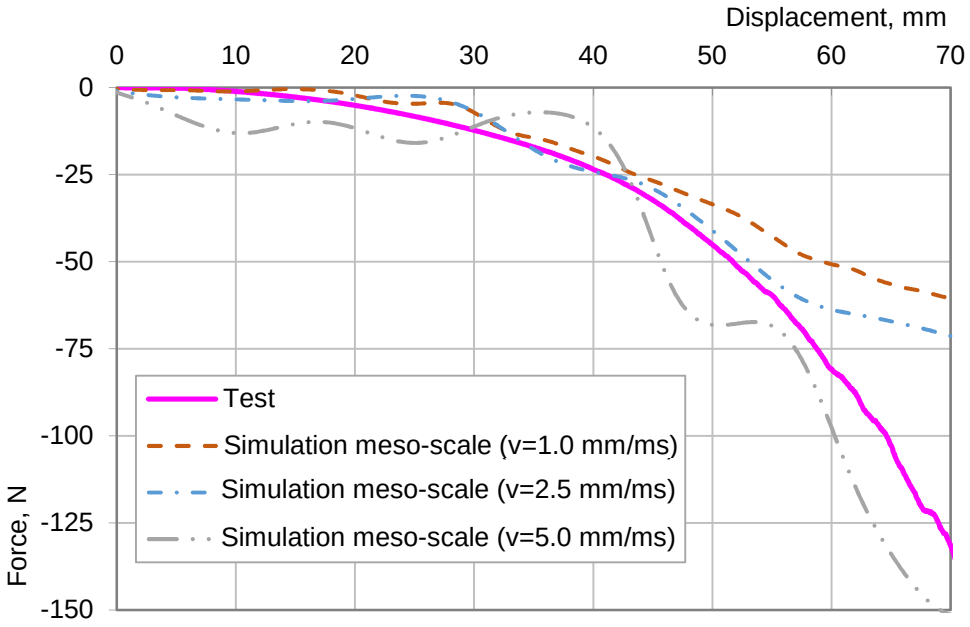

Figure 5.16 Hemisphere draping force versus displacement diagrams from test and simulations (stitch data from fabric stretch test)

Hemisphere draping simulation results obtained using stitch data from fabric stretch and picture frame tests differ slightly. Figure 5.17 shows comparison of force acting on a hemisphere during the test and the two numerical analysis results. Simulation using picture frame stitch data underestimates reaction force slightly compared to the simulation using stitch data from a fabric stretch test.

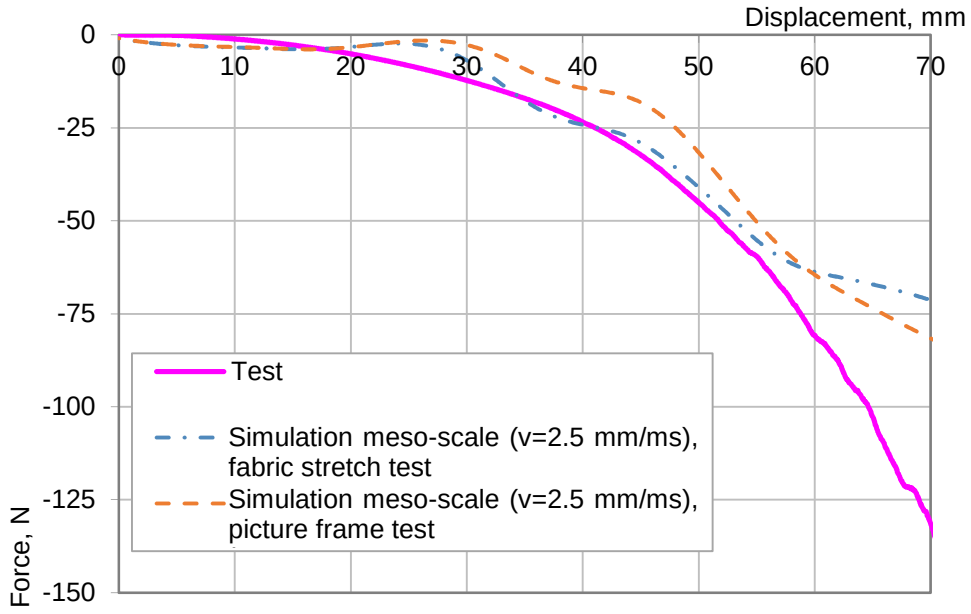

Figure 5.17 Hemisphere draping force versus displacement diagrams from test and simulations (stitch data from fabric stretch and picture frame tests)

A qualitative comparison of draped hemispheres from test and simulation is shown in Figure 5.18; in the areas where tows undergo lengthwise compaction localised buckling can be observed both in test and simulation. A quantitative comparison of shear angles is given in Figure 5.19.

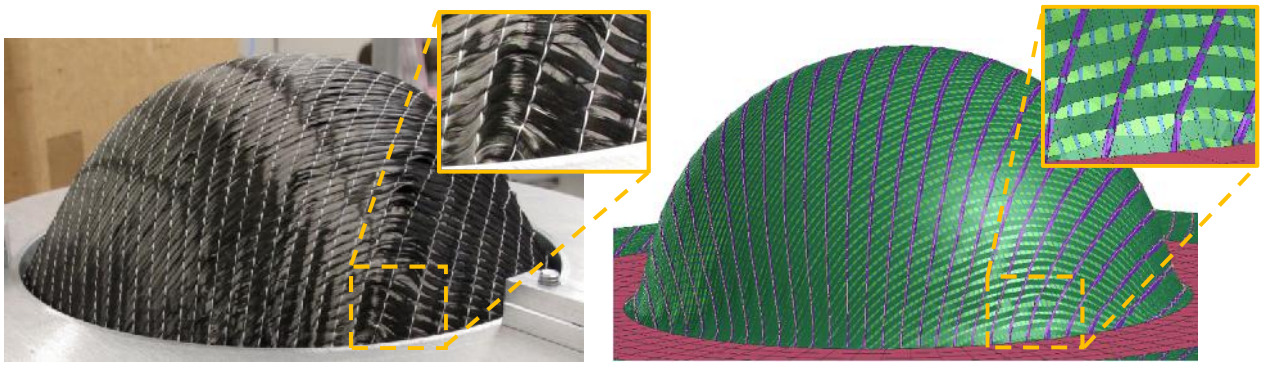

(a) (b)

Figure 5.18 View of final draping results: a) test and b) simulation

A detailed study of shear angles has found that stitch properties do influence shear angle results. Stiffer stitch elements hinders shear deformation in 'positive' shear angle quadrants of the hemisphere, as shown by the curve labelled 'Simulation meso-scale, fabric stretch test' in Figure 5.19. Hemisphere simulation using lower stiffness stitch data obtained from picture frame test provides better shear angle prediction in 'positive' shear angle regions where stitches are loaded in tension, as shown by the curve labelled 'Simulation meso-scale, picture frame test' in Figure 5.19. These results suggest that complex interaction between tows and stitch needs to be addressed more carefully. Possible causes for poor simulation results and measures to improve the model will be discussed in the discussion and future work chapters of this thesis.

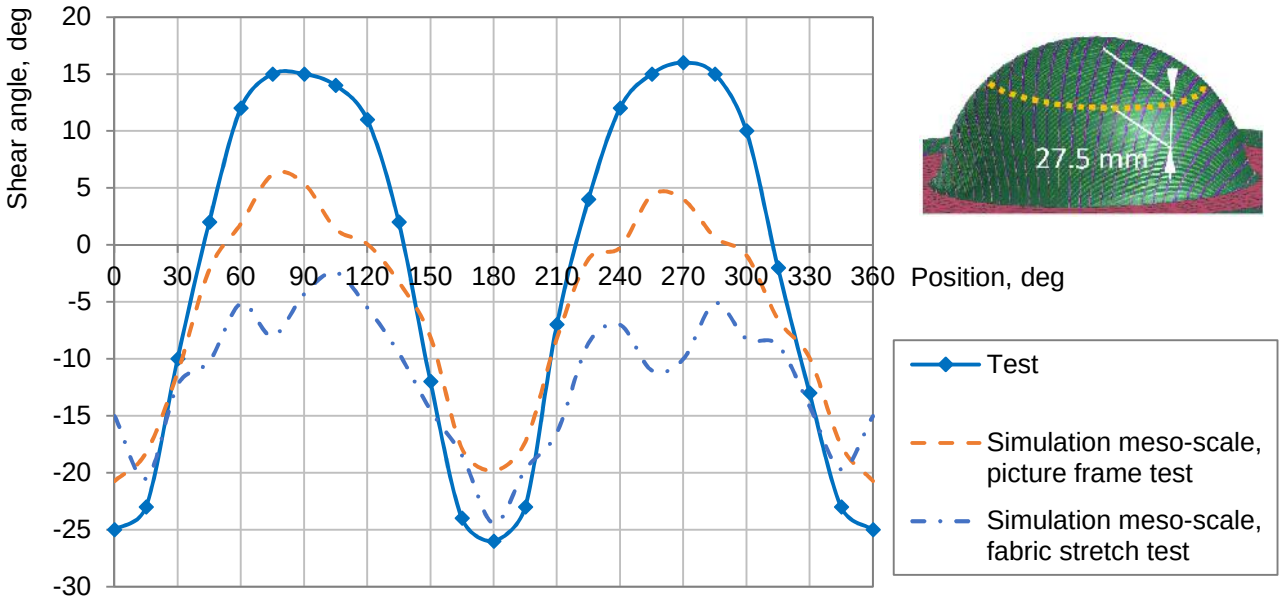

Figure 5.19 Shear angle distribution over the circumference of the hemisphere from test and simulations with different stitch properties

5.2 Meso-scale fabric model permeability estimation

The main mesoscopic irregularity in NCF is created by the stitching pattern which has an important impact on permeability ([171], [263]). A regular structure of the model should possess average permeability parameters which would lead to adequate representation of the infiltration process. Tow permeability is assumed to be represented by UD NCF permeability due to the similar dense fibre filament spacing in a tow (tests in sections 3.1.2 and 3.2.1). Inter-tow gaps are smaller in the physical fabric compared to the numerical model and have varying cross section area as can be seen in Figure 5.22a. Thus a gap element permeability is first estimated analytically and then calibrated numerically to fit the flow propagation observed in an unsheared fabric radial infusion test. Permeability of stitch elements is also estimated numerically, since no direct measurement is possible.

5.2.1 Unsheared meso-scale fabric model permeability estimation

As described in section 5.1.1, the fabric FE infusion model is divided into three distinct zones; namely, tow, gap and stitch elements. These zones are shown in Figure 5.20 where tow zone elements have principal permeability directions defined in element coordinate frame to assign orthotropic permeability values. Stitch and gap permeabilities are considered to be isotropic.

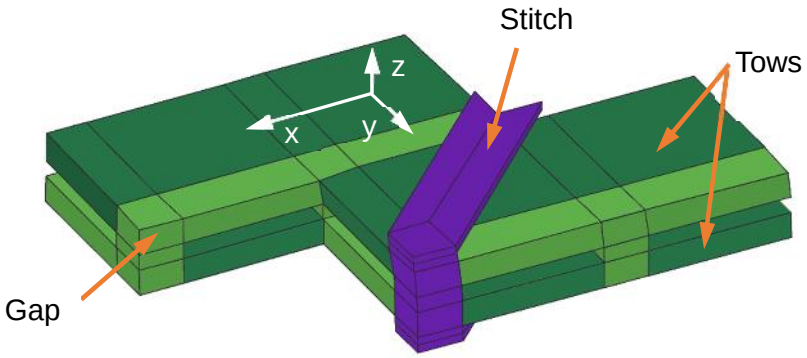

Figure 5.20 Zones in fabric FE model for infusion simulation

The through-thickness permeability of the tow elements is estimated numerically using a simulation of the UD NCF test from section 3.2.1. A FE model of the infusion specimen section was created in PAM-RTM [247] with boundary conditions resembling the test configuration, as shown in Figure 5.21a. With in-plane permeability of the fabric known (section 3.1.2), K_{zz} was chosen to provide an agreement of flow on top and on bottom of the preform (Figure 5.21b). This calibration led to a value of K_{zz} =3.0E-15 m^2 for through thickness permeability.

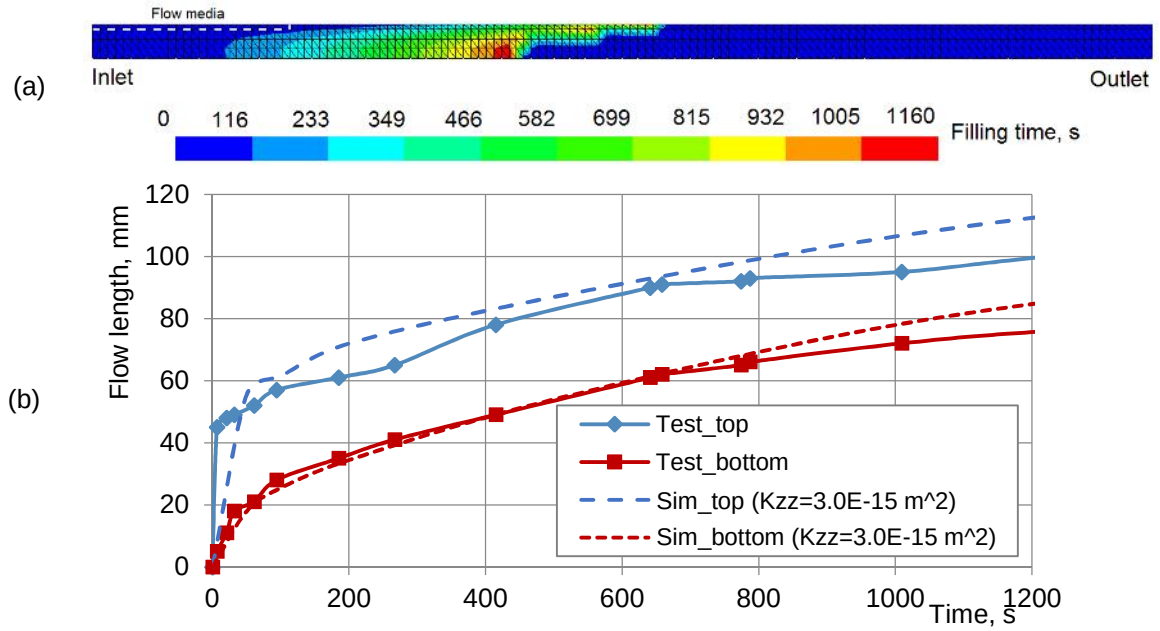

Figure 5.21 UD NCF through-thickness permeability estimation: a) simulation model and b) flow length versus time diagrams from test and simulation

Gap elements permeability was estimated analytically and then calibrated numerically. Rectangular cross section gaps may exhibit higher permeability (up to a factor of 3.7) compared to gaps of the same area but having a more realistic lenticular shape [116], however, due to the scale of the model with only one element through the tow cross section and for simplicity reasons gaps were assumed to have a rectangular cross section with calibration of the permeability for the correct flow behaviour.

The permeability of the gap elements was first quantified analytically using the rule of mixtures (equation (5.8)). The size of the macro-channels cross section area was estimated from the section micrograph of the $(0/90)_{12}$ laminate as shown in Figure 5.22a. From a false colour image in Figure 5.22b the gaps cross section area was estimated to be about 5%. Since no more views were available it was assumed that 0° plies, parallel to the plane of the section, occupies half of the image area. Therefore the gap volume fraction in a single ply is estimated to be 10%.

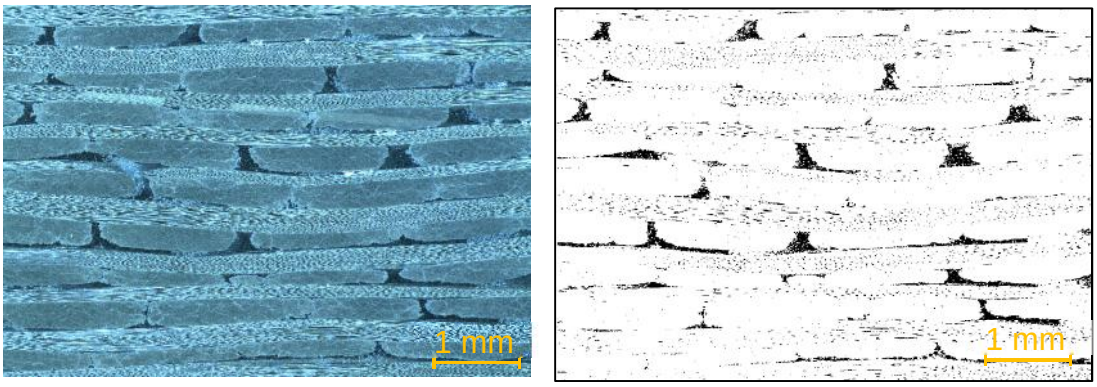

(a) (b)

Figure 5.22 Cross section of biaxial NCF $(0/90)_{12}$: a) micrograph and b) approximate gaps cross section area

Gap permeability is estimated by applying an equivalent permeability equation from [264]:

$$K_{\text{gap}} = \frac{K_{\text{xx\_fabric}} \cdot V_{\text{f\_fabric}} - K_{\text{xx\_tow}} \cdot V_{\text{f\_tow}}}{V_{\text{f\_gap}}}, \tag{5.8}$$

where $K_{\text{xx\_fabric}}$ – fabric permeability, m^2,

$V_{\text{f\_fabric}}$ – fabric fibre volume fraction,

$V_{\text{f\_tow}}$ – tow volume fraction in a ply,

$K_{\text{xx\_tow}}$ – tow permeability, m^2,

$V_{\text{f\_gap}}$ – gap volume fraction in a ply.

With biaxial NCF permeability data from section 3.1.1, tow permeability data from section 3.1.2, and tow-gap volume ratios, the gap permeability in a physical fabric is estimated as:

$$K_{\text{gap\_fabric}} = \frac{1.51 \cdot 10^{-11} \cdot 1.0 - 3.60 \cdot 10^{-12} \cdot 0.90}{0.10} = 1.19 \cdot 10^{-10} (\text{m}^2). \tag{5.9}$$

An equivalent gap permeability estimation for the numerical model yielded a lower value (-58%) due to a larger gap-to-tow elements volume (cross section) ratio in the model:

$$K_{\text{gap\_model}} = \frac{1.51 \cdot 10^{-11} \cdot 1.0 - 3.60 \cdot 10^{-12} \cdot 0.75}{0.25} = 4.96 \cdot 10^{-11} (\text{m}^2). \tag{5.10}$$

Fabric in-plane permeabilities K_{xx} and K_{yy} are indirectly coupled by the intra-ply elements and stitch elements which connect perpendicular gap rows in the two adjacent plies as shown in Figure 5.23. Thus, flow along the x-axis direction in the lower ply contributes to flow along the y-axis direction in the upper ply.

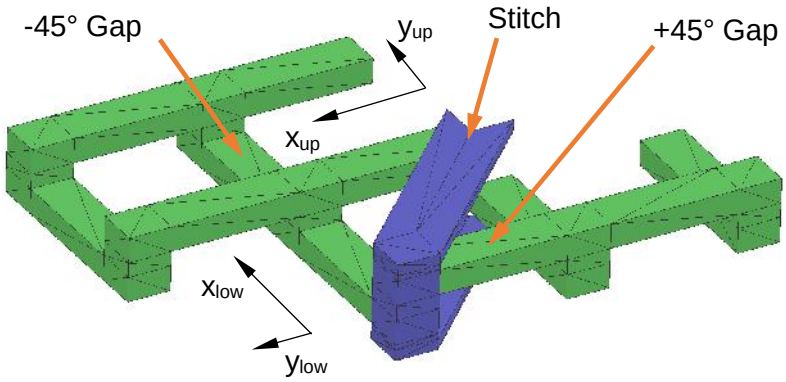

Figure 5.23 Gap and stitch elements in a biaxial NCF unit cell

From hemisphere infusion test results in section 4.3 (Figure 4.18) it was found that moderate flow front advance occurred along the stitches. Therefore a radial infusion test on a single layer of fabric

is performed in order to estimate stitch element permeability in the FE model as shown in Figure 5.24b. The model parameters have been determined in the following order:

1. tow in-plane permeability was set according to data in section 3.2.1; through-thickness permeability was estimated as shown in Figure 5.21, and initial gap permeability K_{gap_model} set equal to 4.96E-11 m^2 as estimated using equation (5.10);
2. stitch element permeability was calibrated to obtain agreement of flow front propagation in the stitch direction corresponding to data points 'Test_x' in Figure 5.24b: K_{stitch}=1.0E-10 m^2;
3. initial gap element permeability was adjusted to obtain agreement with test flow front in the direction perpendicular to the stitch and corresponding to data points 'Test_y' in Figure 5.24b: K_{gap_model} =4.96E-11 m^2 → K_{gap_model} =2.0E-11 m^2;
4. a slight adjustment of stitch permeability was necessary due to flow coupling through the gap elements: K_{stitch}=1.0E-10 m^2 → K_{stitch}=1.2E-10 m^2.

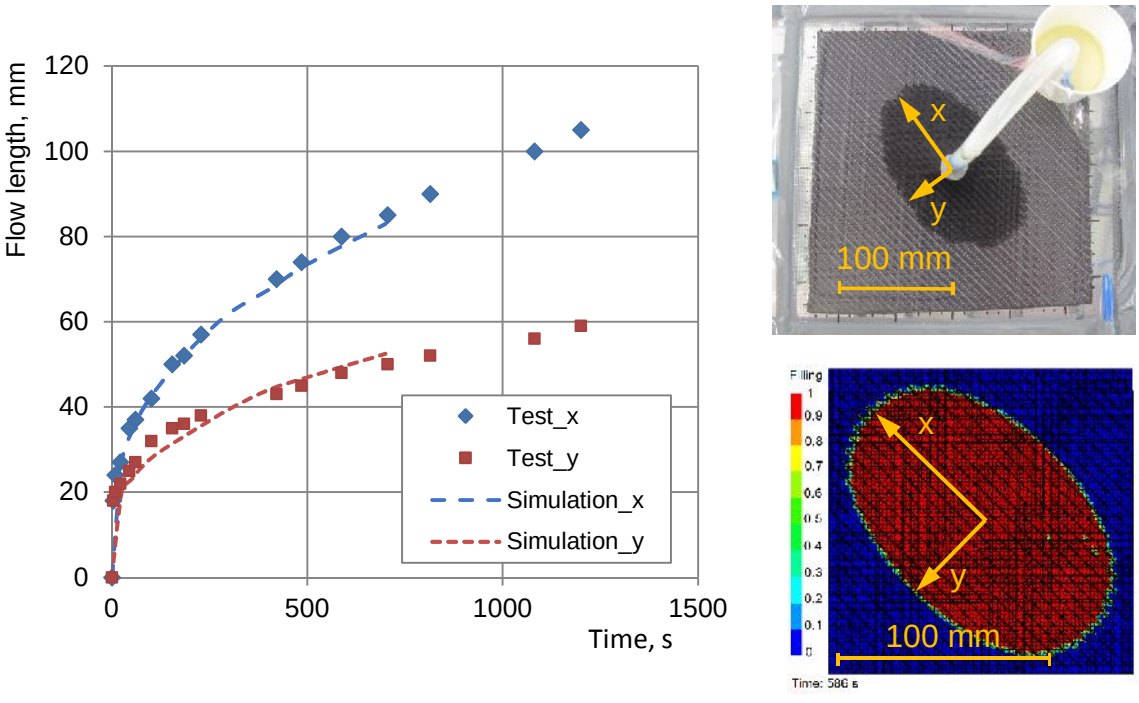

(a) (b)

Figure 5.24 Radial infusion test and calibrated simulation: a) flow length versus time diagram and b) test and simulation model states at 586 s

A summary of permeability data for biaxial NCF with chain stitch fabric model is given in Table 5.2.

Fabric constituent	K_{xx}, m²	K_{yy}, m²	K_{zz}, m²	Remarks
Tow	3.60E-12	1.48E-12	3.00E-15	Test (section 3.1.2) and numerical estimation
Gap	2.0E-11			Numerical calibration
Stitch	1.2E-10			Numerical calibration

Table 5.2 Permeability data used for the meso-scale infusion simulation model (unsheared)

5.2.2 Sheared meso-scale fabric model permeability estimation

As a partial validation of the fabric infusion model, before its application to the hemisphere analysis in section 5.3, tests and simulations were performed on a flat sheared biaxial NCF sheets. Fabric specimens were sheared to +15° and -25° as shown in Figure 5.25. In the first case the stitches are stretched, whereas in the second case stitches are compressed. Corresponding FE models of sheared fabric are shown in Figure 5.26, which were obtained by simulating picture frame shear process in PAM-CRASH [262].

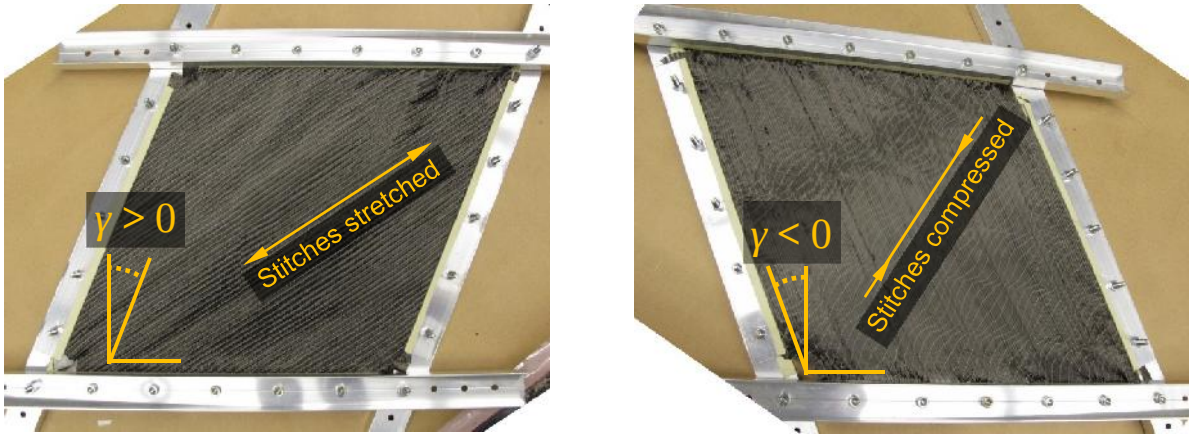

(a) (b)

Figure 5.25 Sheared biaxial NCF: a) stitches stretched and b) stitches compressed

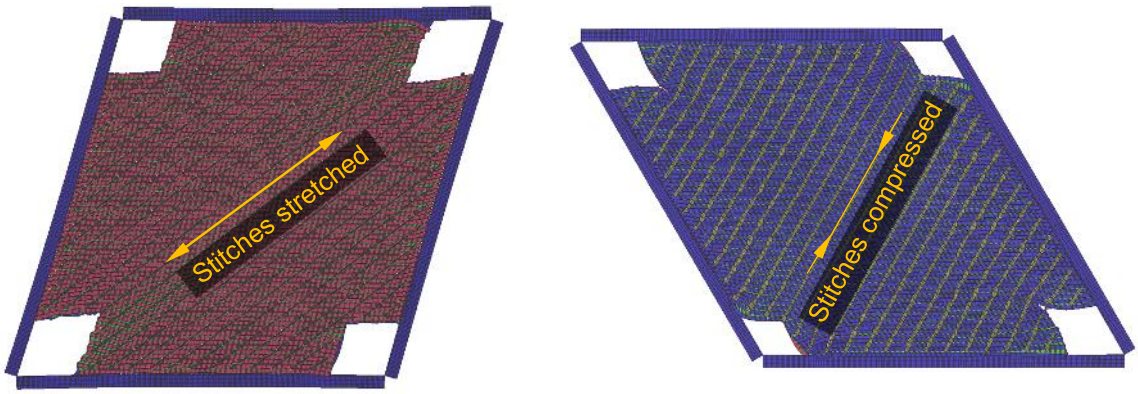

(a) (b)

Figure 5.26 FE models of sheared biaxial NCF: a) stitches stretched and b) stitches compressed

Figure 5.27 shows radial infusion tests and simulations of the sheared fabric specimens. In the case of +15° shear angle with stitches stretched flow in the gaps contributes to the flow in the stitches direction (Figure 5.28b) and an elliptical flow front is obtained as shown in Figure 5.27a. In the case of -25° shear angle with stitches compressed, the angle of the tow relative to the stitches increases (Figure 5.28c) resulting in nearly round shape of the flow front propagation (Figure 5.27b).

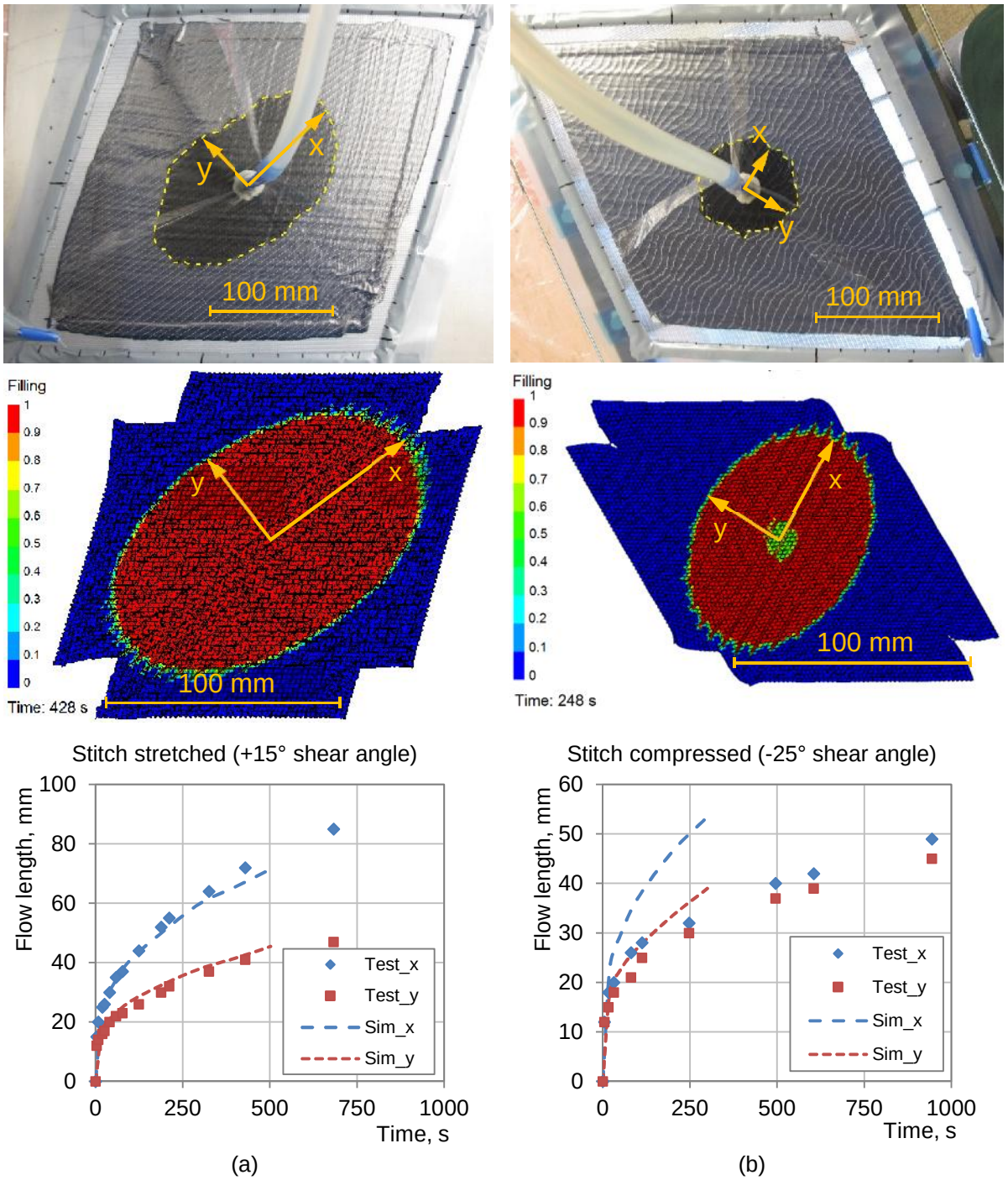

Figure 5.27 Sheared biaxial NCF radial infusion tests and simulations: a) +15° and b) -25° shear cases

Closer investigations of sheared models made inherent change of some geometrical model parameters under shear deformation apparent, as illustrated in Figure 5.28. Due to deformation of

fabric model the cross section area of the stitches reduces by about 30% when the model is sheared to +15° and increases by about 75% when the model is sheared to -25°. In both cases gap cross section area reduces by about 4% and 10% respectively.

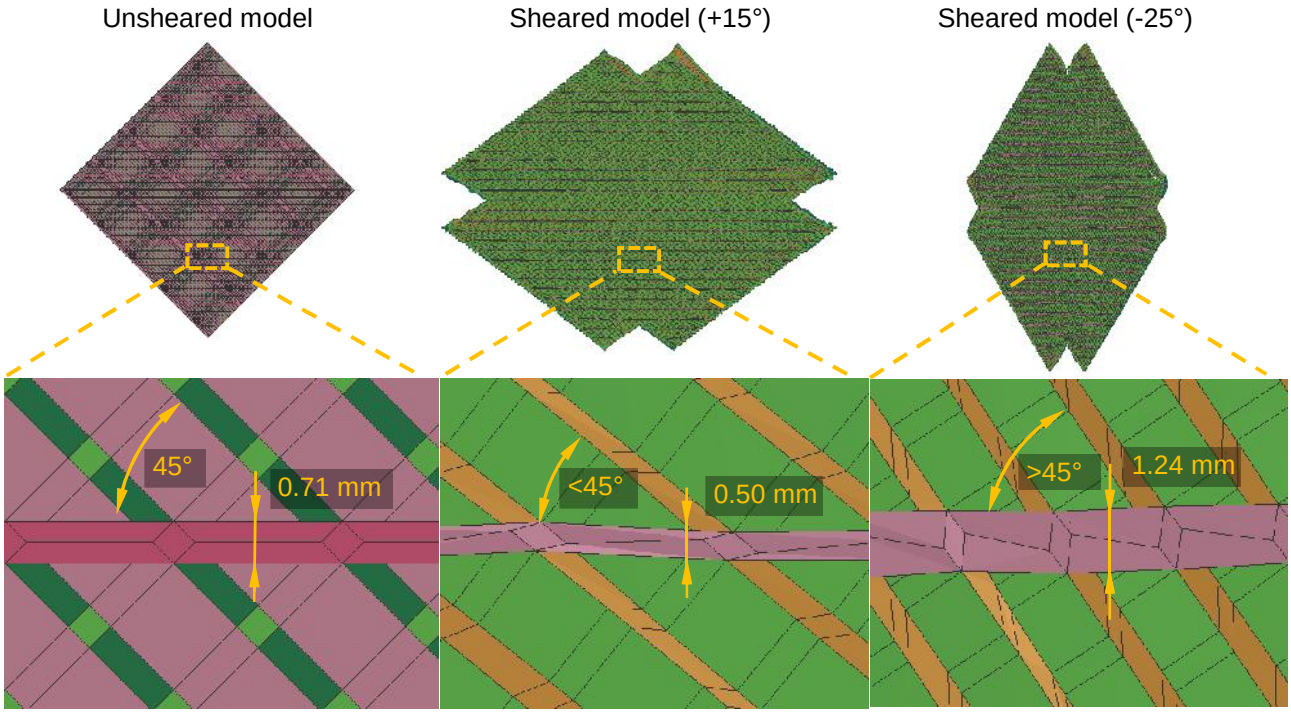

Figure 5.28 Stitch width measured on a) unsheared, b) sheared to +15° and c) sheared to -25° fabric models

Changes in stitch and gap dimensions inevitably modify the flow behaviour for the numerical model of sheared fabric. Figure 5.27a shows slightly slower predicted flow along the stitch direction in the +15° shear model where the stitch cross section area is reduced. For the -25° shear model the increase of stitch cross section area leads to much faster flow along the stitches as can be seen in Figure 5.27b.

It has to be noted that these tests have been performed in series using the same resin mix which resulted in resin viscosity change in the relevant time span of about 1.5 hours (Figure 5.29). This could partially explain the generally slower flow front propagation for the -25° specimen infusion test case (Figure 5.27b). However, viscosity change has been taken into account in the simulations, and it is not responsible for the difference in resin flow front shape observed for the two cases.

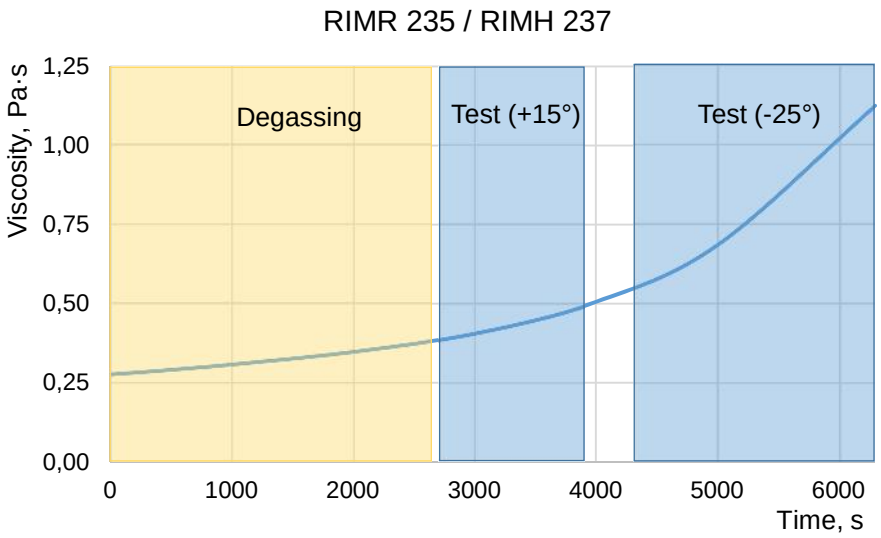

Figure 5.29 Resin viscosity versus time diagram for sheared fabric infusion tests

A new calibration was thus performed to obtain stitch and gap permeabilities (Table 5.3) for improved simulation results for the fabric specimen sheared to -25° (Figure 5.30).

Fabric constituent	K_{xx}, m²	K_{yy}, m²	K_{zz}, m²	Remarks
Tow	3.60E-12	1.48E-12	3.00E-15	Test (sections 3.1.2, 3.2.1) and numerical estimation
Gap	2.0E-11 → 0.70E-11 (-65%)			Re-calibration
Stitch	1.2E-10 → 0.20E-10 (-83%)			Re-calibration

Table 5.3 Permeability data used for meso-scale infusion simulation model sheared to -25°

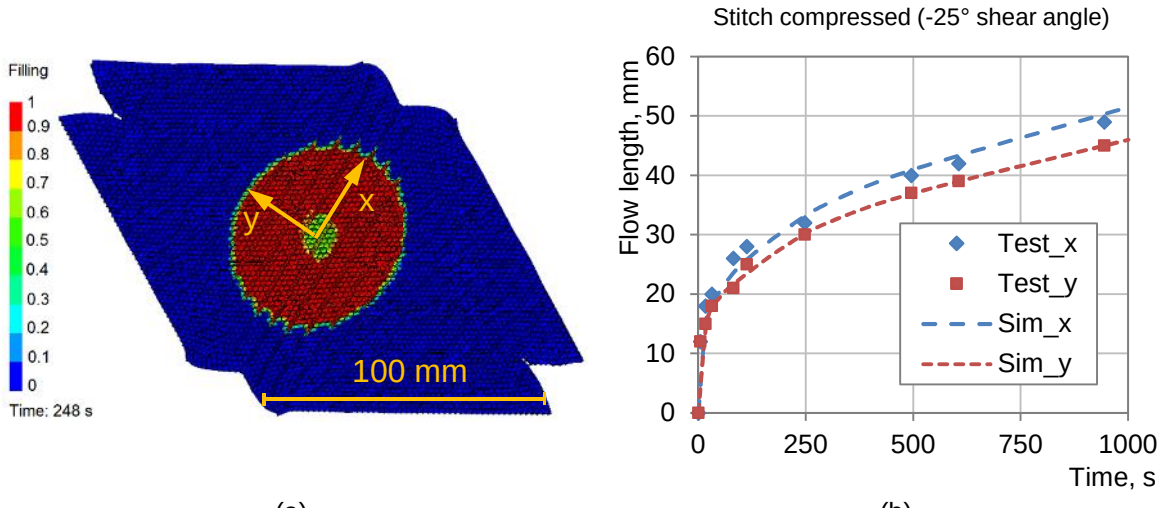

(a) (b)

Figure 5.30 Sheared (-25°) biaxial NCF re-calibrated infusion simulation: a) flow front at 248 s and b) flow length versus time diagrams

It can be concluded that due to shear deformation fabric model dimensions change and significantly modify the overall flow behaviour. Permeability values estimated from an unsheared fabric tests are thus not valid for the sheared model. Stitch plays an important role in the model flow behaviour especially if it is compressed and its cross section area increases considerably.

5.3 Hemisphere infusion simulation at meso-scale

Some details on the hemisphere infusion test are given in section 4.3, with the same flow front view image repeated here in Figure 5.31a. The draped mesh from the meso-scale hemisphere analysis in section 5.1.7 is directly used here for an infusion simulation study with the PAM-RTM software [247]. The model consist of about 450.000 tetrahedral elements. Tow, gap and stitch permeabilities (Table 5.2) were assigned to corresponding elements, together with orthotropic directions of the fibres. Since stitching is loaded in tension over most of the upper hemisphere area, no differentiation regarding permeability values with respect to change of stitch geometry (increase of cross section area) was performed.

The macro-scale hemisphere infusion simulation used similar test setup to that presented in section 4.3, with resin inlet defined at the top of the hemisphere (atmospheric pressure) and vacuum at the outlet around the periphery (0 kPa). Figure 5.31 shows a qualitative comparison of the test and simulation results for infusion state at 23 minutes. The simulation is seen to give promising results and does correctly predict orthotropic flow with principal permeability direction along the stitches.

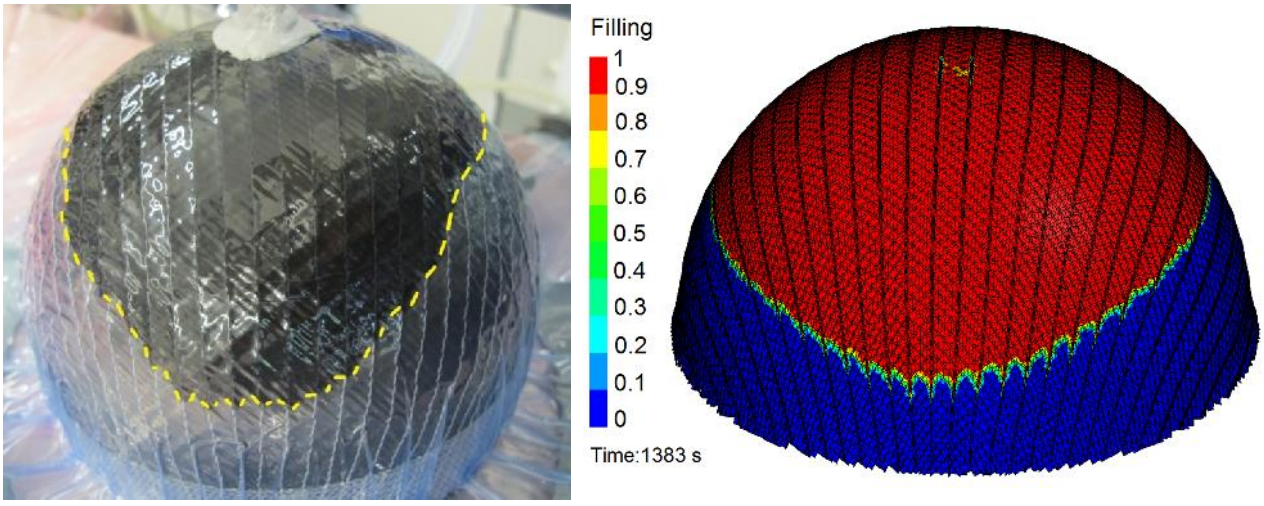

(a) (b)

Figure 5.31 Hemisphere infusion views at 23 min: a) test and b) meso-scale simulation

5.4 Summary of meso-scale draping an infusion simulation

A meso-scale finite element modelling approach for biaxial non-crimp fabric coupled drape-infusion simulation was developed, presented and validated in this chapter. A unit cell model consisting of tow, gap and stitch elements was introduced together with tests for all necessary mechanical properties characterisation. The tow material model was constructed by combining two models, readily available in PAM-CRASH [262] simulation package, to model the stiff fibres (longitudinal response) with a non-linear compaction model for correct transverse deformation response. This combined model was then calibrated against through-thickness compaction, shear and bending tests; also, intra-ply, inter-ply and ply-to-tool friction data was defined. Stitches were treated as bar elements whose mechanical properties were found to be important for correct shear deformation behaviour and had to be calibrated against the test data. Validation of the numerical model using a hemisphere draping test showed good agreement considering punch force. The model also reproduced local tow buckling which was observed experimentally in the regions of tow lengthwise compression. Predicted shear angle distribution along the circumference of the hemisphere was, however, poor compared to the test measurements. Relative movement of tows in upper and lower plies is mostly influenced by stitch properties, thus complex interaction between the fabric constituents (stitch-tow interaction) requires further research.

Coupling of the drape and infusion simulation was successfully made. The infusion model required tow, gap and stitch permeabilities to be measured or estimated. Tow properties were obtained from test measurements, gap and stitch permeabilities were estimated from analytical models and then improved by numerical calibration. Once calibrated the undeformed model is capable to recreate test results, but additional permeability calibration may be needed for the sheared fabric model. The geometry of the model constituents such as cross section area of gaps and stitches changes during shear deformation, thus permeability parameters need to be adjusted accordingly. Draped hemisphere infusion simulation, however, yielded good results close to experimental observations, because geometrical changes of fabric structure in the infused region were small.

The possibility to control many model parameters increases overall complexity of the simulation, but also provides advantages over simpler macro-scale modelling approaches. Inclusion of important fabric structure features such as stitches provides advantages for phenomenological modelling. Generally, the presented numerical model has provided promising results which can serve as a basis for further research.

6 LRI process simulation at macro-scale

Liquid resin infusion under vacuum and flexible membrane is another example where fabric deformations influence permeability. In this case main deformation mode is through-thickness compaction, rather than shear. LRI differs in many aspects from infusion in a rigid mould and requires a dedicated simulation approach. In this chapter commercial simulation package PAM-RTM [247] will be used to simulate VARI type process at the macro-scale to illustrate some limitations of commercial tools for this type of analysis. Additionally, infusion simulation will be made using a dedicated in-house code from [230] which is able to take into account specific features of vacuum infusion under flexible membrane and correctly represent phenomena such as preform relaxation and non-linear pressure field.

Several strategies will be applied to obtain preform permeability versus compliance data, which can be done either directly using compaction testing, or indirectly by employing DIC measurements during infusion combined with numerical analysis. Important observations will be made regarding modelling of flow in distribution medium and it will be shown that DM permeability is orthotropic at the considered macroscopic scale.

6.1 Demonstrator tests

A demonstrator representing one module of an aircraft structure, consisting of a stiffened panel with four C-stringers is used for these investigations. The component demonstrator is shown in Figure 6.1 where the central part is stiffened with a foam core and small L-profiles that support the C-stringers at the edges of the panel. A schematic cross section of the assembly and infusion configuration are shown in Figure 6.2.

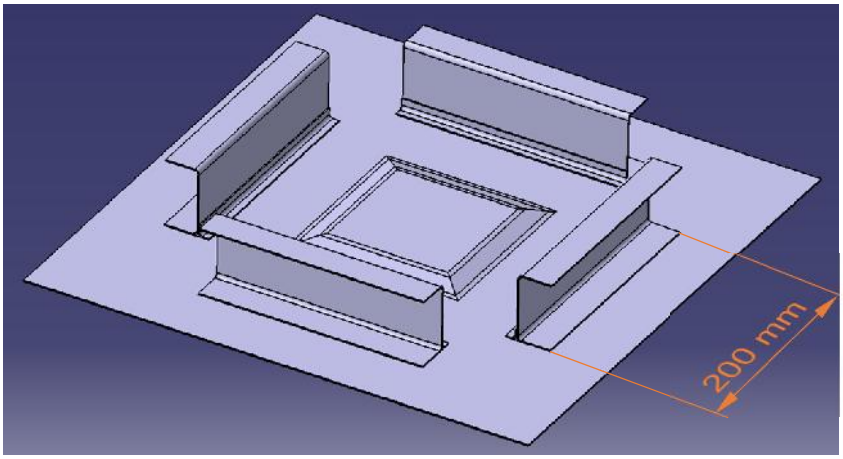

Figure 6.1 Demonstrator model

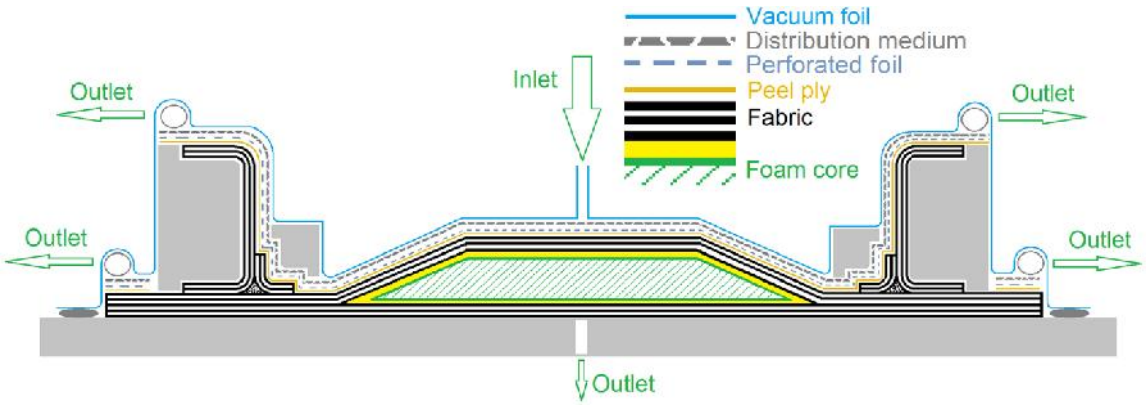

Figure 6.2 Schematic cross section of the demonstrator infusion setup

A quasi-unidirectional fabric G1157 D1300 [253] was used to build the part with a stack of +45/-45/-45/+45 plies forming the base on which foam core was placed with another 4 similar plies on top. C-stringers and L-profiles were also formed from 4 fabric plies in the same layup as the base. Supporting caul plates for stringers were made of transparent Plexiglas blocks allowing visual observation of the resin flow. Two infusion configurations that differed in placement of distribution medium were considered in these studies:

- setup I, where the whole surface area of the part was covered with DM;
- setup II, where DM was selectively removed from C-stringers and around the perimeter of the part to limit the outflow of resin.

The part was infused using RIMR-235 epoxy resin with RIMH-237 hardener, with a vacuum pressure of 230 kPa at outlets and atmospheric pressure at the inlet. Infusion tests for the two configurations are presented in the following sections.

6.1.1 Setup I

The whole surface of setup I demonstrator was covered with distribution medium, except for the inner side of the C-stringers. Views of the infusion test views are depicted in Figure 6.3. The resin flow front advanced rapidly in the distribution medium and penetrated through the fabric layup thickness. In about 300 s the base panel was filled with the complete part, including the C-stringers, filling in about 800 s.

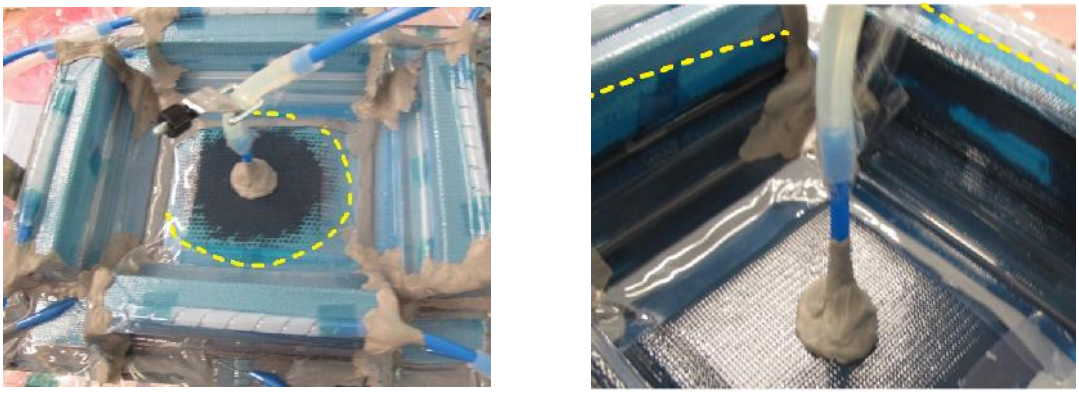

a) 17 s b) 241 s

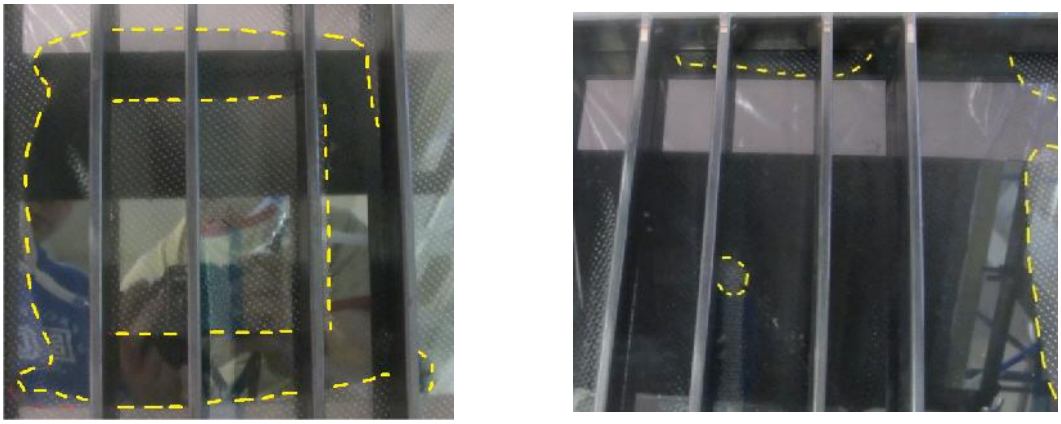

c) 317 s d) 776 s

Figure 6.3 Demonstrator (setup I) infusion test views with corresponding filling times

After the part was demoulded it was inspected for any infusion defects. It was noted there were some dry spots on the bases and corner radii of the C-stringers (Figure 6.4a and Figure 6.4b) and resin-free areas on the panel under the stringers (Figure 6.4c). These infusion defects have formed due to non-ideal placement of the distribution medium and imperfections of setup preparation leading to racetracking along the edges of the caul plates. Dry areas on the base panel formed due to convergent flow around the C-stringers. The infusion setup was modified to avoid these defects and the test repeated in setup II.

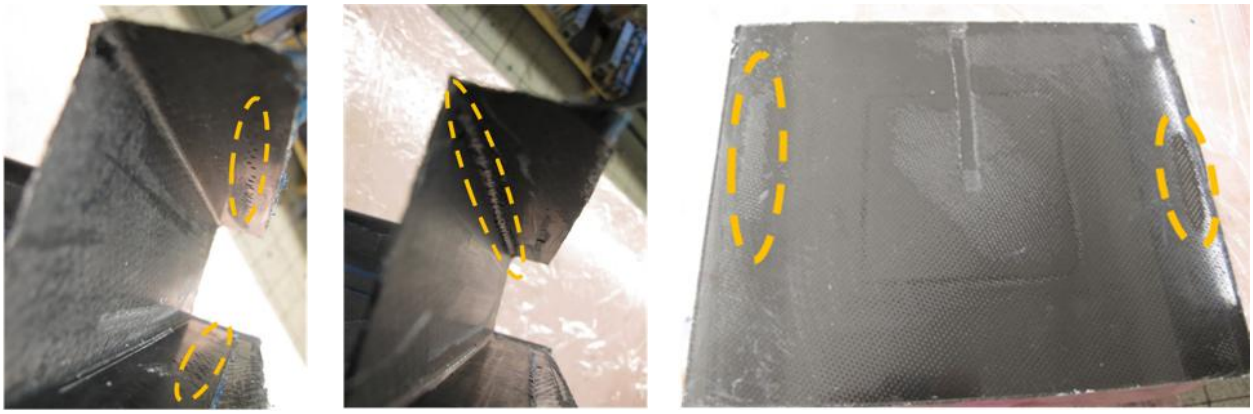

(a) (b) (c)

Figure 6.4 Defects on the cured part (setup I): a) C-stringer, b) corner radius of the C-stringer and c) base panel

6.1.2 Setup II

Modification of the original infusion setup included partial removal of the distribution medium from the C-stringers and the base panel as can be seen in Figure 6.5a. The resin outflow from the stringers has been slowed allowing more time for resin to penetrate in the though-thickness direction. Convergent flow patterns around the C-stringers were avoided by removing the distribution medium around the perimeter of the part. Modified infusion test views are given in Figure 6.5.

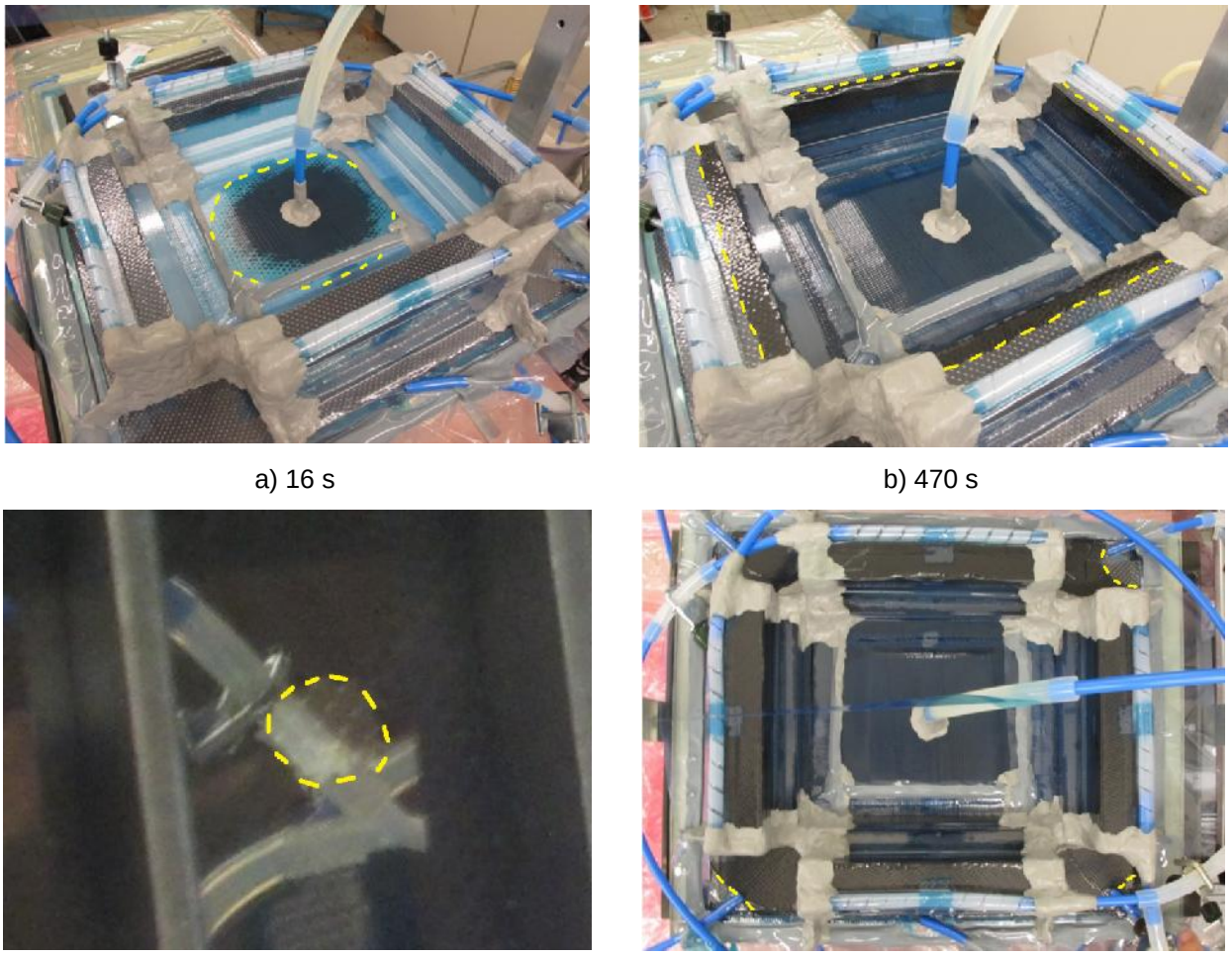

a) 16 s b) 470 s

c) 655 s d) 875 s

Figure 6.5 Demonstrator (setup II) infusion test views with corresponding filling times

The new infusion setup resulted in slightly longer infusion time (875 s), but the previously observed defects were eliminated (Figure 6.6). Both demonstrator infusion test configurations will be compared to the infusion simulations using the commercial software PAM-RTM [247] and the dedicated VARI process simulation code developed at IFB.

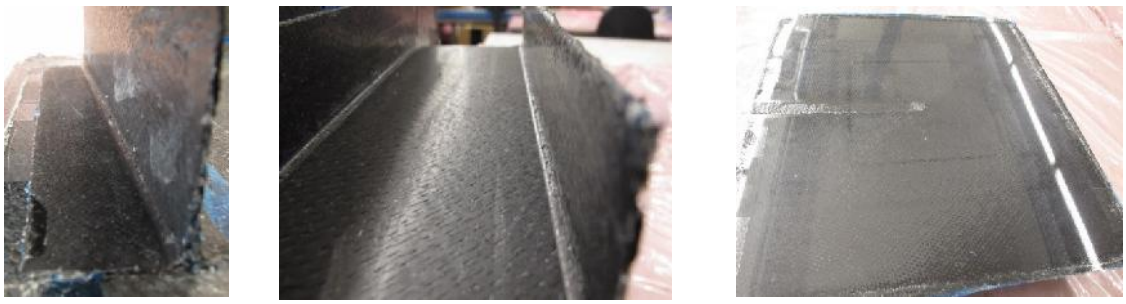

(a) (b) (c)

Figure 6.6 Views of cured part (setup II): a) C-stringer, b) corner of the C-stringer and c) base panel

6.2 RTM process simulation (PAM-RTM)

Infusion simulations using PAM-RTM software [247], which is designed for the RTM process simulation, were performed for the demonstrator under setup I and II conditions. Current PAM-RTM capabilities of VARI process simulation are limited to plain 2D analysis and thus cannot describe the 3D through-thickness flow that occurs in the infusion tests. Nevertheless, it was felt important to investigate how infusion test and simulation results compare using different simulation approaches.

A finite element model of one quarter of the demonstrator consisting of 600.000 tetrahedral elements was created using one finite element per ply thickness as illustrated in Figure 6.7. Principal permeability directions, inlet, outlet ports and pressure boundary conditions were set in accordance with the test setup. Materials permeability data from chapter 3 was used as summarised in Table 6.1.

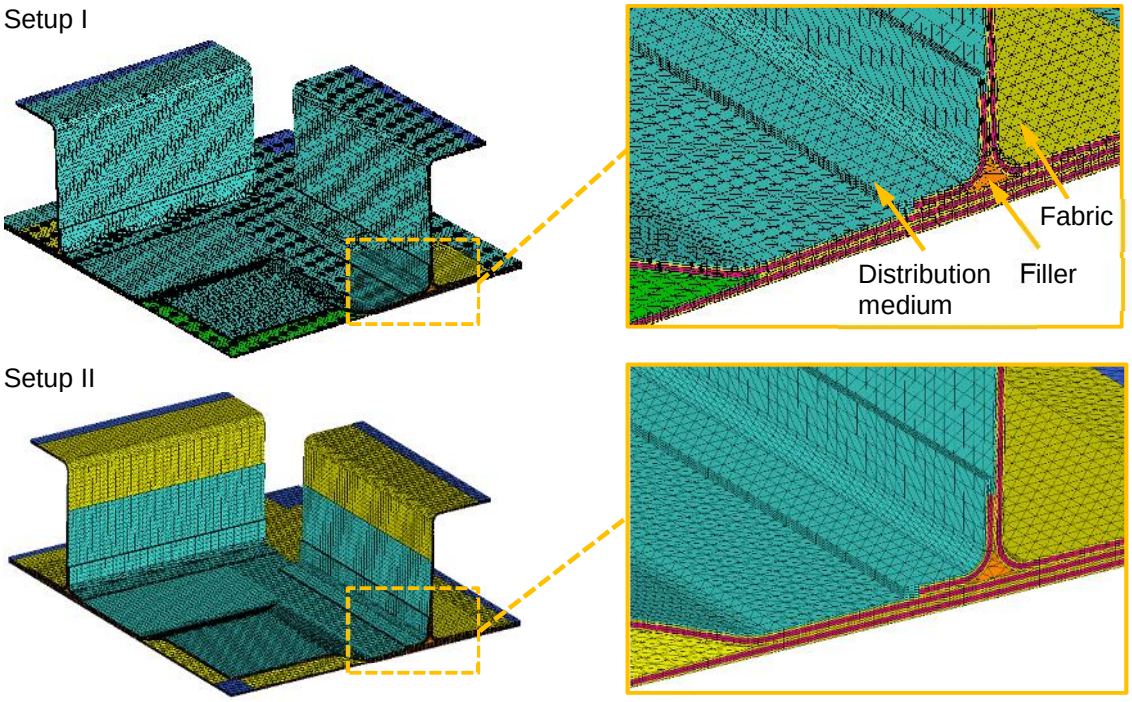

Figure 6.7 Setup I and II of the FE simulation model

Material	K_{xx} , m²	K_{yy} , m²	K_{zz} , m²
Fabric (quasi-UD G1157 D1300)	2.11E-11	3.08E-12	4.93E-13
Filler (UD NCF)	3.60E-12	1.48E-12	3.00E-15
Distribution medium	4.30E-10		

Table 6.1 Permeability data for demonstrator infusion simulation using PAM-RTM

Views of the resin flow from test and simulation using PAM-RTM for setup I and II are presented in Figure 6.8 and Figure 6.9 respectively. Simulation results differ significantly from the experimental observations with final filling times from the simulations, for both setups, found to be a factor of 8-10 times longer than in the corresponding experiments. The flow front propagation pattern, however, did show a generally good agreement to tests.

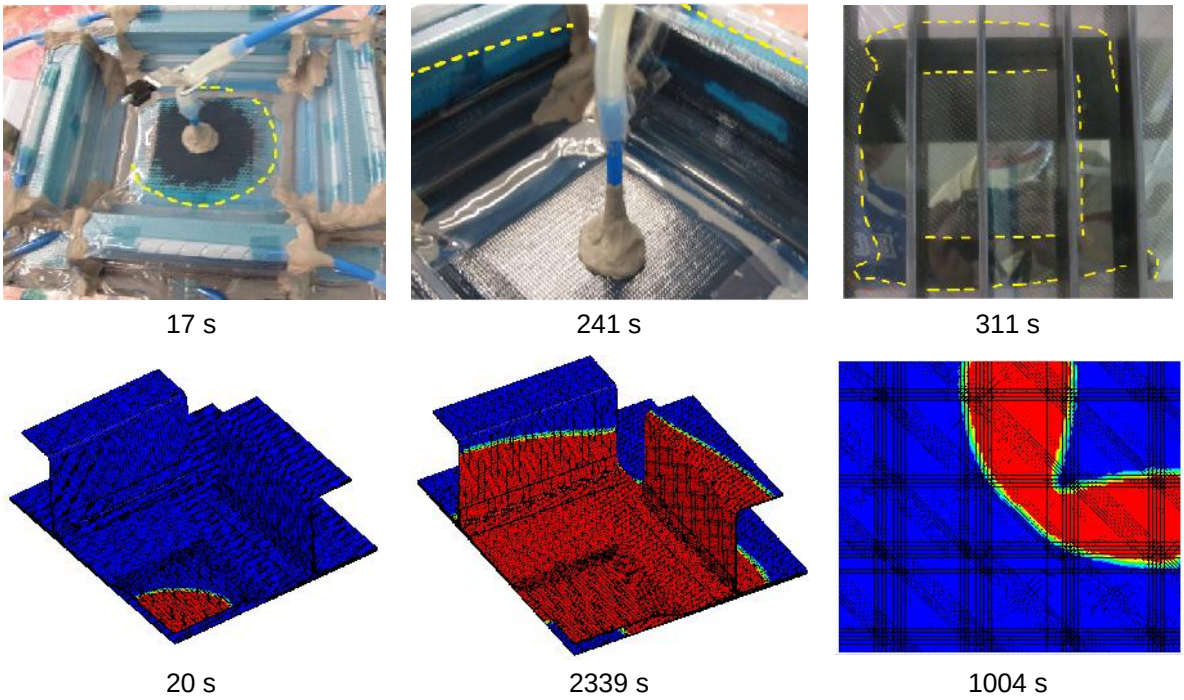

Figure 6.8 Filling times from test and simulation (setup I)

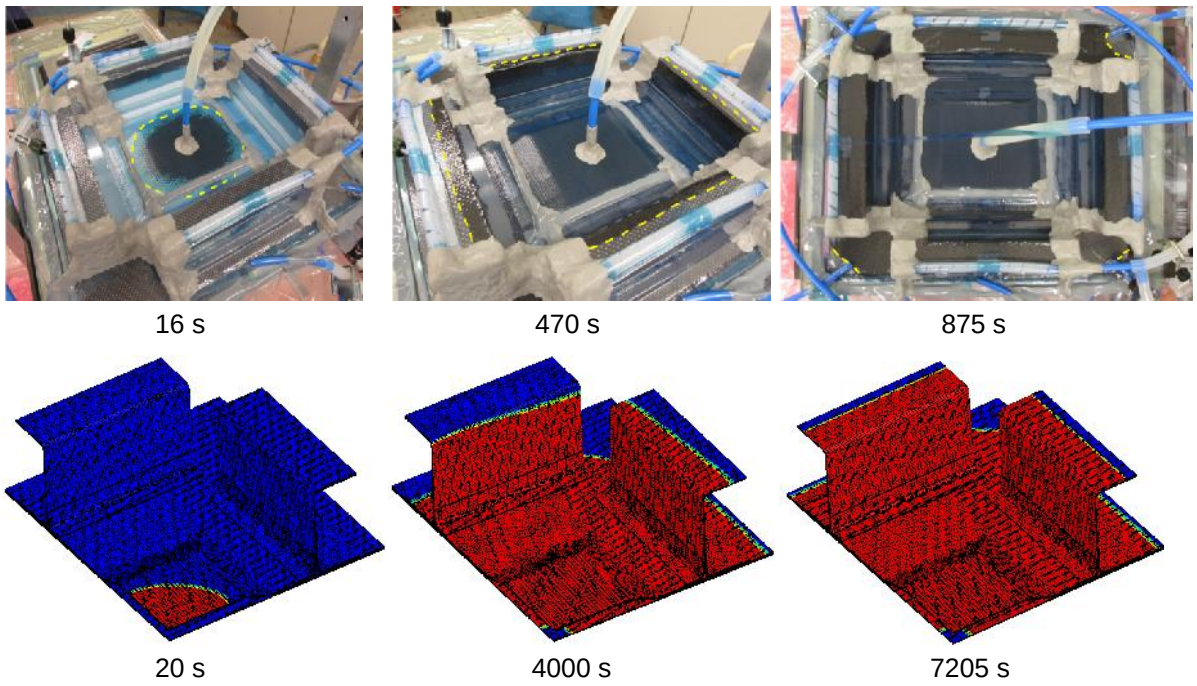

Figure 6.9 Filling times from test and simulation (setup II)

The significant error in the filling time resulted from neglect of VARI process specific phenomena. That is, due to flexible vacuum bag variable pressure field over the part is created which, in turn, changes thickness, permeability and porosity of the preform. VARI process simulations taking these effects into account are presented in the next section.

6.3 VARI process simulation (IFB in-house code)

A cross section model of one half of the demonstrator is used for a 2D VARI process simulation (Figure 6.10). The ply layup and inlet/outlet configuration is similar to the 3D model presented in the previous section. Material characterisation is done accounting for the process specific phenomena such as variation of pressure field and its effect on preform thickness change. This leads to the change of fibre volume fraction which, in turn, influences permeability of the preform in space and time. Data from quasi-unidirectional fabric permeability tests (sections 3.1.3 and 3.2.2) was used together with additional tests and numerical analysis to estimate fabric permeability over the range of compaction pressures 0-100 kPa. Permeabilities are defined as functions of pressure exploiting the Carman-Kozeny relationship (equation (2.35) in section 2.4.1).

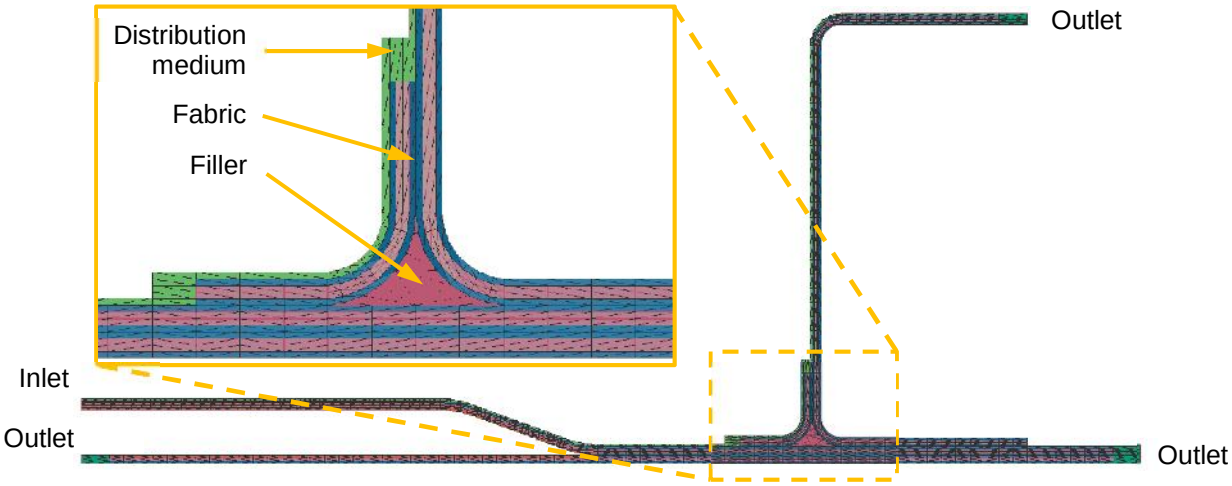

Figure 6.10 Demonstrator 2D section FE model for VARI process simulation

6.3.1 Estimation of fabric permeability as a function of fabric compliance

The relationship between fabric permeability and fibre volume fraction, or compaction pressure, can be obtained using several alternative strategies. These approaches are summarised in Table 6.2. The first and the second approaches rely on fabric compaction tests for fabric loading and unloading behaviour. The third and the fourth methods are alternative iterative approaches that exploit thickness change information from DIC measurements in combination with numerical analysis of pressure distribution over the preform.

<table>
<tr><th></th><th colspan="4">Test and analysis strategy</th><th>Data obtained</th></tr>
<tr><td rowspan="4">Experimental measurements</td><td>I. Approach</td><td>II. Approach</td><td>III. Approach</td><td>IV. Approach</td><td rowspan="3">$h = f(P)$</td></tr>
<tr><td colspan="2">Compaction test:
 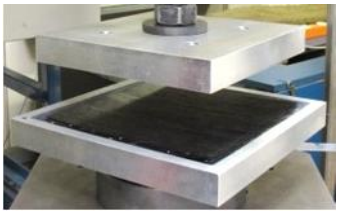 </td><td colspan="2">VARI test (with ARAMIS DIC):
 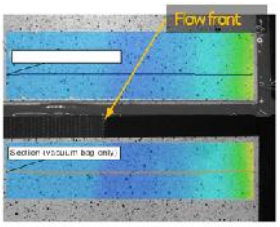 </td></tr>
<tr><td>Loading</td><td>Unloading</td><td>Linear pressure distribution</td><td>Non-linear pressure distribution</td></tr>
<tr><td colspan="4">Fibre volume fraction versus thickness</td><td>$V_f = f(h)$</td></tr>
<tr><td>Estimation</td><td colspan="4">Carman-Kozeny equation: $K = k\frac{(1-V_f)^3}{V_f^2}$</td><td>$K = f(V_f)$</td></tr>
<tr><td></td><td colspan="4">Permeability versus pressure</td><td>$K = f(P)$</td></tr>
</table>

Table 6.2 Relationship between fabric permeability and pressure estimation strategy

6.3.1.1 Compaction tests

Cyclic compression tests were performed to obtain fabric loading and unloading response data. Square specimens with 141x141 mm size and a $(0/90/90/0)_2$ layup were saturated with water and placed between aligned compaction plates. Figure 6.11 shows the experimental setup and the measured pressure versus thickness curves for four sequential load-unload cycles. After each load cycle the fabric was allowed to relax for three minutes before reloading.

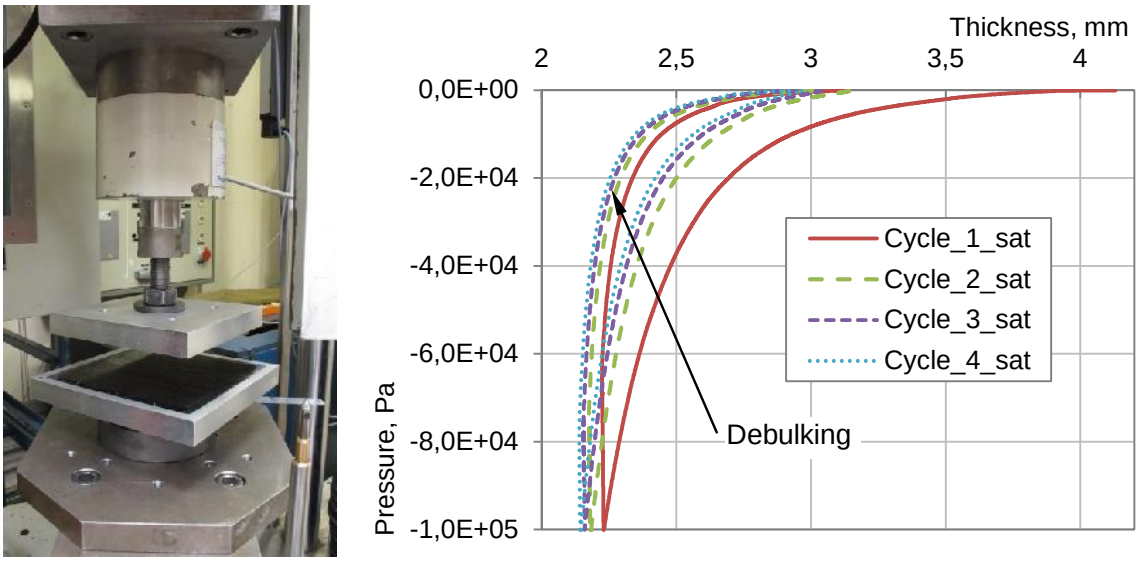

Figure 6.11 Fabric compaction test: a) setup view and b) compaction pressure versus thickness diagrams

When thickness of the preform changes the fibre volume fraction and porosity will also change. Fibre volume fraction was measured from specimens of a cured preform which was infused under vacuum bag and had different thickness over its length as illustrated in Figure 6.12. The standard DIN29971 [256] procedure was used to calculate fibre volume fraction giving results for various preform thicknesses as shown in Figure 6.13a. Combined with compaction test results, fibre volume fraction versus compaction pressure dependency is obtained for loading and unloading cases and depicted in Figure 6.13b.

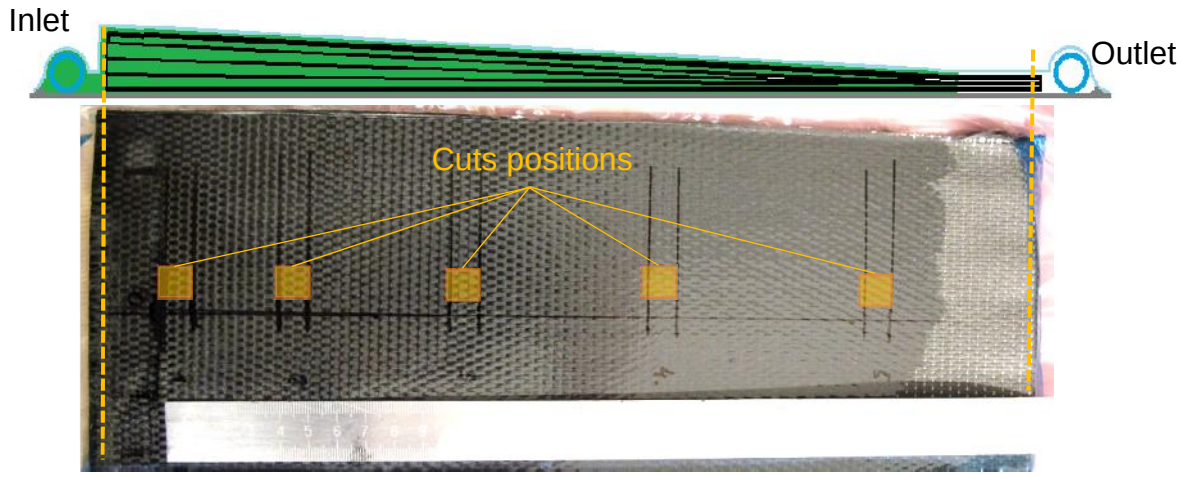

Figure 6.12 Location of specimens extracted for fibre volume fraction versus thickness function estimation

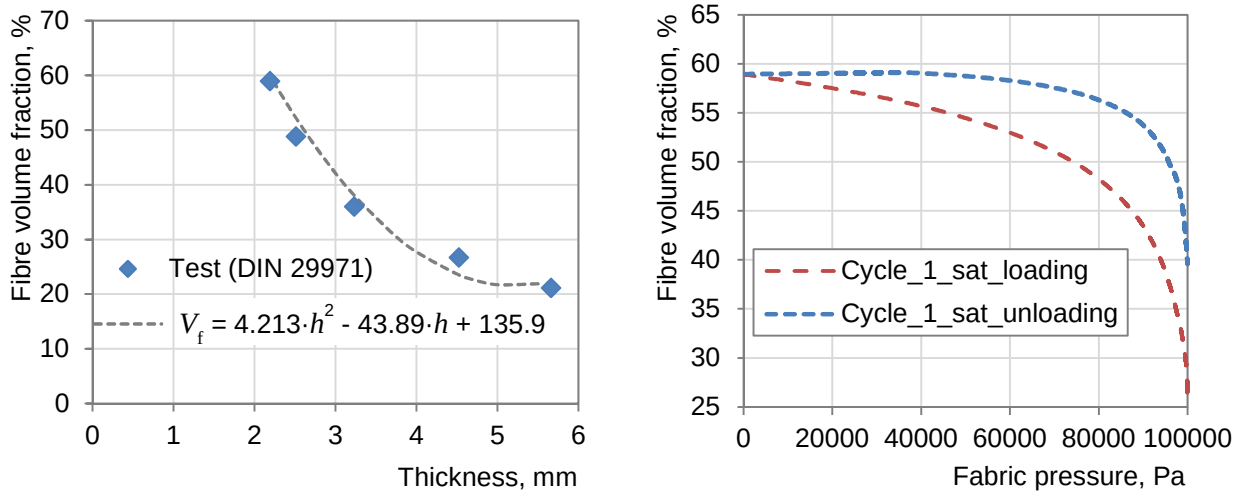

Figure 6.13 Fibre volume fraction versus a) preform thickness and b) fabric pressure diagrams

6.3.1.2 Permeability versus compaction pressure

A limited number of tests were available for permeability estimation under different compaction pressure. A summary of measurements from sections 3.1.3 and 3.2.2 is given in Table 6.3.

Absolute outlet pressure, kPa	K_{xx}, m²	K_{yy}, m²	K_{zz}, m²	Fibre volume fraction
0	2.11E-11	3.08E-12	4.93E-13	0.590
40	2.37E-11	-	-	0.552
60	1.86E-11	-	-	0.542

Table 6.3 Summary of G1157 fabric permeability data

The relationship between permeability and fibre volume fraction was estimated using a modified Carman-Kozeny relationship [117]:

$$K = k\frac{(1-V_f)^3}{V_f^2}, \tag{6.1}$$

where k – Carman-Kozeny constant, m^2.

The constant k was obtained for each of the three data sets of permeability and fibre volume fraction; these results are summarised in Table 6.4. The average k value was found to be equal to 8.14E-11 m^2. Through-thickness permeability K_{zz} versus V_f was estimated using a single point available (K_{zz}=4.93E-13 m^2 and V_f =0.590).

Fibre volume fraction	K_{xx}, m^2	Carman-Kozeny constant k, m^2	k (average), m^2	K_{zz}, m^2	Carman-Kozeny constant k, m^2
0.590	2.11E-11	1.07E-10	8.14E-11	4.93E-13	2.49E-12
0.552	2.37E-11	8.04E-11		-	
0.542	1.86E-11	5.68E-11		-	

Table 6.4 Carman-Kozeny constants for K_{xx} and K_{zz}

Permeability versus fibre volume fraction plots for K_{xx} and K_{zz} are given in Figure 6.14a and Figure 6.14b respectively. With fibre volume fraction versus pressure information from Figure 6.13b, the permeability versus pressure relationship is obtained and shown in Figure 6.15, together with test data points. These diagrams will be used in the next section as input for the 2D strip cross section flow simulation model.

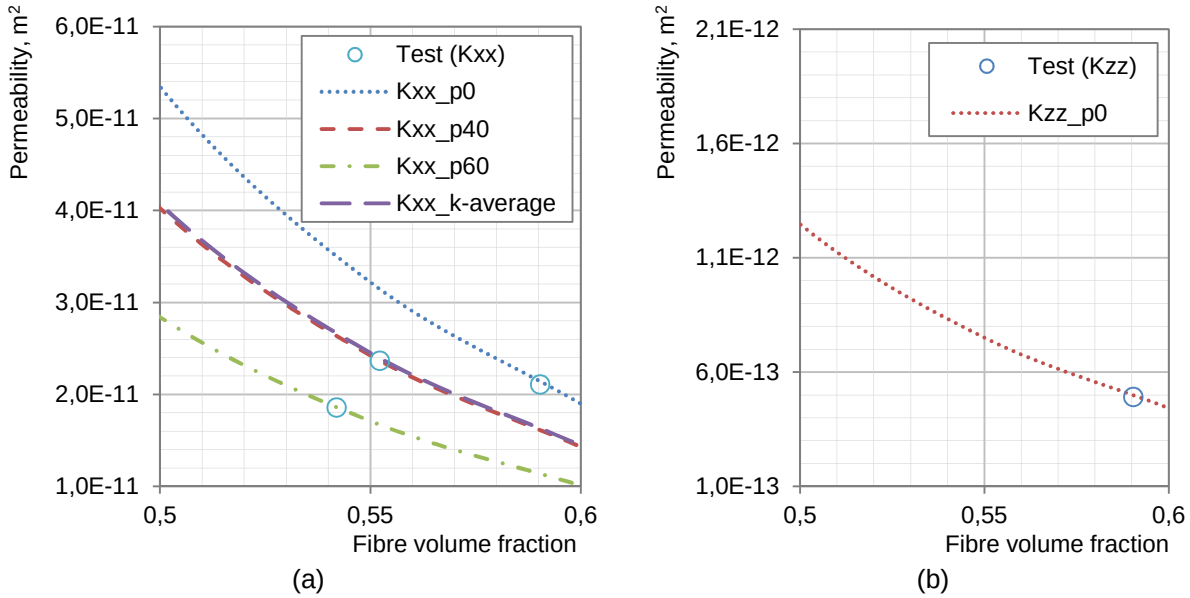

Figure 6.14 Quasi-UD NFC permeability versus fibre volume fraction diagrams: a) in-plane and b) through-thickness permeabilities

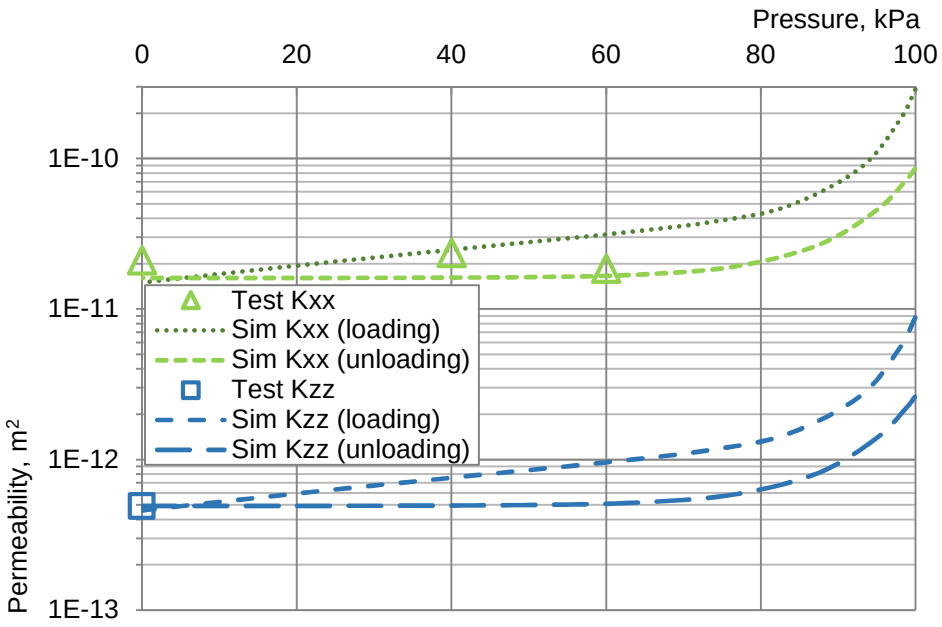

Figure 6.15 Permeabilities (K_{xx}, K_{zz}) versus fabric compaction pressure diagrams (using loading and unloading compaction test data)

6.3.1.3 Simple strip simulation model

Material properties obtained in the previous subsection are validated using a simple 2D fabric cross section model shown in Figure 6.16. Details on the flow analysis which exploited a control volume FE approach can be found in section 2.5 and references [245] and [230].

First, following approaches I and II in Table 6.2, fabric compaction data was extracted from loading and unloading curves of the first cycle. Functions relating permeability and pressure from Figure 6.15 are given in Table 6.5.

Figure 6.16 FE model of the fabric strip cross section

Approach	Simulation input data		
	$V_f(P)$	$K(P)$, m² ($[P]$ = kPa)	Viscosity
I.	Test (loading) V_f = 0.590 + 8.78E-6· ·(1-exp(9.85E-2· P))	K_{xx} = 1.61E-11+2.09E-17·exp(0.15· P) K_{zz} = 4.92E-13+1.0E-18·(0.145· P)	Manufacturer datasheet (23°C with 30 min mixing and degassing time), Appendix I
II.	Test (unloading) V_f = -2.38E-7·exp(0.135· P) + +596·exp(-2.07E-3· P)	K_{xx} = 1.5E-11+2.64E-13· P+ + 6.24E-20·exp(0.221· P) K_{zz} = 4.92E-13+6.56E-15· P+ + 1.52E-20·exp(0.20· P)	

Table 6.5 2D strip model infusion simulation input data (loading and unloading compaction tests)

Thickness distribution obtained from 2D infusion simulation is compared with experimental measurements using the ARAMIS DIC system in Figure 6.17. It can be observed that use of loading and unloading data from the compaction test leads to different thickness distribution results. Thickness at the inlet end of the preform is overestimated when using loading test data (+34%), while use of unloading data leads to better agreement with DIC measurements (-4%).

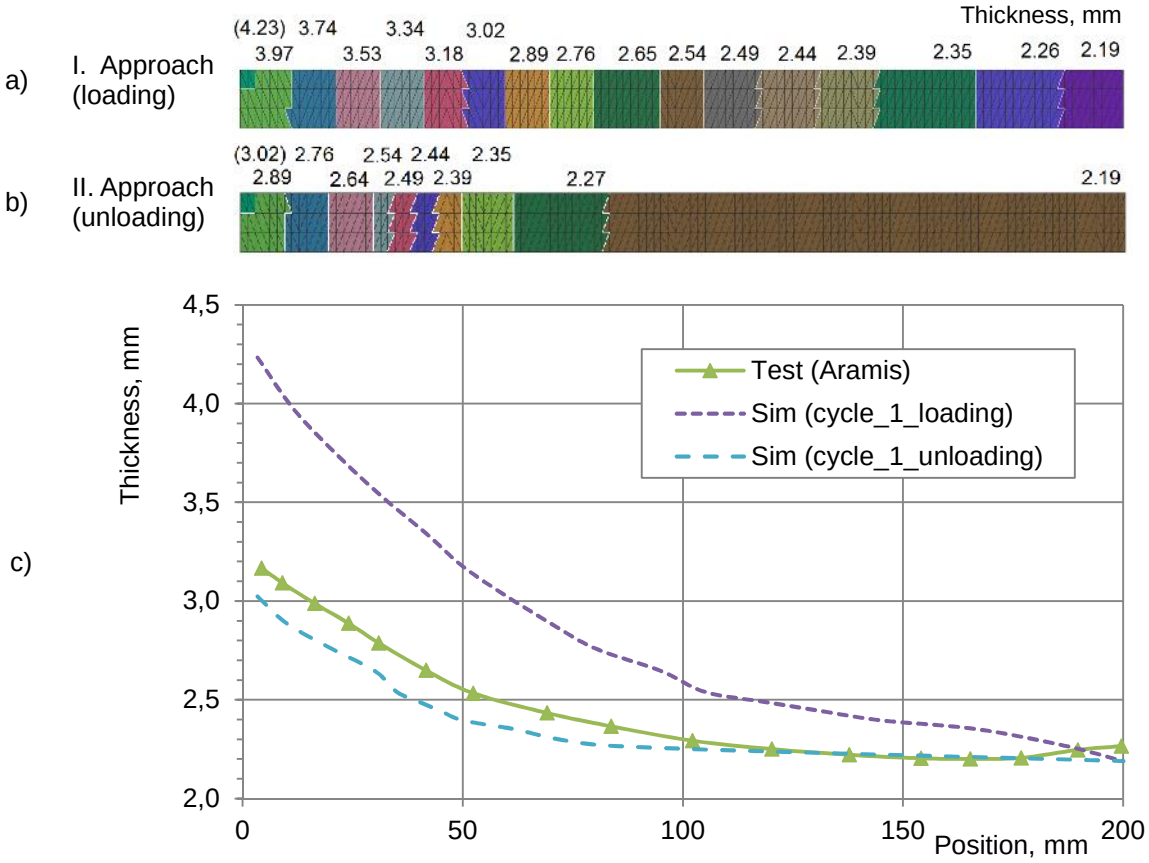

Figure 6.17 Preform thickness contour plots exploiting a) loading test data, b) unloading test data and c) thickness versus position diagrams from test and simulations

Neither loading nor unloading compaction test may, however, describe the actual LRI process properly. Compaction of an already saturated preform leads to increase of pressure due to the

resistance of fluid flowing out of the preform as illustrated in Figure 6.18a. During unloading of the compressed preform resin is drawn back into increasing pore volumes of the fabric causing an increase in measured force and calculated pressure values (Figure 6.18b). In actual LRI process, however, resin migrates through the preform causing increase in thickness (Figure 6.18c) and it is not the increase in thickness what drives the flow in the case of uniform unloading of the specimen. Thus alternative strategy to quantify compaction properties of the preform have been considered.

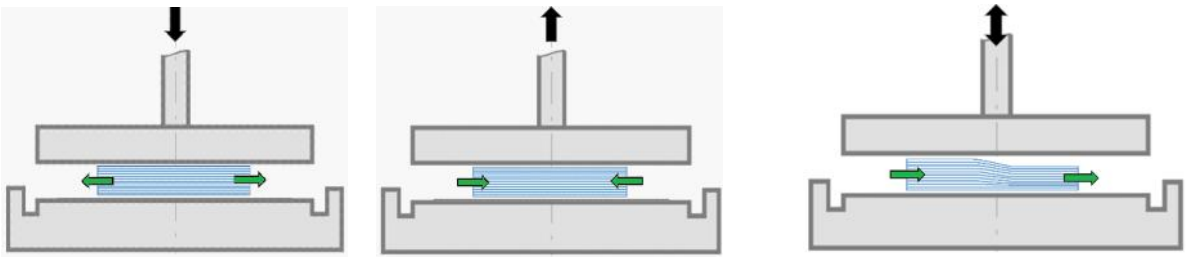

a) Loading (saturated) b) Unloading (saturated) c) LRI infusion

Figure 6.18 Schematic illustration of resin flow during: a) loading, b) unloading and c) LRI infusion

Resin pressure sensors are normally used to precisely monitor pressure field during LRI infusion. Unfortunately, these were not available for this experimental work. Instead, a combination of fabric thickness measurements in VARI test and numerical simulations were used to obtain an improved relationship between fabric thickness (V_f) and resin pressure.

Pressure distribution between inlet and resin flow front is linear for RTM infusion and only approximately linear in LRI due to non-linear relaxation of the preform. However, this assumption is used here as a first estimate to define a fibre volume fraction versus pressure and permeability versus pressure relationships for initial simulation input. In Figure 6.19a an assumed linear resin pressure distribution over the infusion length of 200 mm is depicted. This information is used together with experimental thickness data in Figure 3.9b to construct a new fibre volume fraction versus resin pressure curve in Figure 6.19b and permeability versus resin pressure curve in Figure 6.20. Corresponding algebraic expressions for these functions are given in Table 6.6.

Approach	Simulation input data		
	$V_f(P)$	$K(P)$, m² ($[P]$ = kPa)	Viscosity
III.	Initial assumption of linear pressure distribution V_f = -4.04E-2·exp(2.26E-2· P) + + 0.632·exp(1.54E-3· P)	K_{xx} = 1.51E-11·exp(-1.68E-3· P) + +4.48E-13·(5.8E-2· P) K_{zz} = 4.83E-13·exp(-1.50E-3· P) + +1.1E-14·(6.02E-2· P)	Manufacturer datasheet (23°C with 30 min mixing and degassing time), Appendix I
IV.	Non-linear pressure distribution (result of III. approach) V_f = -2.87E-6·exp(0.111· P) + + 0.592·exp(-1.80E-4· P)	K_{xx} = 1.55E-11+6.55E-14· P + + 3.42E-21·exp(0.25· P) K_{zz} = 4.71E-13+1.54E-15· P + + 1.48E-21·exp(0.22· P)	

Table 6.6 Simulation input data (initial linear and subsequent non-linear pressure distribution)

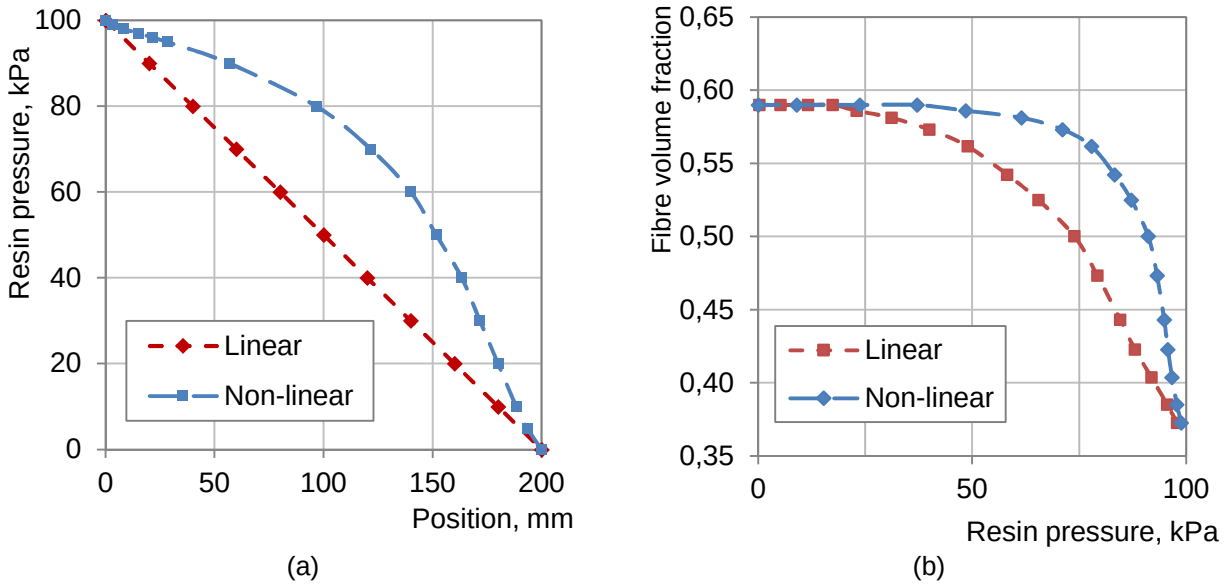

Figure 6.19 Pressure estimation in the simulation: a) resin pressure distribution over the preform and b) fibre volume fraction versus resin pressure for the linear and non-linear cases

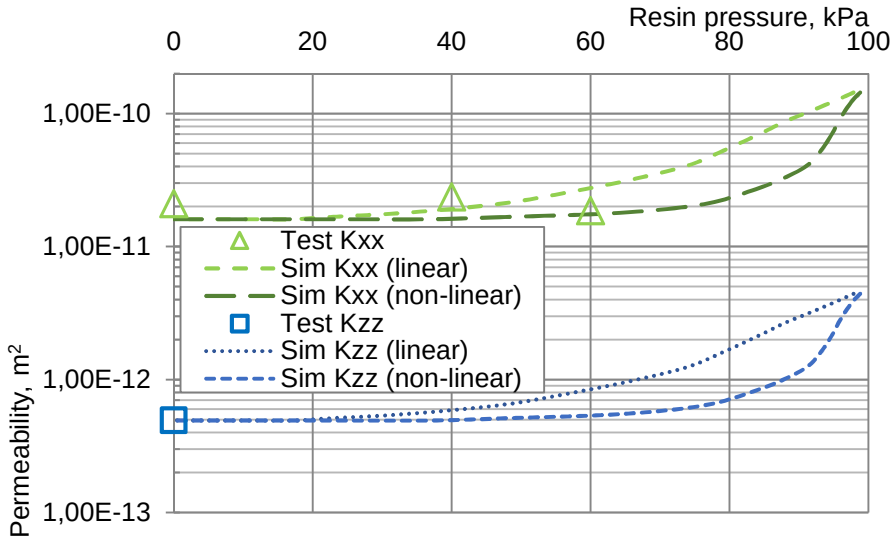

Figure 6.20 Permeability (K_{xx}, K_{zz}) versus resin pressure diagrams (assuming linear and non-linear pressure distribution)

Several strip model infusion simulations were run with data from Table 6.6. Figure 6.21c shows a poor agreement between test and simulation for thickness distribution when using linear pressure distribution assumption. The resin pressure field obtained in this simulation is, however, non-linear as shown by the line with square symbols in Figure 6.19a. This non-linear pressure distribution is used again to re-compute $V_f(P)$, $K_{xx}(P)$, $K_{zz}(P)$ dependencies for the next iteration. Its input data is given in Table 6.6 (IV. approach) and shown in Figure 6.19 by curves labelled 'Non-linear', and Figure 6.20 by curves labelled 'Sim Kxx (non-linear)' and 'Sim Kzz (non-linear)'. Simulation results are shown in Figure 6.21b and Figure 6.21c.

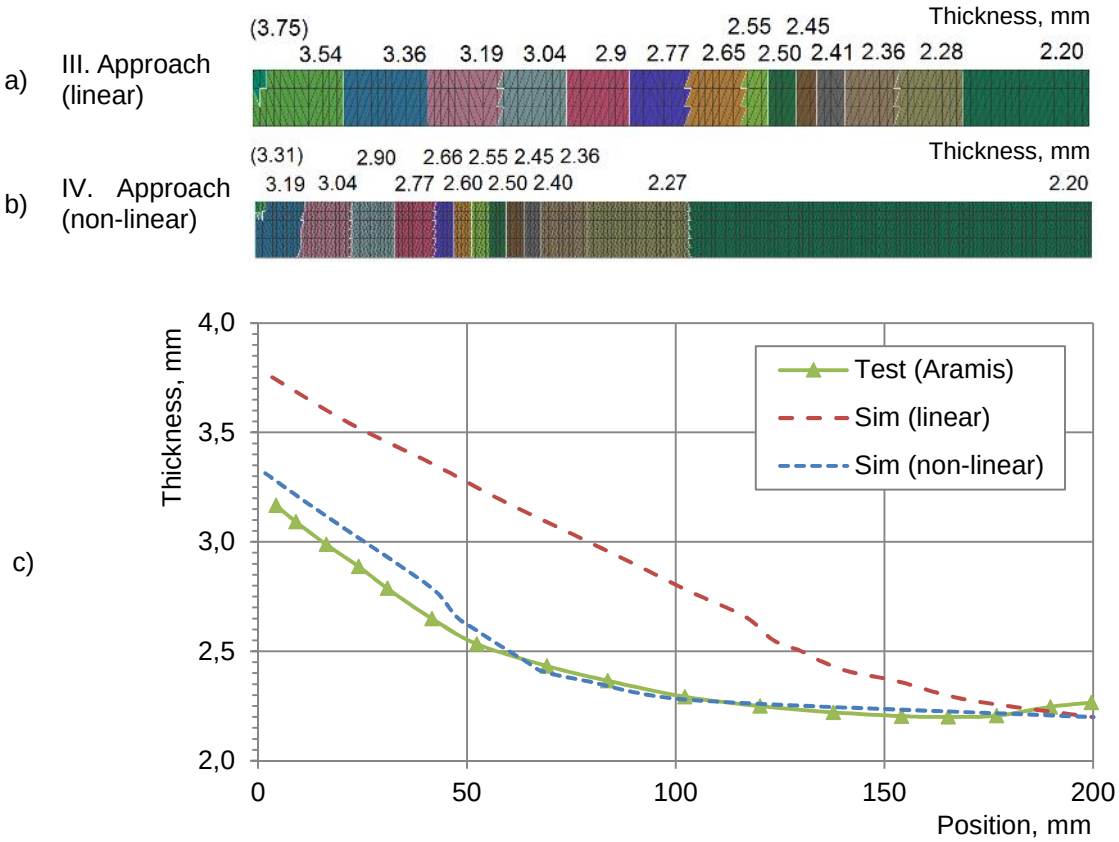

Figure 6.21 Preform FE model thickness contour plots exploiting a) linear, b) non-linear pressure distribution assumptions and c) thickness versus position diagrams from test and simulation

Simulation using non-linear pressure assumption shows better agreement with experimental measurements over the whole preform length compared to the results obtained using unloading compaction test data as compared in Figure 6.22. Thus numerical estimation of preform relaxation behaviour from VARI type infusion simulation may be considered as an alternative to fabric compaction testing.

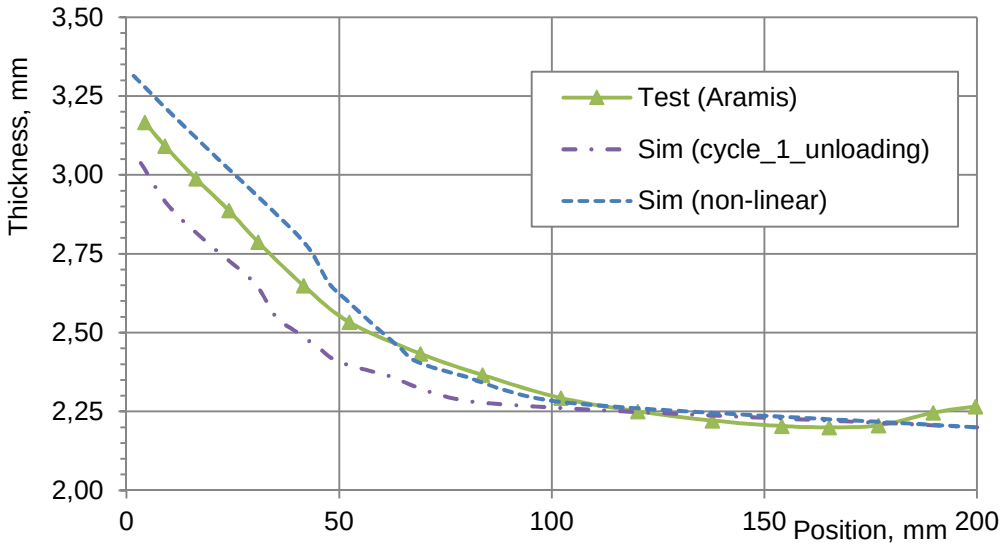

Figure 6.22 Thickness versus position diagrams from test and simulations

6.3.2 Estimation of distribution medium orthotropic permeability

In order to estimate permeability for the distribution medium the 2D strip model from the previous section was modified by adding a row of elements to represent DM as shown in Figure 6.23. The separation and perforated foils are not modelled, however, they do have an impact on the flow behaviour by delaying the through-thickness flow. As will be shown, defining orthotropic permeability of the distribution medium can take the effect of these additional foils into account and can give good reproduction of resin flow results observed in tests.

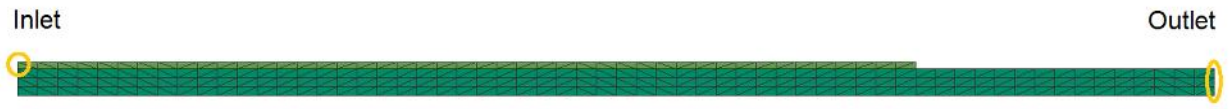

Figure 6.23 FE model of a fabric strip cross section with distribution medium

Fabric permeability and compliance data obtained in the previous section (IV. approach with non-linear pressure distribution) is used in this analysis. An initial simulation is done with the assumption of isotropic DM permeability ($K_{xx\_FM} = K_{zz\_FM}$ =4.3E-10 m^2). This was estimated from in-plane flow through the distribution medium in a typical VARI setup as presented in section 3.1.4. Flow front propagation on top and bottom of the preform from test and simulation are compared in Figure 6.24b with contour plots of filling times given in Figure 6.24a.

a)

K_{xx_FM} = 4.3E-10 m^2

K_{zz_FM} = 4.3E-10 m^2

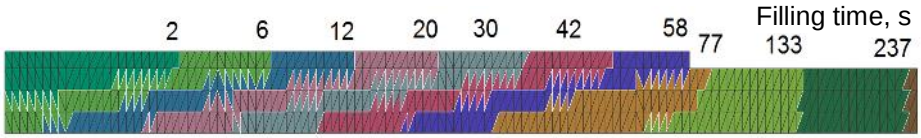

b)

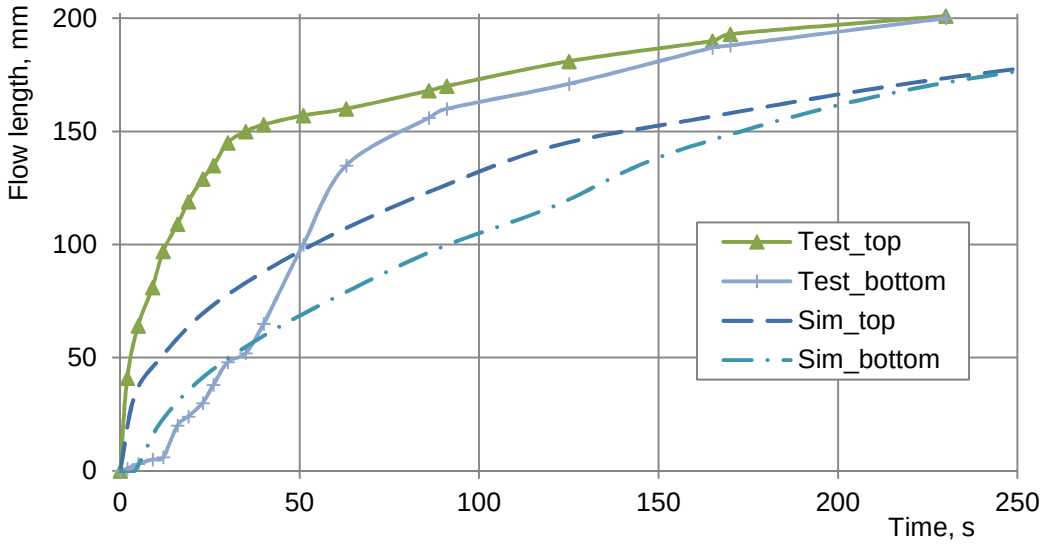

Figure 6.24 FE simulation with isotropic DM permeability: a) flow length contour plot and b) flow length versus time diagrams from test and simulation

The simulation results demonstrate slower in-plane flow on the top of the preform in the distribution medium compared to the test. Since the in-plane and through-thickness flows are coupled, reduction of through-thickness permeability of the distribution medium would limit the flow into the fabric and increase the in-plane resin propagation speed. The assumption of distribution medium to be isotropic is therefore invalid.

Within a few iterations DM permeabilities K_{xx_FM} and K_{zz_FM} were adjusted to obtain a good agreement with test measurements. The 'optimised' values for K_{xx_FM} and K_{zz_FM} are 9.5E-10 m^2 and 1.0E-13 m^2 respectively, i.e. the former was increased by 120% and the latter reduced by more than 3 orders of magnitude. Using these values a good agreement for both upper and lower flow front propagations is obtained as shown in Figure 6.25a and Figure 6.25b. The larger difference between the in-plane and through-thickness permeabilities (about 2 orders of magnitude) can be explained by the effect the separation and perforated foils have on the through-thickness flow process. These foils hinder immediate resin sink in the through-thickness direction and increase in-plane flow speed in the DM.

a)

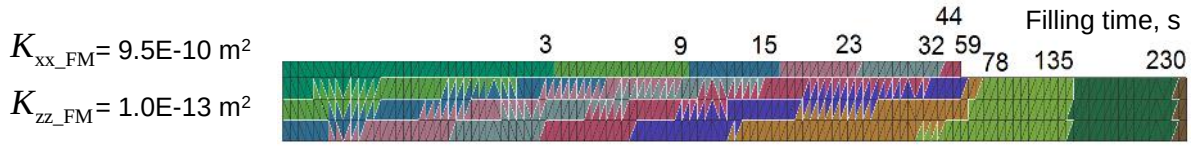

b)

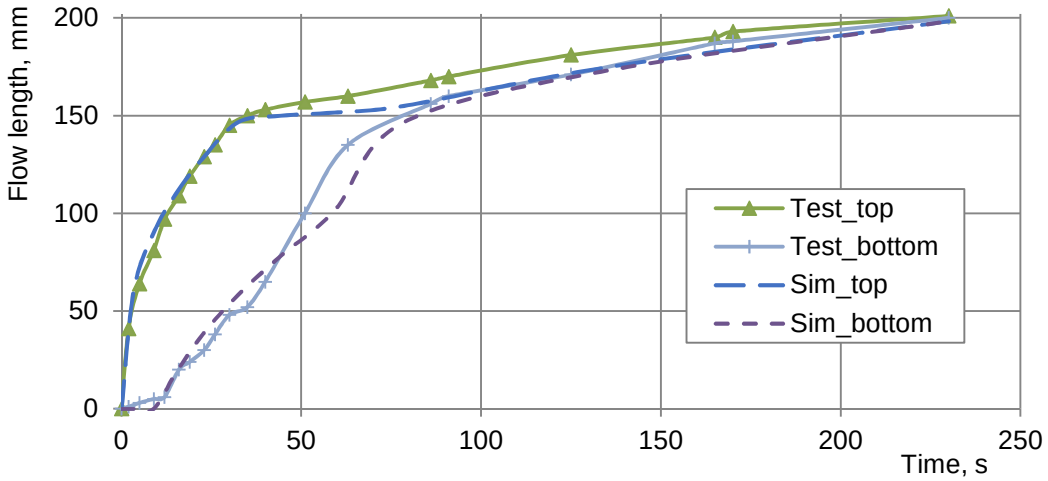

Figure 6.25: FE simulation with orthotropic DM permeability: a) flow length contour plot and b) flow length versus time diagrams from test and simulation

6.3.3 Demonstrator study

The 3D demonstrator structure from section 6.2 has been simplified to a 2D cross section and analysed using [230] code as a VARI process. It has to be noted that quasi-UD NCF permeability was measured only in the principal permeability direction (K_{xx}), whereas selected cross section of the part lies in a plane with +45/-45 fabric directions. The model was scaled in x-direction to

approximately compensate for this as shown in Figure 6.26. Both demonstrator setups (I and II) having different placement of distribution medium were considered.

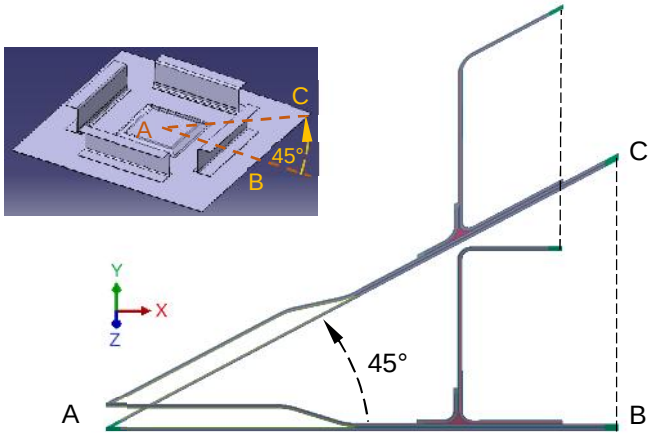

Figure 6.26 Scaling of demonstrator 2D model cross section

Simulation results for the first infusion configuration with DM on all upper surfaces are shown in Figure 6.27. A reasonable agreement to test measurements with properly represented fast flow through the distribution medium, followed by delayed fabric impregnation, is obtained. The analysis predicted a slightly longer infusion time of ~1230 s compared to the test 800 s.

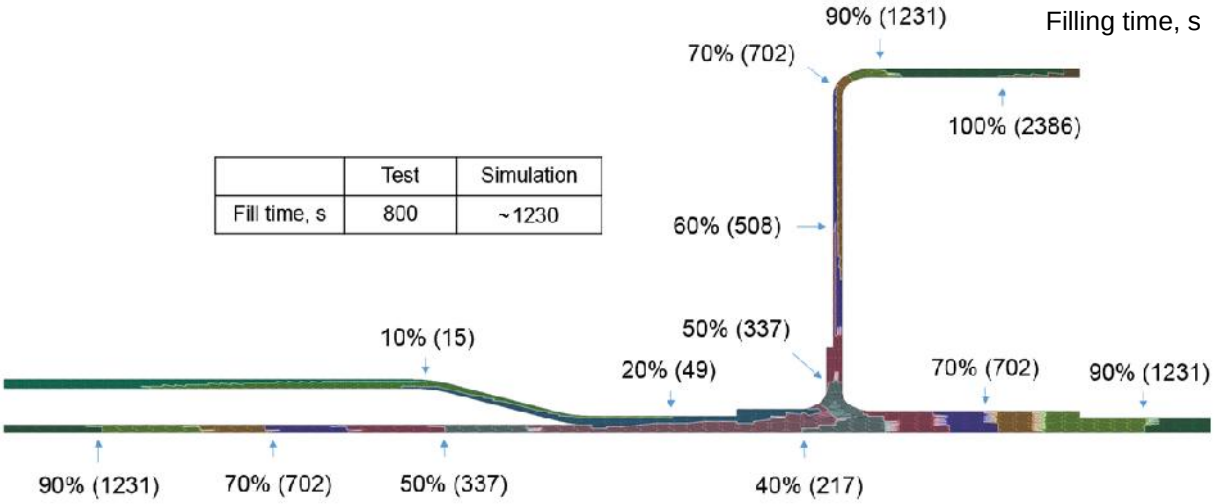

	Test	Simulation
Fill time, s	800	~1230

Figure 6.27 Filling time contour plot or demonstrator part 2D section (setup I)

Simulation results for the second infusion configuration with the DM elements removed from the upper part of the C-stringer are depicted in Figure 6.28. The time for the resin to reach the middle of the C-stringers upper plate is about 470 s in the test (Figure 6.9) which differs from the simulation with 666 s. The whole filling process also takes longer in the simulation with ~1250 s compared to the test 875 s.

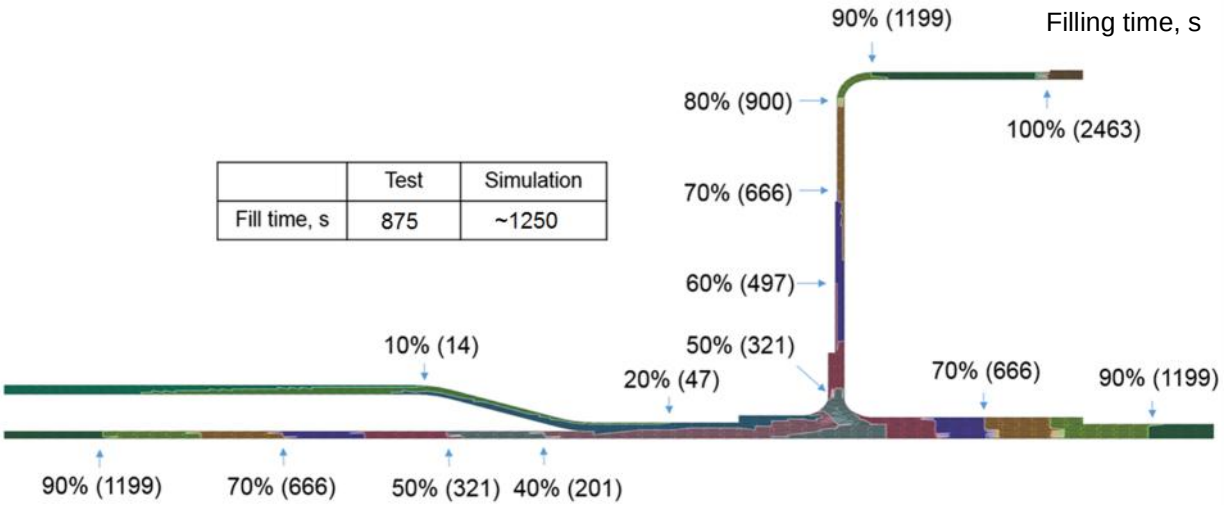

Figure 6.28 Filling time contour plot of demonstrator part 2D section (setup II)

Discrepancies between predicted and actual filling times may be explained by the simplifications of the model. For example, 2D analysis ignores diverging (radial) resin flow front and any effect of racetracking is neglected. Obtained estimations, however, are much improved compared to the RTM type simulation from section 6.2 where VARI effects are completely ignored.

6.4 Summary of macro-scale LRI process simulation

LRI under a flexible membrane was investigated for a demonstrator consisting of a stiffened sandwich panel with attached stringers. Several infusion tests have been performed in different configurations that have varied placement of distribution medium in an attempt to ensure complete part saturation and avoid dry zones. Respective numerical simulations using a commercial RTM process simulation software was used to illustrate some limitations of the commercial tool which, as may be expected, yielded much longer fill times compared to experimental observations. This is due to process induced material properties variation that are ignored in RTM type infusion simulation. In LRI flexible membrane leads to non-linear pressure field and corresponding changes in preform thickness, fibre volume fraction, porosity and permeability which must be taken into account in the simulation.

Consequently, characterisation of the preform permeability has been undertaken with respect to preform compliance. This was accomplished using a simple strip infusion test in VARI configuration and a dedicated 2D VARI process simulation code. It was demonstrated that fabric compressibility data can be extracted from fabric compression testing or, alternatively, using DIC measurements of preform thickness in combination with numerical analysis.

Another important observation was made regarding the distribution medium permeability. Resin flow through the preform in a VARI setup with DM on top of perforated foil and separation ply cannot be

accurately modelled with an isotropic DM assumption. Orthotropic DM permeability data has been determined which resulted in good agreement between the test and simulation.

Two variations of a final demonstrator cross section 2D infusion analysis were performed using an in-house VARI process simulation code. Despite the 2D simplification, good comparison to tests was obtained that showed markedly better results than commercial software dedicated to RTM process simulation.

7 Discussion

The literature review in chapter 2 highlighted the deformation mechanisms of textile preforms, and the difficulty to characterise constitutive laws to describe a fabric for draping simulations. Certain textiles have a complex architecture that cannot be accurately modelled using a state-of-the-art macro-scale approaches. Adopting a meso-scale approach has potential for greater accuracy, however, far more parameters are required to describe the numerical model; ultimately, a reasonable trade-off between increased complexity, CPU cost and accuracy must be sought.

The presented meso-scale model of biaxial NCF exploits a ‘just fine enough’ approach to discretisation at the tow level and is designed so that it is capable of representing inter-tow sliding, in-plane and out-of-plane tow buckling, in addition to the major deformation mechanisms such as bending, compaction and shear. A particular aim of the fabric model meshing strategy was that it would be suitable for coupled drape and infusion simulation in a deformed state for reasonably large components. Difficulties encountered in some stages of numerical modelling and material characterisation are discussed below including constitutive modelling, draping simulation, permeability characterisation and coupling between the drape and infusion processes.

LRI process simulation using an in-house code, capable to take into account preform permeability dependent on compliance, demonstrated the necessity of both a dedicated simulation tool and correct material permeability characterisation for analysis of such processes as VARI. Two strategies to characterise fabric behaviour during infusion were tried; namely, compaction testing and DIC measurements with numerical analysis. Results obtained from these two methods were close to each other and validated both approaches as equivalent options for fabric compliance characterisation.

7.1 Hemisphere draping simulation

Fabric shear characterisation tests using picture frame and bias extension tests may result in considerable data scatter due to inherent variability of the fabric such as unparalleled fibres within tows and bridging of fibres between the tows and stitches. Only a limited number of fabric shear tests have been possible that have shown qualitatively reasonable results; however, more testing would be required to gain greater confidence in quantitative shear measurements that have been used in this thesis.

Modelling of individual tow deformation is important for overall deformation behaviour, and has presented several challenges. Tow in-plane shear is an important factor contributing to in-plane shear stiffness, particularly for small fabric shear angles [7]. The presented numerical model,

however, neglects in-plane tow shear resistance, whereas out-of-plane tow shear has been used to characterise fabric bending behaviour. Also, in-plane tow compaction was neglected with only through-thickness compaction of the fabric being considered. At high shear angles (>30°) the in-plane compaction mode is important and additional tests and calibration would be needed to properly include this effect for improved shear modelling.

Intra-ply friction caused by friction between adjacent tows of the same ply, adds to the shear resistance since contacting area of filaments increases with shear deformation. In the numerical model, however, intra-ply friction becomes active only when a certain contact distance (0.13 mm) is reached between the tows, and this distance remains constant thereafter during relative intra-ply tow sliding. Thus in an early shear stage only inter-ply friction, from friction between the tows of adjacent plies, is active and contributes to shear stiffness; this contribution depends on application of a normal compaction load.

Hemisphere draping simulation results from the state-of-the-art macro-scale (section 4.2.2) and meso-scale analyses (section 5.1.7) are compared in Figure 7.1. Simple and CPU efficient macro-scale analysis is found to give good agreement for shear angle distribution over the circumference of the hemisphere with only a few degrees of difference to experimental measurements at points of maximum shear angle. The force needed to drape the macro-scale hemisphere model is, however, overestimated as shown in Figure 7.2a. As can be seen from the same figure, high fabric bending stiffness is causing wrinkling of the fabric between the blank holder rings reducing the effective friction force. However, bending stiffness, which was calibrated from bending tests in +45/-45 and 0/90 fabric directions and averaged, is the major contributing factor leading to this overestimation of blank holder force.

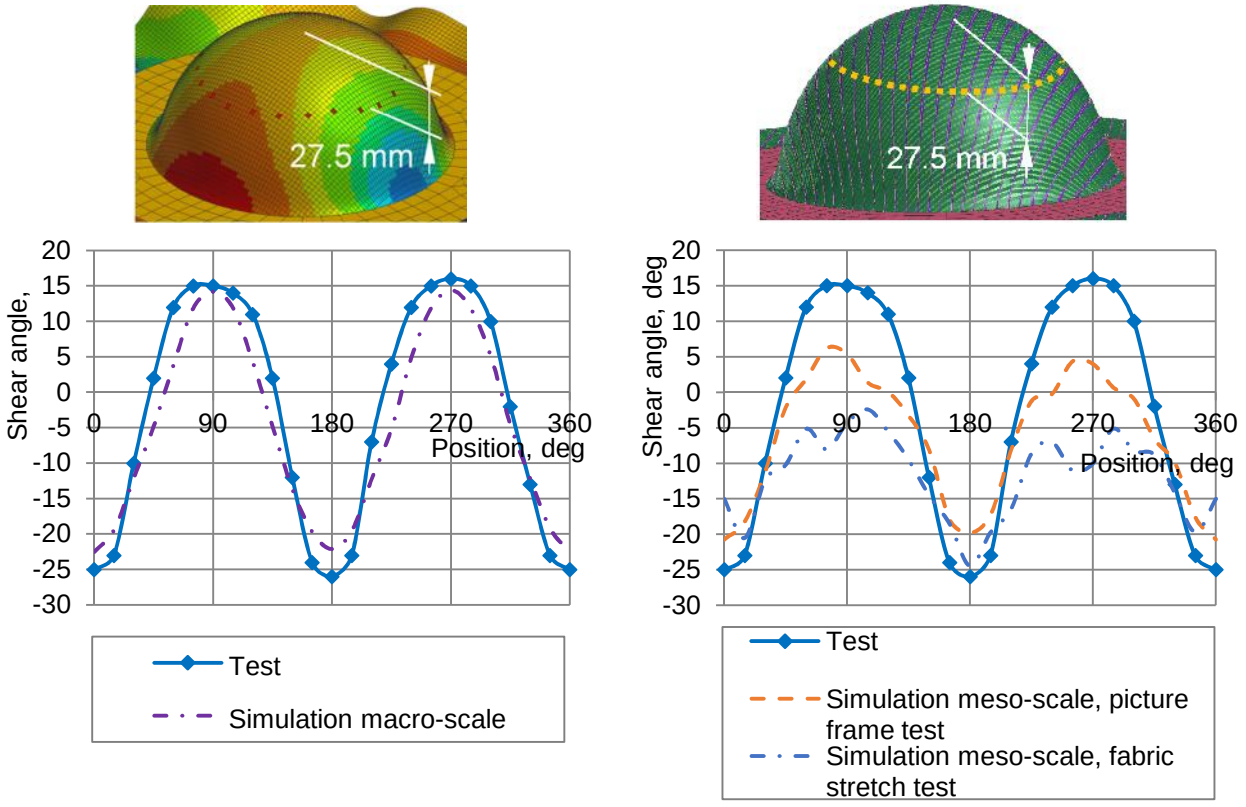

(a) (b)

Figure 7.1 Shear angle versus position diagrams from hemisphere draping a) macro-scale simulation and b) meso-scale simulations

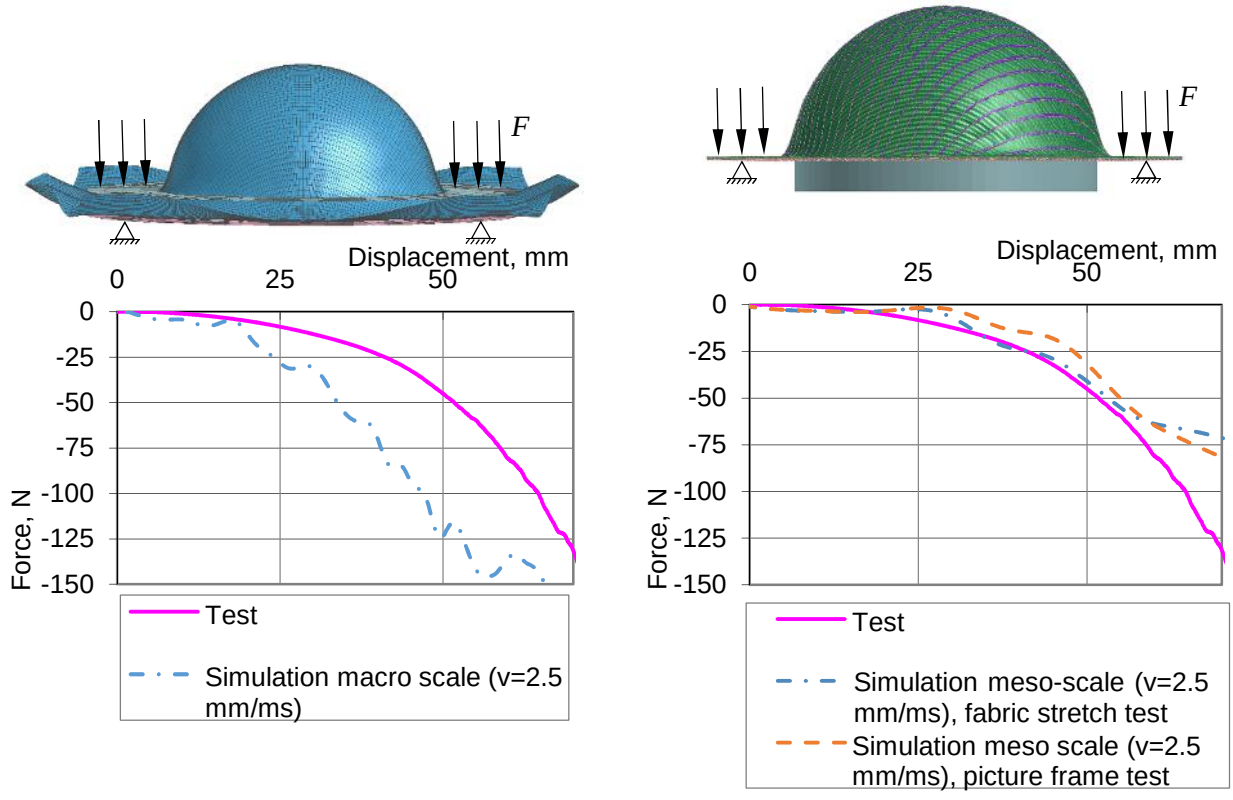

(a) (b)

Figure 7.2 Punch force versus displacement from hemisphere draping test and a) macro-scale simulation and b) meso-scale simulations

Meso-scale fabric draping analysis resulted in better forming force prediction as shown in Figure 7.2b; however, shear angle differed significantly form the test measurements being underestimated by 5 to 15 degrees (Figure 7.1b). The largest error is observed in the ‘positive shear angle’ range, i.e. in the areas where stitches undergo tension and thus counteract shear deformation. Stitch properties obtained from fabric stretch tests and picture frame tests were used with stitches being stiffer in the former case; this implies that a better representation of stitch tension stiffness properties and their kinematic behaviour is needed for more accurate fabric shear behaviour.

7.2 Permeability measurement

A simple permeability measurement method exploiting a 1D flow test setup was developed and used in this thesis. Care has been taken to ensure repeatability of the results as far as preparation of the specimens and test procedures are concerned. However, in infusion experiments some phenomena were observed, which have an influence on measurement results and may not be avoided in most testing setups (either linear or radial) or in real part infusions. Such phenomena include increased flow velocity at the interfaces of fabric and testing plate surface, qualitatively different flow in the same type of reinforcement fabric and interaction of in-plane and through-thickness flows. These aspects of permeability testing are discussed in more detail below.

7.2.1 Flow at the interfaces

Resin flow at the boundary surface of a specimen may be considerably different to the flow in the centre of the tested medium. Different materials such as foam core combined with NCF may form a channel-pore system with higher permeability, similar to resin channel system between fabric and mould surface which was considered in [21] and [136]. Resin flow in structural parts, which have foam inserts such as the demonstrator in chapter 6, will exhibit accelerated surface flow effects, and this needs to be taken into account in the infusion simulation.

A set of 1D tests was performed to illustrate the effect that different surfaces have on the fluid flow. Specimens with different interfaces were prepared including (Figure 7.3):

a) foam-glass interface,
b) foam-fabric-glass interface,
c) fabric-glass interface.

Constant thickness of the layups was maintained using a glass plates fixed on the specimens once vacuum pressure was applied. In case b (foam-fabric-glass) only a few layers of fabric were used making through-thickness flow negligible. As can be seen in Figure 7.3d resin flow is much faster in

the fabric specimen where one side has a foam interface (curve labelled ‘Test (b)’) compared to a fabric on glass specimen (curve labelled ‘Test (c)’).

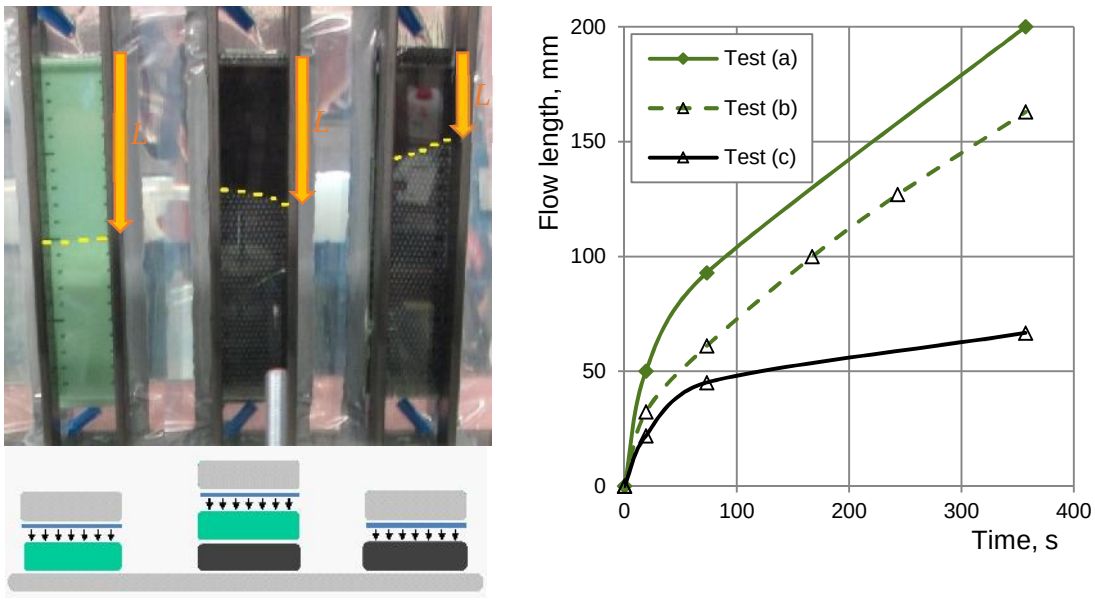

(a) (b) (c) (d)

Figure 7.3 Foam interface equivalent permeability estimation test: a), b), c) test and schematic layup views and d) resin flow length versus time diagrams

7.2.2 Principal permeability directions of biaxial NCF

Radial infusion permeability tests on biaxial NCF with binder and without binder were performed, yielding qualitatively different results concerning the principal permeability directions. In the case of bindered fabric preferential flow along the upper ply fibre tows was observed, whereas similar fabric without binder showed a clear preferential flow in the stitches direction (Figure 7.4a and Figure 7.4b respectively).

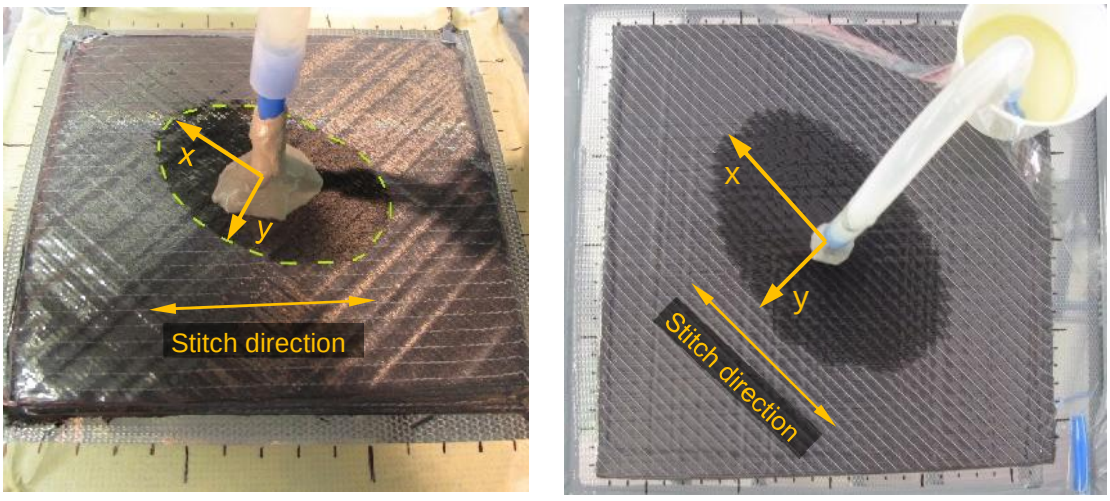

(a) (b)

Figure 7.4 Principal permeability direction of biaxial NCF: a) with binder and b) without binder

Since no measurement of unbindered fabric permeability was made, except for calibration purposes in section 5.2, hemisphere infusion simulation at the macro-scale was performed using bindered fabric permeability data (section 3.1.1). In [147] it was reported that unsaturated permeability of woven fabric specimens with 2% and 4% tackifier reduced by a factor of 2. This effect may partially explain the poor agreement between test and macro-scale infusion simulation results; however, the macro-scale model still does not have the capability to account for the presence of stitches and their influence on preferential flow direction.

7.2.3 Flow discrepancies in 1D flow test

The majority of permeability test setups rely either on visual monitoring of the flow front propagation or on measurements using embedded sensors. In both cases only surface flow can be detected. Larger or smaller voids, depending on the material structure, form on the specimen surface boundary, for example the foam-fabric interface discussed earlier, or vacuum bag-fabric interface. Fluid is likely to advance faster on the surface where voids can aid resin flow depending on pressure (or flow rate) boundary condition and fibre properties that govern capillary effects. Materials with pronounced tow-gap structure are especially prone to exhibit such an effect. In Figure 7.5a a cross section of the cured quasi-UD NCF (G1157 D1300) specimen (5 mm thick) is depicted with a resin flow front in parabolic shape as marked in Figure 7.5b. Such surface effects may be negligible if the preform thickness is small. In such a case, however, it is conceivable that measured permeability is higher than actual fabric permeability due to surface flow effect.

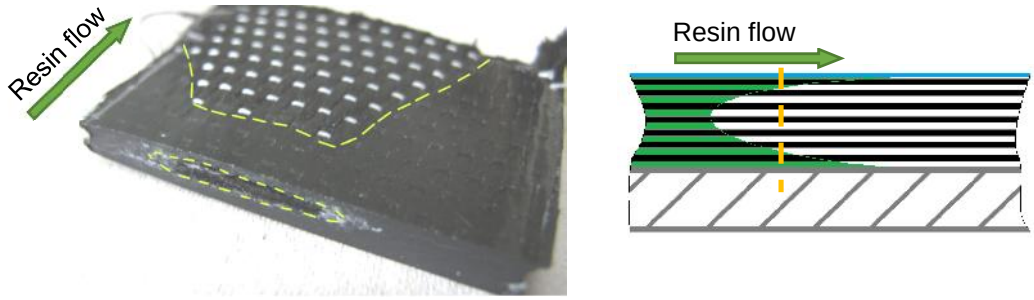

(a) (b)

Figure 7.5 Interface flow effect: a) cross section of the cured specimen and b) schematic illustration of the flow front shape

7.2.4 Distribution medium orthotropic permeability

Distribution medium is considered to be isotropic in all publications to date known to the author. Due to very high permeability it would be difficult to actually measure through-thickness permeability of a

single DM layer and compare it to in-plane permeability. Stacking of DM layers is not appropriate due to a nesting effect on the results. On the other hand, assumption of isotropic distribution medium is justified, if additional media such as separation and perforated foils are also represented in the model. These foils delays resin sink into the preform and make coupled three-dimensional flow apparent, that is reduction of through-thickness flow by separation foils increases the in-plane flow in distribution medium. Such through-thickness flow delay in a model consisting only of preform and distribution medium is conveniently taken into account by using an orthotropic permeability for the distribution medium as was done here. Simulations exploiting such an approach showed good agreement to tests. It is also conceivable that DM permeability values obtained in such way is to a higher extent inherent to the combination of particular foils and, to a lesser extent, to the preform. Further research is needed on this topic.

7.3 Hemisphere infusion simulation

A hemisphere infusion test was performed in a VARI setup, i.e. under flexible cover (Figure 7.6a). Hemisphere infusion simulations, both at macro- and meso-scales, were performed using the PAM-RTM [247] simulation software where VARI capabilities are limited to 2D flow and thus were not exploited in any of the simulations here. Due to this reason quantitative comparisons must be treated with caution. Qualitative views of the flow front, however, is enough to compare the models at different modelling scales and highlight some observations. Figure 7.6a shows a VARI hemisphere infusion test with a clear anisotropic flow and principal permeability directions along and transverse to the stitches; the flow is dominated by race tracking caused by resin channels forming near the stitches. This cannot be properly represented by a macro-scale infusion model as shown in Figure 7.6b.

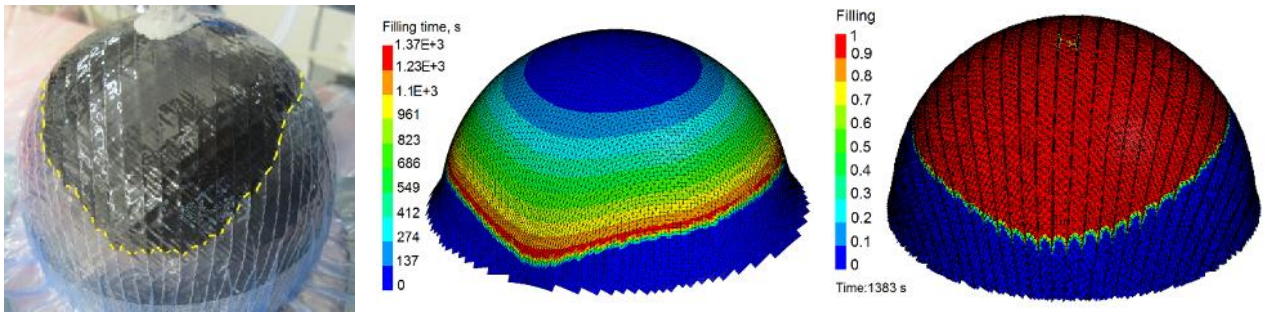

23 min (a) | 23 min (b) | 23 min (c)

Figure 7.6 Hemisphere infusion a) test, b) macro-scale simulation and c) meso-scale simulation

A meso-scale hemisphere infusion simulation was performed using unsheared fabric permeability data and reasonably good agreement to test was obtained as shown in Figure 7.6c. However, as

discussed in section 5.2, shearing of the meso-scale FE model does lead to the cross section area changes of gap and stitch elements which, in turn, has a profound influence on the flow behaviour. Infusion simulation of a flat fabric model sheared to +15° (stitch in tension) resulted in good flow front prediction, whereas a similar simulation on -25° sheared specimen overpredicted flow propagation due to substantially increased cross section area of the stitch elements. A reasonable agreement between meso-scale hemisphere infusion simulation and test was obtained because most of the infused area is sheared to the 'positive' shear angles with stitches stretched and thus permeability values obtained from unsheared fabric specimen are valid. In general, however, redefinition of permeability would be necessary for the gap and stitch elements that have increased cross sectional area.

Another aspect of flow modelling in a gap between the tows is the shape of the gap itself. The shape of an undeformed inter-bundle channel is assumed to be rectangular, whereas in reality it is closer to hyperbolic quadrilateral shape [166]. Normalised permeabilities for different gap cross sections are shown in Figure 7.7 indicating a 20% difference in permeability for rectangular and cusp shaped gaps with a large variation in range depending on width to height ratio. A complex interaction between the flow in a gap and stitch pore network should be investigated in more detail.

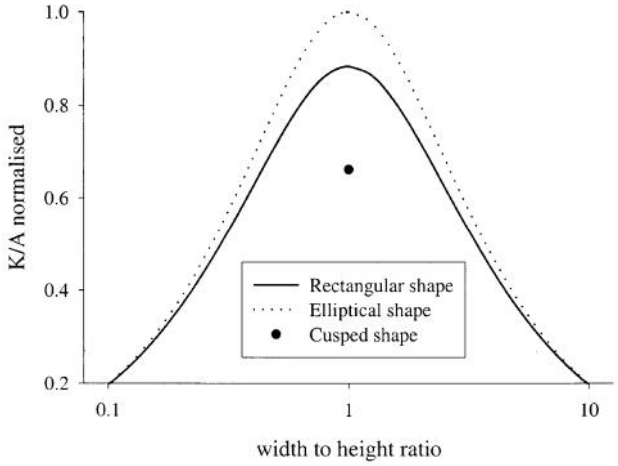

Figure 7.7 Normalised permeability versus ratio of the gap width to height [166]

A closer look at the inter-gap finite elements connecting the two plies in the draped hemisphere model shows heavily distorted elements, especially in regions of high shear angle where tow rotation and relative slippage are most pronounced, as shown in Figure 7.8. Poor element quality will reduce accuracy of the simulation and a remeshing scheme could be considered in the future work as a possible remedy.

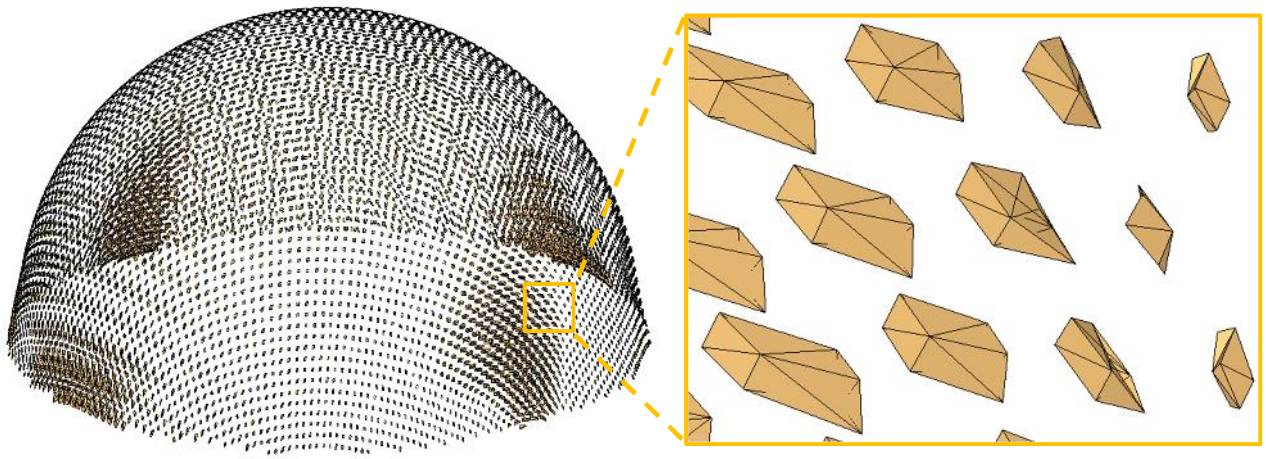

Figure 7.8 Inter-ply gap elements of the hemisphere infusion model

7.4 VARI process simulation

The importance of preform compliance modelling in VARI type infusion was demonstrated in section 6.3 on a stiffened panel demonstrator. A simplified 2D cross section model was not able to replicate some important effects observed in real part such as radial flow front and racetracking at radii, and this resulted in a slightly higher predicted fill time. However, it still provided a far better estimation of the part fill time compared to RTM type infusion simulation, mainly because preform permeability was taken into account as a function of its compliance.

Fabric compliance characterisation is conventionally done by performing compaction tests to measure fabric compaction stiffness versus thickness. Exploitation of unloading compaction data provides input for an accurate estimation of the preform pressure field in a VARI setup. Alternatively, as was shown in this thesis, preform compliance characterisation can be done by combining optical measurements of preform thickness and an iterative simulation scheme. In this instance a non-linear pressure distribution field, which is usually monitored in-situ by pressure sensors, was predicted numerically employing the Carman-Kozeny relationship with fibre volume fraction and preform thickness data. Simulations showed a good agreement of preform thickness distribution during infusion compared to experimental measurements, validating the alternative compliance characterisation scheme.

8 Conclusions

Fabric deformation during forming strongly influences permeability for the infusion. In this thesis two types of deformation have been investigated; namely shear and compaction, and their effect on permeability. State-of-the-art macro-scale modelling method was presented and some of its limitations for coupling drape-infusion analysis highlighted as a motivation for more detailed modelling at a meso-scale. Meso-scale model was used to analyse biaxial stitched NCF draping behaviour with shear as a main deformation mode, and its influence on infusion. Compaction deformation during LRI was analysed at macro-scale using a 2D cross section model of a fabric and dedicated code for VARI process simulation. Increased model and simulation complexity leads to higher computational cost, nevertheless, the price of more detailed analysis is acceptable today and is likely to decrease further in the future.

Refining fabric model by stepping from macro- to meso-scale has allowed explicit representation of fabric constituents such as fibre tow bundles and stitch thread. Mechanical material parameters were derived from appropriate tests including bending, compaction and shear experiments on fabric specimens. A new material model for fibrous tows was created by merging two constitutive material models for lengthwise stiff fibres and non-linear transverse compaction behaviour. Stitch properties characterisation was found to be complicated, and two alternative tests were exploited for calibration using a fabric stretch test and the picture frame shear test.

The developed meso-scale model is capable to represent major fabric deformation mechanisms such as out-of-plane bending, compaction and unsymmetric shear. Additionally, other important phenomena such as tow in-plane buckling, inter-ply sliding (with friction between the plies) and intra-ply sliding, with friction between adjacent tows, were taken into account. These phenomena are not able to be tackled at the macro-scale using conventional mapping or FE methods. Comparison of simulated draping results with a hemisphere draping test showed a high sensitivity of model shear behaviour to stiffness properties of the stitch; however, neither the picture frame, nor the fabric stretch test provided data with which shear angle distribution could be predicted accurately. It has been found that the complex interaction between tows and stitches during fabric deformation makes both their modelling and material characterisation a challenging task. Some suggestions on the model improvement are given in the future work section of this thesis.

Coupling between drape and infusion analysis at the meso-scale raises expectations that draped preform infusion analysis can be performed with fabric permeability characterisation done from a single undeformed specimen test. This would be a great advantage; tedious permeability testing at various shear angles and mapping procedures would be unnecessary. In this instance, tow permeability data was obtained from experimental testing on compacted UD fabrics, and inter-tow gap and stitch element permeabilities were obtained from initial analytical estimations and additional

calibration on unsheared specimen. Ideally, the rearrangement of tows in a deformed model should a-priory lead to proper permeability properties in the deformed fabric. This, however, is only partially achieved with the current model.

Hemisphere infusion simulations using draped fabric architecture have shown the superiority of the proposed meso-scale modelling methods, over traditional macro-scale methods, since preferential flow in stitch domain could be represented causing dominant flow advance in the stitches direction. This was shown to be in agreement with experimental observations. Closer investigation of simulated flow in sheared fabric models, however, found that gap closure, or opening, has a major effect on flow propagation speeds which could not be well predicted. A strategy to account and compensate for such deformation mechanisms by modification of local permeability needs to be developed. Additionally, a slight modification of the unit cell model by inclusion of ‘bridging’ elements between adjacent tows (fibres running through several tows) could also be considered. This would give better agreement with real fabric architecture, and counteract the formation of uninterrupted flow in excessively expanded gap channels which were observed, for example, on the top of the draped hemisphere model.

For the hemisphere infusion simulation an RTM type analysis that assumes constant permeability properties and rigid cavity height was used. Nevertheless, this was sufficient to demonstrate the feasibility of coupling between shear and infusion processes. In vacuum assisted infusion such as VARI, however, pressure change causes changes to fibre volume fraction and permeability, thus analysis of the presented meso-scale hemisphere model would require such options to be integrated in the 3D infusion simulation. As a first step in this direction, a 2D fabric cross section model was analysed with dedicated in-house VARI simulation code and compared with simple 1D infusion experiments.

It was shown that variable fabric permeability which depends on fibre volume fraction can be obtained exploiting either fabric compaction testing or, alternatively, optical measurements of a preform thickness change during VARI in combination with numerical simulation. In the first case it was shown that compaction specimen unloading data range does properly represent fabric relaxation during saturation in VARI process. In the second case it was shown that compaction tests can be omitted, and similar results obtained from preform thickness measurements during an actual VARI test.

Simplified 2D analysis also yielded a further important observation regarding modelling of highly permeable distribution medium used in a VARI setup; namely, that resin flow tends to propagate very fast in-plane and then sink much slower in the through-thickness direction, which is the main function of distribution medium. Additional foils such as perforated ply and peel ply contributes to the slower through-thickness flow behaviour which is conveniently modelled using an orthotropic DM permeability in the presented numerical model with calibration to experimental data obtained from tests.

The following section lists some suggestions on how draping and infusion analysis model could be improved and further developed in the future work.

9 Future work

The meso-scale modelling approach presented can generally be applied to model other types of NCFs, for example unidirectional or multiaxial stitched fabrics. The methodology could, potentially, be used in design and optimisation stages of fabrics with complex architecture and mechanical behaviour as in [265]. However, certain aspects should be addressed in more detail to improve the present model. Improvements to the draping modelling could include:

- representation of tow in-plane shear and lateral compaction,
- representation of tow thickness change as a function of shear angle or lateral compaction,
- improvements to the methodology for characterisation of stitches with stitches sliding relative to the yarns in particular,
- improved frictional contact modelling for adjacent tows.

The model is capable to accommodate large deformations due to plies sliding resulting, however, in highly distorted inter-ply elements. Though negligible in draping analysis, these elements are used as a through-thickness flow domain in the infusion simulation potentially degrading numerical performance and accuracy. A remeshing or element quality correction algorithm could be considered to improve the numerical performance.

Improved infusion simulation modelling could additionally benefit from the following aspects:

- verification and automatic modification of model permeability parameters in a sheared state,
- finite element quality correction,
- modification of the model for multi-layered preform modelling,
- implementation of VARI process simulation in 3D.

With implementation of measures listed above it should be possible to obtain a more versatile simulation model capable to accurately predict draping and infusion behaviour in a virtual domain.

References

[1] Intergovernmental Panel on Climate Change, Climate Change 2014 Synthesis Report, https://www.ipss.ch/.

[2] European Environment Agency, http://www.europa.eu/themes/transport.

[3] S. Carosela, Analyse und Verbeserung des Faserablegeverfahrens Tailored Fibre Placement zur kostenoptimierten Preformherstelung, Universität Stuttgart, 2015.

[4] K. Birkefeld, Virtuelle Optimierung von Geflecht-Preforms unter Berücksichtigung von Fertigungsaspekten, Universität Stuttgart, 2013.

[5] G. Creech, Mesoscopic Finite Element modelling of Non-Crimp Fabrics for drape and failure analyses, Cranfield University, 2006.

[6] A. Pickett, Textiles Process simulation and coupled mesoscopic composite analysis, The Faculty of Aerospace Engineering and Geodesy of the University of Stuttgart, 2010.

[7] H. Lin, M. J. Clifford, A. C. Long and M. Sherburn, “Finite element modelling of fabric shear,” *Modelling and Simulation in Materials Science and Engineering,* vol. 17, pp. 1-16, 2009.

[8] M. Fouinneteau, Damage and failure modelling of carbon and glass 2D braided composites, Cranfield University, 2006.

[9] U. Mohammed, C. Lekakou and M. G. Bader, “Experimental studies and analysis of the draping of woven fabrics,” *Composites: Part A,* vol. 31, pp. 1409-1420, 2000.

[10] O. Rozant, P. E. Bourban and J. A. E. Månson, “Drapabiltity of dry textile fabrics for stampable thermoplastic preforms,” *Composites: Part A,* vol. 31, pp. 1167-1177, 2000.

[11] C. Lekakou, S. Edwards, G. Bell and S. C. Amico, “Computer modelling for prediction of the in-plane permeability of non-crimp stitch bonded fabrics,” *Composites: Part A,* vol. 37, pp. 820-825, 2006.

[12] D. Samir and S. Hamid, “Determination of the in-plane shear rigidity of carbon non-crimp fabric from bias-extension data test,” *Journal of Composite Materials,* vol. 48(22), pp. 2727-2736, 2014.

[13] M. Duhovic, P. Mitschang and D. Bhattacharyya, “Modelling approach for the prediction of stitch influence during woven fabric draping,” *Composites: Part A,* vol. 42(8), pp. 968-978, 2011.

[14] A. C. Long, Design and manufacture of textile composites, Cambridge England: CRC Press, Woodhead Publishing, 2005.

[15] S. V. Lomov and I. Verpoest, “Model of shear of woven fabric and parametric description of shear resistance of glass woven reinforcements,” *Composite Science and Technology,* vol. 66, pp. 919-933, 2006.

[16] N. Hamila and P. Boisse, “Simulations of textile composite reinforcement draping using a new semi-discrete three node finite element,” *Composites: Part B,* vol. 29, pp. 999-1010, 2006.

[17] U. Mohammed, C. Lekakou, L. Dong and M. Bader, “Shear deformation and micromechanics of woven fabrics,” *Composites: Part A,* vol. 31, pp. 299-308, 2000.

[18] A. Cherouat, H. Borouchaki and J. L. Billoët, “Geometrical and Mechanical draping of composite fabric,” *Revue Européenne des Éléments,* vol. 14, pp. 693-707, 2005.

[19] D. S. Ivanov and S. V. Lomov, “Compaction behaviour of dense sheared woven preforms: Experimental observations and analytical predictions,” *Composites: Part A,* vol. 64, pp. 167-176, 2014.

[20] B. Chen, A.-D. Cheng and T.-W. Chou, “A nonlinear compaction model for fibrous preforms,” *Composites: Part A,* vol. 32, pp. 701-707, 2001.

[21] B. Chen, E. Lang and T.-W. Chou, “Experimental and theoretical studies of fabric compaction behaviour in resin transfer molding,” *Materials Science and Engineering,* vol. 317, pp. 188-196, 2001.

[22] Z. R. Chen, L. Ye and T. Kruckenberg, “A micromechanical compaction model for woven fabric preforms. Part I: Single layer,” *Composite Science and Technology,* vol. 66, pp. 3254-3262, 2006.

[23] P. Boisse, A. Gasser and G. Hivet, “Analysis of fabric tensile behaviour: determination of the biaxial tension-strain surfaces and their use in forming simulations,” *Composites: Part A,* vol. 32, pp. 1395-1414, 2001.

[24] S. Comas-Cardona, P. Le Grognec, C. Binetruy and P. Krawczak, “Unidirectional compression of fibre reinforcements. Part 1: A non-linear elastic-plastic behavior,” *Composites Science and Technology,* vol. 67, pp. 507-514, 2007.

[25] S. Bickerton, M. J. Buntain and A. A. Somashekar, “The viscoelastic compression behaviour of liquid composite molding preforms,” *Composites: Part A,* vol. 34, pp. 431-444, 2003.

[26] D. Heider and J. J. Gillespie, “VARTM Variability and Substantiation,” in *Proceedings of FAA JAMS*, Seatle, WA, 2010.

[27] Q. Govignon, S. Bickerton and P. A. Kelly, “Simulation of the reinforcement compaction and resin flow during the complete resin infusion precess,” *Composites: Part A,* vol. 41, pp. 45-57, 2010.

[28] B. Chen and T.-W. Chou, “Compaction of woven-fabric preforms in liquid composite molding processes: single-layer deformation,” *Composites Science and Technology,* vol. 59, pp. 1519-1526, 1999.

[29] N. C. Correia, F. Robitaille, A. C. Long, C. D. Rudd, P. Šinaček and S. G. Advani, “Analysis of the vacuum infusion moulding process: I. Analytical formulation,” *Composites: Part A,* vol. 36, pp. 1645-1656, 2005.

[30] L. Ye, T. Kruckenberg and R. Paton, “Static and vibration compaction and microstructure analysis on plain-woven textile fabrics,” *Composites: Part A,* vol. 39, pp. 488-502, 2008.

[31] R. Umer, S. Bickerton and A. Fernyhough, “The effect of yarn length and diameter on permeability and compaction response of flax fibre mats,” *Composites: Part A,* vol. 42, pp. 723-732, 2011.

[32] J. F. Kessels, A. S. Jonker and R. Akkerman, “Fully 2.5D flow modeling of resin infusion under flexible tooling using unstructured meshes and wet and dry compaction properties,” *Composites: Part A,* vol. 38, pp. 51-60, 2007.

[33] F. Klunker, S. Aranda, G. Ziegman, P. Fideu, P. Baisch and A. Herrmann, “Permeability and compaction models for non crimped fabrics to perform 3D filling simulations of vacuum assisted resin infusion,” in *Proceedings of 9th International Conference on Flow Processing in Composite Materials (FPCM9)*, Montréal (Québec), 2008.

[34] M. H. Andersson, S. T. Lundström and R. B. Gebart, “Numerical model for vacuum infusion manufacturing of polymer composites,” *International Journal of numerical Methods for Heat and Fluid Flow,* vol. 13(3), pp. 383-394, 2003.

[35] Q. Govignon, S. Bickerton, J. Morris and P. A. Kelly, “Full Field monitoring of the resin flow and laminate properties during the resin infusion process,” *Composites: Part A,* vol. 39, pp. 1412-1426, 2008.

[36] D. Yuexin, T. Zhaoyuan, Z. Yan and S. Jing, “Compression Responses of Preform in Vacuum Infusion Process.,” *Chinese Journal of Aeronautics,* vol. 21, pp. 370-377, 2008.

[37] Q. Govignon, S. Bickerton and P. A. Kelly, “Simulation of the complete resin infusion process,” in *Proceedings of the 9th International Conference on Flow Processing in Composite Materials (FPCM-9)*, Montréal (Québec), 2008.

[38] B. Yenilmez, M. Senan and E. M. Sozer, “Variation of part thickness and compaction pressure in vacuum infusion process,” *Composites Science and Technology,* vol. 69, pp. 1710-1719, 2009.

[39] B. Yenilmez and E. M. Sozer, “Compaction of E-glass preforms in the Vacuum Infusion Process, A: Characterization experiments,” *Composites: Part A,* vol. 40, pp. 499-510, 2009.

[40] N. Pearce and J. Summerscales, “The compressibility of a reinforcement fabric,” *Composites manufacturing,* vol. 6, pp. 15-21, 1995.

[41] Z. R. Chen and L. Ye, “A micromechanical compaction model for woven fabric preforms. Part II: Multilayer,” *Composites Science and Technology,* vol. 66, pp. 3262-3272, 2006.

[42] F. Robitaille and R. Gauvin, “Compaction of Textile Reinforcements for Composites Manufacturing. I: Review of Experimental Results,” *Polymer Composites,* vol. 19(2), pp. 198-216, 1998.

[43] M. J. Buntain and S. Bickerton, “Modeling forces generated within rigid liquid composite molding tools. Part A: Experimental study,” *Composites: Part A,* vol. 38, pp. 1729-1741, 2007.

[44] S. V. Lomov, I. Verpoest, T. Peeters, D. Roose and M. Zako, “Nesting in textile laminates: geometrical modelling of the laminates,” *Composites Science and Technology,* vol. 63, pp. 993-1007, 2003.

[45] J. M. Bayldon and I. M. Daniel, “Flow modeling oft eh VARTM process including progressive saturation effects,” *Composites: Part A,* vol. 40, pp. 1044-1052, 2009.

[46] P. Potluri and T. V. Sagar, “Compaction modelling of textile preforms for composite structures,” *Composite Structures,* vol. 86, pp. 177-185, 2008.

[47] D. B. Mastbergen, “Simulation and Testing of Resin Infusion manufacturing Processes for Large Composite Structures,” Montana State University, 2004.

[48] J. Timms, S. Bickerton and P. A. Kelly, “Laminate thickness and resin pressure evolution during axisymmetric liquid composite moulding with flexible tooling,” *Composites: Part A,* vol. 43, pp. 621-630, 2012.

[49] F. Robitaille and R. Gauvin, “Compaction of Textile Reinforcements for Composites Manufacturing. II: Compaction and Relaxation of Dry and H2O-Saturated Woven Reinforcements,” *Polymer Composites,* vol. 19(5), pp. 543-557, 1998.

[50] Z. Cai and T. Gutovski, “The 3-D Deformation Behavior of a Lubricated Fiber Bundle,” *Composite Materials,* vol. 26(8), pp. 1207-1237, 1992.

[51] W. A. Walbran, B. Verleye, S. Bickerton and P. A. Kelly, “Prediction and experimental verification of normal stress distributions on mould tools during Liquid Composite Moulding,” *Composites: Part A,* vol. 43, pp. 138-149, 2012.

[52] J. A. Acheson, P. Simacek and S. G. Advani, “The implications of fibre compaction and saturation on fully coupled VARTM simulation,” *Composites: Part A,* vol. 35, pp. 159-169, 2004.

[53] A. G. Prodromou and J. Chen, “On The relationship between shear angle and wrinkling of textile composite preforms,” *Composites: Part A,* vol. 28, pp. 491-503, 1997.

[54] P. Harrison, M. J. Clifford and A. C. Long, “Shear characterisation of viscous woven textile composites: comparison between picture frame and bias extension experiments,” *Composites Science and Technology,* vol. 64, pp. 1453-1465, 2004.

[55] B. Zhu, T. X. Yu and X. M. Tao, “An experimental study of in-plane large shear deformation of woven fabric composite,” *Composites Science and Technology,* vol. 67, pp. 252-261, 2007.

[56] A. A. Skordos, C. Monroy Aceves and M. P. Sutcliffe, “A simplified rate dependent model of forming and wrinkling of pre-impregnated woven composites,” *Composites: Part A,* vol. 38, pp. 1318-1330, 2007.

[57] S. Allauoi, P. Boisse, P. Chatel, N. Hamina, G. Hivet, D. Soulat and E. Vidal-Salle, “Experimental and numerical analyses of textile reinforcement forming of a tetrahedral shape,” *Composites: Part A,* vol. 42, pp. 612-622, 2011.

[58] W.-R. Yu, J. S. Lee, S. J. Hong and T. J. Kang, “The effect of blank holder force on the stamp forming behaviour of non-crimp fabric with a chain stitch,” *Composites Science and Technology,* vol. 67, pp. 357-366, 2007.

[59] A. P. Mouritz, H. Kong and R. Paton, “Tensile extension properties and deformation mechanisms of multiaxial non-crimp fabrics,” *Composite Structures,* vol. 66, pp. 249-259, 2004.

[60] P. Boisse, S. Bel, N. Hamila and F. Dumont, “Finite element model for NCF composite reinforcement preforming: Importance of inter-ply sliding,” *Composites: Part A,* vol. 43, pp. 2269-2277, 2012.

[61] I. Verpoest and S. V. Lomov, “Virtual textile composites software WiseTex: Integration with micro-mechanical, permeability and structural analysis,” *Composites Science and Technology,* vol. 65, pp. 2563-2574, 2005.

[62] G. Creech and A. K. Pickett, “Meso-modelling of non-crimp fabric composites for coupled drape and failure analysis,” *J Mater Sci,* vol. 41, p. 6725–6736, 2006.

[63] J. L. Hu and Y. T. Zhang, “The KES Shear Test for Fabrics,” *Textile Research,* vol. 67(9), pp. 654-664, 1997.

[64] J. Wang, J. R. Page and R. Paton, “Experimental investigation of the draping properties of the reinforcement fabrics,” *Composites Science and Technology,* vol. 58, pp. 229-237, 1998.

[65] S. Kawabata, “The standardisation and analysis of hand evaluation,” The Textile machinery Society of Japan, 1980.

[66] P. Potluri, D. A. Perez Ciurezu and R. B. Ramgulam, “Measurement of meso-scale shear deformations for modelling textile composites,” *Composites: Part A,* vol. 37, pp. 303-314, 2006.

[67] J. Cao, R. Akkerman, P. Boisse, J. Chen, H. S. Cheng, E. F. de Graaf, J. L. Groczyca, P. Harrison, G. Hivet, J. Launay, W. Lee, L. Liu, S. V. Lomov, A. Long, E. de Luycker, F. Morestin, J. Padvoiskis, X. Q. Peng, J. Sherwood , T. Stoilova, X. M. Tao, I. Verpoest, A. Willems, J. Wiggers, T. X. Yu and B. Zhu, “Characterization of mechanical behaviour of woven fabrics: Experimental methods and benchmark results,” *Composites: Part A,* vol. 39, pp. 1037-1053, 2008.

[68] L. Li, Y. Zhao, H. Vuong, Y. Chen, J. Yang and Y. Duan, “In-plane shear investigation of biaxial carbon non-crimp fabrics with experimental tests and finite element modeling,” *Materials and Design,* vol. 63, pp. 757-765, 2014.

[69] R. M. Sidhu, R. C. Averill, M. Riaz and F. Pouboghrat, “Finite element analysis of textile composite preform stamping,” *Composite Structures,* vol. 52, pp. 483-497, 2001.

[70] K. Potter, “Bias extension measurements on cross-plied unidirectional prepreg,” *Composites: Part A,* vol. 33, pp. 63-73, 2002.

[71] T. Gereke, O. Döbrich, M. Hübner and C. Cherif, “Experimental an computational composite textile reinforcement forming: A review.,” *Composites: Part A,* vol. 46, pp. 1-10, 2013.

[72] A. S. Milani, J. A. Nemes, R. C. Abeyaratne and G. A. Holzapfel, “A method for the approximation of non-uniform fibre misalignment in textile composites using a picture frame test,” *Composites: Part A,* vol. 38, pp. 1493-1501, 2007.

[73] A. K. Pickett, “Composites material model for draping simulation,” Institute for Aicraft Design, University of Stuttgart, 2008.

[74] S. V. Lomov, M. Barbuski, T. Stoilova, I. Verpoest, R. Akkerman, R. Loendersloot and R. H. ten Thije, “Carbon composites based on multiaxial multiply stitch preforms. Part 3: Biaxial tension, picture frame and compression tests of the preforms,” *Composites: Part A,* vol. 36, pp. 1188-1206, 2005.

[75] W. R. Yu, P. Harrison and A. Long, “Finite element forming simulation for non-crimp fabrics using a non-orthogonal constitutive equation,” *Composites: Part A,* vol. 36, pp. 1079-1093, 2005.

[76] G. B. McGuinness and C. M. Ó Brádaigh, “Characterisation of thermoplastic composite melts in rhombus-shear: the picture frame experiment,” *Composites: Part A, 1998; 29: 115-132,* vol. 29, pp. 115-132, 1998.

[77] X. Q. Peng, J. Cao, J. Chen, P. Xue, D. S. Lussier and L. Liu, “Experimental and numerical analysis on normalization of picture frame tests for composite materials,” *Composites Science and Technology,* vol. 64, pp. 11-21, 2004.

[78] J. Skelton, “Fundamentals of fabric Shear,” *Textile Research journal,* 1979.

[79] G. Lebrun, M. N. Bureau and J. Denault, “Evaluation of bias-extension and picture-frame test methods for measurement of Intraply shear properties of PP/glass commingled fabrics,” *Composite Structures,* vol. 61, pp. 341-352, 2003.

[80] F. Loix, P. Badel, L. Orgéas, C. Gendreau and P. Boisse, “Woven fabric permeability: From textile deformation to fluid flow mesoscale simulations,” *Composites Science and Technology,* vol. 68, pp. 1624-1630, 2008.

[81] P. Boisse, B. Zouari and A. Gasser, “A mesoscopic approach for the simulation of woven fibre composite forming,” *Composites Science and Technology,* vol. 65, pp. 429-436, 2005.

[82] X. Peng and Z. U. Rehman, “Textile composite double dome stamping simulation using a non-orthogonal constitutive model,” *Composites Science and Technology,* vol. 71, pp. 1075-1081, 2011.

[83] K. Vanclooster, S. V. Lomov and I. Verpoest, “Experimental validations of forming simulations of fabric reinforced polymers using an unsymmetrical mould configuration,” *Composites: Part A,* vol. 40, pp. 530-539, 2009.

[84] C. Cherif, Textile Werkstoffe für den Leichtbau, Berlin Heidelberg: Springer-Verlag, 2011.

[85] J. Page and J. Wang, “Prediction of shear force using 3D non-linear FEM analyses for a plain weave carbon fabric in a bias extension state,” *Finite Elements in Analysis and Design,* vol. 38, pp. 755-764, 2002.

[86] Standard Test Method for Stiffness of Fabrics. Designation: D 1388-96, Reaprooved 2002, http://www.astm.org/DATABASE.CART/HISTORICAL/D1388-96R02.htm.

[87] X. Peng and F. Ding, “Validation of non-orthogonal constitutive model for woven composite fabrics via hemispherical stamping simulation,” *Composites: Part A,* vol. 42, pp. 400-407, 2011.

[88] S. V. Lomov, I. Verpoest, M. Barbuski and J. Laparre, “Carbon composites based on multiaxial multiply stitched performs. Part 2. KES-F characterization of the deformability of the preforms at low loads,” *Composites: Part A,* vol. 34, pp. 359-370, 2003.

[89] A. Pickett, A. Erber, T. von Reden and K. Drechsler, “Comparison of analytical and Finite Element simulation of 2D braiding,” *Plastics, Rubber and Composites,* vol. 38(9/10), pp. 387-395, 2009.

[90] D. M. Mulvihill, O. Smerdova and M. P. Sutcliffe, “Friction of carbon fibre tows,” *Composites: Part A,* vol. 93, pp. 185-198, 2017.

[91] J. L. Gorczyca, J. A. Sherwood and J. Chen, “A friction model for use with a commingled fiberglass-polypropylene plain-weave fabric and the metal tool during thermostamping,” *Revue Européenne des Éléments,* Vols. 14(6-7), pp. 729-751, 2005.

[92] P. Badel, E. Vidal-Sallé and P. Boisse, “Computational determination of in-plane shear mechanical behaviour of textile composite reinforcements,” *Computational Materials Science,* vol. 40, pp. 439-448, 2007.

[93] A. C. Long and C. D. Rudd, “A simulation of reinforcement deformation during the production of preforms for liquid moulding processes,” *Part B: Journal of Engineering Manufacture,* vol. 208, pp. 269-278, 1994.

[94] Y. Miao, E. Zhou, Y. Wang and B. A. Cheeseman, “Mechanics of textile composites: Micro-geometry,” *Composites Science and Technology,* vol. 68, pp. 1671-1678, 2008.

[95] H. Finckh, “Numerische Simulation der mechanischen Eigenschaften textile Flächengebilde – Gewebeherstelung,” in *LS-DYNA Anwenderforum*, Bamberg, 2004.

[96] C. Mack and H. M. Taylor, “Fitting of Woven Cloth to Surfaces,” *Journal of the Textile institute Transactions,* vol. 39, pp. 477-488, 1956.

[97] L. Dong, C. Lekakou and M. G. Bader, “Processing of Composites: Simulations of the Draping of Fabrics with Updated Material Behaviour Law,” *Composite Materials,* vol. 35(2), pp. 138-163, 2001.

[98] A. C. Long, B. J. Souter, F. Robitaille and C. D. Rudd, “Effects of fibre architecture on reinforcement fabric deformation,” *Plastics, Rubber and Composites,* vol. 31(2), pp. 87-97, 2002.

[99] S. G. Hancock and K. D. Potter, “The use of kinematic drape modelling to inform the hand lay-up of complex composite components using woven reinforcements,” *Composites: Part A,* vol. 37, pp. 413-422, 2006.

[100] S. B. Sharma and M. P. Sutcliffe, “A simplified finite element model for draping of woven material.,” *Composites: Part A,* vol. 35, pp. 637-643, 2004.

[101] F. Trochu, A. Hammami and Y. Benoit, “Prediction of fibre orientation and net shape definition of complex composite parts,” *Composites: Part A,* vol. 27, pp. 319-328, 1996.

[102] L. Dong, C. Lekakou and M. G. Bader, “Solid-mechanics finite element simulations of the draping of fabrics: a sensitivity analysis,” *Composites: Part A,* vol. 31, pp. 639-652, 2000.

[103] S. V. Lomov, D. S. Ivanov, I. Verpoest, M. Zako, T. Kurashiki, H. Nakai and S. Hirosawa, “Meso-FE modelling of textile composites: Road map, data flow and algorithms,” *Composites Science and Technology,* vol. 67, pp. 1870-1891, 2007.

[104] A. Gasser, P. Boisse and S. Hanklar, “Mechanical behaviour of dry fabric reinforcements. 3D simulations versus biaxial tests,” *Computational Materials Science,* vol. 17, pp. 7-20, 2000.

[105] Open source textile model generator, Polymer Composites Group, The university of Nottingham, http://texgen.sourceforge.net.

[106] S. V. Lomov, I. Verpoest, J. Cichosz, C. Hahn, D. S. Ivanov and B. Verleye, “Meso-level textile composites simulations: Open data exchange and scripting,” *Journal of Composite Materials,* vol. 0(0), pp. 1-17, 2013.

[107] P. Molnár, A. Ogale, R. Lahr and P. Mitschang, “Influence of drapability by using stitching technology to reduce fabric deformation and shear during thermoforming,” *Composites Science and Technology,* vol. 67, pp. 3386-3393, 2007.

[108] A. Pickett, J. Sirtautas and F. Masseria, “Process and challenges for resin infusion simulation of large structural composite parts,” in *CCeV at DLR*, Stuttgart, 2013.

[109] R. Chaudhari, F. Viebahn, M. Karcher, P. Elsner and F. Henning, “Characterization of high-performance composites manufactured by using High-Pressure RTM process variants,” in *Proceedings of 12th SPE Automotive Composites Conference and Exibition (ACCE12)*, Troy, MI, 2012.

[110] S. Bickerton and S. G. Advani, “Experimental investigation and flow visualization of the resin-transfer moldfilling process in a non-planar geometry,” *Composites Science and Technology,* vol. 57, pp. 23-33, 1997.

[111] S. W. Tsai, Strength and life of composites, Stanford: Department of Aeronautics and Astronautics, Stanford University, 2008.

[112] Bavaria Yachtbau GmbH, https://www.bavaria-yachtbau.com/de.html.

[113] Siemens AG, Siemens Wind Power, http://www.siemens.com/global/en/home/markets/wind/turbines/technology/blades.html.

[114] K. Hoes, D. Dinescu, H. Sol, R. S. Parnas and S. V. Lomov, “Study of nesting induced scatter of permeability values in layered reinforcement fabrics,” *Composites: Part A,* vol. 35, pp. 1407-1418, 2004.

[115] E. B. Belov, S. V. Lomov, I. Verpoest, T. Peters, D. Roose, R. S. Parnas, K. Hoes and H. Sol, “Modelling of permeability of textile reinforcements: lattice Boltzmann method,” *Composites Science and Technology,* vol. 64, pp. 1069-1080, 2004.

[116] A. Endruweit, X. Zeng and A. C. Long, “Effect of yarn cross-sectional shape on resin flow through inter-yarn gaps in textile reinforcements,” in *Proceedings of 13th International Conference on Flow Processing in Composite Materials (FPCM13)*, Kyoto, 2016.

[117] R. Arbter, J. M. Beraud, C. Binetruy, L. Bizet, J. Bréard, S. Comas-Cardona, C. Demaria, A. Endruweit, P. Ermanni, F. Gommer, S. Hasanovic, P. Henrat, F. Klunker, B. Laine, S. Lavanchy, S. V. Lomov, A. Long, V. Michaud, G. Morren, E. Ruiz, H. Sol, F. Trochu, B. Verleye, M. Wietgrefe, W. Wu and G. Ziegmann, “Experimental determination of the permeablity of textiles: A benchmark exercise,” *Composites: Part A,* vol. 42, pp. 1157-1168, 2011.

[118] G. Morren, M. Bottiglieri, S. Bossuyt, H. Sol, D. Lecompte, B. Verleye and S. V. Lomov, “A reference specimen for permeability measurements of fibrous reinforcements for RTM,” *Composites: Part A,* vol. 40, pp. 244-250, 2009.

[119] E. Hohseni Languri, I. G. Bennet, R. Masoodi and K. M. Pilai, “A reference porous medium made by rapid prototyping as a calibration tool for permeability measurement,” in *Proceedings of 10th International Conference on Flow Processing in Composite Materials (FPCM10)*, Monte Verità, Ascona, 2010.

[120] A. P. Vechart, R. Masoodi and K. M. Pillai, “Design and evaluation of an idealized porous medium for calibration of permeability measuring devices,” *Applied Composites Letters,* vol. 19(1), pp. 35-49, 2010.

[121] N. Vernet, E. Ruiz, S. Advani, J. B. Alms, M. Aubert, M. Barbuski, B. Barari, J. M. Beraud, D. C. Berg, N. Correia, M. Danzi, T. Delavière, M. Dickert, C. Di Fratta, A. Endruweit, P. Ermanni, G. Francucci, J. A. Garcia, A. George, C. Hahn, F. Klunker, S. V. Lomov, A. Long, B. Louis, J. Maldonado, R. Meier, V. Michaud, H. Perrin, K. Pillai, E. Rodriguez, F. Trochu, S. Verheyden, M. Wietgrefe, W. Xiong, S. Zarebma and G. Ziegmann, “Experimental determination of the permeability of engineering textiles: Benchmark II,” *Composites: Part A,* vol. 61, pp. 172-184, 2014.

[122] A. George, Optimization of Resin Infusion Processing for Composite Materials: Simulation and Characterization Strategies, Universität Stuttgart, 2011.

[123] S. Drapier, J. Monatte, O. Elbouazzaoui and P. Henrat, “Characterisation of transient through-thickness permeabilities of Non Crimp New Concept (NC2) multiaxial fabrics,” *Composites: Part A,* vol. 36, pp. 877-892, 2005.

[124] P. B. Nedanov and S. G. Advani, “A method to determine 3D Permeability of Fibrous Reinforcements,” *Journal of Composite materials,* vol. 36, pp. 241-254, 2002.

[125] E. Poodts, G. Minak, E. Dolcini and L. Donati, “FE analysis and production experience of a sandwich structure component manufactured by means of vacuum assisted resin infusion process,” *Composites: Part B,* vol. 53, pp. 179-186, 2013.

[126] A. Endruweit, A. C. Long, F. Robitaille and S. D. Rudd, “Influence of stochastic fibre angle variations on the permeability of bi-directional textile fabrics,” *Composites: Part A,* vol. 37, pp. 122-132, 2006.

[127] Q. Liu, R. S. Parnas and H. S. Giffard, “New set-up for in-plane permeability measurement,” *Composites: Part A,* vol. 38, pp. 954-962, 2007.

[128] F. Klunker, M. Danzi and P. Ermanni, “Fiber deformation as a result of fluid injection: modeling and validation in the case of saturated permeablity measurements in through thickness direction,” *Composite Materials,* vol. 0(0), pp. 1-15, 2014.

[129] J. Bréard, Y. Henzel, F. Trochu and R. Gauvin, “Analysis of Dynamic Flows Through Porous Media. Part I: Comparison between Saturated and Unsaturated flows in Fibrous Reinforcements,” *Polymer Composites,* vol. 24(3), pp. 391-408, 2003.

[130] E. Rodriguez, F. Giacomelli and A. Vázquez, “Permeability-Porosity Relationship in RTM for Different Fiberglass and Natural Reinforcements,” *Composite Materials,* vol. 38(3), pp. 259-268, 2004.

[131] I. Patiño, C. Vargas and J. Vanegas, “Methods for permeability measurements of fibrous reinforced preforms,” *Rev. Fac. Ing. Univ. Antioquia,* vol. 72, pp. 186-202, 2014.

[132] P. Ermanni, “Composites Technologien,” ETH Zürich, 2007.

[133] F. Trochu, E. Ruiz, V. Achim and S. Soukane, “Advanced numerical simulation of liquid composite molding for process analysis and optimization,” *Composites: Part A,* vol. 37, pp. 890-902, 2006.

[134] A. Endruweit, P. Glower, K. Head and A. C. Long, “Mapping of the fluid distribution in impregnated reinforcement textiles using Magnetic Resonance Imaging: Methods and issues,” *Composites: Part A,* vol. 42, pp. 265-273, 2011.

[135] K. Hoes, D. Dinescu, H. Sol, M. Vanheule, R. S. Parnas, Y. Luo and I. Verpoest, “New setup for measurement of permeability properties of fibrous reinforcements for RTM,” *Composites: Part A,* vol. 33, pp. 959-969, 2002.

[136] E. M. Sozer, B. Chen, P. J. Graham, S. Bickerton, T. W. Chou and S. G. Advani, “Characterization and prediction of compaction force and preform permeability of woven fabrics during the resin transfer molding process,” in *Proceedings of 5th Int. Flow Processes in Composite Materials*, Plymouth, UK, 1999.

[137] P. Ouagne and J. Bréard, “Continuous transverse permeability of fibrous media,” *Composites: Part A,* vol. 41, pp. 22-28, 2010.

[138] K. Okonkwo, P. Simacek, S. G. Advani and R. S. Parnas, “Characterization of 3D fiber preform permeability tensor in radial flow using an inverse algorithm based on sensors and simulation,” *Composites: Part A,* vol. 42, pp. 1283-1292, 2011.

[139] B. Cosson, S. Commas-Cardona, S. Bickerton, J. M. Gran, F. Zhang and C. Binetruy, “An optically bassed inverse problem to measure in-plane permeability fields,” in *Proceedings of 10th International Conference on Flow Processing in Composite Materials (FPCM10)*, Monte Verità, Ascona, 2010.

[140] M. A. Yalcinkaya, A. Sarioglu and M. Sozer, “A novel mold design for one-continiuous permeability measurement of fiber preforms,” *Reinforced Plastics and Composites,* vol. 34(11), pp. 915-930, 2015.

[141] C. Fratta, G. Koutsoukis, F. Klunker, F. Trochu and P. Ermanni, “Characterization of Anisotropic Permeability From Flow Front Angle Measurements,” *Polymer Composites,* pp. 2037-2052, 2016.

[142] S. Sharma and D. A. Siginer, “Permeability Measurement Methods in Porous Media of Fiber Reinforced Composites,” *Applied Mechanics Reviews,* vol. 63, pp. 020802-1-19, 2010.

[143] P. A. Kelly and S. Bickerton, “A comprehensive filling and tooling force analysis for rigid mould LCM processes,” *Composites: Part A,* vol. 40, pp. 1685-1697, 2009.

[144] A. Hammami, F. Trochu, R. Gauvin and S. Wirth, “Directional Permeability Measurement of Deformed Reinforcement,” *Reinforced Plastics and Composites,* vol. 15, pp. 552-562, 1996.

[145] J. Slade, K. M. Pillai and S. G. Advani, “Investigation of Unsaturated Flow in Woven, Braided and Stitched Fiber Mats During Mold-Filling in Resin Transfer Molding,” *Polymer Composites,* vol. 22(4), pp. 491-505, 2001.

[146] S. Bickerton, E. M. Sozer, P. J. Graham and S. G. Advani, “Fabric structure and mold curvature effects on preform permeability and mold filling in the RTM process. Part I. Experiments,” *Composites: Part A,* vol. 31, pp. 423-438, 2000.

[147] G. Estrada, C. Vieux-Pernon and S. G. Advani, “Experimental Characterization of the Influence of Tackifier Material on Preform Permeability,” *Journal of Composite Materials,* vol. 36(19), pp. 2297-2310, 2002.

[148] M. Devillard, K. T. Hsiao, A. Gocke and S. G. Advani, “On-line Characterization of Bulk Permeability and Race-tracking During Filling Stage in Resin Transfer Molding Process,” *Composite Materials,* vol. 37(17), pp. 1525-1541, 2003.

[149] H. S. Sas, E. B. Wurtzel, P. Simacek and S. G. Advani, “Effect of relative ply orientation on the through-thickness permeability of unidirectional fabrics,” *Composites Science and Technology,* vol. 96, pp. 116-121, 2014.

[150] V. H. Hammond and A. C. Loos, “The Effects of Fluid Type and Viscosity on the Steady-State and Advancing Front Permeability Behaviour of Textile Preforms,” *Journal of Reinforced Plastics and Composites,* vol. 16(1), pp. 50-72, 1997.

[151] S. Bickerton, P. Šimaček, E. Guglielmi and S. G. Advani, “Investigation of draping and its effects on the mold filling process during manufacturing of a compound curved composite part,” *Composites: Part A,* vol. 28, pp. 801-816, 1997.

[152] A. Hammami, F. Gauvin and F. Trochu, “Modeling the edge effect in liquid composites molding,” *Composites: Part A,* vol. 29, pp. 603-609, 1998.

[153] C. H. Shin and L. J. Lee, “Effect of Fiber Architecture on Permeability in Liquid Composite Molding,” *Polymer Composites,* vol. 19(5), pp. 626-639, 1998.

[154] L. Ding, C. Shih, C. Liang, C. Zhang and B. Wang, “In situ measurement and monitoring of whole-filed preform for liquid composite molding processes,” *Composites: Part A,* vol. 34, pp. 779-789, 2003.

[155] Y. Hou, S. Comas-Cardona, C. Binetruy and S. Drapier, “Gas transport in fibrous media: Application to in-plane permeability measurement using transient flow,” *Composite Materials,* vol. 47, pp. 2237-2247, 2012.

[156] C. M. Hickey, J. G. Timms and S. Bickerton, “Compaction response and air permeability characterisation of out-of-autoclave prepreg materials,” in *Proceedings of 11th International Conference on Flow Processing in Composite Materials (FPCM11)*, Auckland, 2012.

[157] E. Saldaeva, Through thickness air permeability and thermal conductivity analysis for textile materials, University of Nottingham, 2009.

[158] N. Wegh, M. Wagner, D. Gaudlitz, H. Finckh and M. Klein, “Numerical simulation of filling process in resin transfer molding,” in *Proceedings of 13th International Conference on Flow Processing in Composite Materials (FPCM13)*, Kyoto, 2016.

[159] C. L. Lai and W. B. Young, “Model Resin Permeation of Fiber Reinforcements After Shear Deformation,” *Polymer Composites,* vol. 18(5), pp. 642-647, 1997.

[160] S. Mekic and B. Bakke, “Radial infusion models for permeability measurements of compressed fibrous beds,” *International Journal of Multiphase Flow,* vol. 48, pp. 1-10, 2013.

[161] H. Tan and K. M. Pillai, “Multiscale modelling of unsaturated flow in dual-scale fiber preforms of liquid composite molding I: Isothermal flows,” *Composites: Part A,* vol. 43, pp. 1-13, 2012.

[162] B. Z. Babu and K. M. Pillai, “Experimental Investigation of the Effect of Fiber-mat Architecture on the Unsaturated Flow in Liquid Composite Molding,” *Composite Materials,* vol. 38(1), pp. 57-79, 2004.

[163] A. Endruweit and A. C. Long, “A model for the in-plane permeability of triaxially braided reinforcements,” *Composites: Part A,* vol. 42, pp. 165-172, 2011.

[164] A. C. Long, C. D. Rudd, M. Blagdon and P. Smith, “Characterizing the processing and performance of aligned reinforcements during preform manufacture,” *Composites: Part A,* vol. 27, pp. 247-253, 1996.

[165] A. Endruweit, X. Zeng and A. C. Long, “Effect of specimen history on structure and in plane permeability of woven fabrics,” *Journal of Composite Materials,* vol. 49(13), pp. 1563-1578, 2015.

[166] T. S. Lundström, “Lundström TS. The permeability of non-crimp stitched fabrics. Composites: Part A, 2000; 31: 1345-1353,” *Composites: Part A,* vol. 31, pp. 1345-1353, 2000.

[167] J. Verrey, V. Michaud and J. A. Månson, “Dynamic capillary effects in liquid composite moulding with non-crimp fabrics,” *Composites: Part A,* vol. 37, pp. 92-102, 2006.

[168] R. Mathur, D. Heider, C. Hoffmann, W. J. Gillespie, S. G. Advani and B. K. Fink, “Flow Front Measurements and Model Validation in the vacuum Assisted Resin Transfer Molding Process,” *Polymer Composites,* vol. 22(4), pp. 477-490, 2001.

[169] N. R. Pearce, J. Summerscales and F. J. Guild, “Improving the transfer moulding process for fabric-reinforced composites by modification of the fabric architecture,” *Composites: Part A,* vol. 31, pp. 1433-1441, 2000.

[170] N. Kuentzer, P. Simacek, S. G. Advani and S. Walsh, “Correlation of void distribution to VARTM manufacturing techniques,” *Composites: Part A,* vol. 28, pp. 802-813, 2007.

[171] D. S. Cairns, D. R. Humbert and J. F. Mandell, “Modeling of resin transfer molding of composite materials with oriented unidirectional plies,” *Composites: Part A,* vol. 30, pp. 375-383, 1999.

[172] S. Amico and C. Lekakou, “An experimental study of the permeability and capillary pressure in resin-transfer moulding,” *Composites Science and Technology,* vol. 61, pp. 1945-1959, 2001.

[173] A. Endruweit and P. Ermanni, “The in-plane permeability of sheared textiles. Experimental observations and a predictive conversion model,” *Composites: Part A,* vol. 35, pp. 439-451, 2004.

[174] C. Demaria, E. Ruiz and F. Trochu, “In-Plane Anisotropic Permeability Characterization of Deformed Woven Fabrics by Unidirectional Injection. Part I: Experimental Results,” *Polymer Composites,* vol. 28, pp. 797-811, 2007.

[175] L. Skartsis, B. Khomami and J. L. Kardos, “Resin Flow Through Fiber Beds During Composite Manufacturing Processes. Part II: Numerical and Experimental Studies of Newtonian Flow Through Ideal and Actual Fiber Beds,” *Polymer Engineering and Science,* vol. 32(4), pp. 231-230, 1992.

[176] L. Joubaud, V. Achim and F. Trochu, “Numerical Simulation of Resin Infusion and Reinforcement Consolidation Under Flexible Cover,” *Polymer Composites,* vol. 26, pp. 417-427, 2005.

[177] R. C. Lam and J. L. Kardos, “The Permeability and Compressibility of Aligned and Cross-Plied Carbon Fiber Beds During Processing of Composites,” *Polymer engineering and science,* vol. 31(4), pp. 1064-1070, 1991.

[178] R. Gauvin, F. Trochu, Y. Lemenn and L. Diallo, “Permeability Measurement and Flow Simulation Through Fiber Reinforcement,” *Polymer Composites,* vol. 17(1), pp. 34-42, 1996.

[179] M. Louis and U. Huber, “Investigation of shearing effects on the permeability of woven fabrics and implementation into LCM simulation,” *Composites Science and Technology,* vol. 63, pp. 2081-2088, 2003.

[180] N. Kuentzer, P. Simacek, S. G. Advani and S. Walsh, “Permeability characterisation of dual scale fibrous porous media,” *Composites: Part A,* vol. 37, pp. 2057-2068, 2006.

[181] C. Kracke, B. Staudt, S. Bickerton and P. Mitschang, “An experimental study on the influence of flow channel geometry on the flow front progression in resin transfer moulding,” in *Proceedings of 13th International Conference on Flow Processing in Composite Materials (FPCM13)*, Kyoto, 2016.

[182] N. Patel and L. James Lee, “Modeling of Void Formation and Removal in Liquid Composite Molding. Part I: Wettability Analysis,” *Polymer Composites,* vol. 17(1), pp. 96-103, 1996.

[183] K. J. Ahn and J. C. Sefers, “Simulateneous Measurements of Permeability and Capillary Pressure of Thermosetting Matrices in Woven Fabric Reinforcements,” *Polymer Composites,* vol. 16(3), pp. 146-152, 1991.

[184] J. Bréard, G. Saouab and G. Bouquet, “Numerical simulation of void formation in LCM,” *Composites: Part A,* vol. 34, pp. 517-523, 2003.

[185] P. Šimáček and S. G. Advani, “Permeability for a Woven Fabric,” *Polymer Composites,* vol. 17(6), pp. 887-899, 1997.

[186] S. V. Lomov, G. Huysmans, Y. Luo, R. S. Parnas, A. Prodromou, I. Verpoest and F. R. Phelan, “Textile composites: modelling strategies,” *Composites: Part A,* vol. 32, pp. 1379-1394, 2001.

[187] M. A. Spaid and F. R. J. Phelan, “Lattice Boltzmann methods for modelling microscale flow in fibrous porous media,” *Physics of Fluids,* vol. 9, pp. 2468-2474, 1997.

[188] Z. Chen, L. Ye and H. Liu, “Effective permeabilities of multilayer fabric preforms in liquid composite moulding,” *Composite Structures,* vol. 66, pp. 351-357, 2004.

[189] L. Fang, J. Jiang, J. Wang and C. Deng, “Effect of Nesting on the Out-of-Plane Permeability of Unidirectional Fabrics in Resin Transfer Molding,” *Applied Composite Materials,* vol. 22, pp. 231-249, 2015.

[190] J. F. Delerue, S. V. Lomov, R. S. Parnas, I. Verpoest and M. Wevers, “Pore Network Modeling of Permeability for Textile Reinforcements,” *Polymer Composites,* vol. 24(3), pp. 344-357, 2003.

[191] T. S. Lundström, “Computational fluid dynamics applied to composites manufacturing,” in *Proceedings of 13th International Conference on Flow Processing in Composite Materials (FPCM13)*, Kyoto, 2016.

[192] J. Dittmann, S. Hügle, P. Seif, L. Kauffmann and P. Middendorf, “Permeability prediction using porous yarns in dual-scale simulation with OpenFoam,” in *Proceedings of 21st International Conference on Composite Materials (ICCM21)*, Xi’an, 2017.

[193] E. E. Swery, R. Meier, S. V. Lomov, C. Hahn, P. A. Kelly and I. Straumit, “Verifications of FlowTex solver using Ansys CFX – examining the permeability prediction method on a range of textile architecture models,” in *Proceedings of 16th European Conference on Composite Materials (ECCM-16)*, Seville, Spain, 2014.

[194] X. Zeng, A. Endruweit, L. P. Brown and A. C. Long, “Numerical prediction of in-plane permeability for multilayer woven fabrics with manufacture-induced deformation,” *Composites: Part A,* vol. 77, pp. 266-274, 2015.

[195] C. Hahn, C. Binetruy, R. Hinterholz and K. Drechsler, “A numerical method of permeability determination for RTM process Simulation,” in *Proceedings of 11th International Conference on Flow Processing in Composite Materials (FPCM11)*, Auckland, 2012.

[196] I. Straumit, C. Hahn, E. Winterstein, B. Plank, M. Wevers and S. V. Lomov, “Computation of permeability of a non-crimp carbon textile reinforcement based on x-ray computed tomography images,” in *Proceedings of 13th International Conference on Flow Processing in Composite Materials (FPCM13)*, Kyoto, 2016.

[197] I. Straumit, C. Hahn, E. Winterstein, B. Plank and S. V. Lomov, “Computation of permeability of a non-crimp carbon textile reinforcement based on X-ray computed tomography images,” *Composites: Part A,* vol. 81, pp. 289-295, 2016.

[198] J. Dittmann, S. Hügle and P. Middendorf, “Numerical 3D permeability prediction using computational fluid dynamics,” in *Proceedings of 13th International Conference on Flow Processing in Composite Materials (FPCM13)*, Kyoto, 2016.

[199] G. W. Lee, N. J. Lee, J. Jang, K. J. Lee and J. D. Nam, “Effects of surface modification on the resin-transfer moulding (RTM) of glass-fibre/unsaturated-polyester composites,” *Composites Science and Technology,* vol. 62, pp. 9-16, 2002.

[200] R. Bridson and M. Müller-Fisher, “Fluid Simulation, SIGGRAPH 2007 course notes, The University of British Columbia,” 10 August 2007. [Online]. Available: http://www.cs.ubc.ca/_rbridson/fluidsimulation.

[201] I. Rybak, Mathematical modeling of coupled free flow and porous medium systems, Institut fuer Angewandte Analysis und Numerische Simulation, Lehrstuhl fuer Angewandte Mathematik, Universität Stuttgart, 2016.

[202] P. Celle, S. Drapier and J. M. Bergheau, “Numerical modelling of liquid infusion into fibrous media undergoing compaction,” *European Journal of Mechanics A/Solids,* vol. 27, pp. 647-661, 2008.

[203] H. Darcy, Les fontaines publiques de la Ville de Dijon, Dalmont, Paris, 1856.

[204] C. Binétruy, B. Hilaire and J. Pabiot, “The interactions between flows occurring inside and outside fabric tows during RTM,” *Composites Science and Technology,* vol. 57, pp. 587-596, 1997.

[205] N. Patel and L. James Lee, “Modeling of Void Formation and Removal in Liquid Composite Molding. Part II: Model Development and Implementation,” *Polymer Composites,* vol. 17(1), pp. 104-114, 1996.

[206] D. H. Lee, W. I. Lee and M. K. Kang, “Analysis and minimization of void formation during resin transfer molding process,” *Composites Science and Technology,* vol. 66, pp. 3281- 3289, 2006.

[207] C. H. Park, A. Lebel, A. Saouab, J. Breard and W. I. Lee, “Modeling and simulation of voids and saturation in liquid composite molding processes,” *Composites: Part A,* vol. 42, pp. 658-668, 2011.

[208] M. Grujicic, K. M. Chittajuallu and S. Walsh, “Effect of shear, compaction and nesting on permeability of the orthogonal plain-weave fabric preforms,” *Materials Chemistry and Physics,* vol. 86, pp. 358-369, 2004.

[209] P. C. Carman, “Fluid flow through granular beds,” *Trans.Inst. Chem Engrs.,* vol. 15, pp. 150-166, 1937.

[210] B. R. Gebart, “Permeability of Unidirectional Reinforcements for RTM,” *Journal of Composite Materials,* vol. 26(8), pp. 1100-1133, 1992.

[211] M. K. Um and W. I. Lee, “A Study on Permeability of Unidirectional Fiber Beds,” *Reinforced Plastics and Composites,* vol. 16(17), pp. 1575-1590, 1997.

[212] M. A. Choi, M. H. Lee, J. Chang and S. J. Lee, “Permeability modelling of fibrous media in composite processing,” *J. Non-Newtonian Fluid Mech.,* vol. 79, pp. 585-598, 1998.

[213] L. Skartsis, J. L. Kardos and B. Khomami, “Resin Flow Through Fiber Beds During Composite Manufacturing Processes. Part I: Review of Newtonian Flow Through Fiber Beds,” *Polymer Engineering and Science,* vol. 32(4), pp. 221-239, 1992.

[214] G. Francucci, E. S. Rodríguez and A. Vázquez, “Study of saturated and unsaturated permeabililty in natural fiber fabrics,” *Composites: Part A,* vol. 41, pp. 16-21, 2010.

[215] H. L. Liu and W. R. Hwang, “Permeability prediction of fibrous porous media with complex 3D architectures,” in *Proceedings of 11th International Conference on Flow Processing in Composite Materials (FPCM11)*, Auckland, 2012.

[216] B. Caglar, D. Salvatori, E. M. Sozer and V. Michaud, “A tool for minimization of race-tracking effects in permeability measurements,” in *Proceedings of 13th International Conference on Flow Processing in Composite Materials (FPCM13)*, Kyoto, 2016.

[217] T. Roy, C. Dulmes and K. M. Pillai, “Experimental investigations of the unsaturated flow in liquid composite molding,” in *Proceedings of the 5th Canadian International Composites Conference*, Vancouver, 2005.

[218] K. M. Pillai and M. S. Munagavalasa, “Governing equations for unsaturated flow through woven fiber mats. Part 2. Non-isothermal reactive flows,” *Composites: Part A,* vol. 35, pp. 403-415, 2004.

[219] Y. de Parseval, K. M. Pillai and S. G. Advani, “A Simple Model for the Variation of Permeabilty due to Partial Saturation in Dual Scale Porous Media,” *Transport in Porous Media,* vol. 27, pp. 243-264, 1997.

[220] K. M. Pillai, “Governing equations for unsaturated flow through woven fiber mats. Part 1. Isothermal flows,” *Composites: Part A,* vol. 33, pp. 1007-1019, 2002.

[221] K. M. Pillai, “Modeling the Unsaturated Flow in Liquid Composite Moling Processes: A Review and some Thoughts,” *Composite Materials,* vol. 38(23), pp. 2097-2118, 2004.

[222] P. Simacek and S. G. Advani, “Modeling resin flow and fiber tow saturation induced by distribution media collapse in VARTM,” *Composites Science and Technology,* vol. 67, pp. 2757-2769, 2007.

[223] F. Zhou, J. Alms and S. G. Advani, “A closed form solution for flow in dual scale fibrous porous media under constant injection pressure conditions,” *Composites Science and Technology,* vol. 68, pp. 699-708, 2008.

[224] PORE-FLOW, http://www.poreflow.com/index.htm.

[225] Liquid Injection Molding Simulation software LIMS, University of Delaware, http://www.ccm.udel.edu/software/lims-software/, 2013.

[226] S. Bickerton, E. M. Sozer, P. Šimáček and S. G. Advani, “Fabric structure and mold curvature effects on preform permeability and mold filling in the RTM process. Part II. Predictions and comparisons with experiments,” *Composites: Part A,* vol. 31, pp. 439-458, 2000.

[227] V. Antonucci, M. Esposito, M. R. Ricciardi, M. Raffone, M. Zarrelli and M. Giordano, “Permeability characterization of stitched carbon fiber preforms by fibre optic sensors,” *eXPRESS Polymer Letters,* vol. 5(12), pp. 1075-1084, 2011.

[228] J. Hu, Y. Liu and X. Shao, “Effect of Stitches on the Permeability of Interbundle Channels in Stitched Fabrics,” *Textile Research,* vol. 73(8), pp. 691-699, 2003.

[229] M. Nordlund and T. S. Lundström, “Numerical Study of the Local Permeability of Noncrimp Fabrics,” *Journal of Composite Materials,* vol. 39(10), pp. 929-947, 2005.

[230] J. Sirtautas, A. K. Pickett and A. George, “Materials characterisation and analysis for flow simulation of liquid resin infusion,” *Applied Composites Materials,* vol. 22, pp. 323-341, 2015.

[231] F. Klunker, S. Aranda, W. Wu, W. Surjoseputro, H. Behnke and G. Ziegmann, “Modelling the Resin Infusion Process, Part I: Flow Modeling and Numerical investigation for Constant Geometries,” *Journal of Plastics Technology 7,* vol. 5, pp. 179-205, 2011.

[232] X. Sun, S. Li and L. James Lee, “Mold Filling Analysis in Vacuum-Assisted Resin Transfer Molding. Part I: SCRIMP Based on a High-Permeable Medium,” *Polymer Composites,* vol. 19(6), pp. 807-817, 1998.

[233] K. T. Hsiao, R. Mathur, S. G. Advani, J. W. Gillespie and B. K. Fink, “A closed Form Solution for Flow during the Vacuum Assisted Resin Transfer Molding Process,” *Manufacturing Science and Engineering,* vol. 122, pp. 463-475, 2000.

[234] A. Gokce, M. Chohra, S. G. Advani and S. M. Walsh, “Permeability estimation algorithm to simultaneously characterize the distribution media and the fabric preform in vacuum assisted resin transfer molding process,” *Composites Science and Technology,* vol. 65, pp. 2129-2139, 2005.

[235] H. Nakatani, K. Adachi and K. Osaka, “Resin impregnation behaviour in thick carbon fibre composite with a corner during VARTM process,” in *Proceedings of 13th International Conference on Flow Processing in Composite Materials (FPCM13)*, Kyoto, 2016.

[236] J. Lugo, P. Simacek and S. G. Advani, “Analytical method to estimate multiple equivalent permeability components from a single rectilinear experiment in liquid composite molding process,” *Composites: Part A,* vol. 67, pp. 157-170, 2014.

[237] F. R. J. Phelan, “Simulation of the Injection Process in Resin Transfer Molding,” *Polymer Composites,* vol. 18(4), pp. 460-476, 1997.

[238] P. Šimaček and S. G. Advani, “Desirable features in Mold filling Simulations for Liquid Composite Molding Processes,” *Polymer Composites,* vol. 24(4), pp. 355-367, 2004.

[239] F. Klunker, S. Aranda, W. Wu, W. Surjoseputro and G. Ziegmann, “Modelling the Resin Infusion Process. Part II: Deformation of Textiles and Applications to VARI Processes,” *Journal of Plastics Technology 8,* vol. 2, pp. 180-205, 2012.

[240] J. F. Kessels, A. S. Jonker and R. Akkerman, “Optimising the flow pipe arrangement for the resin infusion under flexible tooling,” *Composites: Part A,* vol. 38, pp. 2076-2085, 2007.

[241] E. Díaz, C. Sanz and J. A. García, “Validation of flexible permeability characterization methods in numerical simulation of infusion process,” in *Proceedings of 10th International Conference on Flow Processing in Composite Materials (FPCM10)*, Monte Verità, Ascona, 2010.

[242] P. Simacek and S. G. Advani, “An efficient scheme to model resin flow in a deformable porous media using RTM infusion simulation,” in *Proceedings of 12th International Conference on Flow Processing in Composite Materials (FPCM12)*, Twente, 2014.

[243] P. A. Kelly and S. Jennings, “Nonconforming finite elements for liquid composite molding process simulations,” in *Proceedings of the 8th International Conference on Flow Processing in Composite Materials (FPCM8)*, Douai, 2006.

[244] T. G. Gutowski, T. Morigaki and Z. Cai, “The Consolidation of Laminate Composites,” *Composite Materials,* vol. 21, pp. 172-188, 1987.

[245] M. J. Robinson and J. B. Kosmatka, “Vacuum assisted resin transfer molding simulation for thick laminate structures,” in *Proceedings of 49th AIAA/ASME/ASCE/AHS/ASC Structures, Structural Dynamics, and Materials*, Schaumburg, IL, 2008.

[246] S. C. Joshi, Y. C. Lam and X. L. Liu, “Mass conservation in numerical simulation of resin flow,” *Composites: Part A,* vol. 31, pp. 1061-1068, 2000.

[247] PAM-RTM, ESI Software Engineering Systems International, 99 rue des Solets, SILIC 112, 94513 Rungis Cedex, France, 2006.

[248] RTM-Worx flow simulation software and Controlled Vacuum Infusion technology POLYWORX, Netherlands, http://www.polyworx.com/pwx.

[249] myRTM Program for simulating the mould-filling phase of the Resin Transfer Molding (RTM) process, Hochshule für Technik Rapperswil, Institut für Werkstofftechnik und Kunststoffverarbeitung (IWK), https://www.myrtm.ch.

[250] J. Slade, E. M. Sozer and S. G. Advani, “Fluid impregnation of Deformed Preforms,” *Reinforced Plastics and Composites,* vol. 19(7), pp. 552-568, 2000.

[251] E. Heardman, C. Lekakou and M. G. Bader, “In-plane permeability of sheared fabrics,” *Composites: Part A,* vol. 32, pp. 933-940, 2001.

[252] SAERTEX GmbH & Co.KG, https://www.saertex.com.

[253] HexForce® and HexPly® Aerospace Selector Guide, http://www.hexcel.com/Resources/SelectorGuides/Aerospace_SelectorGuide.pdf.

[254] Flugzeug-Union Süd GmbH, http://www.fus.de/.

[255] EPIKOTE™ Resin MGS_ LR 235 and EPIKURE™ curing agent MGS_ LH 233-238. Technical data sheet. Momentive Specialty Chemicals Inc., www.hexion.com.

[256] Aerospace, unidirectional carbon fibre-epoxy sheet and tape prepreg, technical specification, Norm DIN29971; 1991-09.

[257] ARAMIS digital image correlation measuring system, http://www.gom.com/de/messsysteme/aramis.html.

[258] WELA Handelsgesellschaft GmbH, http://www.wela-handelsgesellschaft.de/cms/en/node/132.

[259] Novoflow GmbH, http://www.novoflow.com/.

[260] PAM-FORM Theory Guide, ESI Software Engineering Systems International, 99 rue des Solets, SILIC 112, 94513 Rungis Cedex, France, 2006.

[261] D. S. Ivanov, C. Van Gestel, S. V. Lomov and I. Verpoest, “In-situ measurements of fabric thickness evolution during draping,” in *Proceedings of Esaform Conference*, Belfast, UK, 2011.

[262] PAM-CRASH, ESI Software Engineering Systems International, 99 rue des Solets, SILIC 112, 94513 Rungis Cedex, France, 2006.

[263] A. Endruweit, P. McGregor, A. C. Long and M. S. Johnson, “Johnson MS. Influence of the fabric architecture on the variations in experimentally determined in-plane permeability values,” *Composites Science and Technology,* vol. 66, pp. 1778-1792, 2006.

[264] R. Chen, C. Dong, Z. Liang, C. Zhang and B. Wang, “Flow modeling and simulation for vacuum assisted resin transfer molding process with the equivalent permeability method,” *Polymer Composites,* vol. 25(2), pp. 146-164, 2004.

[265] T. Ishikawa, R. Matsuzaki, T. Okabe and S. Yashiro, “Meso-structure optimisation of non-crimp fabric for resin transfer molding,” in *Proceedings of 13th International Conference on Flow Processing in Composite Materials (FPCM13)*, Kyoto, 2016.

Appendices

Appendix I: Resin viscosity diagrams

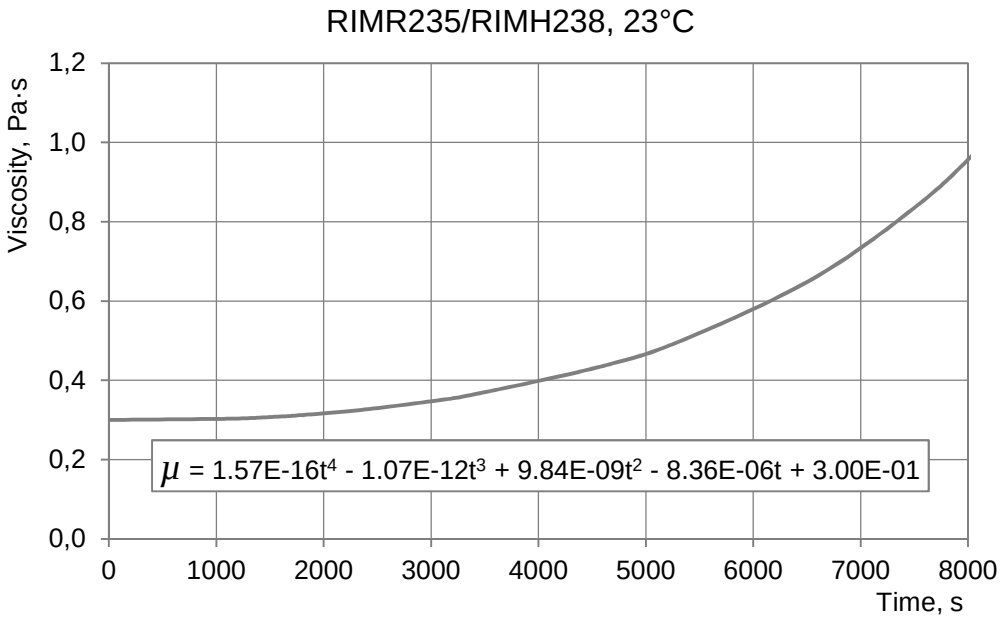

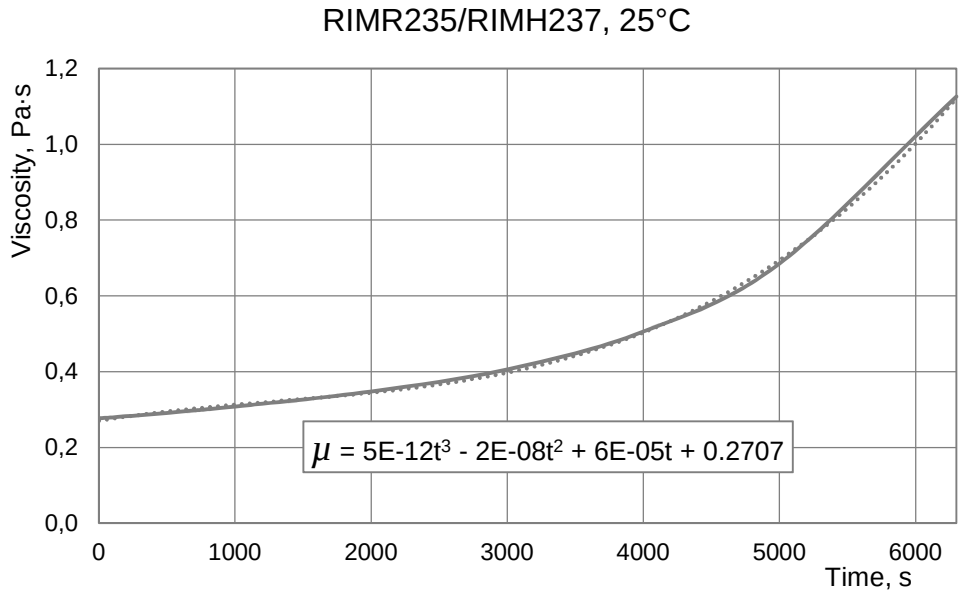

Appendix II: Picture frame dimensions

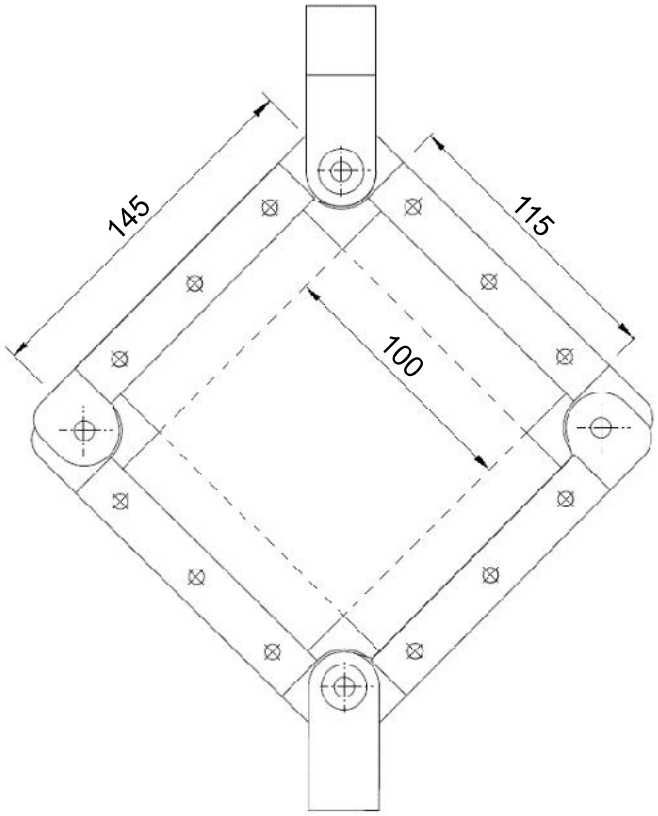

Appendix III: Biaxial NCF shear model input

Biaxial NCF shear stiffness versus shear angle diagram obtained from test

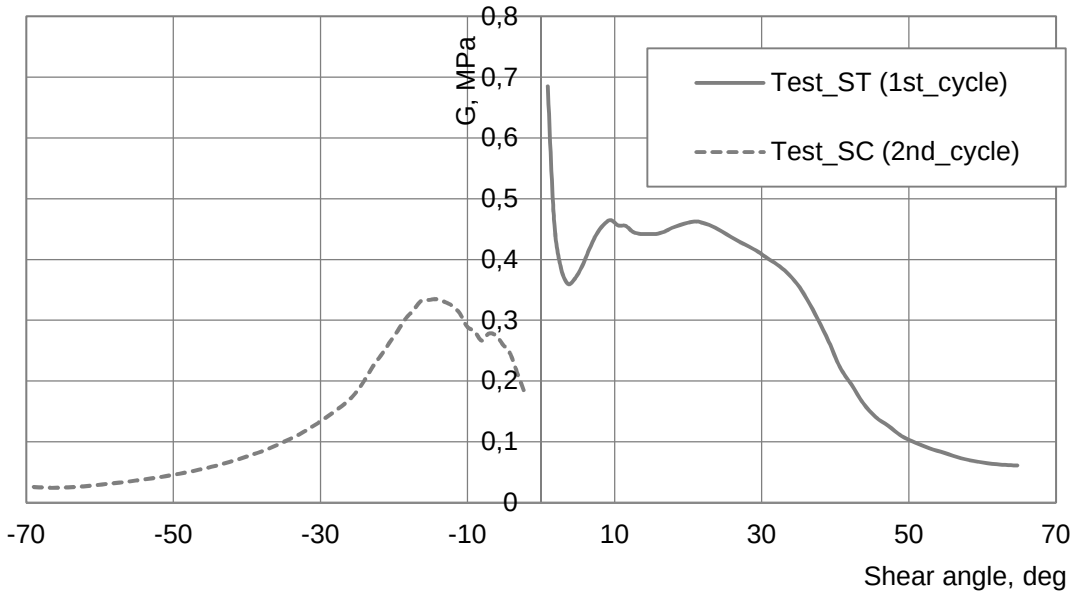

Initial and calibrated biaxial NCF shear stiffness characterisation input curves

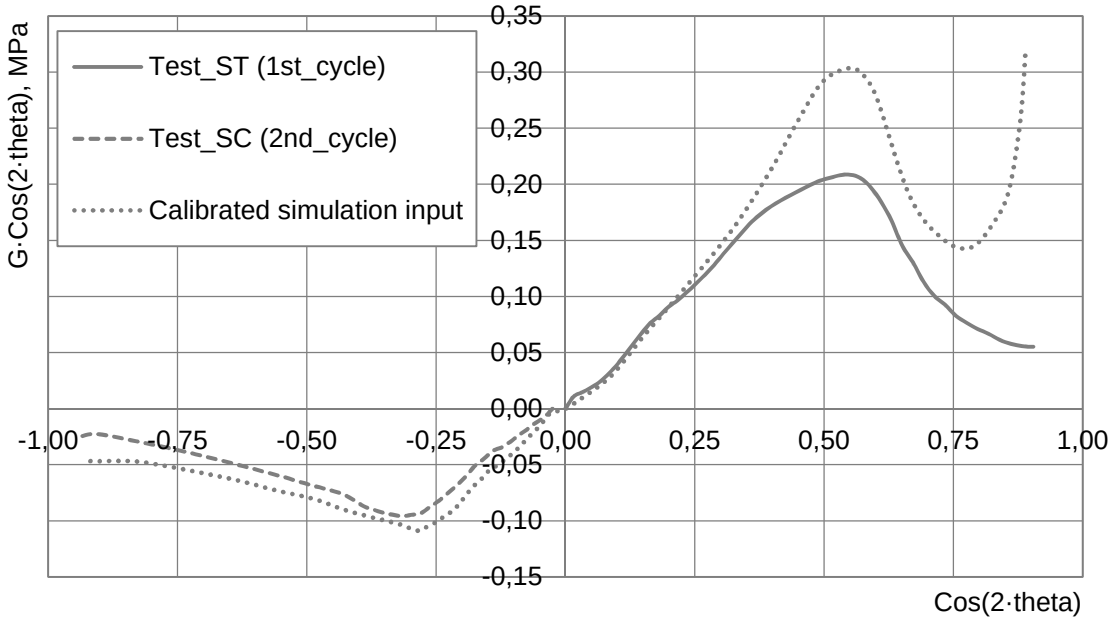

Index of Figures

Index of Tables